UNIVERSITÉ DE STRASBOURG

Laboratoire des Systèmes Photoniques

École Doctorale Mathématiques, Sciences de l'Information et de l'Ingénieur

**UdS – INSA – ENGEES**

# THÈSE

présentée pour obtenir le grade de

**Docteur de l'Université de Strasbourg**
**Spécialité : Photonique**

par

**Cédric Perrotton**

# Design et développement d'un capteur à fibre optique pour la détection d'hydrogène

Soutenue publiquement le 13 janvier 2012

**Membres du jury**

| | |
|---|---|
| Professeur Hans ZAPPE | Président/Rapporteur |
| Professeur Serge HABRAKEN | Rapporteur |
| Professeur Bernard DAM | Examinateur |
| Docteur Daniel HUSSON | Examinateur |
| Docteur Nicolas JAVAHIRALY | Examinateur |
| Docteur Oudea Coumar | Membre invité |
| Professeur Patrick MEYRUEIS | Directeur de thèse |

**Laboratoire des systèmes photoniques** **EA 3426**

# Acknowledgement

This work has been done in the Laboratoire des Systèmes Photonique at the Uniersity of Strasbourg, and in collaboration with the MECS group at TuDelft. A part of this work has be done in the Griessen's group, at the Vrije University of Amsterdam. This work was funding by the region Alsace. The funding from the Nederlandse Organisatie voor Wetenschappelijk Onderzoek NWO through the Sustainable Hydrogen Programme of Advanced Chemical Technologies for Sustainability program is gratefully acknowledged.

I would like to thank the members of my reading committee, Prof. Hans Zappe, Prof. Serge Habraken, Prof. Bernard Dam, Dr. Daniel Husson, Dr. Nicolas Javahiraly, Dr. Oudea Coumar and Prof. Patrick Meyrueis for taking the time to assess my manuscript. Your advices were greatly appreciated.

I would like to gratefully and sincerely thank all people who participate to this work. First of all, I would like to thank Prof. Patrick Meyrueis, Ayoub Chakari and Nicolas Javahiraly for supervising this work. I have really appreciated their confidence in me. I would like to thank Prof. Bernard Dam for welcoming me in his team in Delft and supervising my work. I gratefully thank him for his criticisms and his corrections. I would like to thank Prof. Ronald Griessen for accepting me as a scientific visitor in his group in Amsterdam, which gave me the opportunity to develop this experience abroad. I would like to sincerely thank Martin Slaman and Herman Schreuders for their great help ! They contributed a lot to the experimental work and most of it let me a place to work. Thanks to Ruud Westerwaal and Thijs Mak for their help on the Mg-Ti experiments. It has been very nice working with you. I would like to thank Pierre Pfeiffer, Sylvain Lecler, Yoshi Takakura, Marek Basta, Victorien Raulot, Bruno Serio, Lennard Mooje, Ali Dabirian, Arjen Didden, Yevheniy Pivak, Valerio Palmisano, Andrea Baldi, Matteo Filippi and Joost Middelkoop for their help and useful talks. A special thanks to Marc Beuret for his support.

During this strange adventure that a phd is, I have met a lot of people that make this adventure pleasant, hopefully. I would like to thanks all of you. Dhwajal Chavan, Grzegory Gruca, Jan H. Rector, Kier Heeck, David Iannuzzi and the Italian team, I spent a very nice time in Amsterdam thanks to you. Thanks to my colleagues at the MECS group who helped me to fit and enjoy my new dutch living environment. It was a real pleasure to work there : discussing results in group meeting, chatting, eating cake and drinking coffee... enjoying a sunny borrel by eating a French cheese ! A great thanks to my colleagues at the Laboratoire des Système Photonique for their encouragements.

Finally, I would like to thank Héloïse Quillay for believing in me and my family for everything...

## Résumé

La détection de l'hydrogène est une priorité environnementale. De nombreux capteurs à hydrogène ont déjà été développés, mais aucun d'eux ne répond aux exigences de l'industrie. Les capteurs à fibres optiques, électriquement isolés, sont d'excellents candidats pour fonctionner dans des environnements explosifs. Notre objectif est de développer un capteur à fibres optiques intrinsèque par Résonance de Plasmon de Surface pour la détection d'hydrogène. Dans cette thèse, nous étudions deux designs de capteurs à hydrogène. Le premier, basé sur la modulation d'amplitude, se compose d'une couche mince de Pd déposé sur le coeur de la fibre multimode, après avoir enlevé la gaine optique. Dans le second, basé sur la modulation de longueur d'onde, nous remplaçons la couche de Pd par un empilement de couches (Au / $SiO_2$ / Pd). Dans cette thèse, nous démontrons que les capteurs plasmoniques peuvent être une solution pour développer des capteurs à hydrogène fiables et rapides. Enfin, nous étudions des alliages de Mg comme matériaux sensibles à l'hydrogène afin d'optimiser la plage de détection des capteurs à hydrogène.



## Abstract

Hydrogen detection is an environmental priority. Numerous hydrogen sensors have been developed, but none of them meet the industry requirements. Optical fiber sensors, electrically isolated, are excellent candidates for operating in explosive environments. Our goal is to develop an intrinsic optical fiber sensor based on Surface Plasmon Resonance. In this thesis, we study two optical fiber hydrogen sensors. The first sensor, based on amplitude modulation, consists of a thin Pd layer deposited on the multimode fiber core, after removing the optical cladding. The second design, based on wavelength modulation, consists of replacing the single Pd layer by a Au/ $SiO_2$/ Pd multilayer stack. We demonstrate in this thesis that plasmonic sensors may be a solution to develop fast and reliable fiber hydrogen sensors. Finally, we study Mg alloys as hydrogen sensitive material in order to improve the detection range of hydrogen sensors.

# Content

# Introduction

## Introduction

« It appears [...] that the air produced from sugar by fermentation, as well as discharged from marble by solution in acids, consists of substances of different nature », H. Cavendish.

Henry Cavendish produced artificially the hydrogen gas from the Paracelse's work, and considered it as a discrete substance in 1766. He discovered, in particular that the combustion of this substance produces water in 1781. Defined as « inflammable air », Lavoisier called it later Hydrogen, « hydro »and « gen »" come from the Greek water and engender respectively. Hydrogen is constituted of two hydrogen atoms which are the simplest atom known (one electron and one proton) and the most abundant chemical element, account for about 75% of the total mass of the Universe.

Hydrogen is used in diverse industry, such as chemical, pharmaceutical, food, semiconductor and aerospace industry. However, industry based on the use of gaseous hydrogen meet safety issue due to the physical, chemical properties of hydrogen and the operating pressure and temperature range [1].

- Hydrogen is a flammable and highly explosive gas. The lower flammability point of hydrogen is 4 % in air and with an upper limit of 74.5%. Hydrogen accidents can cause fire, detonation and deflagration. For example, in 2011 during the nuclear Fukushima Daiichi disaster hydrogen explosions destroyed the upper cladding of the building housing reactors.

- The hydrogen ignition energy in air is really low : 0.02 mJ. A valve closing may be a source of ignition.

- Being the lightest and the smallest molecule, hydrogen is prone to leak through seals and micro-cracks. Some accidents have already occurred from mechanical failures of the containment vessels, piping, or auxiliary components (brittle failure, hydrogen embrittlement, or freeze-up). Accidents may also happen due to reaction of the fluid with a contaminant, failure of a safety device and operational error [2].

As a colorless, odorless and tasteless flammable gas, hydrogen cannot be detected by human senses. Specific devices are therefore required to detect the dangerous presence of hydrogen. This thesis is devoted to the development of a new hydrogen sensing method based on optical fiber properties to detect hydrogen leaks.

## Context

The first application of hydrogen was for transportation. In the same year than the Mongolfier brother, Alexandre Cesar Charles made a first flight with a balloon filled with hydrogen. The fire tragic accident of Hindenburg airship in 1937, where 35 passengers

died, marked the end of the airship era. Although the accident was not caused directly by hydrogen, the idea of using hydrogen as energy carrier for public balloon transportation had been discarded. Hydrogen was then replaced by helium in balloon airship.

In parallel, the internal combustion engine put on a back shelf the fuel cell invented by Hamphry Davey in 1806 and realized then by Groove in 1839.

Although the NASA has shown the potential of hydrogen on an energy carrier for the shuttles and other space vehicles during last decades, the use of Hydrogen has been limited to chemical, pharmaceutical, food and semiconductor industry. The world hydrogen consumption, about 50 millions of tons per year, is far beyond the coal consumption, that is about 7 billion tons and is expected to reach 10 billion tons by 2030.

Nowadays, hydrogen is presented by some experts as the sustainable energy carrier of the future. The cycle of hydrogen is one of the most ecologic energy solutions. Hydrogen may be produced from the electrolysis of the water from a renewable source like solar electricity. The combustion of hydrogen produces then water, which can be used again for hydrogen production. While wind, sun and nuclear power plants produce electricity intermittently, hydrogen may be stored and converted in electricity on demand. In addition, hydrogen energy may be used as an energy buffer for intermittent energy sources. Finally, hydrogen may be used to produce, store and transport energy. The possible applications are wide ranging. They will spread from public transportation such as automotive to consumer products like batteries for mobile telephones.

Improving the efficiency of the production and storage technologies, reducing therefore the cost, are the major challenges to make possible the « hydrogen economy ». However, safety issues have to be solved in order to use hydrogen as energy on the common life. Hydrogen safety program have been developed to define new codes and standards to guarantee a safe public use of hydrogen technology. One of the measures to be considered is to implement higher safety standards like early leak detection by using smart hydrogen sensors. This new demand of reliable hydrogen sensors boosts the hydrogen sensor research. This interest increase is reflected by the growing number of publications in the last 10 years, shown in fig. 1.

In conclusion, although the hydrogen economy is currently debated and may reveal unsuccessful [3], experts are agree that future hydrogen applications will be effective and abundant. These applications require hydrogen sensors to monitor/control the hydrogen concentration and detect the possible leaks in hydrogen energy systems.

Numerous hydrogen sensors have been already developed. We can classify them into four categories.

**Mass spectrometer sensors :** Mass spectrometry consists of ionizing hydrogen. Ions are separated based on mass in a magnetic field. The mass spectrum is then used to identity and quantify the hydrogen concentration.

**Spectroscopic sensors :** They detect chemical elements by analyzing electromagnetic vibrations. Hydrogen detection can be performed either by Raman spectroscopy or laser plasma induced breakdown spectroscopy. Infrared spectroscopy cannot be used due to the symmetry of the hydrogen molecule. For safety issue the UV spectroscopy is not usable because of the hydrogen absorption spectrum.

**Acoustic sensors** : They are based on the difference in the density and the speed of sound in presence of hydrogen. They are not really design for hydrogen leak detection and show low sensitivity and selectivity.

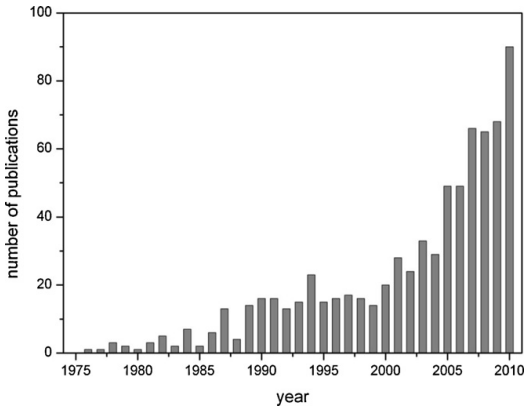


FIGURE 1 – Growth in hydrogen sensor publication since 1976 according to an inquiry in ISI Web of Knowledge, Thomson Reuters, from [4].

« **Chemisorbing** » sensors, mainly represented by solid state sensors, ecompass all devices based on the response of a material/layer sensitive to hydrogen. Measuring the physical and/or chemical changes of the sensing layer gives access to the hydrogen concentration. The measurand is either the conductivity, the thermal conductivity, the electrochemical potential, the work function, the velocity, the mechanical properties or the optical constant. Examples of chemisorbing sensors are : pellistor, thermoelectric, calorimetric, amperometric, potentiometric, cantilever, Metal-Oxide (Mox), Schottky diode, Metal Oxide Semiconductor (MOS) field effect transistor, ..., optical fiber sensor.

Mass spectrometry techniques are widely used for hydrogen detection. However, due to their bulky size and expensive cost, companies search for a better industrial hydrogen sensor. Their difficulties to be embedded as a measuring device made also them an unadaptable solution for industry. For example, in the aerospace shuttle, the gas has to be transported through pipes from the bottom of the shuttle to the analyzing part of the mass spectrometer located at the top. As a result, the response time obtained is slower than required for being optimal [5]. Mass as well as optical spectrometers are in fact more suitable for monitoring than for detecting hydrogen leaks.

In contrast « Chemisorbing »sensors appear as a solution to meet company needs. Solid state sensors are mass produced, inexpensive and already recognized for many sensing applications. This type of sensor is discussed in about 65 % of the hydrogen sensors papers recently published [4]. They show generally a high sensitivity (around hundred ppm) and a good selectivity (with a protective layer to sulfuric damages) with a relatively fast response (inferior to a few second, for the last generation), as described in Tab. 2.

Nonetheless, none of the available commercially or laboratory made hydrogen sensors meet all the specifications demanded for instance by the US Department of energy, given in Tab. 1. All of them exhibit limitations in one or more criteria for being an ideal hydrogen sensor. The optimal sensor will depend on the application and the operating conditions.

**Table 6 – Summary of performance data for each type of commercially available sensor considered in the market survey.[a]**

| Criteria | MOS | | TCD | | CAT | | EC | | MOx | | COMB | | OPT | |
|---|---|---|---|---|---|---|---|---|---|---|---|---|---|---|
| | Min | Max | Min | Max | Min | Max | Min | Max | Min | Max | Min | Max | Min | Max |
| Temperature range (°C) | −40 | 110 | −40 | 55 | −40 | 82 | −40 | 80 | −40 | 80 | −40 | 125 | −15 | 50 |
| Pressure range (kPa) | 70 | 130 | 80 | 120 | 70 | 130 | 90 | 110 | 80 | 120 | 70 | 130 | 75 | 175 |
| Humidity range (% RH) | 5 | 95 | 0 | 99 | 0 | 100 | 10 | 95 | 0 | 100 | 0 | 95 | 0 | 95 |
| Measuring range (ppm) | 200 | 44,000 | – | 100% | – | 40,000 | 15 | 50,000 | 10 | 48,000 | 10 | 100% | 1000 | 100% |
| Response time ($t_{90}$ s) | 2 | | 10 | | 8 | | 5 | | 4 | | 10 | | 60 | |
| Recovery time ($t_{10}$ s) | 10 | | 10 | | 10 | | – | | 10 | | – | | – | |
| Power consumption (mW) | 675 | | 350 | | 256 | | 2.25 | | 150 | | 720 | | 1080 | |
| Lifetime (h) | 87,600 | | 43,800 | | 43,800 | | 26,280 | | 43,800 | | 87,600 | | 44,000 | |

a Where omitted, data were not available from the manufacturer's specifications.

FIGURE 2 – Hydrogen sensor performances from [6]. The principles are described in appendix 1.

| | |
|---|---|
| Sensitivity | 0.1-10% $H_2$ in air |
| Temperature range | -30-80 ∘C |
| Response time | $<$1 s |
| Accuracy | 5% |
| Gas environment | ambiant air, 10-98 % RH range |
| Lifetime | 5 years |
| Selectivity | Prevent interference from hydrocarbon |

TABLE 1 – US Departmental of Energy specification

## Scope and contribution

Hydrogen sensors are required for monitoring hydrogen concentration, detecting hydrogen leaks and hydrogen pre-fires. In this thesis, we focus only on the hydrogen leak detection for general applications.

Contrary to « chemisorption »sensors relied on electrical circuits, optical fiber sensors (O.F.S) are electrically isolated which makes them better suited for operating in explosive environments. There is no risk of gas ignition : the optical fiber sensor has no electrical contacts and does not generate sparks nor relies on heat exchange. Ignition sources reported included mechanical sparks from rapidly closing valves, electrostatic discharges in ungrounded particulate filters, sparks from electrical equipment, welding and cutting operations, catalyst particles, and to lightning strikes [7].

Moreover, the advantages of optical fibers such as geometrical configuration (small dimensions, light weight, geometrical versatility), simplicity of design, remote sensing capability and possibility of distributed or multi-points detection have led many research work to elaborate such sensors.

Numerous optical fiber hydrogen sensors have been already developed based on light phase, polarization, amplitude and wavelength modulation for the last 25 years. However, they are not yet mature in comparison with electrical sensors. O.F.S show actually limitations in order to combine high sensitivity with fast and reproducible response.

The objective of this thesis is to « *d*esign, realize and characterize an optical fiber sensor for hydrogen leak detection ». Based on the state of the art, we have seen that sensors based Pd thin film show a faster and a more reproducible response than sensors based on thick films. That's why, we have decided to focus all our efforts on hydrogen optical fiber evanescent wave sensors based on thin films. In particular, we discuss, here, the potential of Surface Plasmon Resonance (SPR) sensors based on optical fibers for hydrogen detection. Plasmonic sensors appear as a promising trade off between sensitivity and response time. Besides, the advantages of optical fibers sensors remain such as : simplicity of design, multiple sensing points, industrious and low-cost. Finally, we will combine the technology realized with different materials sensitive to hydrogen such as Mg alloys in order to improve the minimal sensing performances and the detection range. Although the cross-sensitivity, related to the material catalytic properties, is also a main issue, it is out of the scope of this thesis.

In summary, this thesis discuss the following questions :

1. What are the best intrinsic optical fiber sensor configurations for hydrogen leak detection ?
2. Which materials have suitable hydrogen sensing properties ?
3. What are the effective possibilities of SPR fiber sensors in the hydrogen sensing domain ?
4. What are the minimal detection level and the dynamic range of the hydrogen sensors realized ? Is it possible to reliably quantify the hydrogen concentration ?

## Organization of this thesis

**Chapter 1** gives an overview of all the existing techniques based on optical fibers to detect and measure hydrogen concentration. The first part explains the principles and describes the performance of Pd optical fiber sensors. Issues for hydrogen sensing are sensitivity, dynamic range, response time and cross-sensitivity. We will compare the response of some sensors to find the most optimal sensor configuration. The second part describes the various materials for sensing in the literature, such as metal alloy hydrides and oxide materials.

**Chapter 2** describes first the theory of Surface Plasmon (SP) and explains why SP Resonance (SPR) can be seen as a promising technique for sensing applications. Finally, we will present an overview ranging from SPR sensors to fiber SPR sensors.

**Chapter 3** focuses on the materials and the methods used in this thesis. We present how we simulate the fiber sensor responses, and how we fabricate and characterize the sensors.

**Chapter 4** presents the response of a Pd-coated multimode fiber sensor that we have fafricated. In this design, a thin Pd layer is deposited on the outside of a multimode fiber core, after removing the optical cladding. We report the total intensity transmitted from the optical fiber, when all the modes are excited, as a function of the hydrogen concentration. The response time and the reproducibility of the sensor response are presented, as well as the effect of $O_2$, to validate the possibility of using this sensor for effective safety applications. Then, a comparative study between our experimental and theoretical results explains how the SP excited at the Pd air interface plays a role on the response. The last

part discusses the optimization and the potential advantages and limitations of such a sensor.

**Chapter 5** proposes a SPR fiber hydrogen sensor design based on wavelength modulation. The sensor consists of replacing on an optical fiber the Pd transducer by a multilayer stack made of Ag, $SiO_2$ and Pd. This structure allows coupling the SP in the NA fiber and takes hence full advantage of the SP sensing. In the first part, we present theoretically the principle of this sensor and the optimization of the proposed structure. The second part demonstrates experimentally the response of this hydrogen sensor.

**Chapter 6** proposes to use a Mg alloys thin film to extend the dynamic range and to decrease the minimal detection of hydrogen sensors . The first part presents the response of a Mg alloys coated on a core of a multimode fiber. We describe the properties of Mg alloys for different film thicknesses 10 and 50 nm. The second part compare the theoretical and experimental response of the previous SPR design with Mg alloys as sensitive layer instead of Pd.

Finally, we conclude this thesis on the performance obtained for hydrogen SPR sensors, their potential in industrial uses and the future perspectives.

# Chapter 1

# Analysis review of optical fiber hydrogen sensors

## 1.1 Introduction

An optical fiber has the fundamental property to guide the light from the input to the output of the fiber. The light guidance is based on the principle of the total internal reflection of the light between two transparent media having different refractive index. Colladon and then Tyndall demonstrated that the light propagates along the curve of the water jet (fig. 1.1b) when the light is injecting into the stream of falling water.

A classical optical fiber is constituted by two cylindrical guides having the same revolution axis. The inside guide called the « core »has a refractive index ($n_c$) inferior to the outside guide ($n_g$) called the « cladding ». Typically, the core and the cladding are made of silica, while the latter is doped (e.g by a germanium dioxide) in order to realize the difference of refractive index. The cladding is usually protected with a polymer coating and a jacket. The coating provides flexibility and robustness to a silica fiber. Due to the intrinsic energy losses in the material, the light is attenuated during the propagation. Optimization engineering in optical fiber consists of improving the light propagation with maintaining the flexibility of the fiber.

The light propagation is described by propagation laws. That is to say that the guided light satisfies the wave equations in the both fiber media : the core and the cladding. The propagation characteristics and the field distributions of the guided waves must satisfy the boundary conditions at the interface of two different media and the radiation condition for fields that extend to infinity [8]. Thus, the eigenmodes of the Maxwell equation define the existence of guided modes, characterized by a propagation constant that is function of the frequency ($\beta(w)$). For example, fig. 1.2 shows the intensity patterns of the guided modes of a step-index multimode fiber. Any light propagating in an optical fiber can be considered as a superposition of different waveguide modes. The number of modes is determined by a normalized frequency V :

$$V = \frac{2\pi}{\lambda} aNA \tag{1.1}$$

where $\lambda$ is the wavelength of the propagating light and a is the radius of the core of the optical fiber. Typically, we can distinguish two kinds of classical optical fibers from their mode structures : multimode and single mode fibers. For V inferior or equal to 2.405, the optical fiber supports only one mode. Straightforward, single mode fibers present a small diameter (inferior to 8 $\mu$m) while the multimode fibers have a typical diameter of

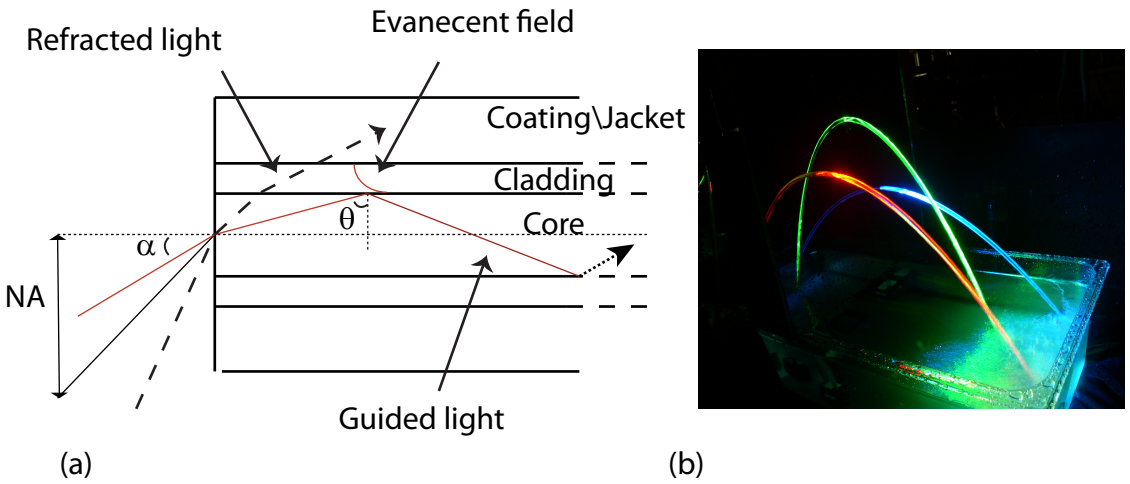


Figure 1.1 – (a) Schematic propagating ray through an optical fiber via total internal reflection at the core-cladding interface (b) Light fountain, reproduced with permission of Sébastien Forget (université paris 13/CNRS).

100 $\mu$m. It is interesting to note that the the light can be described with a ray analysis for multimode fibers because of the large dimensions of the core compared to the wavelength of the light. The guided modes are finally associated to « bound ray » [9] : a bound ray defines a group of mode having the same propagation constant $\beta$ (degenerate modes). For a step index multimode, the propagation constant is associated to the injection angle $\alpha$, by :

$$\beta = \frac{2\pi}{\lambda} n_{core} cos(\theta) \ , \ with \ \ \theta = \frac{\pi}{2} - \arcsin(\frac{n_0}{n_{core}} \sin\alpha) \tag{1.2}$$

with $n_0$ the refractive index of the medium surrounding the optical fiber. Assuming a ray approach, fig. 1.1a shows a possible way for a meridian ray propagating through the optical fiber, injected with an angle $\alpha$. Most of the energy is confined in the optical fiber core. However, a non negligible part of the light energy is also transported via the optical cladding as an evanescent wave. At every total reflection, the reflected light is indeed associated with an evanescent wave, which decreases exponentially in the cladding. The criterion of total reflection limits the angle of incidence of the propagating light through the optical fiber. The numerical aperture of an optical fiber (NA) defines the limit angle ($\alpha_c$) where the rays can propagate in the fiber :

$$NA = n_0 sin(\alpha) = \sqrt{n_c^2 - n_g^2} \tag{1.3}$$

Optical fibers serve mainly in telecommunication for high band pass transmission over a long distance, but optical fibers have been lately used for sensing applications. In this context, we study in this thesis the use of optical fibers as sensor for detecting hydrogen leak.

An optical fiber sensor is a sensor in which the physical quantity (temperature, pressure, strain, etc.) to be measured modulates the transmitted light. We distinguish intrinsic and extrinsic optical fiber sensors (O.F.S) as depicted in fig.1.3.

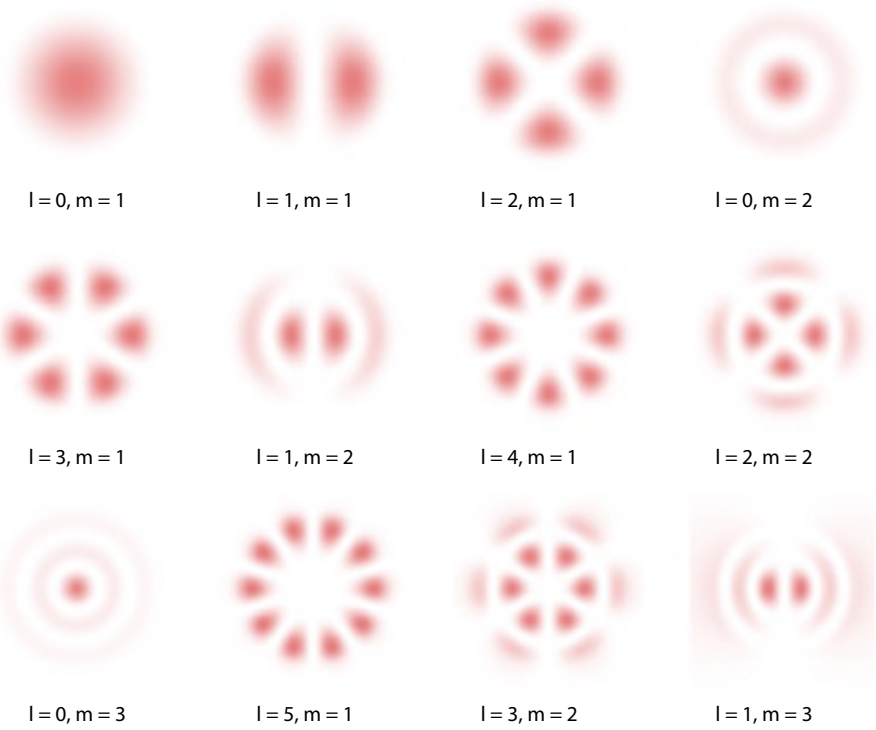


Figure 1.2 – Intensity profiles of the modes of a step-index multimode fiber, linear polarized ($LP_{lm}$) [10].

**Extrinsic fiber sensors** : the optical fiber acts as a simple guide to collect and lead the light to and from the transducer (that will modulate the light). The transducer is either set between two optical fibers for transmission measurement or is positioned on one end of the optical fiber for reflective measurement. For hydrogen detection, the transducer modulates the propagating light when it interacts with hydrogen.

**Intrinsic fiber sensors** : the optical fiber itself is the transducer. The modulation of the light results from the modulation of the opto-geometrical and physica properties of the optical fiber. This deformation results from exterior constraints applied to the optical fiber. Paradoxically, the optical fiber is generally recognized in telecoms for its insensitivity to the exterior pertubations. The challenge for designing O.F.S is to make the optical fiber only sensitive to the parameter that is to be measured. For hydrogen detection, the response to hydrogen is made possible by depositing a hydrogen sensitive layer on the core or cladding of an optical fiber. The hydrogen interaction with the sensing layer results in changing the optical properties of the fiber, inducing a light modulation. By measuring this modulation, we measure the hydrogen concentration.

For hydrogen detection, the existing hydrogen O.F.S use mostly Palladium (Pd) as transducer due to its high catalytic activity and high solubility of hydrogen [11]. Pd has the ability to dissociatively split and absorb hydrogen. Rare-earth (Ytterbium), Magnesium (Mg) based alloys [12, 13] or oxide materials (tungsten oxide ($WO_3$) [14, 15, 16], vanadium ($V_2O_5$) [17] ) are a possible alternative to Pd, but they still require Pd to dissociate hydrogen or to prevent oxidation. Recently, it has been shown that the use of Pd

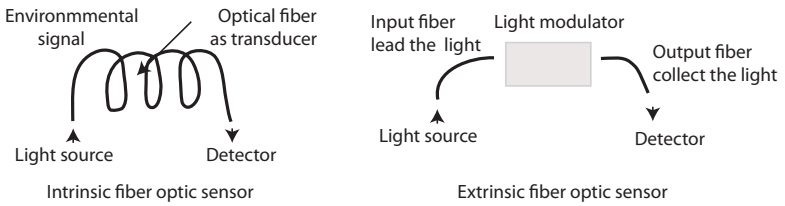


Figure 1.3 – Principle of intrinsic and extrinsic fiber.

alloys may improve the cross-sensitivity performance of the sensor.

We present, here, a review of optical fiber hydrogen sensors based on Pd. Pd can be considered as a « model »for other metal hydride systems. Besides, the Pd hydrogen systems are well characterized in bulk [11, 18], cluster [19, 20] or thin film [21] forms. In the first part, we focus on the principles of hydrogen O.F.S. We discuss then their performance regarding their configurations. The choice of a sensitive material is discussed in a third parts. Finally, we conclude by introducing the challenges for designing an ideal hydrogen O.F.S based on a metal hydrides approach, and which designing direction seem the best to take.

## 1.2 Pd hydrogen sensing systems

### 1.2.1 Bulk Palladium film

Pd forms a metal hydride (M-H) when it absorbs hydrogen atoms [11]. The reaction is exothermic, $\Delta H = -19kJ.(mol.H)^{-1}$. The hydrogenation process consists of the following steps :

1. physisorption at the surface,
2. dissociation of the hydrogen molecules into atoms and chemisorption,
3. surface penetration of hydrogen atoms : hydrogen atoms diffuse from a surface site to a subsurface site,
4. diffusion of hydrogen atoms through the metal layer,
5. hydride formation (and a diffusion through the hydride metal)

The hydrogenation process is reversible, and shows an hysteresis between the ab- and the de-sorption. The pressure composition isotherms (pcT) of a Pd-H system define the thermodynamic equilibrium of the hydride formation. Figure 1.4 shows the Pd pcTs for different temperatures. For temperatures lower than the critical temperature, we observe two regimes separated by a pressure plateau. Each regime corresponds to a phase called $\alpha$ and $\beta$. The pressure plateau corresponds to the phase transition, where both phases coexist.

**$\alpha$ phase :** With a low hydrogen pressure, hydrogen behaves as a gas in the host metal lattice. The hydrogen is diluted into the Pd lattice ; the so-called $\alpha$ phase. The hydrogen atoms occupy randomly, or in ordered way the interstitial sites (octahedral sites) of the f.c.c Pd at high and low temperature, respectively [23]. At room temperature, the solubility is smaller than 0.01. The solubility defines the number of hydrogen atom in the host metal

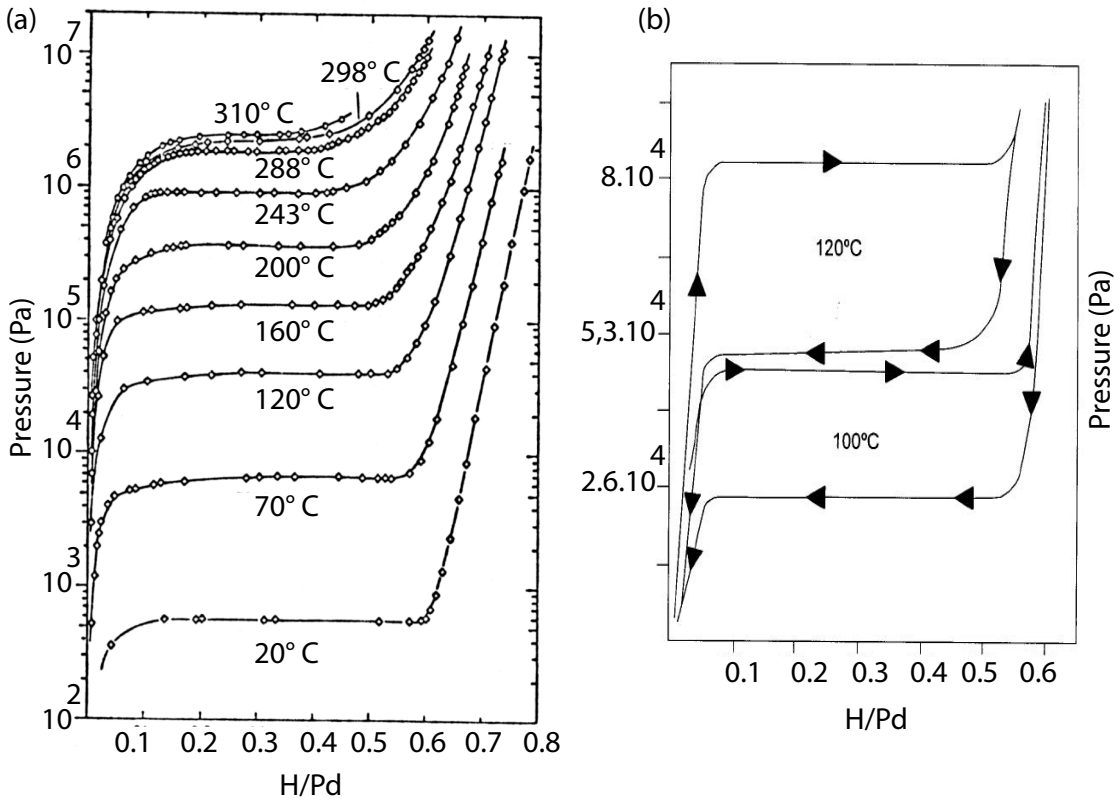


Figure 1.4 – (a) Pd Pressure composition isotherm for H in Pd [22, 18]. (b) Example of hysteris in a Pd thick film [11]

lattice (H/Pd). The solubility is related to the externally applied hydrogen pressure with the Sieverts' constant $k_{Sieverts}$, where the H-H interaction is neglected :

$$C_H = k_{Sieverts}\sqrt{P^{\circ}_{H_2}} \tag{1.4}$$

where $C_H$ is the equilibrium hydrogen concentration in the metal (i.e solubility).

$\beta$ **phase :** At higher concentration, and below the critical temperature, the H atoms are located in all the available interstitial site. Small zones of large hydrogen concentration are formed due to the H-H attractive interactions. The hydrogen can not be longer described as a gas in the host metal lattice. When the hydrogen pressure increases above the pressure plateau, the metal lattice expands due to the H-H interactions. The growth of the lattice structure offers new sites for hydrogen atoms, which then induce again its expansion due to new H-H interactions. The metal hydride is in the transition phase region. Hydrogen atoms diffuse then into this dense phase to reach equilibrium ; the so-called $\beta$ phase. We emphasize that the lattice structure might change for hydrides of other metals than Pd.

**Phase transition** The $\alpha$-$\beta$ phase separation takes place a constant external gas pressure, which result in a presence of a pressure plateau in pct. The $\alpha$ and $\beta$ phase are in equilibrium. Thus, the Van' t Hoff equation characterizes the pressure plateau and shows its temperature dependence :

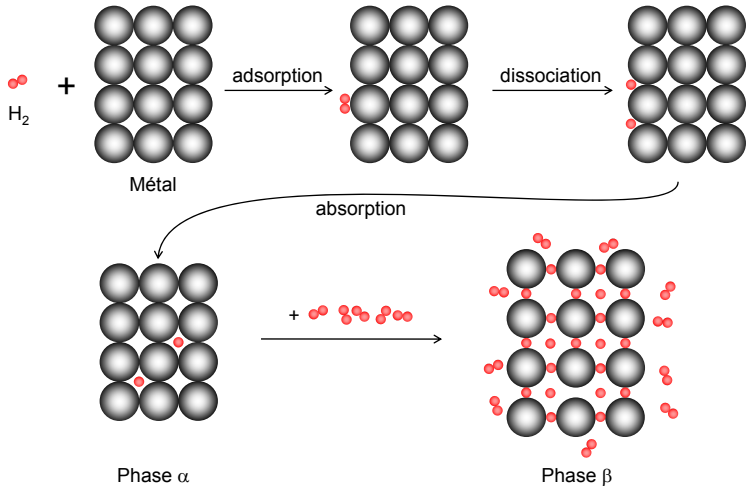


Figure 1.5 – The schematic description of the hydrogenation of Pd [24].

$$p_{plateau} = p_0.e^{-\frac{n.\Delta H^{\alpha\to\beta}}{RT}+\frac{n.\Delta S^{\alpha\to\beta}}{R}} \tag{1.5}$$

where $\Delta H^{\alpha\to\beta}$, $\Delta S^{\alpha\to\beta}$ and n are respectively the enthalpy, the entropy of hydride formation and the number of moles. Above the critical temperature, the pressure plateau disappears, and only one regime is observed.

**Hysteresis :** The plateau pressure for hydrogen absorption is higher than the one for desorption. This hysteresis is well characterized, but its origin is still debated.

### 1.2.2 Thin Pd film

The phase transition generates large compressive stresses due to the lattice mismatch. Whereas the bulk film can freely expand, the thin film, clamped to a substrate, cannot freely expand in the in-plane direction. Hydrogenation of thin film induces then large compressive stress and strain. The pcTs are slightly different between bulk and thin film. Typically,

1. the hydrogen solubility of the $\alpha$ phase increases,
2. the critical temperature is reduced,
3. the phase transition exhibits a slope pressure plateau,
4. the hysteresis width is changed.

In fact, the differences in the microstructure of the film (grain boundaries, defect, dislocations and vacancies) account for different hydrogen absorption thermodynamics and kinetics. For example, it is understandable that the surface and subsurface sites contribution neglected in bulk system become important for nanometric film. The micro structural aspect is out of the scope of this thesis. More information can be found for thick film in [25],

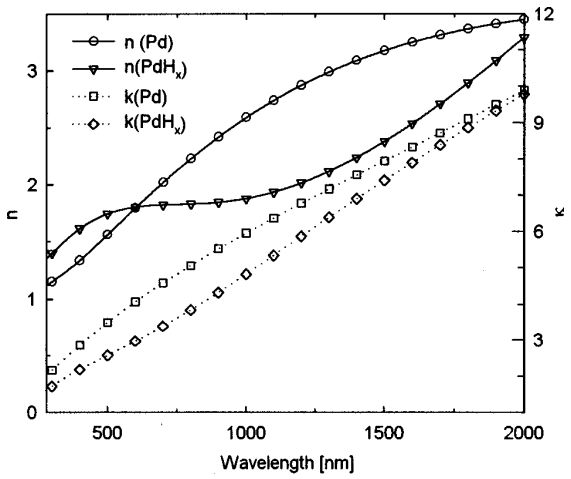


Figure 1.6 – optical constants of 10 nm thin Pd in the metal and hydride state

for thin film and cluster in [26, 27, 28]. We only keep in mind that the Pd isotherms between different Pd films may be different due to the sample preparation.

### 1.2.3 Metal properties upon hydrogenation

During the transformation of Pd into the hydride form, the mechanical, the electrical, and the optical properties of the metal are altered. The lattice constant expansion of Pd is about 0.4 % for the $\alpha$ phase, and 3.5 % for the $\beta$ phase [11]. The volume density of free electrons (Fermi level) decreases which results in a decrease of the real ($\epsilon_1$) and imaginary parts ($\epsilon_2$) of the complex permittivity of Pd. Figure 1.6 shows the complex refractive index $\tilde{n}$ (with $\tilde{n} = n - ik$) of the Pd and Pd hydride. The metal hydride becomes « less metallic ». From an electrical point of view, the Pd conductivity decreases upon hydrogenation. [1]

## 1.3 Optical fiber hydrogen sensors based on Pd - Principles

### 1.3.1 A typical hydrogen sensor response based on Pd

Hydrogen sensors based on Pd measure the Pd physical changes during the hydride formation. From the Pd physical changes, related to the hydrogen solubility, we can have access to the hydrogen concentration in the surrounding environment. Thus, the sensor responses show typically the same aspects as than the pcT curves. At room temperature,

- for hydrogen concentration corresponding to the $\alpha$ phase, the signal changes slightly due to the low hydrogen solubility in the metal ;
- at the phase transition, a large change is observed corresponding to a large increase of hydrogen amount in the metal ;
- for hydrogen concentration corresponding to the $\beta$ phase the signal saturates since the Pd hydride film is completely hydrogenated.

For optical sensors, we measure etheir changes of the Pd dielectric permittivity and/or the expansion of the Pd lattice constant. The challenge for designing an O.F.S for hydrogen

1. The conductivity increases for disconitous Pd films, characterized by an island microstructure. Due to the expansion of Pd, the Pd islands bond together, increasing the number of bridge for the conductivity [29].

leaks detections, is to make sensitive the optical fiber to $\alpha$-phase, when small changes occur. Furthermore, the dynamic range is an issue when hydrogen quantification is required. Note that the hysteresis is not an issue in our case, but it is important when the quantitative monitoring of hydrogen concentrations is required.

### 1.3.2 Phase modulated hydrogen sensor responses

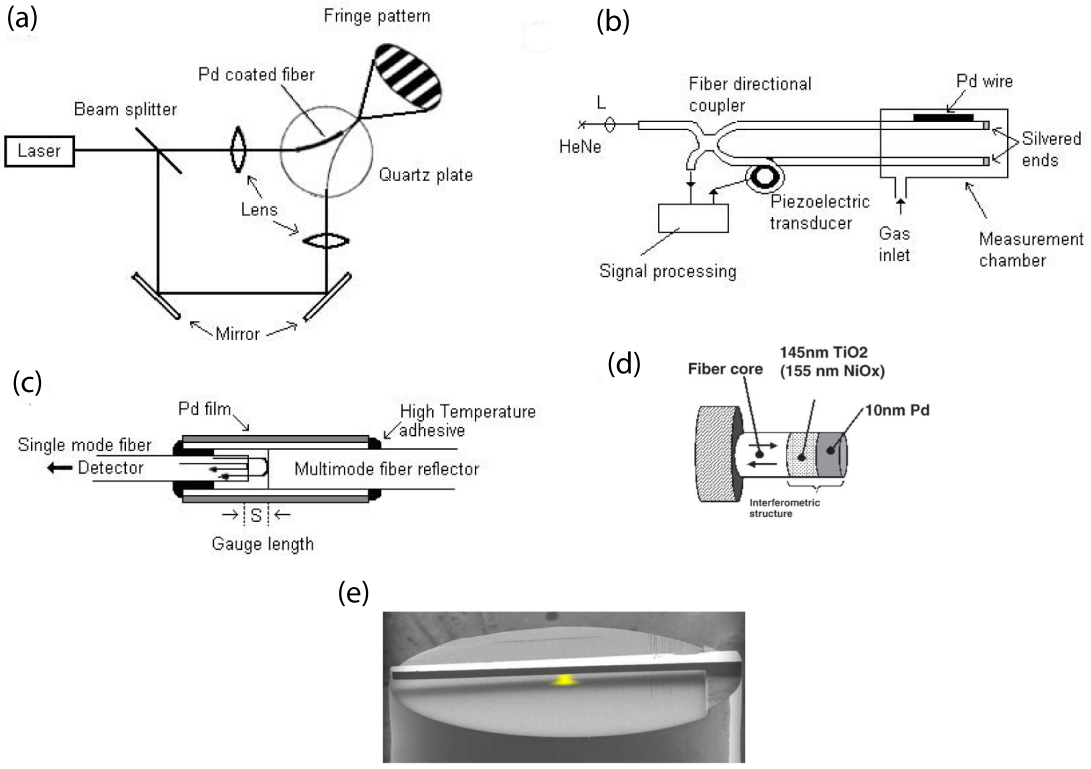


Figure 1.7 – Interferometer design for optical fiber hydrogen sensors : (a) Mach-Zehnder, (b) Michelson, (c) Fabry-Perot fiber, (d) FP interferometer sensor developed by Maciak et al. [30] and (f) optical fiber tip cantilever.

#### 1.3.2.1 Butler's interferometer

**Description :** Butler [31, 32] developed the first O.F.S for hydrogen detection in 1984. The device consists of a Mach-Zehnder fiber interferometer, fig. 1.7a. It combines two single mode optical fibers (ITT-1601) with optical elements to realize the interferometer. The light of a He-Ne laser, 0.5 mW, is split by a beam splitter, and injected into both optical fibers by lenses. One is sensitive to hydrogen, whereas the second is insensitive. The jacket is mechanically removed for both optical fibers over a length of 3 cm. A Pd layer of 10 $\mu$m thickness is sputtered in Ar with an initial 10 nm thick Ti layer (providing a good adhesion between the metal and the optical fiber) on the first unjacketed fiber, whereas a Pt layer is deposited on the second one in order to maintain as possible the same temperature dependence between both optical fibers. Both optical fibers are glued

to a fused quartz plate to rigidify the structure.

**Principle :** The Pd expansion upon hydrogenation results in stretching one optical fiber in both axial and radial directions, and changing its effective path length. The change in optical path length results at the output of the interferometer in a fringe pattern, visually observable and recordable with a simple photo-detector. The shift of the fringe is then related to the hydrogen concentration. The signal resolution is limited by the noise which comes from the sensitivity of the sensor to vibrations and sound.

**Typical response :** The hydrogenation was carried out with different carrier gases ($Ar, N_2$, dry air) showing different responses times. They observed that the response time, in order of few minutes, was longer than the hydrogen diffusion constant in Pd. From these observations, they suggested that the kinetics is dominated by the surface reactions at room temperature.

Finally, they estimated a detection range from $10^{-4}$ % (1 ppm) to 3 % $H_2$.[2] The lower limit is limited by the temperature fluctuation. The upper limit corresponds to the $\beta$-phase. In fact, they considered only the regime of the $\alpha$-phase in order to relate the hydrogen partial pressure to the hydride composition (Sieverts equation). In 1988, they reported a response in a range from $2.10^{-6}$ % (20 ppb) to 3 % $H_2$ for different film thicknesses deposited by sputter and electro-deposition [32], fig. 1.7a.

For a concentration above 0.1 % $H_2$, the experimental results follow the Sieverts equation, taking into account the linear relationship between the lattice constant and hydrogen content [33]. At lower concentration, a large deviation is observed. The observed fringe shift is larger than expected from Sieverts equation, suggesting an additional trapping site for hydrogen. The authors assumed that the fringe shift observed is likely due to the binding of « free »particle at the surface (or subsurface).

Theoretically, the optical path length in the fiber core is related to the strain in the fiber core by the elasto-optic relation [34] :

$$\frac{\Delta\phi}{\phi} = e_z - \frac{n^2}{2}[2e_r(p_{11} - p_{44}) + e_z(p_{11} - 2p_{22})] \tag{1.6}$$

where n the index of refraction of the fiber, $P_{ij}$ the Pockels coefficients, and $e_z$ and $e_r$ the axial and radial strain in the fiber core. Butler et al. studied theoretically the sensor response by solving the stress-strain relationships for this structure with the appropriate boundary conditions. They considered a one dimensional model which only takes into account the axial strain (and assumes a given value for the radial strain).

#### 1.3.2.2 Interferometer development

Farahi [35] demonstrated the feasibility of an all single mode optical fiber Michelson interferometer for $H_2$ sensing, fig. 1.7b (a Michelson interferometer is a Mach-Zehnder interferometer that has been folded back upon itself). A He-Ne laser, 0.2 mW is split into two single mode fibers and recombined by a fiber direction coupler FC. The measurement is based on a pseudo-heterodyne scheme [36] to eliminate the differential drift in the arms of the single mode fiber interferometer. A part of the reference fiber is wound onto a driven

2. Hydrogen concentration under $10^5$ Pa at 20°. In the following, 100 % $H_2$ means a hydrogen pressure of $10^5$ Pa. Note that we refer to the volumetric percentage.

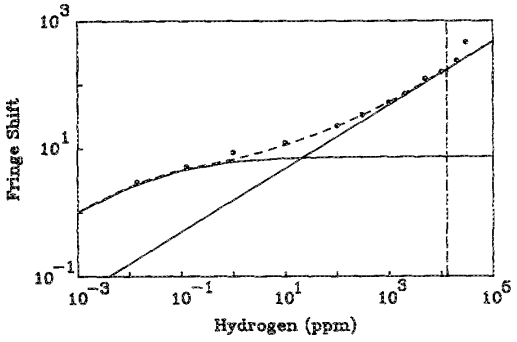


Figure 1.8 – The fringe shift for a fiber sensor as a function of hydrogen concentration. The vertical dashed line indicates the upper edge of the alpha phase boundary. The straight solid line is the Sieverts law component of the response and the curved line is the response from the deeply bound sites (these sites correspond likely to binding at a free-metal-surface) described by a Langmuir isotherm. The dashed line is the sum of these two contribution [32].

piezoelectric cylinder. The signal is therefore modulated at a frequency of the applied voltage. On the sensing fiber, a Pd wire, with a length and a diameter respectively of 6 cm and 500 $\mu$m, is attached on the optical fiber (without the jacket) using quick-setting epoxy resin. As noted by the authors themselves, it is, however, preferable to coat the optical fiber by sputtering in order to produce the thickness desired.

As for Butler's sensor, the Pd expansion upon hydrogenation causes a change of the fiber sensing length, which results in a phase retardance. The thermally induced effect of the hydrogenation (exothermic reaction) is small compared to the axial strain, when the reaction takes place at room temperature and at low concentration ($\alpha$-phase). The sensor responses to a range of 0.0054 % (54 ppm) to 1,5 % $H_2$ in $N_2$ at a atmospheric pressure, with a response time of few minutes. The resolution is $2.10^{-3}$ % limited by the differential thermal fluctuations.

In order to avoid polarization problems and to detect a single axial strain, Zeakes developed in 1994 an extrinsic Fabry-Perot (FP) interferometric sensor, fig. 1.7c [37]. The device consists of putting a multimode fiber at a distance S from a single mode fiber, in a glass alignment tube, to realize a FP cavity. A 2 $\mu$m layer of Pd is sputtered on this tube.

Upon hydrogenation, the Pd expansion changes the length of the cavity S. The output intensity is described by :

$$I = I_0 \left[1 + \cos 1 + \frac{4\pi S}{\lambda}\right] \tag{1.7}$$

where $\lambda$=1300 nm is the source wavelength. As a result, the intensity of the light is modulated as a function of hydrogen concentration. The sensor response was verified at 0.5 % and 5 % $H_2$ in $N_2$, showing the fringe shift, with a response time faster than a minute. Furthermore, the response is not reproducible over hydrogenation cycles due to the delamination of the Pd film.

The presented hydrogen interferometer sensors are based on the Pd expansion, and use thick films. Pd thick films show a poor reproducibility over ab-desorption cycles. After few cycles, irreversible micro-cracks appear. Moreover, the observed response time is too slow

for safety application due to the diffusion limitation, as will be explained in section 1.4. Therefore, this technology has been put apart during a decade. Recently, interferometers have received renewed attention due to their high sensitivity potential. New designs based on thin films have been studied as presented below.

Iannuzzi [38] proposed a hydrogen fiber top cantilever sensor. The sensor consisted of realizing a FP cavity between the fiber tip and the cantilever, fig. 1.7e. The light scattered back into the fiber encounters an optical fiber coupler, which couples 50 % of the reflected beam into another fiber, aligned with an infrared photodiode. A 150 nm Pd film, with a 10 nm chromium substrate layer, is deposited on the cantilever.

The output of the photodiode W, as for Zeakes's sensor, is given by

$$W = W_0(1 - Vcos(\frac{4\pi d}{\lambda})) \tag{1.8}$$

where d is the distance between the fiber-to-air and the air-to-cantilever interfaces,$\phi$ a constant, V the fringe visibility relative to the interference of the three reflected signals, and $W_0$ is the midpoint output. Due to the Pd expansion in presence of hydrogen the cantilever bends, which results in changing the cavity length. The sensor responses to 4% $H_2$ in Ar. However the performances of the device are seriously damaged over ab-desorption hydrogen cycles.

Maciak et al. developed a simple optical FP fiber interferometer. It consisted of a deposited layered sensing structure made of (145 nm) $TiO_2$ and (10 nm) Pd at the tip of the optical fiber, depicted in fig. 1.7d. The first mirror is realized at the fiber/$TiO_2$ boundary, whereas the Pd layer plays the role of the second mirrors and promote the dissociation of hydrogen. The $TiO_2$ layer is the resonance cavity of the interferometer, and the sensitive layer. According to the authors, the contribution of the Pd layer to the optical signal is minimum. The sensor responses to 1 % from 3.5 % $H_2$ in synthetic air, with a response time is faster than 1 min. The response is reproducible. A large change is obtained at 2 % and the signal response saturated after. We conclude from the hydrogen response that the sensor response is likely due to the hydrogenation of the Pd layer.

Lately, Kim et al. [39] proposed a Mach-Zehnder fiber optic interferometer realized by two identical long-period gratings ; each had a 500 $\mu$m period, and was characterized by a length of 20 mm and a centre-to-centre distance of 50 mm. A 50 nm thick Pd film was uniformly deposited over the cladding of a single-mode fiber. This sensor is sensitive to the change of the refractive index of the Pd. During Pd hydrogenation, the effective index of the cavity changes, which result in changing the effective optical path length. The response sensor was only measured at a concentration of 4% $H_2$ in $N_2$. The response time is approximately 8 min.

### 1.3.3 Polarization modulated hydrogen sensor responses

**Description :** In continuation of Butler's interferometric fiber sensors, Dessy et al. developed in 1992 a hydrogen sensor based on polarization modulation by using a Pd thin film [40]. In this case, the sensor did not use the Pd expansion, but the heat released from the chemical reaction. The device consisted of a single mode birefringence fiber maintained in a metal sheath. The cladding was removed on a part of the fiber and replaced by a 6

nm Pd layer.

**Principle :** The change in temperature during the reaction causes a change in the birefringence of the optical fiber. Orthogonal modes $HE_{11x}$ and $HE_{11y}$ propagate both therefore trough the fiber with different propagation constants. Due to the coupling between both modes, the polarization is changed. The strain induces by the Pd expansion is neglected ; the sensor acts in fact as a thermal sensor.

**Typical response :** The sensor detects a concentration range from 1 to 10% $H_2$ in an inert gas. The response time of the sensor is about 1 minute at a concentration of 2.8 % $H_2$.

### 1.3.4 Intensity modulated hydrogen sensor responses

#### 1.3.4.1 Micro-mirror sensors

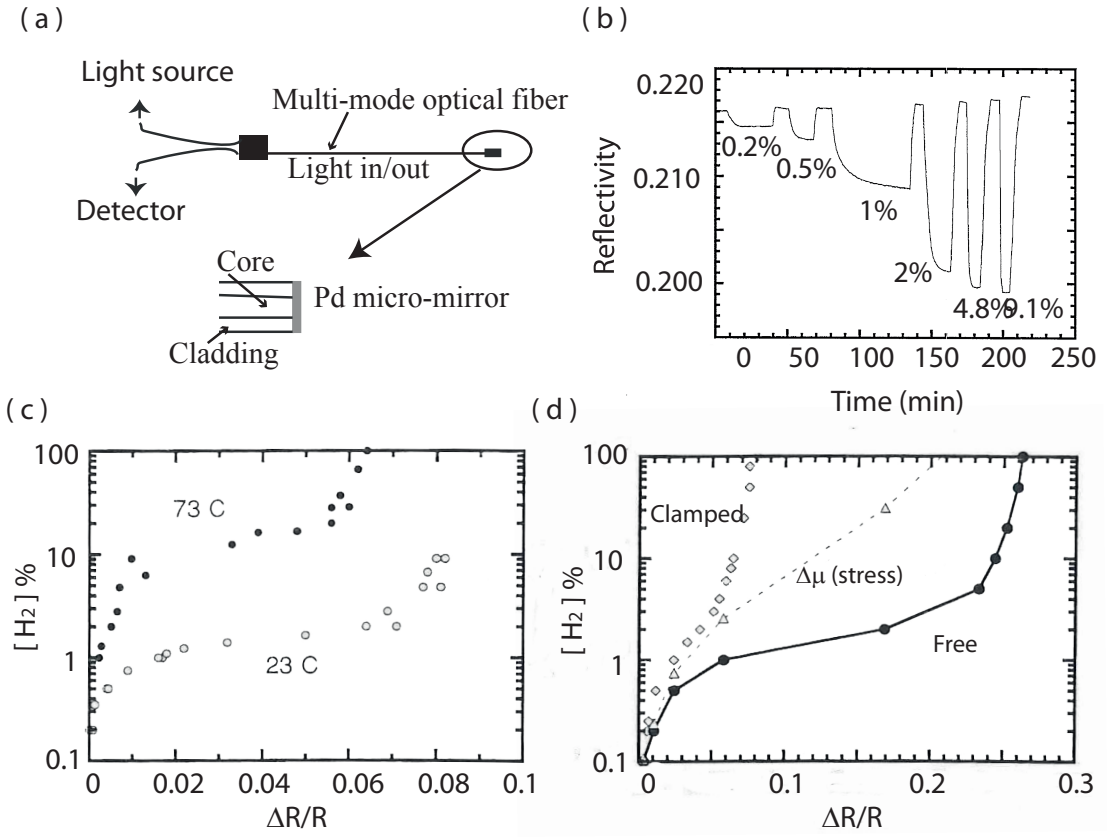


Figure 1.9 – (a) Schematic of optical fiber hydrogen sensor based on micro-mirror (b) Response of the Butler's micro-mirror sensor to different $[H_2]$ from [41] (c-d) Hydrogen concentration vs. reflectivity change for 10 nm Pd film at (c) two different temperatures and (d) for clamped and unclamped film. The dash line represents the theoretical stress in the clamped film, from [42]

**Description :** Micro-mirror sensors [41, 43, 42, 44] constitute probably the most mature and simple hydrogen sensing devices. A Pd thin film is deposited on one cleaved end of

a (multimode) optical fiber. The other end of the optical fiber is connected to a Y coupler, which allows to illuminate the sensing film and to collect the reflected light from the latter, fig. 1.9a.

**Principle :** The reflectance R (and transmittance T) of the Pd film changes as a function of $H_2$ uptake due to a decrease of the Pd hydride refractive index. By measuring the reflected intensity, the optical change is related to hydrogen concentration

**Typical response :** In 1991 Butler et al. described the response of a 10 nm Pd film deposited on a multimode fiber end, with a 125 $\mu$m diameter. Figure 1.9b shows the reflected light for different hydrogen concentrations. The reflectance changes continuously depending on the hydrogen concentration [42, 45]. In particular, they have observed that the reflectivity change is a measure of the composition of the Pd hydride. The plot of the relative change in reflectivity as a semi-log function of $H_2$ concentration, shows the pressure composition isotherms (pcT) of Pd for different temperatures, fig. 1.9c. The slope of the plateau region observed is characteristic of thin films, section 1.2.2.

The sensor response is reproducible over hydrogen cycles, but different responses are obtained for identical sensors. The authors suggested that this difference comes from an uncontrollable parameter during the deposition process. They observed, in fact, two trends for the change in the relative reflectivity, independent of the thickness of the film (10-70 nm). While some thin films exhibits reversible micro-blistering and micro-cracking, some films shows permanent mechanical failure of film, like thicker films (100 nm Pd [46]). The micro-blistering and micro-cracking are eliminated by depositing a 1-2 nm thick Ni underlayer as an adhesive agent, improving the sensor reproducibility. Besides, the change in reflectivity for Ni/Pd film upon hydrogenation is reduced compared to Pd film. The level and the width of the plateau region are different as depicted in fig. 1.9d (circle symbol and line for the Pd/Ni and Pd film, respectively). The authors proposed that this difference is due to the clamping effect of the Pd on the substrate (quartz or Ni). Reversible micro-blistering, so-called buckles, and clamping effect, have been now well investigated and proved to be related to the stress relaxation [26].

#### 1.3.4.2 Micro-mirror development

In continuation of Butler's work, Bevenot et al. described in 1998 the response of a 13 nm Pd deposited on a multimode fiber, 400 $\mu$m core diameter, in a wide range of temperatures : between -196 and 23° C [45]. As previously noted, the response change depends on the temperature and is explicitly related to the pcT curves. A larger signal change is obtained at lower temperature since the level of pressure plateau decreases and its width increases. On the other hand, the response time is slower at low temperature. A response time of 14 s and 100 min is respectively obtained at 23° C and $-45$° C for 4 % $H_2$ in $N_2$. To improve the temperature range of the sensor, they proposed to heat the sample with a power laser diode in order to enhance the response time, as it will be described in section 1.4.2.

Lately, Kazemi et al. developed a micro-mirror based on colorimetric material [47]. The colorimetric material consisted of inserted Pd into a porous substrate. This micro-mirror sensor showed a very good reproducibility and reliability. They proved the reliability of the sensor by performing the test at the EELV/Delta IV engine stand at NASA-Stennnis Space Center.

#### 1.3.4.3 Characterization of Pd thin film :

In addition to the micro-mirror results, several studies have been reported to characterize the hydrogenation of Pd thin films deposited on flat substrate. These studies emphasized the relation between the optical change and the pressure composition isotherm (pcT). As these studies are based on flat substrate, they provide a simple tool to investigate the properties of Pd thin films, and consequently optimize the performances of hydrogen sensors based on Pd.

In 1996 Garcia et al. studied the transmittance of Pd thin films. The film is deposited on glass substrate, and is illuminated by an optical fiber. The transmitted light through the sample is then collected by a second otpical fiber. As for reflectance measurement, the graph of the optical transmittance as a function of hydrogen concentration on a logarithm axis, fig. 1.10a, shows the pcT curves [48], in agreement with the literature.

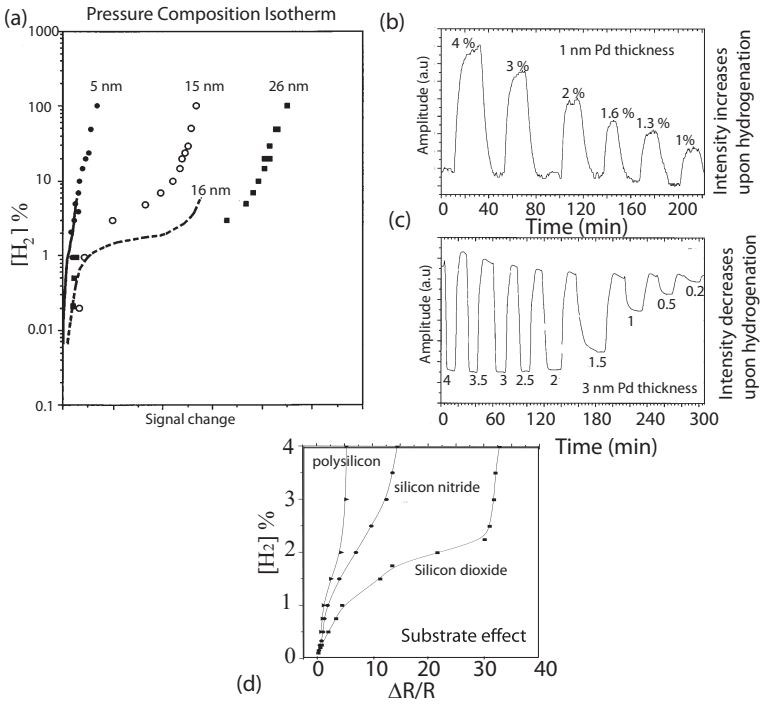


Figure 1.10 – (a)Measured isotherm by transmittance for Pd at 25°, from [48] The dash line is the isotherm reported by Frazier et al. [49](b) Reflectivity change as a function of $[H_2]$ for 1 and 3 nm Pd film (c) Relative change of the reflectivity vs. $[H_2]$ for different substrates .

Later, Kalli et al. [50] studied the reflectivity of a Pd film varying from a thickness of 1 nm to 30 nm, and characterized the $\alpha$- and $\beta$-phase transition after both single and multiple gas cycles from their reflectivity measurements. In particular, they demonstrated that the change of reflectivity depends on the thickness of the Pd film and on the nature of the substrate. Figure 1.10b and c show respectively the reflectivity for 1 nm thick and 3nm thick Pd film upon hydrogen exposure. Remarkably, the reflectivity increases upon hydrogenation for a thickness inferior to 3 nm, whereas the reflectivity decreases upon hydrogenation for thicker film as previously described. Figure 1.10d shows the influence

of the used substrate on the hydrogen response. A higher change is obtained for $SiO_2$ as substrate. Moreover, they observed that structural changes of the palladium film on the silicon nitride, induced via exposure to hydrogen due to surface energy effects, resulted in the creation of nanostructures.

In continuation, Matelon et al. [51] showed that the response time depends strongly on the different substrates used. Maximum values of 700 s for Pd/Si and 3700 s for Pd/Al2O3 were for instance recorded at pressures corresponding to Pd hydride $\alpha$ to $\beta$ phase transition. They attributed this difference to the substrate roughness which modifies the Pd subsurface microstructure.

Finally, let us mention that optical transmittance study of metal/metal hydride thin film has been proposed for investigating and identifying new hydrogen storage materials (hydrogenography) [52, 53].

#### 1.3.4.4 Evanescent wave hydrogen sensor responses

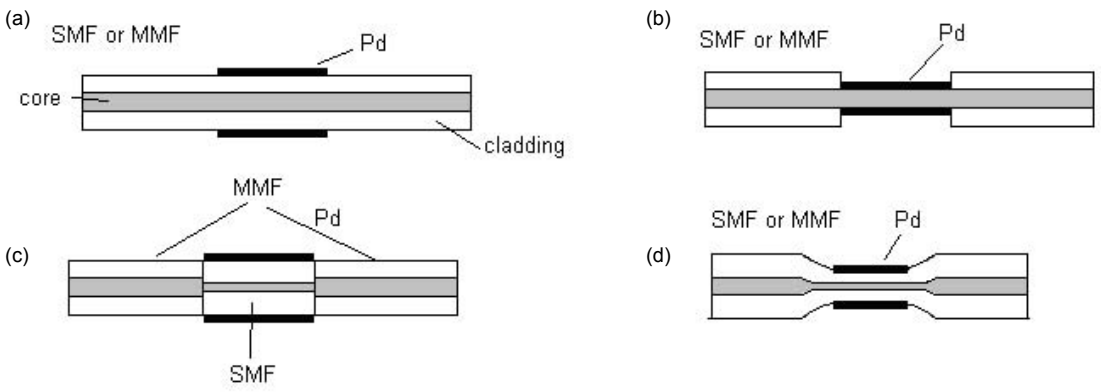


Figure 1.11 – Schematic of the optical fiber hydrogen sensor based on evanescent field. Pd coated on the (a) cladding,(b) core and (d) tapered core of MMF or SMF. (c) Pd coated on heterostructure

**Tabib-Azar's evanescent sensor**

In 1999 Tabib-Azar et al. [54] proposed an optical fiber hydrogen sensor which takes advantage of the evanescent fields associated to the guided light. The device consisted of removing the optical cladding of a multimode fiber (50 $\mu$m) and replacing it by a 10 nm Pd film, with an interaction length of 1.5 cm. The optical fiber is illuminated with a light source with a wavelength of 650 nm. In presence of hydrogen (between 0.2-0.6% $H_2$ in $N_2$), the transmitted intensity increases with a response time of about 30 s, fig. 1.12a. The intensity change is a function of hydrogen concentration, fig. 1.12b. According to the authors, the increase in intensity is explained by the decrease of the imaginary part of the Pd refractive index upon hydrogenation. In fact, the transmitted light is less attenuated through the Pd hydride section since the Pd hydride is less absorbing than Pd. In addition, the author claimed that the change in the real part of the Pd refractive index result in an effective phase change in the guided light. However, we beleive that the situation in this case is slightly different. Since the optical cladding is removed and replaced by a Pd film, the Pd layer plays now the role of the optical cladding. Consequently, the numerical

aperture of the fiber is modulated by the sensing section. Upon hydrogenation, the change of the real part of refractive index resulst also in changing the transmitted intensity since the NA of the sensing section will be changed.

**Evanescent sensor development :**

Evanescent wave (EW) sensors are based on the alteration of the evanescent field of the propagating mode. In the general case of optical fiber (multimode, single mode, tapered fiber...), the transmission intensity $I_t$ of a fiber, when exposed to hydrogen, can be expressed by [55] :

$$I_t = I_0 exp(-2r\Delta\alpha L) \tag{1.9}$$

$I_0$ is the transmitted optical power without hydrogen. r is the ratio of the power of the evanescent waves on the total power of the light guided. r depends on the configuration : r is inferior to 1 %, about 1 %, inferior to 20 %, superior to 50 % and can reach 100 % for respectively a multimode, a hetero-structure, a tapered multimode fiber, a single mode fiber and a nano fiber. L is the interaction length. $\Delta\alpha$ is the variation of absorption between the absorption coefficient of the Pd hydride and the Pd film. The sensitivity of the sensor is tuned by both parameters r and L. The sensitivity of the sensor is enhanced when their bothvalues increase.

Villatoro et al. reported the response of a Pd coated- single mode tapered fiber (SMTF [56, 57]), a -multi-mode tapered fiber (MMTF [55]) and a -nano tapered fiber [58].

For **SMTF** [56], a 12 nm Pd layer with a length of 1.5 cm was deposited on the tapered fiber. The transmitted intensity increases upon Pd hydrogenation since $\Delta\alpha < 0$. The intensity change was hydrogen dependent, fig 1.12d, in a range from 1.8 to 10 % $H_2$ in Ar. Besides, the sensor was polarization independent : the same response for TE- and TM polarization was obtained. The sensor was also wavelength dependent : a large intensity change is observed for the longer wavelengths in the spectral range of 900-1600 nm, fig. 1.12a.

Although **MMTF** show a lower sensitivity than SMTF, it was proposed by Villatoro et al. as a more robust and convenient sensor. The sensor consisted of depositing a 15 nm Pd layer on the taper waist over a length of 1 cm [55] . The waist was in the range of 30-70 $\mu$m. Two Pd layers were deposited over the taper, on the uniform section, with one layer every 180 °. The measurements were carried out with a LED at a wavelength of 850 nm, with an optical power of 20 $\mu$m. The transmitted intensity increased upon Pd hydrogenation ($\Delta\alpha < 0$), fig. 1.12e. They detected hydrogen concentrations ranging from 0.3 to 3.5% $H_2$. The minimal value was limited by the intensity noise present in the signal. Above 3.5 % $H_2$, the signal was saturated for all taper waist sensors considered. Nevertheless, the sensor performance can be adjusted with the taper diameter, fig. 1.12f in the detected range. The maximal change was found for thinner waist diameter on account of the maximum evanescent field coupling in the Pd layer. A response time of 30 s was found at 2 % with a recovery time of 90 s in Ar. The authors suggested that this response time was mainly driven by the diffusion of the hydrogen atoms into the Pd film. After cycling, the response time and the recovery time become 40 s and 100 s. According to the authors, this increase was due to the degradation of the Pd over cycles. In spite of the possible degradation, the response is reproducible.

For **nano tapered fibers** [58], a 4 nm Pd film was deposited on a nano tapered waist of a single mode fiber (SMF). They used the standard telecommunication optical fiber (Corning SMF-28). The waist diameter was limited to 1300 nm for handling reasons. The length interaction was 2 mm. The source was a laser diode emitting at a wavelength of 1550 nm. The intensity decreases with the increase of the hydrogen concentration in a range from 0.8 to 5.2 % $H_2$ in Ar, fig. 1.12c. This change in intensity is opposite to the response reported for the EW sensors, (where the decrease in the absorption coefficient of the Pd hydride cause an increase in intensity). The authors did not discuss this increase in intensity. The design of tapered fiber sensors allows to decrease the interaction length. This length is, for instance, only 2 mm for the nano-taper sensor. The authors estimate that this length can be decreased to a few hundred of micrometers. Nevertheless, tapered optical fibers such as TSMF showed a poor reproducibility due to inaccuracies during the fabrication process [59]. The fabrication of tapered fiber made also the sensor very fragile.

An optical **hetero-structure** fiber was recently proposed by Luna-Moreno et al. [60] to realize a very robust sensor with a high sensitivity. The hetero-structure was made of a 3-8 mm length single-mode fiber, coated with a 10 nm-thick Pd and Pd alloy film, sandwiched between two multimode fibers. Due to the diameter mismatch of the optical fiber core, the light is guided by the cladding of the single mode fiber. The evanescent field is hence strongly coupled in the sensitive layer. The intensity increases upon Pd hydrogenation from 0.8 to 4.6 % $H_2$ in Ar. The relative change in intensity increased with longer interaction length.

Kim et al. presented in 2007 a **side polished single mode fiber** as a hydrogen sensor [61]. A jacket-removed SMF was embedded in a quartz fiber holding groove and side-polished. The radius of curvature of the circular groove was 50 cm. After polishing, the cladding thickness left was 2 $\mu$m. The interaction length was 2.46 mm. A 20, 100 and 40 nm Pd films were respectively deposited on the side-polished surface by thermal evaporator. The length of the fiber between the output polarizer and the transducer was only 2 cm in order to minimize the possible polarization entanglement. The hydrogen measurement were performed at 1 and 2 % $H_2$ in Ar at a wavelength of 1550 nm. The sensor principle is based on the propagation losses of the guided mode. The intensity increased upon Pd hydrogenation for the TM polarization, but the TE response of the sensor was negligible. According to the authors, the TE polarization field cannot penetrate into the metal deeply enough to be affected by the metal film. Consequently, the TE polarization can be served as a reference. Finally, the response and recovery time were 100 s and 150 s, respectively.

We conclude the review of evanescent hydrogen sensors by mentioning the work done by Barmenkov et al. [62]. To introduce the measurement of hydrogen concentration into the time domain, they placed the Pd tapered fiber as a hydrogen sensing element in a fiber laser cavity based on an Er-doped fiber laser. The attenuation of the sensing element upon hydrogenation decreased the cavity losses, which result in decreasing the buildup time. By measuring the changes in the laser buildup time, they had access to the hydrogen concentrations.

#### 1.3.4.5 Surface Plasmon hydrogen sensor response

Surface Plasmon resonance (SPR) sensors can be considered as a variety of EW sensors. Because surface plasmon may propagate at the interface between a Pd thin film and

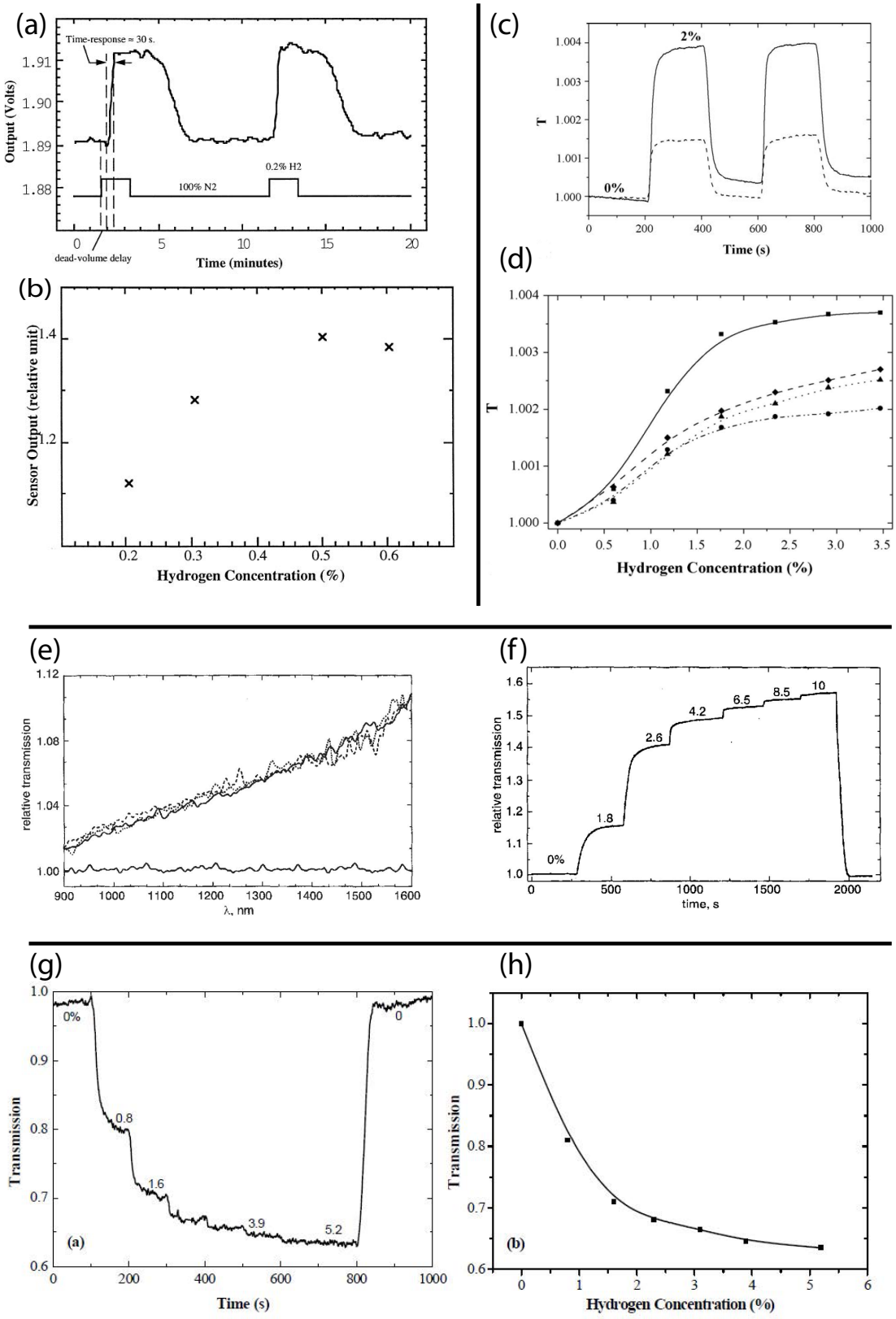


FIGURE 1.12 – (a-b) Unclad multimode fiber's response [54] (c-d) Multimode tapered fiber's response [55] : (c) time response for a taper diameter of 30 (solid line) and 60 $\mu$ m (dash line) (d) $I/I_{H_2}$ vs. $H_2$ for samples of different taper diameter : 30 (squares), 40 (rhombs), 50 (triangles) and 60 $\mu$ m (dots) [55]. (e-f) Single mode tapered fiber's response (g-h)Nano tapered fiber's hydrogen response : time and dynamical range [58]

a dielectric medium, the EW presented above may sometimes considered as SPR sensors. Strictly speaking, EW is considered as a SPR sensor when the guided light matches with the wavevector of the surface plasmon, as we will be described in chapter 2.

**Description :** In 1998 Bevenot et al. demonstrated an optical fiber hydrogen sensor based on SPR [45]. The sensor consisted of a Pd layer deposited on the mutimode fiber core (diameter of 400 $\mu$m, NA=0.48), after removing the optical cladding over a length of 2 cm. Note that the design is similar to Tabib-Azar's sensor. The light was injected into the optical fiber with an appropriate angle of incidence and at a given wavelength (670 nm). The hydrogen concentration was determined by measuring the change in the transmitted intensity of the mode groups excited. The hydrogen response of the sensor depends strongly on the incident angle. From theoretical simulation, an optimal angle of 12° was found for 4% $H_2$.

**Typical response :** The measurements were carried out in a hydrogen range of 0.8-100%. The intensity increases and changes as a function of hydrogen, in the same way than the pressure composition isotherm (pcT) of Pd. The response of the sensor is related to the two phases : $\alpha$ and $\beta$, for the concentration range of 0.8-1 % $H_2$, and 3-100 % $H_2$, respectively. Between 1-3 % $H_2$, the response strongly varies representing the phase transition. The response time varies between 3 s for 100% $H_2$ and 300 s for concentration corresponding to the phase transtion. Finally, they achieved a two-points detection by inserting two sensing section along an optical fiber.

**Principle :** The authors claimed that the change is caused by the modification of the SPR due to the variation in the Pd complex permittivity. Although the SPR resonant angle occurs at an angle beyond the fiber numerical aperture (NA), the modification is observable due to the presence of a wide SPR peak, as discussed in chapter 4. They assumed that the intensity changes only for the TM polarized light since the SP is only excited for TM polarization.

### 1.3.5 Wavelength modulated hydrogen sensor response

#### 1.3.5.1 Fiber Bragg Grating sensor :

**Description :** Sutapun et al. proposed the design of a Fiber Bragg Grating (FBG) sensor for hydrogen detection [63] in 1999. The sensor was realized by depositing a 560 nm Pd layer onto the optical cladding of a SMF (5-10$\mu$m/125$\mu$m), where a FBG (with Bragg wavelength of 829.73 nm) was previously inscribed. A part of the cladding was etched and the final cladding had a value of 35 $\mu$m.

**Principle :** The expansion of the Pd hydride upon hydrogenation stretched the fiber. The periodicity and the effective index are altered which resulted in shifting the Bragg wavelength (fig. 1.13a). This FBG hydrogen sensor acts in fact as a pure strain sensor. The determination of the Bragg wavelength enables to quantify the $H_2$ concentration. In their case, the resolution of the spectrometer of 0.14 nm was not adequate to measure the Bragg wavelength shift (less than 0.1 nm). They determined the shift by applying a spline-fitting routine to the data measured, fig. 1.13.

**Typical response :** The Bragg wavelength increases linearly as a function of $H_2$ concentration in the range of 0.3-1.8 % $H_2$. After exposure to 1.8 % $H_2$, the Pd coating peeled off, which destroys the sensor. The authors proposed to add a thin adhesion layer to overcome the Pd degradation.

#### 1.3.5.2 Grating development :

FBG are insensitive to the surrounding medium refractive index since the resonance results from the core modes coupling. In 1996 Meltz et al. [64] proposed to use FBG written in D-fibers to make the FBG sensitive to the surrounding medium refractive index via evanescent wave interactions.

In this direction, Tien et al. [65] deposited, in 2008, a Pd film on a side-polished fiber over a length of 12 nm (SMF-28, 10 $\mu$m/125 $\mu$m). A FBG was previously inscribed (grating period of 0.534$\mu$m, length of 20 mm : resonance 1545 nm) in the optical fiber. Consequently, a thin Pd film (20 nm thick Pd ) can be used because of the evanescent field interactions. The wavelength resonance shifts to higher wavelength in presence of hydrogen. The shift increases with the increase of hydrogen for a range of 20 to 70% $H_2$.

In continuation of this work, Schroder et al. studied the response of such sensor in a range of 1-5 % $H_2$. They pointed out that the evanescent coupling came from the excitation of the SP at the Pd air interface. Consequently, the sensor is TM polarization dependent. The response time is the order of the minutes.

In 2007 Maier et al. developed a new sensor package to amplify the strain caused by the Pd expansion [66]. The sensor consisted of a semicircular cross-section palladium tube in which a fiber containing FBG was attached coaxially under tension to a mounting element. Upon hydrogenation, the Pd half tube expanded. The axial component of this expansion was mechanically collected and redirected into a short section of fiber containing a FBG. A minimal thickness of 300 $\mu$m has to be chosen to ensure the stability of the sensor.

Trouillet et al. [67] proposed, in 2006, to replace the short period grating (FBG) by a Long Period grating (LPG). The device consisted of depositing a 50 nm Pd layer on a SMF (Corning SMF 28) by thermal evaporation, after removing the jacket. Contrary to FBG sensors, which use the fundamental mode propagating through the core, LPG sensors are mainly based on the coupling between the cladding modes and the evanescent or Surface Plasmon at the interface between the Pd coating and the outer medium. Therefore, the sensor is sensitive to the change of the Pd refractive index. The determination of the shift of the loss peaks gave an access to the hydrogen concentration. At 4% $H_2$, a shift in the order of -5 to -7 nm toward the lower wavelengths was observed in comparison a shift of 14 pm was obtained for FBG ( 50 nm Pd deposited on fiber with FBG).

In conclusion, depending on the optical fiber sensor, the sensor measures the hydrogen concentration either by measuring the Pd hydride expansion, the Pd refractive index or the heat release, as described in table 1.1.

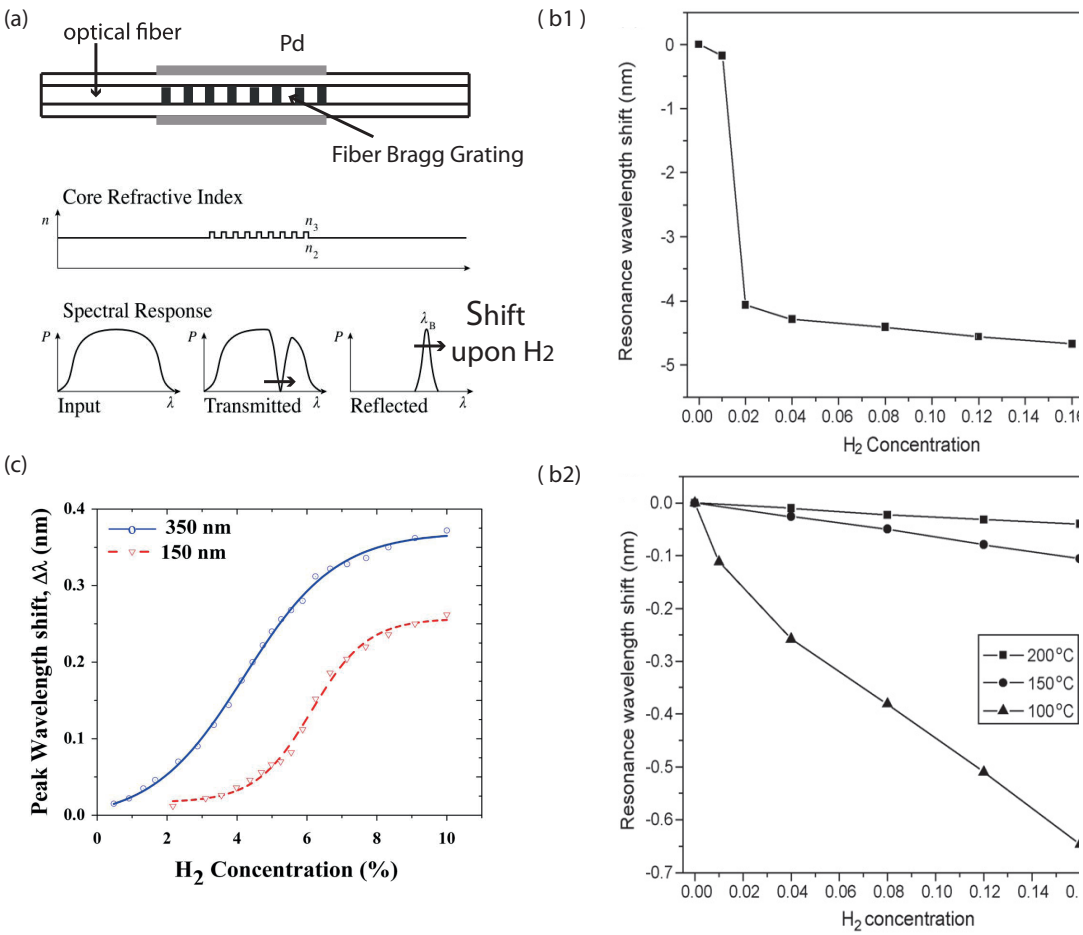


Figure 1.13 – (a) Schematic of a typical hydrogen sensor based on Pd-coated fiber Bragg grating (FBG) (b-c) The response of (b) Wei et al. 's LPG sensor [68] and (c) Buric et al.'s FBG sensor for different Pd thicknesses [69]. The sensor responses are described by the sensitivity considered as a function of hydrogen concentration.

## 1.4 Discussion on $H_2$ O.F.S performances

### 1.4.1 Hydrogen concentration range

The performance reported in the literature for the various sensor technologies are summed up in the table 1.2 and depicted in fig. 1.14.

**Phase modulated** : The dynamic range of interferometric hydrogen sensors, based on Pd thick films, are limited by the $\alpha$-phase. For concentration above the pressure plateau, the Pd layer is deteriorated. Nevertheless, hydrogen interferometric sensors show the highest sensitivity for very low concentrations. The minimal detection is estimated to be a few ppb, and is mainly limited by the temperature fluctuations.

**Amplitude modulated** : The hydrogen fiber sensors based on amplitude modulation show different dynamic ranges, but the dynamic range is typically between 0.5 % to 100 % $H_2$. Above 3 % of $H_2$ in Ar, most of the sensors saturate due to the formation of the $\beta$ phase

| Modulation | | Pd change in | | |
|---|---|---|---|---|
| | | Optical | Mechanical | Temperature release |
| phase | | X | X | X |
| polarization | | No | negligible | X |
| amplitude | | X | negligible | No |
| Wavelength | FBG | No | X | |
| | EW FBG | X | X | |
| | LPG | X | X | |

Table 1.1 – Operating mechanism of optical fiber hydrogen sensors. FBG : Fiber Bragg Grating, EW : evanescent wave, LPG : Long Period Grating.

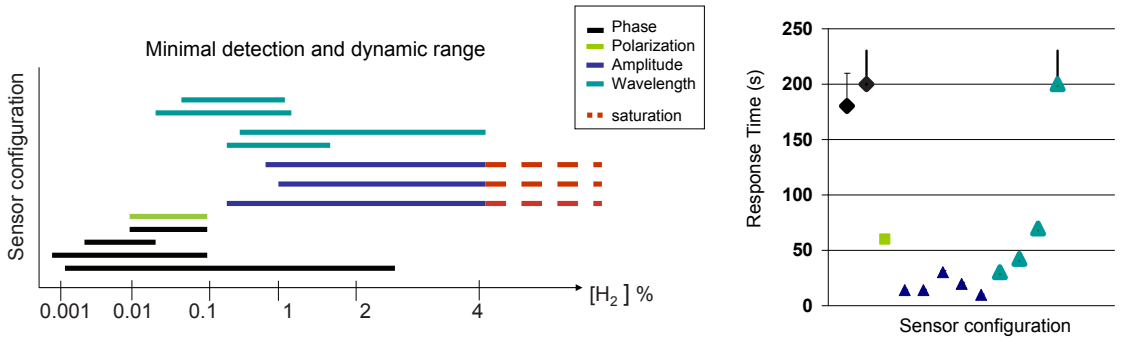


Figure 1.14 – Reported performances of existing hydrogen fiber sensors.

(all hydrogen sites are occupied in the metal lattice). The minimal detection is around a value of 0.1-0.5 % for these sensors, and it is mainly limited by the light fluctuation. A stable light source could decrease this minimum as well as a reference source. The minimal detection is maximal for the nano tapered fiber sensor. The authors estimated to be 0.05 % $H_2$. Around 2 %, a large change is often obtained : for example 1.8-4.2 % and 2%-3% for SMTF [70] and SPR [71], respectively. In concluions, the response of amplitude sensor is related to the Pd pcT curves, as pointed out in micro-mirror section (thin films on substrates). However, there are some discrepancies in the response of the sensors, as described in the following.

- The response saturates above 0.5 %, 2.3 %, 4.2 % for the MMF [54], MMTF [55] and SMTF [56, 70], respectively. The saturation of MMF evanescent sensors above 0.5 %, fig. 1.12b, is probably due to an error in gas mixing. Additional data above the 0.6 % for this sensor should allow us to comment on this behavior.
- EW and SPR sensors show higher sensitivity when the Pd hydride is in the $\alpha$-phase, or in the $\beta$-phase, in comparison with micro-mirrors systems. The SMTF [70] sensor, for instance, saturates above 4.2 %, but a change in the signal is still observable and measurable until 10 % $H_2$.

**Wavelength modulated** : The response of the sensors describes the allure of the Pd isotherm, as depicted in fig. 1.13. The dynamic range is analogue to the O.F.S based on amplitude modulation. In addition, the minimal detection is comparable to evanescent sensors. The best value for the minimal detection for FBG is 125 ppm with the « bridge »design [66].

We conclude that regarding the dynamic range & minimal detection, the $H_2$ sensitivity of the optical fiber sensor can be tuned by the appropriate configuration. Nevertheless, the sensor response is limited by the pressure composition isotherm of the Pd film used. The level and the slope of the equilibrium pressure plateau as well as the hydrogen solubility are determined by : the microstructure of the Pd (i.e the deposition condition : deposition pressure, sputtering deposited or evaporated), the Pd thickness, the nature of the substrate (related to the surface energy), and the exterior parameters such as the temperature or the gas environment. Therefore, the comparison between the responses may be slightly different since the measurements were carried in different laboratories conditions. The observed difference between the presented sensors could actually be due to the morphology of the Pd rather than the sensor itself.

### 1.4.2 Response times of hydrogen optical fiber sensors, at room temperature condition

**Reported response time at 4 % $H_2$ :** Interferometric and FBG hydrogen O.F.S based on Pd thick films respond in an order time of few minutes. Whereas evanescent and micro-mirror based on nanometric film respond in an order of a dozen seconds. We conclude the response time depends strongly on the Pd thickness. As a rule of thumb : the thinner is the Pd film, the faster is the response. The fast response (10 s at 4%, room temperature) is obtained for nano taperer fiber sensor using a 3 nm Pd film based on amplitude modulation. In fact, we can distinguish three regimes with some particular cases, see table 1.2 :

- For a Pd thickness above 1 $\mu$m, the response time is in an order of minutes.
- For a Pd thickness between 50 and 350 nm, the response time is better than 30 s.
- For a Pd thickness between 10-15 nm $\mu$m, the response time varies from 14 to 30 s.

The observed discrepancy for film having the same thickness is likely due to the experimental condition such as the deposition conditions, the feed flow, the measurement cell, the room temperature and the gas environment.

**$H_2$ concentration dependence :** The response time depends on the hydrogen concentration. This relation is governed by the rate limited step. The response time is determined by the hydrogen surface adsorption, the surface penetration, the surface dissociation, the bulk diffusion and Pd hydride formation.

Kay et al. demonstrated that the diffusion is the limiting step for bulk thick film [73]. [3] However, the diffusion is fast enough to reasonably neglect the atomic diffusion for Pd thin film. The diffusion coefficient of the H atoms through the Pd film is $D_\alpha = 10^{-7} cm^2/s$ and $D_\alpha = 10^{-7} cm^2/s$ in both $\alpha$ and $\beta$ phases. As an example, the response time, predicted by a diffusion limited process, is 40 $\mu$s for a 20 nm thick $\alpha$ phase Pd hydride film [74], which is far inferior to the observed response time. Therefore, the surface dissociation or the diffusion (taken into account the surface penetration and the Pd hydride formation) is the kinetic limited step.

At this time, no consensus was found between scientists. Some works show the initial absorption rate is linearly proportional to the $H_2$ pressure, whereas others show a square dependence. [4]. The morphology, the quality of the surface could explain the difference ob-

3. Some studies indicated that the dissociative chemisorption of H2 at the surface is the limiting step. Kay and al. [73] assumed this observation is probably due the contamination of the surface.

4. If the dissociative chemisorption is rate limiting step, the initial absorption rate is linearly proportional to the $H_2$ pressure. While a absorption step involves that the initial rate depends linearly upon the

| Device | Minimal detection limit | Sensitivity at 4% $H_2$ | $[H_2]$ range % | Pd thickness | Response time at 4%$H_2$ | Resolution (+) |
|---|---|---|---|---|---|---|
| Mach-Zender [31, 32] | $10^{-4}$ % | | $10^{-4}$-3 % | 10 $\mu$m | | $10^{-4}$ % |
| Michelson [35] | $2.10^{-6}$ % | | $2.10^{-6}$-0,1 % | 500 $\mu$m | 3 min | $2.10^{-6}$ % |
| Fabry-Perot [37] | 3,5 $10^{-3}$ %(predicted) | | | 2 $\mu$m | | |
| Bridge configuration [66] | $10^{-2}$ % | | $10^{-2}$-0.1% | 125 mm | few day | $1{,}6.10^{-5}$ |
| Polarization modulated [40] | | | 1-10% | 6 nm | 1 min (2,8 %) | |
| Micro-mirror [41] | 0,2% | 26 % | 0,2-100 % | 10 mm | | |
| Micro-mirror [44] | 1% | 17 % | 1-100 % | 13 mm | 17 s | |
| SPR [71] | 0,8% | 26%(****) | 0,8-100 % | 12 nm | 14 s | |
| TSMF [56] | 1,8 % | close to 50 % | 1,8 - 10% | 12 nm | | |
| TMMF [55] | 0,3 % | 0,37 % | 0,3-3,5% | 15 nm | 30 s | |
| MMF [54] | 0,2 % | 40 %(****) | 0,2-0,6% | 10 nm | 20 s | |
| Hetero-structure [60] | 0,8 % | 0,6% | 0,8-5% | 10 nm | | |
| Nano fiber [58] | 0,05 % estimated | close to 35 % | 0.8-5.2% | 4 nm | 10 s | |
| FBG [63] | 0,2% | | 0,3-1.8 % | 560 nm | | $1.95.10^{-2}$ nm/1% $H_2$ (*) |
| FBG [67] | | 14 pm | 4% | 50 nm | 2 min | |
| FBG [72] | 0.5% | 0.37 nm (350 nm Pd); 0.26 nm (150 nm Pd) | 0.5-10% | 350 nm, 150 nm | 30 s (**) | |
| FBG [66] | $125.10^{-4}$% | 2.8 nm | $125.10^{-4}$ - 0.1 % | 300 $\mu$m | few days (at 100 ppm $H_2$) | 0.7 pm/$10^{-4}$% |
| LPG [67] | | 5.7 nm (depends on modes) | 4% | 50 nm | | |
| LPG [66] | 2.7 $10^{-2}$% | 43 pm (1% $H_2$) | - 4% | 40 nm | inferior to 42 s (1% $H_2$) | |
| LPG [68] | 1% | 4 nm | 1-18% | 70 nm | inferior to 70s | |
| LPG [65] | 20% | | 20-100% | 20 nm | | |

Table 1.2 – Compared performances of existing hydrogen sensors. The sensitivity S defines the change in the signal measured in presence of hydrogen, i.e the fringes shifts, the ratio between the intensity with and without hydrogen ($I_{H_2}/I_0$), the shifts of the resonant wavelengths ($\lambda_{resonance_{H_2}} - \lambda_{resonance}$) for the phase, amplitude and wavelength modulations, respectively. (+) The resolution is given by the authors. However, since the response is non linear, the resolution could be also non linear. (*) determined in the linear phase. (**) 2s if the Pd film is heated (***) We determined a sensitivity of 12 % from their sensor responses. (****We determined a sensitivity of 10 % from their sensor responses.)

served. In our study, we simply consider that the response time is faster for higher $[H_2]$ than lower $[H_2]$. Nevertheless, several works reported that the response time is slow down for hydrogen pressure corresponding to the pressure plateau [44, 74]. This phenomenon is attributed to the strain induced by the phase transformation during the expansion of the crystal lattice. Below the phase transition, there is no significant mechanical changes. Above the phase transition, a driven force enhance the absorption although the metal hydride passes by the transition phase. This is due to the difference in thermodynamics.

**Recovery time :** The recovery of the sensor is always superior to the hresponse time of the sample. The de-hydriding time can be enhanced in an oxygen atmosphere. Oxygen on the surface of Pd will induce the formation of OH and $H_2O$ molecules [76], which significantly increases the desorption rate.

**Cross-sensitivity :** Let us mention that the response time is also affected by the presence of other chemical reactions at the Pd surface, as described in section. 1.4.4.

### 1.4.3 Temperature effects on O.F.S hydrogen sensors

**Pressure composition isotherm dependences :** The Pd pcT characterize the phase behavior of metal hydrides. As described in section 1.2, the hydrogen solubility decreases at higher temperature, and the phase transition tend to disappear. Consequently, at a higher temperature the sensor response shows a decrease in sensitivity [45, 66, 68], but this condition makes easier hydrogen quantification due to the apparition of a slope plateau. For all hydrogen sensors based on metal hydrides, we need to measure/control continuously the ambient temperature in order to calibrate the sensor response.

**Sensor dependences :** The O.F.S itself is generally altered in its functions by the temperature. For example, the response of LPG sensors depend on the temperature, and the resonant wavelength shift is significant in comparison to the shift induced by $H_2$ [66]. Wei et al. reported that the change for 4 % $H_2$ in He is smaller than the change induced by 1° C temperature variations for a $H_2$ FBG sensor [68]. To realize a hydrogen fiber sensor, the exterior and gas temperature variations have to be measured in order to calibrate the sensor response. For that, a temperature sensor can be added in the hydrogen sensing fiber, for instance.

**Effect of temperature on O.F.S response time :** The temperature affects also the response time. The kinetics of the hydrogenation is enhanced by increasing the temperature (Arrhenius'relation) and is drastically decreased for low temperatures. Bevenot et al. proposed to heat the surface by light radiation in order to get an acceptable response time at cryogenic temperature [44]. The design of the resulting device consisted of a Pd film micro-mirror deposited at the end of a first optical fiber. The hydrogen concentration is measured by a reflectivity measurement. A second optical fiber is used to heat the Pd surface by using light radiation aimed at the entrance of this optical fiber. Buric et al. proposed recently to use FBG to couple the radiated light to the sensitive layer when it is deposited around the core/cladding [72].

$[H_2]$, i.e following the Sieverts law in $\alpha$ phase. [75]

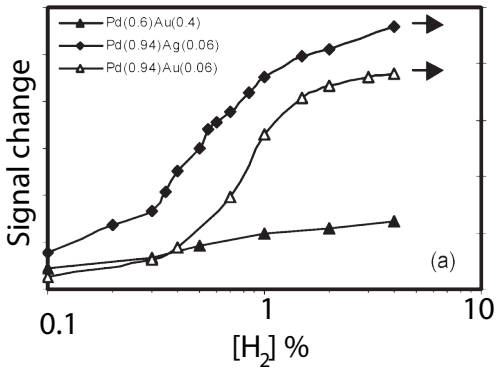


Figure 1.15 – Hydrogen concentration dependence of reflectance signal change for 20 nm thin films of $Pd_{0.94}Ag_{0.06}$, $Pd_{0.94}Au_{0.06}$, and $Pd_{0.6}Au_{0.4}$.

### 1.4.4 Cross-sensitivity in hydrogen optical fiber sensors technologies

The performance of the hydrogen sensors previously described and summed up in Tab. 1.2 have been validated in an inert environment. For safety applications, the sensor has to operate in air and in presence of other gases for specific applications. Pd is preferably used due to its catalytic properties. Nevertheless, other chemical reactions than hydrogenation can occur at the Pd surface. The presence of other gases such $O_2$, CO, $H_2O$, $H_2S$ and so forth interfere with the absorption of hydrogen. For example :

- Butler showed the sensor response time is longer in air than in inert environment [43]. At low concentration, the response is much slower in air than in $N_2$. As found by Petersson. [76], the Pd surface is dominated by adsorbed O below the critical ratio of $H_2$ to $O_2$ partial pressures ($P_{O_2}/P_{O_2} = 0.4$). Similar to $O_2$, humidity and CO cause the increase in the response time by blocking the active Pd sites [77]. Note that at elevated temperature (80°C), the cross-sensitivity is reduced [77].
- The presence of $O_2$, is also capable of limiting the amount of $H_2$ absorped due to the formation of OH and $H_2O$ onto the Pd surface [13]. The change of the sensor signal may be different, resulting in false alarms.
- The presence of $H_2S$ makes the Pd insensitive, which permanently destroys the sensor.

The Pd cross-sensitivity is a challenge to address for realizing an efficient and reliable $H_2$ sensor. However, few studies present the sensor response in oxygen, humidity or pollutant environment. The cross sensitivity is mainly a material issue. Regarding the O.F.S, sensors based on monitoring the surface characteristics as EW, SPR, LPG sensors are expected to be the more sensitive to these cross effects [66]. Although oxygen does not penetrate/diffuse in bulk Pd, oxygen is able to penetrate to the interface layer for thin and island film.

There are currently two solutions to circumvent the Pd-cross-sensitivity : the use of Pd alloys instead of Pd [77], and/or the use of a protective layer [13].

## 1.5 Sensitive materials for hydrogen sensing

### 1.5.1 Pd alloys

The hydrogen pressure composition isotherm (pcT) of high alloy content Pd shows only one phase. Such Pd alloys does not present a $\alpha$-$\beta$ transition. The advantages of Pd alloys

are :

- **Hydrogen quantification** : The dynamic range can be extending because of the absence of a pressure plateau. In addition, the saturation is obtained at higher hydrogen concentration. On the other hand, the sensor sensitivity may be limited due to the low ydrogen solubility (i.e. small optical contrast).
- **Hydrogen monitoring** : The hysteresis decreases.
- **Reproducibility** : The absence of transition phase decreases the stress inside the alloys upon hydrogenation. The sensing film presents no blisters or cracks, is more stable over time and under repeated hydrogen exposure. Consequently, Pd alloys improve the reproducibility of the responses and the sensor lifetime [77, 60].
- **Fast response** : Because of the reduction of the internal stress in the film and atomic intermixing of Pd, the absorption of hydrogen by Pd alloys is enhanced. Consequently, Pd alloys sensors show a faster response compare to Pd film [74].
- **Cross-sensitivity** : Pd alloys decrease the cross-sensitivity of Pd.

Several system has been studied, Pd-Ag, Pd-Al, Pd-Au, Pd-Cr, Pd-Cu, Pd-Mg and Pd-Ni. The reader could find more information in ref. [78, 79, 80]. As an example of the Pd alloys advantage, let us consider two examples based on Pd-Au.

- Figure 1.15, from [74], shows the hydrogen concentration dependence of the reflectivity change of a 20 nm of Pd-Au deposited on glass substrate. A LED illuminated perpendicularly the substrates, the light is then collected behind the sample. The films were annealed at $200°C$ in Ar for 1h. The cure process improves the change in the reflectance of the films upon hydrogenation, and stabilizes the microstructure of the Pd alloys films [74]. By increasing the Au content, the change in reflectance (due to the formation of the Pd alloy hydride) shows clearly the diminution of the phase transition. On the other hand, the amplitude change of the signal decreases drastically for alloy with highest Au content.
  Zhao et al. demonstrated also that the $Pd_{0.6}Au_{0.4}$ films shows a faster response upon hydrogenation than Pd film, and that alloying reduce the cross-sensitivity. Nevertheless, the response time is still longer with contaminant agents at the Pd alloy surface [77].
- Luna-Moreno et al. deposited a $Pd_{0.6}Au_{0.4}$ film on a heterostructure (multimode fiber sandwiches between two single mode fibers). The response of the sensor based on Pd alloys is slightly faster than the one based on Pd [60] : 24 s vs 23 s and & 17 s vs 15 s for 2 and 4 % $H_2$ in $N_2$, respectively. Due to the absence of phase transition, the sensor shows a nearly linear response to hydrogen concentration. In return the sensitivity (i.e the relative change) decreases.
  The same group succeeded, in 2011, in decreasing the response time to 2 s (at 4 % $H_2$ in $N_2$) by depositing Pd-Au nanoparticles [81].

### 1.5.2 Metal hydride & Rare earth materials

Huiberts et al. [82] discovered in 1995 that Yttrium and lanthanum hydride show spectacular reversible optical changes on hydrogenation when capped by a Pd layer. While the di-hydride phase is not reversible at room temperature, the film can be switched between the di-hydride and tri-hydride phase. The rare earth material had been considered as the first generation of switchable mirror [83].

Later, Mg alloys, light and cheap, were presented as an alternative [84]. Contrary to

Mg hydrides, which are too stable for de-hydrogenation, the hydrogenation of Mg alloys is a reversible process (at room temperature). Mg alloys show a large optical change upon hydrogenation and an expansion of 30 % in volume. The hydrogenated state occurs for a hydrogen pressure above the pressure plateau of the considered Mg alloys, fig. 1.16. The pressure plateau, $8.8.10^{-3}$% (0.088 mbar) for $Mg_{70}Ti_{30}$ at room temperature, is much lower than for Pd. Consequently, a large optical change is obtained for very low $H_2$ concentrations.

Slaman et al. [13] developed a hydrogen micro-mirror fiber sensor based on Mg alloys. A 50 nm $Mg_{70}Ti_{30}$ layer is deposited at the end of a cleaved multimode fiber (200 $\mu$m/15$\mu$m), covered by a 20 nm Pd layer. The Pd layer is to dissociate the hydrogen and prevents the oxidation of the Mg alloys. Furthermore, a protective coating is depositedin order to prevent the degradations of the sensing films by humidity. In this configuration, the sensitive layer is the Mg alloys, Pd plays only the role of catalyst.

The measurements were carried out in the $H_2$ range of 0.2-1 % in Ar. The sensor can detect a very low hydrogen concentration, inferior to 0.2 % in Ar, but the authors emphasize that the response of the sensor becomes too slow at these concentrations to use the sensor in practical applications. At a wavelength of 635 nm, a relatively fast (50 s at room temperature) and large contrast is obtained at 0.4 % $H_2$ in Ar. The response is reversible in presence of $O_2$, and no significant aging effects are observed . However, a small deviation is obtained for the first cycle due to the mechanical stabilization of the film. Finally, the authors noticed that the response is slower in presence of $O_2$, but can be enhanced by replacing Pd by Pd alloys, as explained in section 1.4.4.

On advantage of metal hydrides as sensing material is to provide a wide range of pressure composition isotherms (pcT). The above example shows that other metal hydrides than Pd could satisfy the requirement for hydrogen sensors. New minimal and dynamic range of the hydrogen sensors, based on metal hydride (Pd), could be achieved. In this frame, Mg-Ti, Mg-Ni [85] or ultrathin Mg film [86] seems the most appropriate candidate to provide a fast and reproducible response. Finally, tuning the alloy content of Mg offers the possibility of hydrogen quantification, thanks to the shape of the pcT curves of $Mg_yTi_{1-y}$ as depicted in fig. 1.16.

### 1.5.3 Tungsten oxide

The reduction of tungsten oxide ($WO_3$) by hydrogen start above 400°, and form a tungsten bronze. The reaction may be described as :

$$WO_3 + xH^+ + xe^- \Leftrightarrow H_xWO_3, \qquad (0 < x < 1) \tag{1.10}$$

The greenish yellow color of the material changes to blue during the hydrogen reduction. Noble metal catalysts, such as Pd or Pt, promote the reaction at room temperature [87]. (The reduction is also accelerated by the presence of water.) The chemical reaction is reversible in presence of oxygen. The re-formation of $WO_3$ is accompanied by the generation of water molecule [88] :

$$2H_xWO_3 + 0.5xO_2 \rightarrow 2WO_3 + xH_2O \tag{1.11}$$

Ito was the first to propose an optical fiber hydrogen sensor based on based on $WO_3$

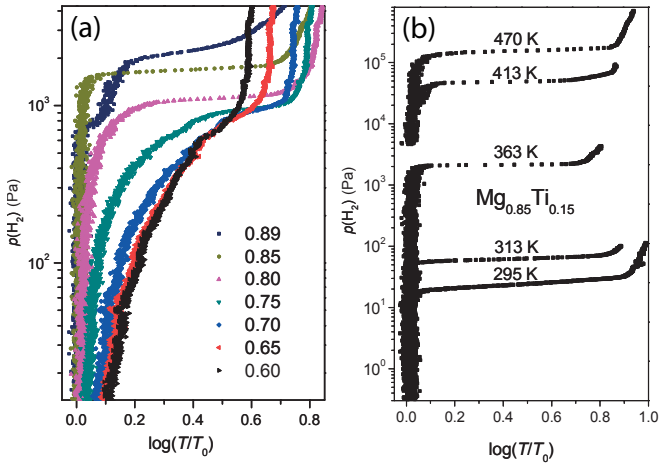


Figure 1.16 – (a) Pressure versus optical-transmission isotherms of a thin $Mg_yTi_{1-y}$film with a continuous gradient in an alloy composition. (b) Pressure versus optical-transmission isotherms for $Mg_{0.85}Ti_{0.15}$ at five different temperatures. The transmission T is normalized to the transmission in the metallic state $T_0$. [26]. The pcT curves have been determyned by hydrogenography.

with a Pd cap layer. Benson et al. proposed then two new sensor designs to improve the response time of the Ito's sensor [14].

The first sensor consisted of coating a 500 nm $WO_3$, with a cap layer of 10 nm Pd at the tip of a cleaved polymer optical fiber. This micro-mirror sensor, based on the changein refectance during the reduction of $WO3$, is a function of hydrogen. ThIn particular, the reduction of $W0_3$ increases the optical absorption coefficient.

The second sensor, developed by Benson, consisted of a stack layer, made of 40 nm Au, 600 nm $WO_3$ and 3 nm Pd deposited onto one face of a prism. The prism is then set at the end of an optical fiber in such a way that the base of the prism is illuminated by the optical fiber. Consequently, the incident light strikes the film at an angle of 45 °. A SPR is observed at a certain wavelength. Since the stack layer acts like a pair of coupled resonators, the resonance wavelength and the resonance amplitude depend on the thickness and the optical constant of the three layers. In presence of hydrogen the SPR peak shifts due the change in the refractive index of the coating.

For both designs, a high sensitivity is obtained but the sensitivity to humidity made $WO_3$ unadoptable for the hydrogen safety applications. As $WO_3$ is nano-porous and exchanges water vapor with air at the equilibrium, this material turn out to be extremely sensitivity to humidity. In fact, the refractive index of $WO_3$ is affected by the amount of adsorbed water. For example, an exposure to dry gases causes a decrease in the $WO_3$ refractive index, which will lead the sensors to false alarms. Furthermore, the response time increases dramatically due to the prolonged exposure of $WO_3$ to humidity : the first response time of a few seconds for a concentration of 0.9% $H_2$ increases to a period of days over time. A sufficient Pd thickness can block the water vapor while still allowing the hydrogen to reach the $WO_3$. In return, the sensor becomes irreversible [14].

Despite of the water issue, several optical fiber sensors based on $WO_3$ have been proposed in the literature this last decade. We describe hereafter some examples.

**Fiber evanescent sensors** : the sensor consists of coating the silica core of an optical fiber of $WO_3$, covered by a Pd (or Pt) layer or dispersed in the sensitive layer to dissociative hydrogen. The change of the absorption coefficient or/and the refractive index of the film due to the reduction of $WO_3$ attenuate the intensity of the propagating light [15, 16, 89, 90].

Sekimoto et al. [15] showed that the use of sol-gel process enhances greatly the response time, compare to a $Pd/WO_3$ dispersed silicone resin ( a response time of 7 min was obtained). According to the authors, the sensor shows higher sensitivity at low hydrogen concentration, and the response tends to saturate above 40 %. The sensitivity of the sensor will depend on the sensing length (generally about 10-20 cm), the thickness and the quality of the sensitive film.

Okazaki et al. [16] investigated then the humidity and temperature dependence of the $Pt/WO_3$ sensor. The humidity does not alter the intensity change of the sensor, but the response and the recovery time gradually become slower, in presence of inert gas or air than in humid environment. Later, the same team finds out contradictive results on kinetics : the sensor shows a higher sensitivity and a faster response in inert atmosphere than in humid environment. The deterioration of the performance results from the promotion of the oxidation reaction by humidity.

**Fiber grating sensors** Caucheteur et al. [91] proposed a hybrid fiber gratings covered by a $WO_3$/Pd stack layer. The hybrid fiber is made of a Fiber Bragg Grating (FBG) and a Long Period Grating (LPG). The LPG provide a light energy coupling to the sensitive layer to enhance the minimal detection, while FBG is used to probe the hydrogen concentration. The measurement is based on the shift of the resonance bands due to the release of heat from the exothermic reaction. The sensor response was investigated in the hydrogen concentration range of 0.9-3 %. The Bragg wavelength shift $\lambda_B$ increases as the hydrogen concentration increases. The change in the $\lambda_B$ is barely dependent on the humidity and the temperature (between $-50°$ to $25°$), but the minimal detection is changed : 0.5 % and 0.9 % in dry air and 90 % wet air, respectively. Although the authors claim a fast response, the response time is not reported.

In conclusion, $WO_3$ seems unadaptable to hydrogen sensor for safety applications because of the slow response time and the drastic humidity dependence of the sensor response. Nevertheless, a protective layer could overcome the cross-sensitivity issue. The protective layer has both to protect the sensitive film from the oxidation, and also to manage the generation of water at its surface for the recovery. In analogy to tungsten oxide, other oxide materials such as Vanadium Oxide have been aslo studied [92, 93, 94, 95].

## 1.6 Conclusion

1) This analytical review of Pd Hydrogen fiber sensors gives an overview about the performance of O.F.S in hydrogen sensing in term of sensitivity, response time, reliability, reproducibility and robustness.

- Interferometric sensors are complex optical devices (lenses, monomode, etc...) and very sensitive to vibrations. Generally based on the Pd hydride expansion, they show a slow response time and a bad reproducibility due to the use of thick Pd films (i.e. optically thick : superior to about 60 nm). The film degradations may be

overcome by limiting the detection range of the sensor to the $\alpha$ range (in order to avoid the phase transformation). At this stage, interferometric sensors are far from being mature to be used in industrial applications. However, interferometer based on thin Pd films may be of interest to detect very low hydrogen concentrations.

- $H_2$ O.F.S based on amplitude modulation are simple devices (LED, multimode, etc...). In return, they are sensitive to all the no-controlled losses which can occur, such as the fluctuation of the light, the change in coupling coefficients between the optical elements and so forth as reported in [96]. Micro-mirrors are the most convenient to handle and can be realized at low-cost. It is conceivable to use these sensors, with very thin films, in industry. If quantification and very high sensitivity are required, metal hydrides with a low equilibrium pressure plateau have to be considered, as explained in section 1.5. Evanescent wave sensors, such as tapered fiber sensors and SPR sensors have been proposed to improve the hydrogen sensitivity, and to quantify the hydrogen concentration. Moreover, they offer the possibility of multi-points or distributed sensing. They show a fast and reproducible responses due to the use of thin films. However, the challenge for these sensors is to make them more robust, insensitive to the surrounding constraints and to make their fabrication reproducible : by the control of the deposition of thin metal layers on an optical fiber.
- The wavelength modulated sensors are very promising for industrial applications due to their possibility of multiplexing, their capacity to realize multi-points sensors, and to measure different constraints by tuning the grating. However, hydrogen FBG sensors show a poor reproducibility of their responses because they are based on the mechanical deformations of a Pd film. Adding an adhesion layer such as Titanium and Nickel will improve the reproducibility of the signal. Recently, new designs based on thinner Pd films (about 70 nm) have been proposed, but their response times are still too slow. As a conclusion, grating hydrogen sensors are not yet commercially ready.

**2)** In spite of the Pd limitations, Pd is still considered as a good material, especially in very thin film forms, in order to realize an effective hydrogen sensor. Replacing then Pd by Pd alloys seems to be a relevant approach. The reliability (cross-sensitivity), the reproducibility (lifetime) and the response time will allow to foresee the merchantability of $H_2$ O.F.S sensor. Nevertheless, finding a material with high catalytic properties and especially without cross-sensitivity is still one of the « key »to realize a fast and reliable hydrogen sensor.

**3)** Finally, an appropriate engineering of the pressure composition isotherm (pcT) of metal alloys allows to tune the detection range. In addition, magnesium alloys, such as $Mg_{70}Ti_{30}$ [12], are promising to reach lower minimal detection.

## 1.7 Proposed sensor

Based on this study, we have decided to realize a Surface Plasmon Resonance (SPR) intrinsic optical fiber sensor. The sensor takes benefit from the fiber advantages, such as remote sensing and the possibility of multi-points detection. On the other hand, the sensor will be expected to show a sensitive, fast and reproducible response. Here, we make use of the fact that SPR sensors in general show a high sensitivity even for very thin metal sensing layers. Furthermore, we use multimode fibers in order to realize robust sensors due to their large core diameter. In addition, the use of multimode fibers is an easy way to

realize and study the response of SPR sensors. Thus, we can investigate the potential of surface plasmon for hydrogen sensing. Our work could then be extended to other structures such as single mode fibers, tapered fibers, side-polished fibers and integrated waveguides. We did not address the cross-sensitivity issue since the cross-sensitivity depends more on the material properties than the optical configuration. Finally, Pd will be used as a sensing material (and model) in order to demonstrate the principle and the possibilities of optical fiber sensors based on metal hydrides. Appropriate materials could be applied in a later stadium in order to overcome the sensor cross-sensitivity issue, and to modify the detection range of optical fiber hydrogen sensors.

Finally, our working hypothesis choices are :

1. Sensitivity : development of SPR sensors
2. Fast and reproducible : development of optical fiber sensors based on Pd thin films.
3. Multi-points sensing : development of an intrinsic optical fiber sensor.
4. Extend the dynamic range : study of different metal hydrides materials ( in intrinsic optical fiber sensor : possibility to juxtapose different hydrogen sensitive materials which results in the detection of different hydrogen concentration ranges).

# chapter 2

# Surface Plasmon sensors - Principle and applications

## 2.1 Introduction

Surface Plasmon Polariton (SPP) is an electromagnetic wave propagating at the metal dielectric interface, which is accompanied by a collective coherent oscillation of free electrons. These waves are non radiatives. They were predicted by R. H. Ritchie [97] in 1957. Powell and Swan demonstrated their existence in electron energy-loss experiments two years later [98]. With a reflection technique, they observed that « the losses affected by surface phenomena were superior to the measurement of the characteristic loss spectrum of electrons transmitted through film ». In 1968, Otto optically showed the presence of SPP on a metal thin film. Illuminating the metal film under certain conditions causes a large drop in reflectivity due to the propagation of SPP at the interface of the metal thin film : the energy of the radiated light is transfered to the SPP. However, SPP was observed, for the first time, by Wood [99] on metallic grating in 1902. Wood observed a rapid variation in intensity, resulting in dark or bright bands, in the spectrum of a continuous light source given by an optical metallic diffraction grating. The variation was obtained for different conditions of incidence but was only present for p polarization, where the magnetic field is parallel to the grating grooves. Inexplicable in the past, they will be termed as « singular anomalies »and now called « Wood anomalies »in the literature. Although scientist pay a considerable attention, the effective role of SPP was found more than half a century afterward, mainly based on the work of Rayleigh, Strong and Fano.

Surface Plasmon Polaritons have played a key role in the understanding of various fundamental properties such as the nature of Van der Waals forces [100], the classical image potential acting between a point classical charge and a metal surface [101, 102], the spatial dispersion on electromagnetic surface modes [103], surface energies [104] and so forth. Plasmonics are now of great interest for nano-photonics engineering due to the strong confinement of the light [105, 106]. Researches spread from Extraordinary Optical Transmission (EOT) [107], near field microscopy, super lensing, sensing, meta-materials, photovoltaics, quantum communication to nano-circuits.

In this thesis, we focus only on the hydrogen sensing application. The potential of SPP

in sensing was largely demonstrated these last years. This chapter [1] discusses the properties of SPP, which account for the developments of Surface Plasmon Resonance (SPR) sensors. After defining the plasmonic terms, we first demonstrate the existence of the SPP at the metal dielectric interface from an electromagnetic point of view. We second study the dispersion relation of SPP to emphasize their evanescent natures (i.e. non radiative waves) and their properties of confinement. Since SPP are non radiative, we third present the methods to excite and observe these waves. Finally, we report a review of SPR and fiber SPR sensors to show how we can realize such sensors.

## 2.2 Definition

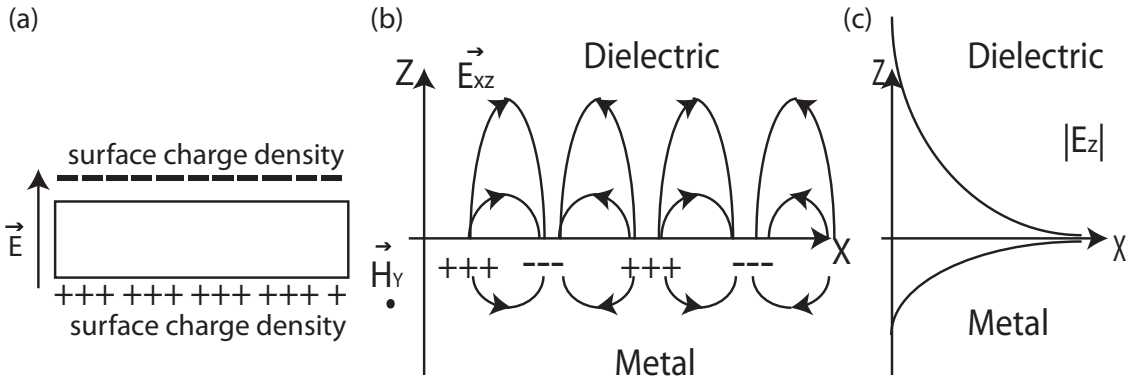


Figure 2.1 – (a) Volume plasmon : longitudinal collective oscillations of the free charges for a slab.(b)Electric field lines of a surface plasmon mode propagating at the metal dielectric interface, accompanied with a surface charge density wave. (c) Confinement of the SP electric field at the metal dielectric interface

**Volume plasmon :** A plasmon is a collective oscillation of a free electron gas. The origin of these oscillation can be understood by considering a metal slab. The collective displacement of the (free) conduction electron cloud compared to the (fixed) positive charge of the ion cores in the metal slab induces a surface charge density $\pm\sigma$ at the slab boundaries (fig. 2.1a). The difference in the surface charge density between the two boundaries creates a homogeneous electric field E inside the metal slab. The repulsive force of the induced electric field initiates then the oscillating mechanical movement of the free electrons. To summarize, the plasmon takes places to opposite the internal polarized field due to the displacement of all electrons. The plasma frequency $w_p$ is the natural frequency of these oscillations. These oscillations are purely longitudinal ($\vec{\nabla}.\vec{D}$=0, with D the electric displacement field). In other word, the associated electric field is in the same direction than the direction of the collective oscillations of the free charges.

**Plasmon Polarition :** When the collective oscillation is induced by a photon, the plasmon is called a plasma polariton.

**Surface plasmon :** At the interface of two media, the longitudinal collective oscillations of free electrons are of a different matter. Contrary to bulk oscillations, the oscillations

1. This chapter is based on the references [108, 109]

of electrons induce a supplementary transverse field ( $\vec{\nabla}.\vec{D}$=0 is no longer satisfied at the interface) which modify the longitudinal field. Roughly speaking, as previously a displacement of charges at the interface causes the collective oscillations as depicted in fig. 2.1b. In addition, the difference of charge between the two interfaces create an electric field perpendicular to the interface. The combination of these two phenomenons (intimately linked by the Maxwell equation) result in the propagation of a SPP : a collective longitudinal oscillations of free charges (plasmon) accompanied by a transverse electromagnetic light propagating at the interface.

Therefore, SPP may be considered either as collective oscillations of electrons, electromagnetic wave or mode, depending on the point of view : solid state physics, electrodynamics or optics, respectively. The term Plasmon polariton explains this bi-character. In the following, we call them Surface Plasmons (SP) as it is commonly done in the literature. We present here the theory of Surface plasmon from the electromagnetic point of view to find out the condition of such oscillations.

## 2.3 Dispersion Relation (DR)

SP is a solution of Maxwell's equation in the absence of external field. To determine the dispersion relation of SP, i.e. the relation between the frequency $w$ and and the wavevector of SP $k^{SP}$ , we solve the maxwell equation at the interface of two media : medium 1 ($\epsilon_1$) and medium 2 ($\epsilon_2$). Because of the longitudinal nature of the collective oscillations, we restrict ourselves to the Transverse Magnetic (TM) polarization ($E_x, E_z$ and $H_y$, $E_y$=0) , so-called polarization p. In fact, the Transverse Electric (TE) fields ($E_x, E_y$ and $H_z$, $E_z$=0), so-called polarization s, are purely transverse fields since $\vec{\nabla}.\vec{D}$=0 at the boundary.

We consider two semi-infinite media. We assume that the medium is isotropic and local, what allow to introduce a dielectric permittivity $\epsilon(w)$. We assume a one dimensional problem, i.e. thereare no spatial variations in the y-direction. The wavector of the SP is composed of a x and z components : $k^{SP} = k_x^{SP} + k_z^{SP}$. The electric field $E_{SP}$ can be written, with Cartesian coordinates, as :

$$E_{SP}(x, y, z, t) = E_0 e^{-j(wt - k_x^{sp} x - k_z^{sp} z)} \tag{2.1}$$

The term $e^{-jwt}$ describes the time dependence. We look for a solution propagating along the x axis and confined at the interface. Thus, the solution obeys Helmöltz equation in both media :

$$\nabla^2 E_i + \mu_i \epsilon_i \frac{w^2}{c^2} E_i = 0 \tag{2.2}$$

with : i=1, 2. By replacing $E_i$ by its expression (eq. 2.1) , we obtain :

$$\begin{aligned} z < 0; \quad E_{x,1} &= E_0 e^{j(k_x^{sp} x + k_{z,1}^{SP} z)} \\ E_{z,1} &= -\frac{k_0 E_0}{k_{z,1}^{sp}} e^{j(k_x^{sp} x + k_{z,1}^{sp} z)} \\ z > 0; E_{x,1} &= E_0 e^{j(k_x^{sp} x - k_{z,d}^{SP} z)} \\ E_{z,2} &= \frac{k_0 E_0}{k_{z,2}} e^{j(k_x^{sp} x - k_{z,2}^{sp} z)} \end{aligned}$$

with $k_{z,i}$ the component of the wavector in the z direction in the medium i (i=1 or 2). Note that the component of the wavector in the x direction in the both media are equal due to continuity of the phase velocity : $k_{x,1}^{sp} = k_{x,2}^{sp}$.

From the continuity condition at the interface of the electric field, we obtain so :

$$\epsilon_1 k_{z,2} + \epsilon_2 k_{z,1} = 0 \tag{2.3}$$

Eq. 2.3 is the dispersion relation of SP. Assuming a non magnetic material, it is only fulfilled at the interfaces between materials with opposite signs of the real part of their dielectric permittivities.

In conclusion, SP propagate only at a metal dielectric interface, i.e. $\epsilon_1 = \epsilon_m$ (metal) and $\epsilon_2 = \epsilon_d$ (dielectric), and SP can only exist for polarization p. [2]

Furthermore, we have :

$$(\epsilon_m \frac{w}{c} =)\ k_m^{SP} = k_x^{SP} + k_{z,m}^{SP} \qquad (\epsilon_d \frac{w}{c} =)\ k_d^{SP} = k_x^{SP} + k_{z,d}^{SP} \tag{2.4}$$

Combining Eq. 2.4 and 2.3 the component of the SP wavector in the x-direction is :

$$k_x^{SP} = k_0 \sqrt{\frac{\epsilon_d \epsilon_m}{\epsilon_d + \epsilon_m}} \tag{2.5}$$

### 2.3.1 Non-lossy metal

To discuss the properties of SP, we use, as a first approximation, the Drude model (metal described by a free electron gas) to describe the permittivity dielectric. We assume a non lossy metal, i.e the relaxation time is identically zero. Thus, the metal dielectric function is written as :

$$\epsilon_m(w) = 1 - \frac{w_p^2}{w(w + j * w_\tau)} = \epsilon_m(w) = 1 - \frac{w_p^2}{w^2} \tag{2.6}$$

with $w_p$ the (volumic) plasmon frequency. Replacing Eq. 2.6 in Eq. 2.5, we obtain the SP propagation constant :

$$k_x^{sp} = \frac{n_1 w}{c} \sqrt{\frac{w^2 - w_p^2}{(1 + \epsilon_1)w^2 - w_p^2}} \tag{2.7}$$

Assuming air the dielectric medium, fig. 2.2 draws the DR of SP propagating at the metal air surface. From Eq. 2.7 two branches (blue and red) are obtained. The dark line represents the light line $k = w/c$. The left of the light line represents the radiated modes. [3]

1. The first branch (blue) is for frequencies larger than : $w_p$. It represents the solution of the equation $\epsilon_m k_{z,d} - \epsilon_d k_{z,m} = 0$, known as the Brewster angle. This branch is not a surface wave. The light radiates into the solid and propagates with a phase velocity larger than c. The metal dielectric constant is seen as a dielectric from the optical point of view : the frequency is above the plasma frequency ($\epsilon_m$ positive and real number).

2. For polarization s, the dispersion relation, $\mu_1 k_{z,2} = -\mu_2 k_{z,1}$ ($\mu$ defines the permeability), is only fulfilled if $\mu_1/\mu_2 = 0$ since $Re(k_1), Re(k_2) > 0$ (required by the confinement to the surface)

3. The dispersion relation of a plane wave $e^{\vec{k}.\vec{r}}$ in a homogeneous medium with $\epsilon_0$ is defined by $\epsilon_0 k_0^2 = k_x^2 + k_y^2 + k_z^2$ , where $k_0 = w/c$ is the wavevector in the free space. All wavevector components $k_i$ of the plane waves are smaller than $k_0$.

2. The second branches (red) is the dispersion relation of SP. SP have a longer wavevector than the light in the adjacent medium : its dispersion curve is lied to the right of the light line. Thus, SP are non radiatives and cannot be coupled to a radiative light. Special phase-matching techniques such as gratings, prisms, are required to excite SP as we will see in section 2.5.
   The confinement of the field at the surface in the z direction is related to $k_x$ (pure real and positive) through eq. 2.4. Consequently, $k_{z,i}$ (i=metal or dielectric meadia) is pure imaginary. The plasmon field is evanescent in the sense that the field is bound at the interface. The field has its maximum at the interface and decays exponentially into both media, as it is shown in fig. 2.1c. The SP electric field from eq. 2.1 can be written as :

$$E_{SP} = E_0 e^{-j(wt - k_x^{sp} x)} e^{-\|k_{z,i}^{sp}\| z} \tag{2.8}$$

   The first term show the propagation of the wave in the x-direction, while the second term leads to the confinement of the field.
   Finally, the DR shows an asymptote for a frequency $w_p/\sqrt{1+\epsilon_{dielectric}}$. At the frequency approaching $w_{SP}$, the mode acquires an electrostatic character because the group velocity tends to 0. For small wavevectors (corresponding to low frequencies :mid-infrared or lower), SP propagation constants are close to the light line, i.e $k_0$. In this regime, SP are known as Sommerfeld-Zenneck waves.
3. Between both branches, we observe a gap where the wave does not propagate since $k_x$ is purely imaginary in the absence of losses (black dash line). Thus, SP do not propagate.

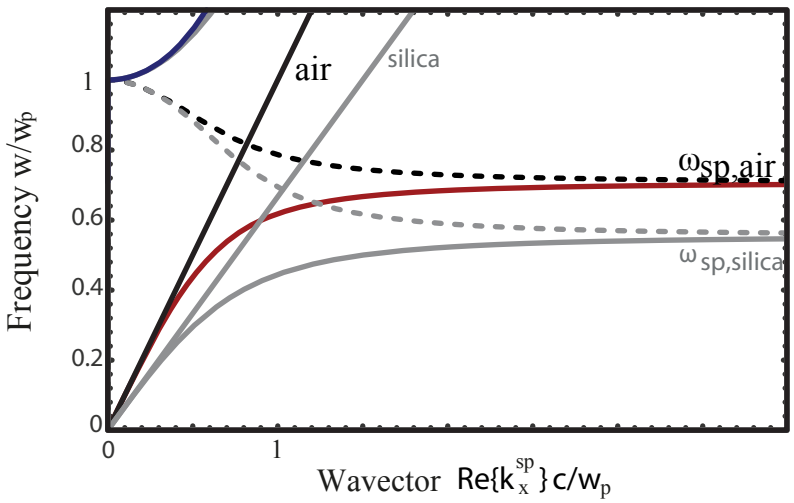


Figure 2.2 – Dispersion relation of the SP at the interface between a Drude metal with no losses and air (red lines) and silica (gray line), from ref [109]. The dash lines are the imaginary part of the propagation constants of the SP.

### 2.3.2 Lossy metal

In a real metal, the dielectric permittivity is actually complex due to the damping of the free electron oscillations and the interband contribution. It is straightforward that

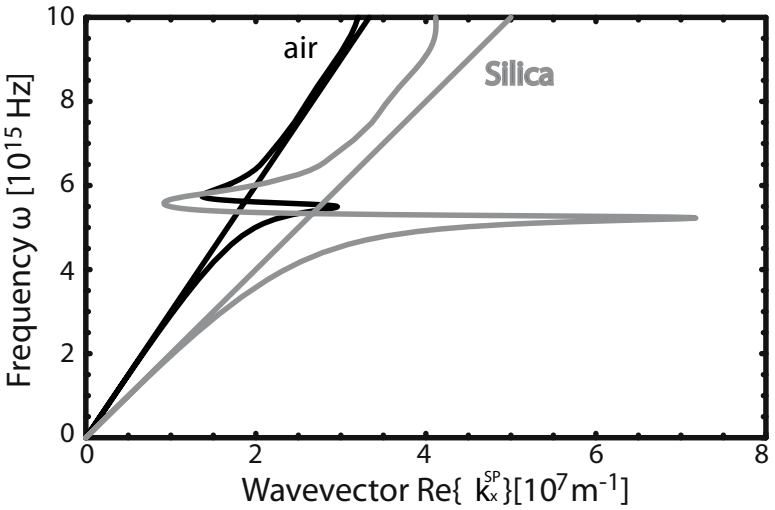


Figure 2.3 – Dispersion relation of SP at a silver/air (black lines) and silver/silica (gray lines) from ref [109]

the ohmic dissipations causes the decay of SP with a characteristic propagation length L. Figure 2.3 shows, in this case, a finite value for the largest wave vector at the surface plasmon frequency limiting thus the confinement of the field. The electric field of SP can be written as :

$$E_{SP} = E_0 e^{-j(wt-k_x^{sp}x)} e^{-\|Im(k_x)\|x} e^{-\|k_{z,i}^{sp}\|z} \tag{2.9}$$

In consluion, SP propagate along the x-direction (first term), with attenuation (second terms),while the field is bound to the interface (third term).

## 2.4 Confinement of the SP field

The component $k_{z,i}^{SP}$ (pure imaginary) defines the confinement of the SP at the metal dielectric interface (i=m, d). The field amplitude decreases exponentially in the both media as $e^{-\|k_{z,i}^{SP}\|z}$. The spatial attenuation $Z_i$ defines the intensity decrease to 1/e and $Z_i = \frac{1}{\|k_{z,i}^{SP}\|}$.

Assuming a real $w$ and $\epsilon_d$ that $\epsilon_{m,i} < \|\epsilon_{m,r}\|$, we obtained :

$$k_{m,z}^{SP} = k_0 \sqrt{\frac{\epsilon_{m,r}^2}{\epsilon_d + \epsilon_{m,r}}} \qquad k_{d,z}^{SP} = k_0 \sqrt{\frac{\epsilon_{d,r}^2}{\epsilon_d + \epsilon_{m,r}}} \tag{2.10}$$

For an example, the spatial attenuation of SP propagating at the silver vacuum interface is respectively about 370 nm and 23 nm in the vacuum and silver, at a wavelength of 600 nm. The attenuation is much larger in the metal than in the dielectric.

The properties of confinement account for the use of SP in :
– Imaging applications : because of the field confinement, the resolution is below the diffraction limit of half the wavelength in the dielectric for a frequency close to $w_{sp}$.

– Sensing application : Due to the confinement of the light at the metal dielectric interface in a thickness of sub-wavelength, SP are sensitive to any perturbation at the surface.

## 2.5 Distance of propagation of the SP field

The imaginary part of the propagative constant $k_x^{SP}$ defines the energy losses that come from the absorption in the metal. The intensity of SP propagating along the x axis on smooth surface decreases exponentially as $e^{-2.Im(k_x)^{SP}x}$. There is no dissipation in the normal direction since the field is evanescent in this direction. The length L after which the intensity decreases to 1/e is given by :

$$L = \frac{1}{2.Im(k_x)^{SP}} \tag{2.11}$$

As an order of magnitude, the length of the SP propagating at a silver air interface is typically 16 $\mu$m (z=180 nm) and 1080 $\mu$m (z=2.6 $\mu$m), at a wavelength of 450 nm and 1500 nm, respectively. The better the confinement is, the lower is the propagation length.

## 2.6 Excitation of Surface Plasmon

### 2.6.1 Optical excitation

From the dispersion relation of SP, we have previously seen that SP cannot be directly coupled by radiated plane waves. At a given photon energy $\hbar w$, a certain momentum $\Delta k_x$ has to be added to the incident light with the wavevector $k_0 = \hbar w/c$, in order to match the both wavevectors (fig. 2.5) :

$$k_x^{SP} = k_0 + \Delta k_x \tag{2.12}$$

in the sense that the both phases velocities match at the interface. There are two main techniques to overcome the wavevector mismatch and couple light into SP modes on a metal surface.

1. The first technique, demonstrated by Otto and Kretschman, is based on Attenuated Total Reflection (ATR) at the interface of a prism.
2. The second technique is based on periodic corrugation. It has to be related to Wood's experiment.

Several other techniques can be found in the literature such as fiber coupling, near field probe, objective with large Numerical Aperture (NA), integrated waveguides, but they can be considered as particular cases of the above techniques.

#### 2.6.1.1 Prism coupling

Otto demonstrated that the evanescent wave from the total reflection of the light at the quartz ($\epsilon_d$) air ($\epsilon_0$) interface can be coupled to SP when a metal layer ($\epsilon_m$) is close to the interface, at a distance of about $\lambda$, as depicted in fig. 2.4a. The propagation constant of the evanescent wavevector increases compared to the incident light. Figure 2.5 shows that the DR of the evanescent wavevector can cross the dispersion relation curves of SP at the metal air interface. At the cross-point, the phase velocity of the SP and the evanescent

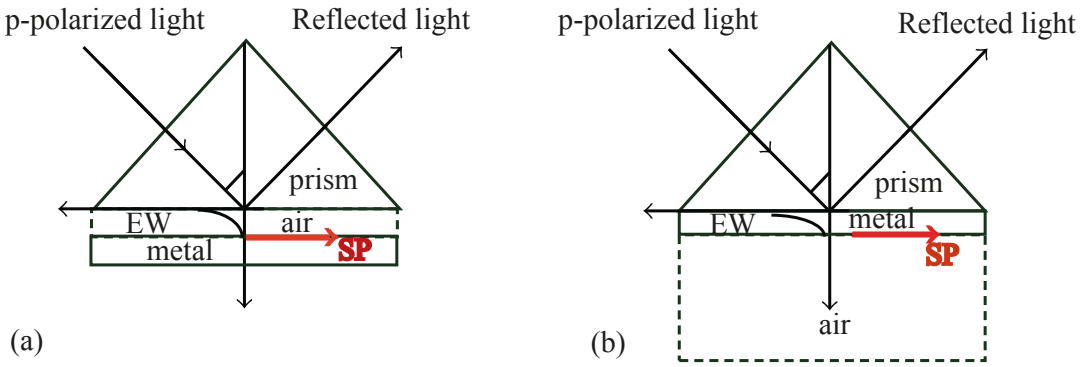


Figure 2.4 – Otto and Raether-Kretchmann's configuration

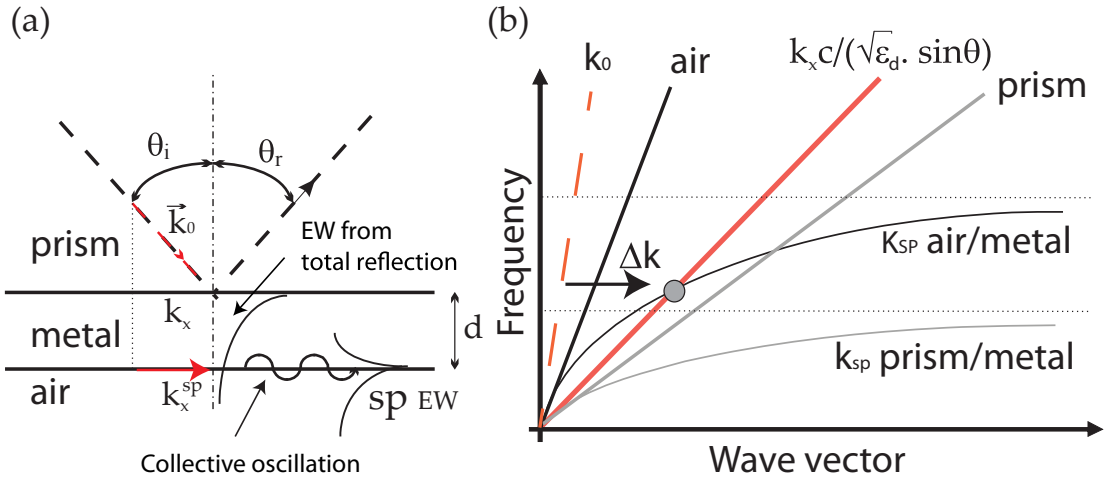


Figure 2.5 – The dispersion of a surface plasmon on a metal/air and metal/silica surface and the dispersion of light in the adjacent dielectric medium respectively.

light match. Finally, the light ($k_0$) is coupled, by the intermediated of the evanescent wave $k_{x,EW}$, to SP when the following match condition is satisfied :

$$k_{0,x} = k_{x,EW} = \sqrt{\epsilon_1 \frac{w}{c}} \sin\theta_0 = k_x^{sp} \tag{2.13}$$

As a result, for all frequencies $w$ and incidence angle $\theta_0$ satisfying 2.13, a SP propagates at the metal dielectric interface.

Kretschmann-Raether demonstrated the existence of SP at the metal air interface, when a thin metal film is deposited on the prism (fig. 2.4b). In the same way, the electromagnetic field decreases exponentially in the film and couples to SP at the metal air interface when the wavevector of the evanescent wave matches with the wavector of the SP. Figure 2.5 shows the DR of SP for a quartz/metal/air in the Kretschmann system. It is interesting to note that the SP at the metal/quartz interface cannot be excited, since their DR is lied

to the right of $c/\sqrt{\epsilon}$.

From Fresnel's equations, we can calculate the reflected light as a function of the incidence angle at a give $\lambda$ :[4]

$$R_{pol.p} = \|\frac{E_r^p}{E_0^p}\|^2 \ (= \frac{\epsilon_d.k_m - \epsilon_m.k_d}{\epsilon_d.k_m + \epsilon_m.k_d} \ ) \ at \ metal - dielectric \ interface \tag{2.14}$$

Figure 2.6a depicts the reflectance as a function of the incident angle at a given wavelength for a three layer system (quartz/Silver/air). These curves will be called Surface Plasmon Resonance (SPR) curves in the following of this thesis. The reflectivity drops when the resonance condition is matched. The energy of the light is transfered to the SP instead of being reflected by the metal. Figure 2.6b illustrates the energy transfer of the light. The intensity of the electric field parallel to the interface is plotted for two angles : at the resonance (red line) and at the total reflection condition (blue line).

The resonance excitation of the SP is proportional to the exciting field strength and the total damping rate [108]. In the sense that the lost energy is due to the inherent absorption inside the metal, but also due to leakage of radiations into the prism (the SP propagation constants lie within the prism light cone). Generally speaking, the interference of the SP excitation with the radiative losses result in the drop of the reflectivity. The evanescent waves from the total reflection induce excitations at the metal/air interface. These excitations radiate light back into the metal film and interfere with the incoming evanescent waves. Then the two waves set interfere destructively since they are in anti phase. By changing the metal thickness, the interference are altered and therefore the SPR curve is altered.

Figure 2.6a demonstrates the effect of a variation of the metal thickness at a constant value $\lambda$ on the position, shape and height of the ATR minimum. If the thickness increases, the back scattered field disappears. While decreasing the thickness, the back-scattered field increases and start interfering destructively with the incoming wave. With a given thickness, the interference is maximal. It can be shown that this resonance is maximal if the damping due to leakage radiation is equal to the damping due to absorption (critical coupling). The damping due to absorption defines the imaginary part of the SP propagation constants for a single layer system metal/dielectric.

It is important to note that the SP propagation constant $k_x^{SP,system}$ for the system presented above are different that the expression established in section 2.3 (eq. 2.5). Contrary to two semi-infinite media, the layers have a finite thickness in the prism. The propagative constant can be, now, written as a sum of a perturbation to the SP propagative constant, $k_x^{SP,0}$, determined in eq. 2.5 :

$$k_x^{SP,system} = \Delta k_x + k_x^{SP,0} \tag{2.15}$$

The propagation constant : $k_x^{SP,system}$ can be analytically or numerically determined [108]. The study of waveguide plasmonics consists essentially of calculating and tuning this propagation constant. For sensing application, we will focus on the shape of the SPR curves. We are interested in the change of the reflective light when the interface conditions are altered, as described in section 2.7. However, both studies give the same information but from different point of views. The position and the width of the peak define respectively the real and the imaginary part of the SP propagation, respectively.

4. The dispersion relation can be obtained from Eq. 2.14 by looking for the poles of the reflection factor.

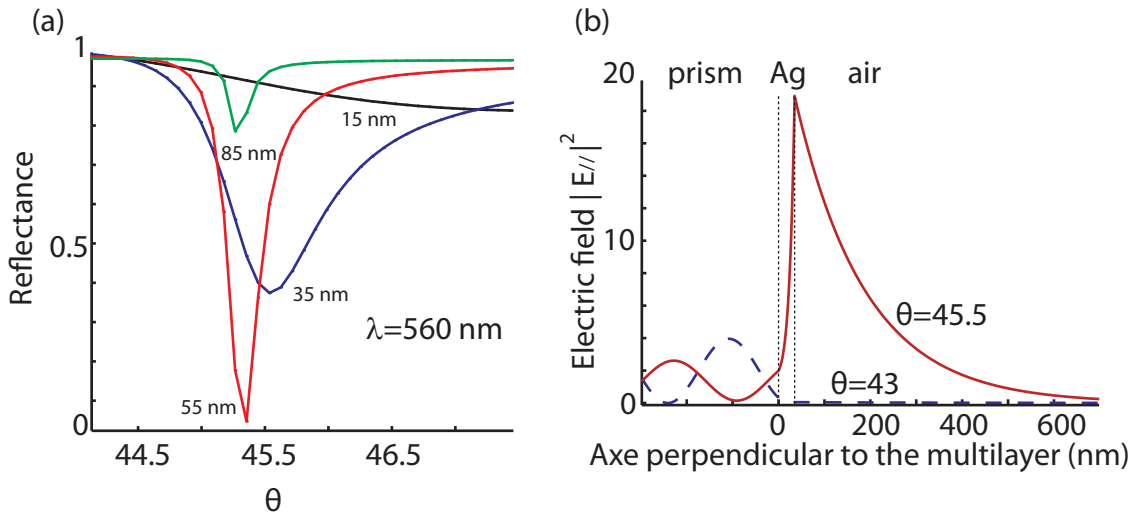


Figure 2.6 – (a)SPR curves for different Silver thicknesses (b) Distribution of the intensity of the electric field inside the prism/35 nm Ag/air multilayer.

#### 2.6.1.2 Grating

SP can also be excited on films in areas with random surface roughness, or manufactured localized scatterers. The wavevector of the radiative light matches the propagation constant of SP due to the add momentum components $\Delta k_x$ provided via scattering :

$$k_x^{SP,system} = k_0 sin(\theta) \mp \Delta k_x \tag{2.16}$$

It results that random surface roughness constitutes an additional loss channel for SP propagation via coupling to radiation. In the case of metallic grating, the match condition is given by :

$$k_x^{sp} = k_0 sin(\theta) + kG_x + lG_y \tag{2.17}$$

where k, l are the integer pair of indices, and $G_x$ and $G_y$ are the Bragg vectors. For a 1D metallic grating $G_x = 2\pi/a_0$ and $G_y = 0$, where the grating pitch $a_0$ defines the size of the first Brillouin zone. The propagation constant of SP for such system can be calculated by Rigorous Couple Wave Algorithm (RCWA), or Finite Difference Time Domain (FDTD).

### 2.6.2 Electron beam

Although in this thesis we put our attention on optical coupling in SP applications, we mention that SP can also be excited from an electron beam from the energy loss of the scattered electrons. For different angles of incidences, scattered electrons transfer different momenta $\hbar k_x$, with $k_x$ the projection of the momentum of the electrons upon the surface of the film. A transfer of energy from electron to SP occurs when the momentum matches with the propagation constant of the SP.

Roughly speaking, the electron beam creates local charges and electric fields on the metal surface. These Charges and fields generate then new charges and electric fields, and so on. As a result, SP propagate on both sides of the electron beam

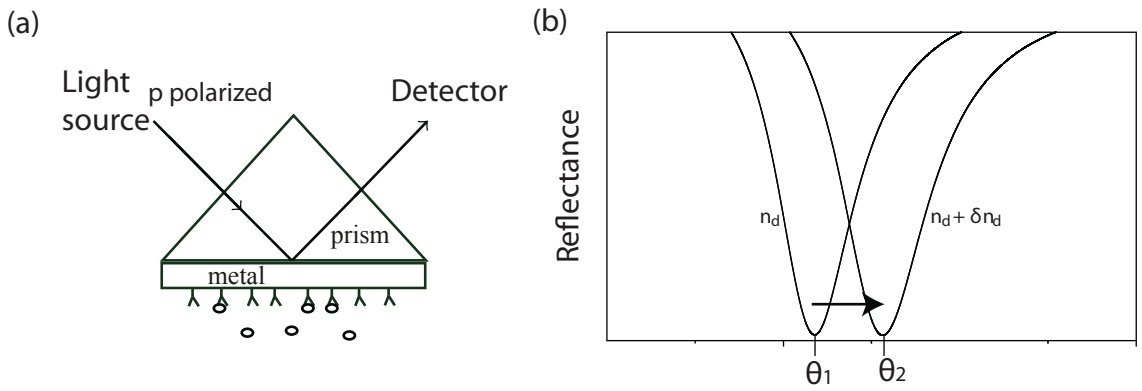


Figure 2.7 – (a) SPR sensors devices The SPR peak shifts due to the change of the transducing medium refractive index. As an example, the molecule bindings result in changing the reflected signal.

## 2.7 Surface Plasmon application in sensing

### 2.7.1 Principle

The large field enhancement effect of the SP close to the surface makes the Surface Plasmon Resonance (SPR) very sensitive to any changes in the boundary conditions. For example, variations in the optical properties of the dielectric medium will affect the shape of the SPR curves, i.e. the propagation constant of the SP. SPR sensors are based on the measurement of one parameter related to SPR curves such as intensity, wavelength and angle of incidence.

SPR sensors contain a probe, a detector, a « coupling structure »and a transducing medium, as shown in fig. 2.7a.

**The probe** is a p polarized light to excite SP, necessary for exciting the longititudinal oscillations.

**The coupling structure** , prism or grating for instance, is required to couple the SP, as previously discussed. The Kretschmann structure is commonly used.

**Transducing medium** transforms the change in the quantity of interest into an optical change. For example, the transducing medium consists of immobilizing molecules onto a metal layer by sol-gel process for biological sensing, as schematically depicted in fig. 2.7a. The refractive index of the active layer is defined by $n_d$. As the molecules of interest interact with the polymer, new bounds are formed resulting in a change of the refractive index of the medium ($n_d + \delta d$). A change in the refractive index of the active layer produces a change in the propagation constant of the SP ($k_x^{SP}$). In particular, the modification of the real part of $k_x^{SP}$ results in shifting the SPR peak, while the width of the peak is altered by the imaginary part of $k_x^{SP}$.

The detector measures one change of the resonant parameter from the reflected light intensity (Inset fig. 2.7a). Thus, the detector measures either :

- the intensity of the reflected light near the resonance,
- the resonant angle,
- the resonant wavelength,
- or the polarization and phase of the reflected light near the resonance.

### 2.7.2 SPR development :

Liedberg et al. [110] demonstrated in 1982 the first SPR bio-sensing and gas detection applications. From then, SPR sensor are well known and mainly developed for biological applications. SPR bio-sensors have been produced by Biacore, Nomadics, Reichert since 1990 [111]. SPR sensors are now widely recognized as a tool for studying the receptor-ligand, antigen-antibody interactions, imaging measurement of DNA [112], the protein expression at cell surface [113] and for monitoring in real time molecular interactions [114].

SPR sensors have been also used in a variety of metrology applications such as chemical sensors in liquid [115] and gas measurements [110] or for thin film characterizations [116]. Reviews of SPR sensors can be found in references [117, 118, 119].

The performance of SPR sensors are determined by (i) the sensitivity, (ii) the Signal Noise Ratio (SNR) & the resolution and (iii) the operating range.

i) The **sensitivity of the sensor** defines the derivative of the monitored SPR parameters (e.g $\theta, \lambda, \dots$) with respect to the quantities to be measured (index of refraction, thickness, the concentration and etc...). For example, the sensitivity is written as : $S = \frac{\partial \lambda_{res}}{\partial n_s}$, for SPR based on a shift of the resonance wavelength as a function of the refractive index $n_s$ of the sensing layer changes.

ii) The **sensor resolution** defines the minimum measurable change in the quantity to be determined. It depends upon the accuracy (spectral resolution for wavelength measurement, for instance) and the dynamic range of the detector. The sensor resolution is also linked to the **SNR**. In the literature, SNR and resolution may be confused.The SNR is characterized by the Full Width at Half Maximun (FWHM) of the SPR peak.

iii) The **operating range** depends on the detector and the probe used (e.g $\theta, \lambda, \dots$). The transducing layer also contributes to define the dynamic range.

A high sensitivity is expected when the field is strongly localized in the sensing medium, while a high resolution is obtained for a narrow and deep resonance curve. Obviously, both are intimately related. A higher localization of the electromagnetic field in the dielectric medium than in the metal medium increases the SP length of the propagation results (less ohmic losses), which results in a narrow resonance. To design a SPR sensor, it is necessary to optimize the dispersion relation of SP for the considered application. The dispersion relation of SP is tailored by the plasmonic multilayer ( material & thickness) and the surrounding environment (around the metal dielectric interface).

**Choice of the Metal layer :** The response curves of SPR sensor are very sensitive to the metal used and the thickness of the metal layer, as previously described and shown in fig 2.6 and on the metal used. The resonance is determined by the dielectric permittivity of the metal. Narrow resonance is obtained for a small damping, i.e. if $\|\epsilon_r\| >> 1$ and $\|\epsilon_r\| >> \|\epsilon_i\|$. As result, the sharpest peak is obtained for the metal whose its dielectric constants have the highest value of the ratio $\epsilon_r/\epsilon_i$. In fact, silver shows a narrower resonance than gold. On the other hand gold is preferably used as a chemically stable element in order to overcome the silver oxidation. Recently, SP based on bi-metallic layer has been proposed to take advantage of the properties of both metals [120]. Other materials such as aluminum and copper have been studied in the literature [121], providing different dynamical ranges. For example, aluminum shows a resonance at larger wavevectors (though

the sensitivity is lower). Finally, the choice of the metal layer depends on the application.

**Engineering the transducing medium :** Engineering the plasmonic multilayer tunes the propagation constant of the SP. Numerous configurations have been studied to enhance the performance of SPR sensors, and to develop then the sensor for multiple sensing applications. For example, we present here four designs.

1. Garces et al. [122] first proposed a four-layer structure to enhance the dynamic range.The multilayer consisted of a prism, a gold layer, an over layer of magnesium fluoride and the dielectric medium to be measured (e.g. biological cell medium). By designing the thickness of each layer, the SPR resonance is tuned. Moreover, they showed that the multilayer structure can increase the toughness as well as the chemical stability of the sensor, avoiding for instance the oxidation of silver. Following this work, Lavers et al. [123] demonstrated that an inserted single low index buffer layer (Magnesium fluoride) underneath the metal tunes the dispersion relation of SP, i.e. the resonant wavelength. By choosing a resonant wavelength where the optical properties of the metal layer are optimum (e.g. in the region where the ohmic losses are reduced), the performance of the SPR sensor are improved.
2. Sarid et al. [124] showed that the propagation length of SP increases by embedding the thin metal layer between two dielectric media, which have their refractive index almost equal. The symmetry/geometry of the structure changes the electromagnetic fields distribution. The electromagnetic fields are mostly contained in the region outside of the metal. Due to the decrease of intrinsic losses, the propagation length of the SP increases significantly. They are called Long Range SP (LRSP). The origin of LRSP is explained by the coupling of two SP. When a dielectric is introduced between prism and metal, fig. 2.8a, two SP may propagate : one at the dielectric metal interface and another one at the metal sensing layer interface. Depending on the thickness of the intermediate layer, both SP can couple with each other. The coupling is maximal when the refractive index of the dielectric and the sensing layer are almost the same : in this case, they have the same propagation constant. Above a certain thickness, the two SP do not overlap. The two SP are degenerated as the metal film decreases. A transverse standing wave is then established. The degenerate SP modes split into symmetric and anti-symmetric modes (depending on the thickness of the metal and dielectric layers). Finally, the enhancement of the field confinement in the surrounding layer result in narrowing the SPR peak for SPR sensors based on prism, for instance. Nevertheless, the use of LRSP structures for sensing in liquid and gaseous environments is not convenient, due to the requirement to match the RIs on both sides of the metal film.
3. Konopsky et al. showed that this refractive index-matching requirement may be circumvented by using a one dimensional (1D) photonic crystal (PC) as a substrate for the metal film [125]. The 1D PC is a simple periodic multilayer stack. Such 1D PC can exhibit photonic bandgaps where the propagation of optical electromagnetic waves is forbidden. By changing the bandgap parameters (e.g. by modifying the thicknesses of the alternating layers in the stack), the LRSP propagation can be excited at the metal interface, bordering an external medium with any refractive index. Furthermore, with this structure the LRSP may occur for « poor plasmonic metal »such as Palladium, as depicted in fig. 2.8b.
4. Lahav et al. proposed to use an additional thin dielectric layer with a high refrac-

tive index over the metal layer [126]. The presence of the high-index dielectric layer increases the electric field at the dielectric-sensing medium interface. Due to the enhancement of the electric field, the sensitivity of the sensor is improved.

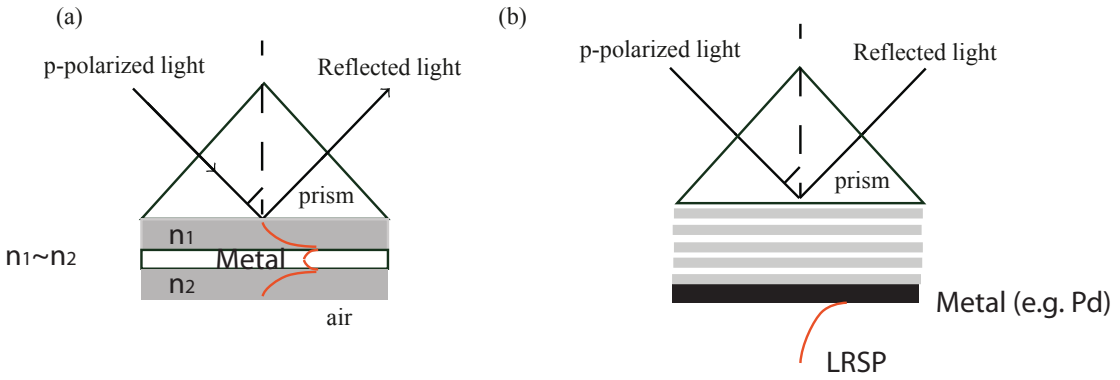


Figure 2.8 – LRSP supported by (a) an insulator-metal-insulator structure and (b) one dimensional photonic crystal.

**Choice of the coupling structure :** The coupling structure plays a role on the performance of SPR sensors. Prism configurations shows usually a higher sensitivity (a sensitivity of refractive index unit (RUI) of $10^{-}7$, $10^{-}6$) than grating configurations (RUI of $10^{-}6$). More details can be found in the reference [127].

**SPR limitations** : As the detection is based on the changes of the refractive index in the vicinity of the surface, the accuracy of the sensor may be dependent on the exterior parameters such as the chemical cross-sensitivity, the humidity, the temperature and so on. Besides, under repeated measurements, the sensor may need to be calibrated. For some applications, it may be difficult to use it out of the laboratory conditions. Several solutions have been proposed to overcome these limitations. As examples, multichannel SPR detection [128, 129] or self-referencing SPR appear suitable [130].

In conclusion, SPR sensors generally employ, now, more layers than the conventional metal/sensing medium system. Multilayer systems give more degrees of freedom in the design of SPR sensors, which allows to control the SPR peak width and the SP field penetration depth ( i.e. to optimize the sensitivity of the sensors), or even to coupled different SP with different penetration depths. Nowadays, the challenge is to continue improving the sensitivity and the SNR & the resolution of SPR sensors, but also to propose new miniaturized devices, develop new sensors for detecting new chemical species in different applications. In addition, the sensors have also to be robust and mass producible in order to use them in industry.

### 2.7.3 Fiber surface Plasmon resonance sensor

In this frame, optical fibers offer the advantage of getting compact sensing devices easily integrable, which take advantage of optical fiber properties, such as the dimension, the capability for remote sensing, multi-channel analysis, the low cost and so forth [131].

Jorgenson proposed in 1993 the first SPR multimode optical fiber. The sensor consisted of a 55 nm thick silver layer deposited onto the core of an optical fiber. A polychromatic light source is coupled to the optical fiber (for a range of incidence defined by the fiber NA). When the resonance condition of the SP is fulfilled, the transmitted intensity at the output of the optical fiber decreases. The resonance condition occurs when the evanescent wave, generated from the reflection of the guided light at the optical fiber core silver interface, matches with the propagation constant of the SP. Thus, the transmitted light drops at a resonant wavelength. The transmitted light shows a SPR peak which is function of the refractive index of the dielectric, fig. 2.9.

The principle is based on the same mechanism than the Kretschmann's structure. The propagated light is coupled to SP by the evanescent field from the total internal reflections (TIR) of the propagated light, as depicted in fig. 2.9. The silica core of the optical fiber replaces the prism. As previously, the SP is excited when the resonance condition matches, i.e. when the propagation constant of the guided modes matches to the propagation constant of the SP. In comparison with prisms, there are multiple reflections. The resonance change is amplified. In return, the width of the SPR peak increases. Moreover, A major difference is that the resonance represents an accumulated spectrum for the entire range of propagating angles, since all are excited. Unlike the prism sensor, the angle of incident light cannot be controlled. This summation of resonance results in broadening the resonance curve. Consequently, the sensitivity and the SNR decrease. SPR fiber sensors based on intensity measurement for selective mode have been described in the literature. However the sensing method for optical fibers is generally based on the modulation of the resonant wavelength, because the wavelength intensity distribution is preserved in an optical fiber. In contrast the angular intensity distribution of light through the fiber suffer from modes mixing as a result of the inherent bending in practical sensing applications. Moreover

Finally, the length of the transducer film, the optical fiber core diameter (both define the number of reflections), and the NA ( defines the light angle acceptance limit) affect the SPR curves. By simulating the sensor, as described in section 3.2, we can optimize each of these parameters.

Researches on SPR fiber sensors have been focused on improving the sensitivity, the SNR & the resolution, as well as on manufacte. Tailoring the plasmon mode by engineering multilayer structures is a route to achieve the best sensitivity, and the best dynamic range for the SPR fiber sensors. This optimization is notwithstanding limited by the NA of the optical fiber. Parallel to the study of the transducer layer, several fiber structures have been proposed to improve performance and manufacturing. As examples, we present below a non exhaustive list of these concepts. Recent reviews of these fibers can be found in [127, 132, 133] for further information.

- Single Mode Fibers (SMF) narrow the SPR peak : only one or few modes of the optical fiber can couple to the SP. SMF sensors are considered to be more sensitive, more accurate and show less noise in comparison to those for multimode fibers [127]. However, the operating range is limited.
- Tapered fibers [134, 135] increase the penetration depth of the evanescent fields. Besides, the length of the sensing area can be decreased. A small length of the sensing area improves the resolution. While a long length of the sensing area results in a deeper and wider resonance due to the absorption of the propagating light into the metal. In addition, Monzon-Hermandez et al. [136] showed that an asymmetric

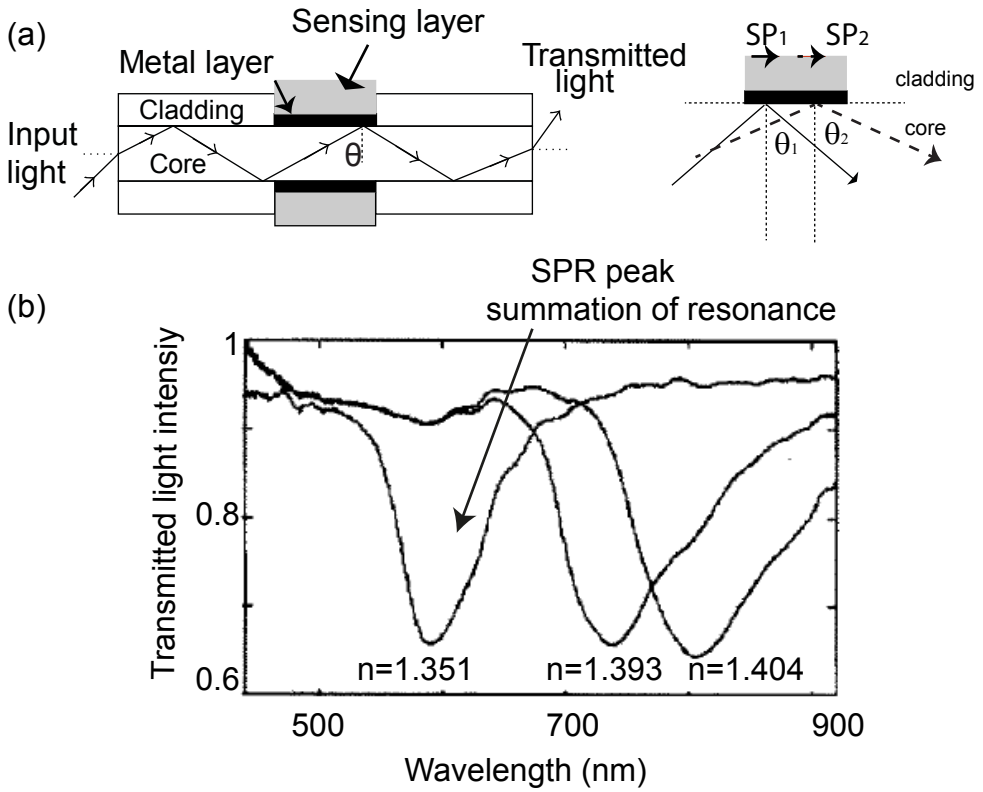


Figure 2.9 – (a) A typical multimode SPR-based fiber optic sensor. (b) The SPR curve corresponding to the transmitted light at the output of the fiber, where a 55 nm silver film was deposited symmetrically onto the fiber core, after removing the cladding. [131]. The SPR peak shifts as a function of the refractive index of the liquid solution surrounding the fiber.

metal coating on a uniform waist SM tapered fiber exhibits multiple resonance peaks. The presence of multiple peaks is due to the variations of the thickness of the metal film. Since the peak occurs at different condition, the dynamic range of sensor is therefore enhanced.

- As for uncladding SMF and tapered fiber, side-polished fibers [137, 138] enhance the interaction between guided light and sensing layer. They overcome the fabrication of homogeneous coating and allow to realize robust SPR fiber sensor.
- Heterostructure, consisting of two optical fibers connected with different core diameters, prone to increase the evanescent light in the cladding layer. This structure enhances the rate of the evanescent field in comparison with the guided field. The coupling of the evanescent light to SP is then more efficient. Besides, this configuration is robust as for side polished fiber, in contrast to SMF where removing the cladding weakens strongly the fiber.
- For SMF, only a part of the guided mode (the evanescent one) is coupled to the SP. To improve this coupling, Nemova et al. proposed to couple the energy of the guided mode to SP by uing gratings such as FBG, LPG and titled grating [139].
- For optical fiber micro-mirror sensors, the resonance condition has to be satisfied when the metal thin film is illuminated with a normal incidence. That's why, the

sensing area can be located at the flat tip of a fiber only for Localized SPR or grating structures [140]. Modified fiber tips with flat or angle structures have been proposed for SPR micro-mirror sensors.

## 2.8 Conclusion

In conclusion, Surface Plasmon Resonance sensors show a high sensitivity to any boundary changes due to the high confinement of the surface plasmon field at the interface. SPR and SPR optical fiber sensors are well characterized. In order to realize and optimize an optical fiber SPR sensor, we have to :

1. choose the coupling structure (i.e. the optical fiber configuration),
2. optimize the dispersion relation of SP. The choice of the materials and the thickness of the layers characterize the propagation constant of SP. In addition, multilayer systems may be used (i) to improve the operating range of the sensor, (ii) to optimize the localization of the electromagnetic field in the sensing medium (i.e. the sensitivity of the sensor) and (ii) finally to improve the propagation length of the SP (i.e. the sensitivity and the SNR & the resolution of the sensor).

# chapter 3

# Methods and material

## 3.1 Introduction to the proposed sensor

The proposed sensors consist of a deposited hydrogen sensitive material on the side of the core of an optical fiber, after removing the cladding over a segment of the fiber, as depicted in fig. 3.1. Basically, the sensor response is based on a locally change of the Numerical Aperture (NA) of the optical fiber due to the sensing section. As we will see, the change in the NA of the sensitive section may be based on SPR depending on the sensitive layers and the fiber parameters used.

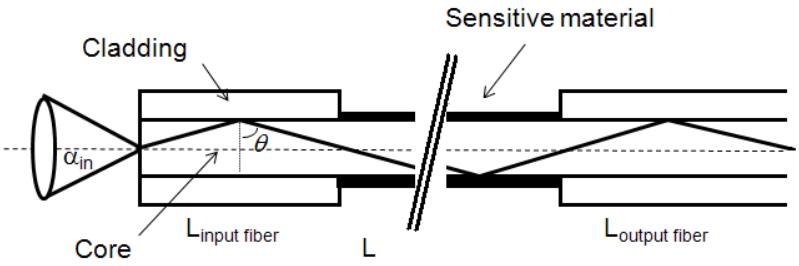


FIGURE 3.1 – Schematic representation of the deposited $H_2$ sensitive material deposition on the optical fiber.

The first part of this chapter presents a simple and reliable method to simulate the SPR response of a multimode fiber sensor, that we have implemented it under Matlab. From that, new interpretations and designs will be proposed in the following chapter. The second part describes the fabrication of the different realized sensors during this thesis.

## 3.2 Model and Simulations

We simulate the multimode fiber sensor in a planar approach. It is well known that a geometric optics approach can be used for multimode fibers. In the ray optic approach, light is represented as a distinct ray which is reflected at the boundary between the core and the cladding of the optical fiber. To take into account the power loss in the absorbing (sensing) cladding, we treat the ray locally as a plane wave at the reflection points [141]. We can consider separately the Transversal Electric (TE) and Transversal Magnetic (TM) polarizations [131], (called also s and p polarization). Finally, the transmitted intensity

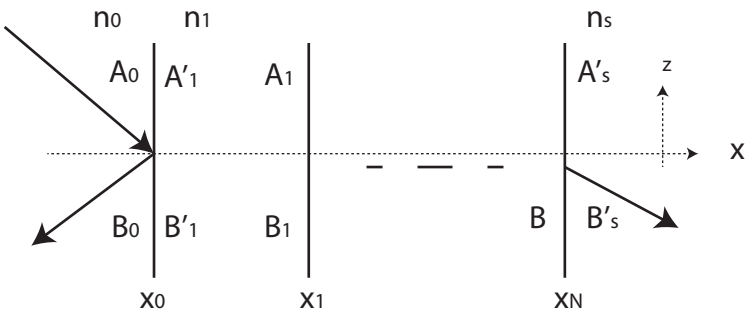


Figure 3.2 – Schematic multilayer structure of isotropic layered media.

through the fiber is calculated by summing the power loss/gain at each reflection over the sensitive area. For that, the reflection coefficient is calculated as a function of the reflection angle by the transfer matrix method [142].

### 3.2.1 Matrix method

We consider a multilayer structure of isotropic layered media and assume the medium is homogeneous in the z direction. The multilayer is described by :

$$n(x) = \begin{cases} n_0, & x < x_0 \\ n_1, & x_0 < x < x_1 \\ \vdots & \\ n_N, & x_{N-1} < x < x_N \\ n_s, & x_N < x \end{cases} \tag{3.1}$$

where $n_i$ is the refractive index of the ith layer, $x_i$ is the position of the interface between the ith layer and the (i+1)th layer, $n_s$ is the refraction index of the substrate, and $n_0$ is the refraction index of the incident medium. The layer thickness $d_i$ is defined as : $d_i = x_i - x_{i-1}, \forall i > 1$.

We look for an electric field plane-wave solution of the wave equation, propagating in the xz plane. We assume that the electric field is either a s or p wave . Due to the symmetry of the problem, the electric field has the form :

$$E = E(x)e^{-j(wt-\beta z)} \tag{3.2}$$

where $\beta$ is the z component of the wave vector and $w$ is the angular frequency.

The electric field in each layer consists of a right-traveling wave and a left-traveling wave. The electric field distribution is written as :

$$E(x) = \begin{cases} A_0 e^{-jk_{0x}(x-x_0)} + B_0 e^{jk_{0x}(x-x_0)} & x < x_0 \\ A_i e^{-jk_{0x}(x-x_i)} + B_i e^{jk_{ix}(x-x_i)} & x_{i-1} < x < x_i \\ A'_s e^{-jk_{sx}(x-x_N)} + B'_s e^{jk_{sx}(x-x_N)} & x_N < x \end{cases} \tag{3.3}$$

where $A_i$ and $B_i$ represent the amplitude of the right and left traveling plane waves at interface $x = x_i$ and $k_{ix}$ is the x component of the wave vectors :

$$k_{ix} = \sqrt{(n_i \frac{w}{c})^2 - \beta^2} = n_i \frac{w}{c} \cos\theta_i \tag{3.4}$$

From the continuity relation and the decomposition of the field, we can write :

$$D_l \begin{pmatrix} A_l \\ B_l \end{pmatrix} = D_{l+1} \begin{pmatrix} A'_{l+1} \\ B'_{l+1} \end{pmatrix}, \begin{pmatrix} A'_{l+1} \\ B'_{l+1} \end{pmatrix} = P_2 \begin{pmatrix} A_{l+1} \\ B_{l+1} \end{pmatrix}, \text{l=0, 1, ..., N N+1 represents s} \quad (3.5)$$

where $D_i$ and $P_i$ define respectively the continuity relation and the travel matrix. They are given by :

$$D_i = \begin{cases} \begin{pmatrix} 1 & 1 \\ n_i \cos\theta_i & -n_i \cos\theta_i \end{pmatrix}, \text{for s wave} \\ \begin{pmatrix} \cos\theta_i & \cos\theta_i \\ n_i & -n_i \end{pmatrix}, \text{for p wave} \end{cases} \quad (3.6)$$

$$P_i = \begin{pmatrix} e^{jk_{ix}d_x} & 0 \\ 0 & e^{-jk_{ix}d_x} \end{pmatrix} \quad (3.7)$$

We finally obtained by recurrence :

$$\begin{pmatrix} A_0 \\ B_0 \end{pmatrix} = M \begin{pmatrix} A'_s \\ B's \end{pmatrix}, \quad (3.8)$$

with M given by :

$$\begin{pmatrix} M_{11} & M_{12} \\ M_{21} & M_{22} \end{pmatrix} = D_0^{-1} \left[ \prod_{l=1}^{N} D_i P_i D_i^{-1} \right] D_s \quad (3.9)$$

The reflectivity R is given by :

$$R = \frac{M_{21}}{M_{11}} \quad (3.10)$$

### 3.2.2 Transmitted power

Finally, assuming no losses in the core of the optical fiber, the total transmitted power $I_{out}$, at a given wavelength $\lambda$, is defined as :

$$I_{out,\lambda} = 1/2( \int_{\theta_c}^{90} |r_p(\theta)|^{2N} I_{0,\lambda}(\theta_{in}) d\theta + \int_{\theta_c}^{90} |r_s(\theta)|^{2N} I_{0,\lambda}(\theta_{in})) d\theta \quad (3.11)$$

with :

$$N = L/(D \times tan\theta), \text{and } \theta = \frac{\pi}{2} - \arcsin(\frac{n_0}{n_{core}} \sin\alpha) \quad (3.12)$$

where L, D and N are respectively the length of the sensitive area, the fiber diameter and the number of reflections along the sensitive area, while $r_s$, $r_p$ are respectively the reflection coefficient for polarization TM and TE, respectively. $\alpha$ is the injection angle. $\theta$ defines the angle between the normal of the reflection interface and the direction of the incident light. $\theta_c$ is the critical angle. $I_0$ defines the angular intensity distribution corresponding to the light source used.

The intensity distribution is assumed to be uniform, simulating a long optical fiber length. The input power distribution along the multimode fiber length is altered due to inherent fiber impurities and inhomogeneities (such as microscopic bends, irregularity of

the core-cladding boundary, and refractive index distribution fluctuations) [143]. For optical fiber length longer than the coupling length $L_c$ ($L_c \cong 1/\alpha_{core}$, with $\alpha_{core}$ the bulk absorption coefficient), the energy of the excited modes is redistributed among all the modes of the optical fiber. $L_c$ is typically of the order of few meters. Furthermore the TE and TM polarized light are assumed to be equally distributed. Only meridian rays are considered [131]. The model does not take into account scattering from possible roughness of the layer and the optical fiber is supposed to be ideal.

The normalized intensity is defined as : $I_{out,\lambda}/\int_{\theta_c}^{90} I_0(\theta)d\theta$.

In conclusion, the expressions 3.11 shows that the performance of the fiber optic SPR sensor depends on the values of the design parameters such as the fiber core diameter, the length of the sensing region, and the numerical aperture (NA).

## 3.3 Fabrication of our proposed sensors

The fabrication process[1] of the sensor is simple but requires delicate handling, especially when the sensor is located at a relatively long distance from an optical fiber end. It follows two steps :

1. The jacket and the optical cladding are properly removed while the surface of the optical fiber is kept as clean as possible.
2. The layer of the chosen detection material is homogeneously deposited on the optical fiber core.

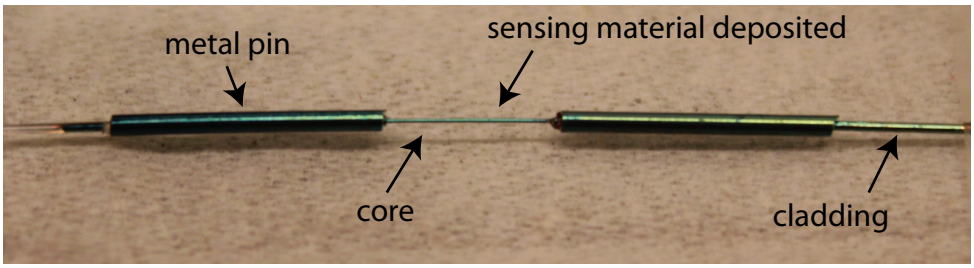


Figure 3.3 – Picture of the optical fiber after removing the cladding and the deposition.

### 3.3.1 Access the optical fiber core by removing the optical cladding

The optimal removing process depends on the type of optical fibers used. Two types of optical fibers are considered : a fiber with a hard polymer coating and cladding on a glass core and a fiber with a polymer coating and silica cladding on a glass core. For the former, the hard polymer serves both as a coating and as an optical cladding. After some tests, it is decided that only fiber with polymer cladding will be used for convenient and safety issues. Optical fibers with polymer cladding avoid etching the cladding with a relative dangerous HF based acid.

1. This section is based on our results, the technical data provided by [144] and from the reference [145].

The used F-MBB optical fiber is produced from Newport company. The core, cladding and buffer are respectively constituted of pure silica, bonded hard polymer and tefzel. The optical fiber dimension and the NA are respectively 200 $\mu$m $\pm$ 4/ 230 $\mu$m $\pm$ 10 / 500 $\mu$m $\pm$30 and 0.37. The operating wavelength is ranging from 500 to 1100 nm. Large diameter make easier the handling and characterization (e.g. coupling between the optical fiber and the light source). In addition, the realized sensor will be more robust than uncladding single mode fibers or tapered optical fibers.

#### 3.3.1.1 Buffer removal

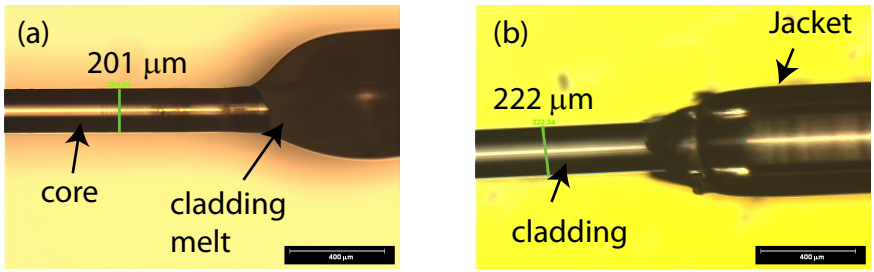


Figure 3.4 – The jacket is removed by (a) a torch flame and (b) a mechanical stripper.

After etching the optical cladding, the jacket is removed either by mechanical stripping, or flame-based techniques.

The mechanical stripping method consists of cutting into the jacket with a diamond tip to fracture it, and then translating the tip along the fiber to take out the jacket from the fiber. This technique is inexpensive, fast and by far the most commonly employed methods to strip the soft jacket, while the burning method has a high risk of fiber breakage due to embrittlement.

For the flame-based method, the jacket and the cladding are both removed. In contrast mechanical strippers remove the tight buffer without damaging the underlying acrylate coating, as depicted in fig 3.4.

The length of the sensing area influences the sensor response, as described in chapter 4. For both techniques, it is very difficult to effectively remove an accurate length of the jacket, especially for lengths shorter than 1 cm. Note that it is allowed to mechanically strip a larger length of the jacket since the polymer cladding maintain the flexibility and the robustness of the optical fiber. Then, the sensing area is obtained by removing a part of the optical cladding over a desired length (e.g. by adding protecting sleeve as explained in the flame based technique).

#### 3.3.1.2 Coating/Cladding removal

The cladding is removed by thermo-mechanical, chemical or vaporization techniques (which include laser- and flame-based techniques). The stripping process can reduce the fiber's mechanical strength and long-term reliability, by degrading the pristine glass surface [145]. We only investigate here the surface of the fiber core. Improper removal of the cladding results in a decrease of the reproducibility of the performance of the SPR sensor.

**Mechanical stripping** : The polymer layer is undamaged after removing the jacket by mechanical stripping. However, increasing the stress or using manually a razor blade , may peel off the polymer layer. From our experimental results, it appears that the most part of the polymer is removed, but a thin film often remains. It is also difficult to know if all the polymer is gone. This technique is rather suited to optical fiber made of dual acrylate coating. The optical fiber has a softer inner layer, which is more easily separated from the glass surface by mechanical stripping.

For the type of optical fibers that we considered, a thermo-mechanical stripping could be convenient. It consists of heating and stripping at the same time. Thermo-mechanical stripping appears to be a good choice when the optical fiber has only one acrylate layer [145].The thermo-mechanical stripper could be used to simultaneously remove the tight buffer and the hard polymer coating/cladding. Unfortunately, we did not have access to this equipment for our experiments.

The last option is to combine mechanical and chemical stripping techniques. It consists of weakening the optical fiber coating by immersing the optical fiber in a solvent such as methylene chloride. The mechanical stripping is therefore facilitated because of the soften and swelling of the coating. This technique did not give satisfying reproducible results. We note that a thin part of the polymer may sometimes be left on the optical fiber core.

**chemical stripping** : This technique is attractive since it does not require mechanical forces that may cause defects on the fiber surface. Since the strength and lifetime of the fiber are well preserved [146], it is often used to remove the protective polymer coating for the applications such as fiber Bragg gratings, optical fiber couplers, applying connectors and for splicing and cleaving. The method consists of using a solvent which etches the polymer coating/cladding.

In this thesis, we have tried acetone, Dynasolve 100 (manufactured by Dynaloy, Inc.) and methylene chloride ( or called dichloromethane). Figure 3.3.1.2 shows respectively the surface of the optical fiber core obtained with these solvents. The optical fibers were immersed a few hours in Dynasolve 100 as recommended by the manufacturer. For procedure with methylene chloride and acetone, the optical fibers are immersed in an ultrasonic bath to accelerate residues removal.

All of these 3 solvents are able to etch the polymer cladding. The polymer peels off, but it may remain on the surface of the fiber core, (fig. 3.3.1.2). Methylene chloride is the most efficient method : a net separation between the core and the cladding is observed, (fig. 3.3.1.2d and i). In order to remove all remaining polymer, we can wipe the surface of the optical core fiber with a lint free tissue, fig. 3.3.1.2e. To avoid any contact we immerse the optical fiber into a second ultrasonic bath of acetone. We found that the combination of methylene chloride with acetone allows completing removal of the cladding as shown in fig. 3.3.1.2f-h. However, we note that it is difficult to control the surface as seen in fig. 3.3.1.2g and j, where some polymer may be left on the optical fiber core. In addition, we do not control the cladding-to-core interface, fig. 3.3.1.2l. If the optical fiber is completely immersed, all cladding is removed at the interface, fig. 3.3.1.2j, contrary to flame based technique as explained in the next paragraph. The process has to be repeated several time to obtain a clean surface. Note that the solvent have to be replaced after several uses to avoid the deposition of polymer particles on the clean optical fiber core.

Let us mention other solvents which are often used according to the literature, but which are not experimentally tested in this work. The solvents are sulfochromic acid [147], sulfuric acid and hot acid (temperature about 200°) [148, 149, 146], a mixture of sulfuric

and methylene chloride [150] or a mixture of sulfuric and nitric acid (for example 95% $H_2SO_4$ and 5% HNO3 by weight). Hot acid can also be effective for silica coating. However, high level safety requirements have to be considered for these solvents [151, 152, 153].

**Vaporization techniques :** They are very fast, avoid the use of dangerous solvents. They do not require mechanical exterior forces and offer a nice surface quality.

Flame based techniques are the most convenient. It is commonly used in the literature, especially for the fabrication of SPR sensors. The optical cladding is removed with a clean flame torch (e.g. propane (or butane) around 1225°C and 1970°C, that are respectively practical and theoretical temperature value in air [154]). The optical fiber must be cleaned before the burning step. Dusts on the surface will cause carbonization traces on the core, and any liquid on the surface will cause pitting [144]. During the treatment process with a Bunsen burner (1570°C is the theoretical temperature value in air [154]), the optical fiber is maintained on a support to avoid bending. A high temperature flame allows removing easily all the polymer. However, if the temperature of the flame is too high, the silica melts. An ideal temperature has to be found for the optical fiber used. After burning the cladding, the core is cleaned with Isopropyl Alcohol (or IPA), using lint free tissue, to remove any carbon residue.

Figure 3.6 shows different surfaces of the optical fiber core after burning. Although this technique is often claimed to give a clean surface, we have observed, in our experiments, that a polymer film is often left on the core, fig. 3.6b, h and i. This residue can be removed by wiping the fiber with a tissue soaked in IPA, fig. 3.6c, or with Dynasolve 100 [155] (or dipped in ), fig. 3.6e, f and l. Nevertheless, as the sensing area is located at a relatively long distance from the optical fiber end, this operation appears to us extremely difficult. Despite our effort, a remaining polymer film is often observed, especially on the cladding-to- core interface, (fig. 3.6a), due to the effective difficulty in accessing it. Removing the residue in a solvent filled ultrasonic bath is found to be much more efficient, as shown in fig. 3.6j and k.

Let us mention that the length of the etching section is limited to a few centimeters in order to handle the optical fiber without breaking it. The optical fiber is maintained on a support in order to avoid bending of the optical fiber core. As a rule of thumb, shortening the length will result in a easier handling of the optical fiber. However, below 0.5 cm, it becomes difficult to burn the cladding without melting the jacket, fig. 3.6g. To control the sensing length, a metal pin have to be used, over a certain length, to protect the portion of the cladding that should not be removed, as shown in fig. 3.3.

A variant is to use an electrical spark (fig. 3.6) which precludes field splicing applications. Specific designs of a splicer can be done. We don't use this technique in this thesis. Other methods such as hot air stream [156], and laser ablation have been recently proposed [157, 158], but we did not have opportunities to use and test them.

In conclusion, we chose the flame based technique for practical reasons. It is efficient and ensures good surfaces. However, burning off the coating significantly reduces the tensile strength of the stripped fiber, to an even greater extent than mechanical stripping [145]. Although chemical stripping is from far the less convenient (due to the toxicity, the risk of hazard accident, the equipment and time-consuming), it has to be considered for long term use of sensors and for reproducibility of the sensor production.

For our last realized sensors, we combine the flame based technique with a fast chemical

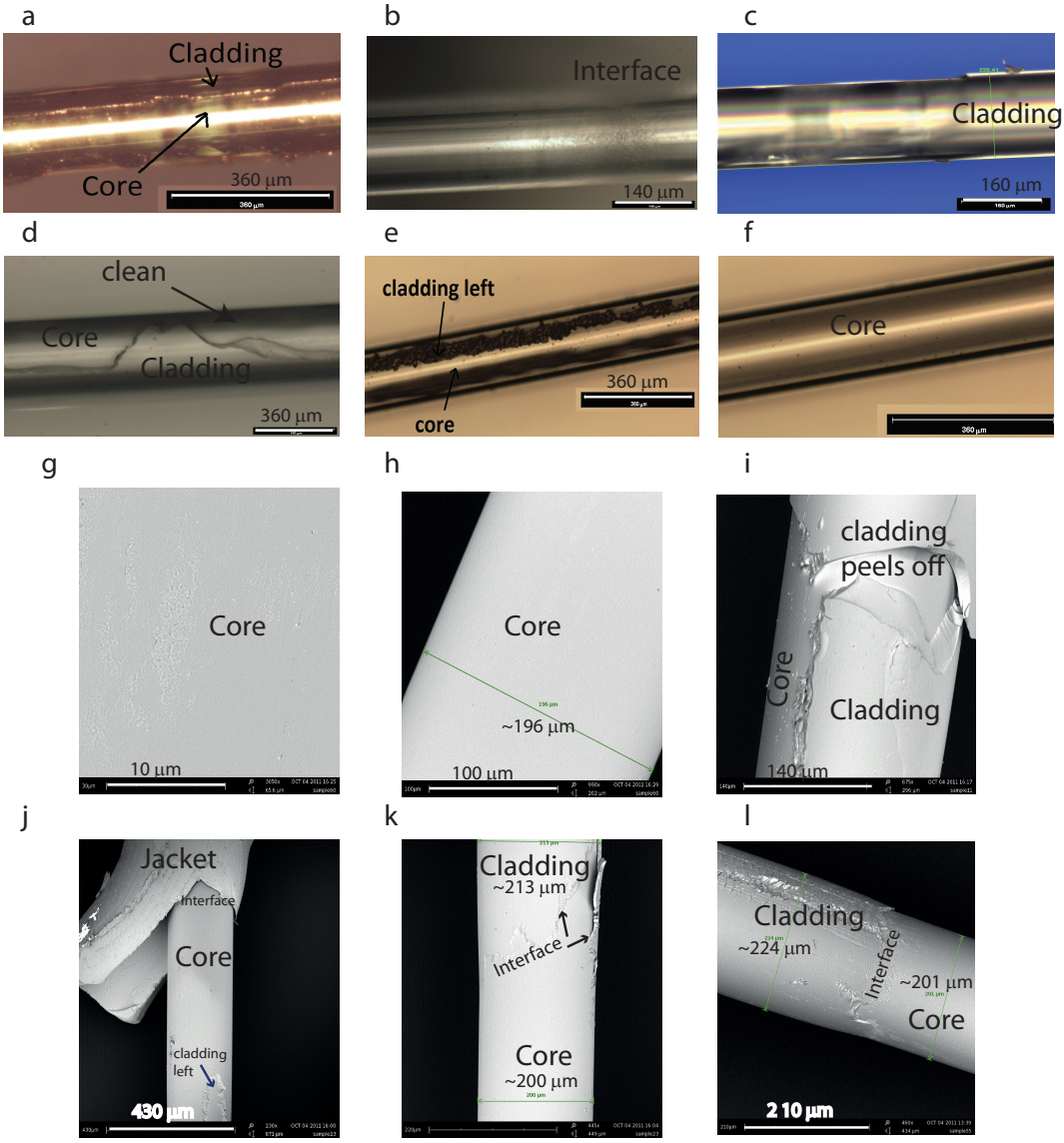


Figure 3.5 – Optical microscope images of a core surface after burning the cladding. SEM images of a core surface after burning the cladding.

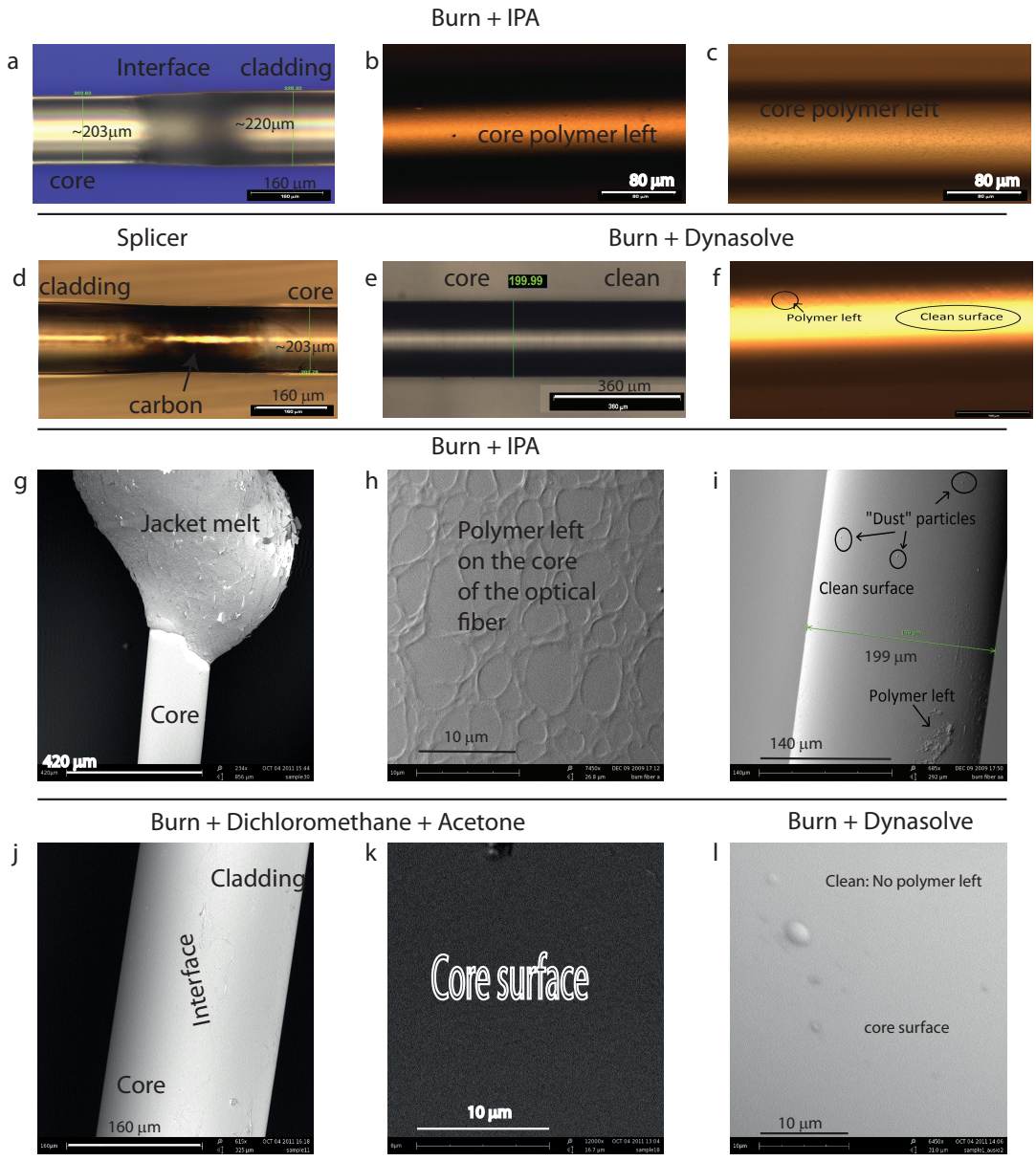


Figure 3.6 – (a-f)Optical microscope images of an optical fiber core cleaned with (a-c) IPA, (d) splicer, (e-f) Dynasolve 100, after burning step. (g-i)SEM images of an optical fiber core cleaned with (g-i) IPA (j,k) dichloromethane and acetone ultrasonic bath and (l) Dynasolve 100, after burning step.

cleaning step to improve the quality of the surface. Beside, as the sensing part is in the length of the optical fiber, we have designed an optical fiber holder to manipulate and immerse it. The stripping step is noticeably more difficult here than operating at the tip of the fiber, where all the techniques presented above seem to be easily done.

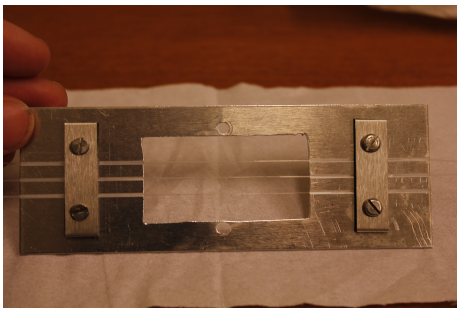

Figure 3.7 – The fiber holder designed to maintain and immerse the fiber during the flame and chemical etching.

### 3.3.2 Deposition

The deposition of the material is done by sputtering. This technique is widespread used for physical vapor deposition. It deposits a reproducible uniform film thickness and conformality of coverage [159] under similar sputtering conditions. The sputtering chamber, fig. 3.8, is constituted of a cathode (the material target) and a anode (the substrate). A discharge ionizes the background gas, which is usually argon. Target atoms are then ejected due to atoms collision between the ionized gas and the material target. The target atoms will deposit on parts of the sputter chamber but most efficiently on a strategically positioned deposited substrate. The gaseous discharge can be realized either by a DC, a capacitive radio frequency RF and a DC or RF associated with a magnet, so-called magnetron sputtering. The magnetic field concentrates the plasma close to the target, and enhances the ion bombardment. The background gas, the pressure, the temperature and the discharge (type, voltage and power) characterize the morphology of the film (it depends on the projectile energy, angle of incidence, distribution and the surface binding energy of the target). Further information are found in ref [159].

In this thesis, we have deposited the thin films by AJA DC/RF magnetron sputtering. RF or DC power supplies are used depending on the material target. The targets are placed off-axis with respect to the optical fiber. In particular, the depositions of the material on the optical fiber were carried out with two different configurations :

1. A motorized substrate holder is vertically set in the center of the chamber, above the material gun (target) with respect to a certain tilt angle. The fiber holder is attached perpendicularly to the substrate holder in order to ensure the rotation along the z axis during the deposition, as described in fig. 3.8a. Due to this configuration, the deposition results in a slight gradient of the thickness along the fiber.
2. The optical fiber is horizontally set in the chamber above the tilted material gun, as described in fig. 3.8b. The two guns perpendicular to the fiber are preferably used to obtain an uniform thickness and composition layer. A controlled electronic motor ensures the rotation of the optical fiber along the y axis.

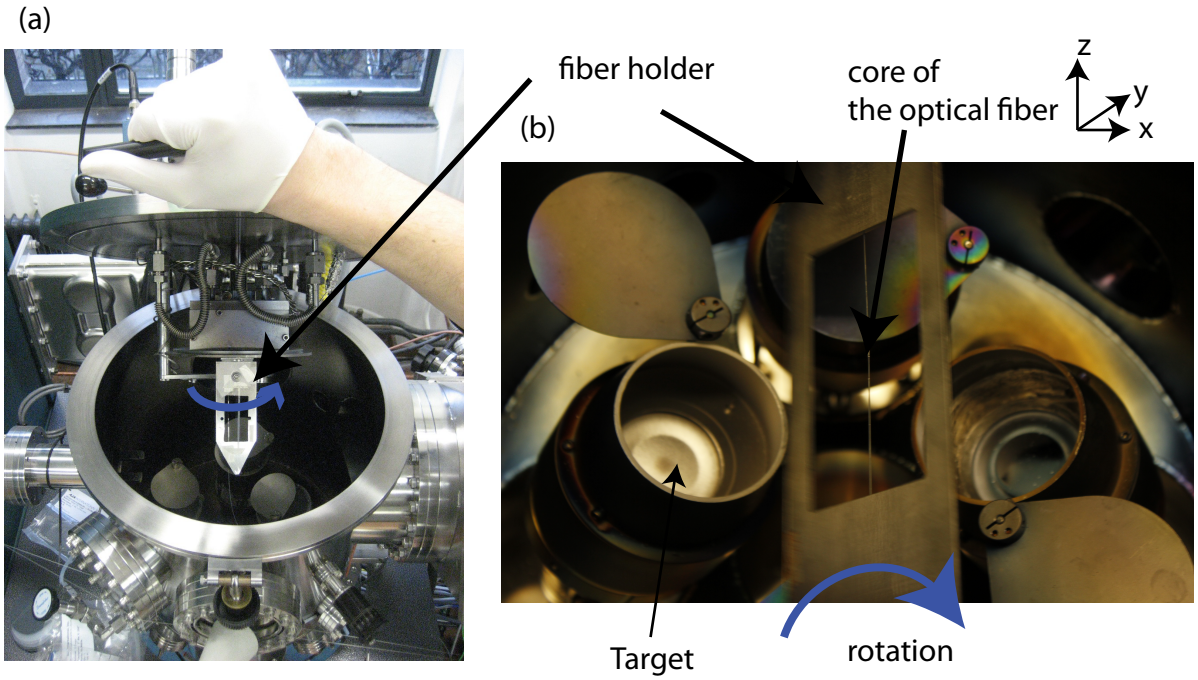


Figure 3.8 – Picture of the (a) AJA magnetron sputtering apparatus with the fiber holder. (a) Configuration 1 and (b) configuration 2.

The deposition rates are characterized by measuring the thickness of the deposited film on a glass substrate. We will mention in the experimental results, the deposition rates (i.e the sputtering parameters) and the configuration used, for the different developed sensors.

## 3.4 Characterization

### 3.4.1 Surface fiber investigation

After each step (etching, deposition), we optically investigate the surface of the sensing area with an optical microscope. After measurements, the optical fiber sensor is investigated with an electron microscope (SEM).

### 3.4.2 Measurement

The measurement setup is described in fig. 3.9. A tungsten halogen light source and an Ocean Optics HR 4000 spectrometer are respectively used as a source and a detector. The optical fiber containing the hydrogen detector is connected via 905 SMA connectors to the source and the detector. The optical fiber is measured in a gas cell. All measurements are performed at atmospheric pressure and room temperature.

- **Light source :** We used a tungsten halogen light source (Mikropack HL-2000-FHSA) emitting in the spectral range of 360 nm-2 $\mu$m. The output is a SMA 905 connector equipped with a lens (adjustable to maximize light coupling into a fiber). The numerical aperture of the source is larger than the fiber NA in order to excite all the fiber modes. The light source is turned on a few minutes (around 5 min) before each measurement to obtain a stabilized intensity, as recommended by the

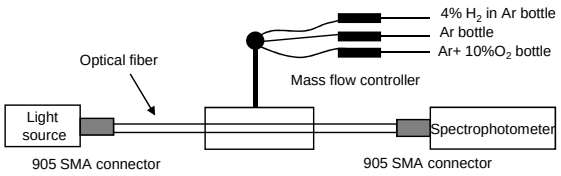


Figure 3.9 – Experimental setup used to study the sensor response to hydrogen.

manufacturer. A drift of 0.3% per hour and a stability of 0.5% are given by the manufacturer. The temperature and humidity range is respectively 5-35° and 5-95% (at 40°) in agreement with our experimental conditions.

- **Spectrometer :** We used the HR4000 spectrometer from Ocean Optics with a SMA 905 connector. The spectrometer is composed of a collimating mirror, a grating, a collection lens, an order-sorting filter and a detector. The collimating mirror is matched to the 0.22 numerical aperture (NA) of an optical fiber. The grating is made of 300 blazed lines. It disperses the cone of light on the detector, which is a linear Charge Couple Devices (CCD) arrays. Each pixel responds to the wavelength of light that strikes it. The optical resolution $Res$ is defined as : $Res_{optical}$ = spectral range/number of pixel × ($Res_{pixel}$). Our resolution is 1.096 nm with a bandwidth ranging from 200 to 1100 nm. Moreover, the spectrometer is equipped with a collection lens and a filter, to ensure aberration-free detection and to block second and third order light from the grating.
- **SMA connection :** SMA connectors offer an easy and efficient way to couple and collect light between the optical fiber and the source/detector. However, due to misalignments, the coupled intensity slightly changes. Furthermore, we use here SMA adapters which may increase the losses at the fiber/source and fiber/detector interface. We circumvent the measured intensity fluctuation between different fibers in our study by performing relative measurements.
- **Flow cell :** The gas cell is made of a plastic box. The cell is not sealed, two holes are present to let the gas escape. If no flow is applied, we can consider that the gas in the cell is the ambient air (presence of humidity). The gas cell is purged with argon for several minutes before all measurements in order to clean the tubing of the gas system and the cell. The experiments are then carried out with a flow of a mixed gas, which contains a chosen concentration hydrogen (up to 4 %) and oxygen (up to 20 %). Flow rates of each gas were individually controlled with mass flow controllers. The total flow is kept at 250 ml/min. We assume a overpressure in the cell which avoids backflow of air form the measurement room. The mixed gas arrived in the gas cell after 7 s, corresponding to the time for the transport of the gas through the pipe.

In conclusion, the NA of the measurement system is limited to the smallest NA. The optical fiber NA used is larger than the spectrometer NA. As a result, the spectrometer filters the higher mode of the optical fiber output. This filtering results in a straight line in the spectrum decreasing the resolution of the system. In order to increase the resolution, the NA of the optical fiber has to be lower than the NA of the spectrometer NA. Unfortunately, a NA of 0.22 involves the use of a silica cladding fiber. Here, the use of an entrance slit of 25 $\mu$m width allows us to improve the resolution. In the following chapter, we will discuss on how this limitation can influence the response of the proposed sensor.

# Chapter 4

# Wavelength response of a surface plasmon resonance palladium coated optical fiber sensor for hydrogen detection

## 4.1 Introduction

In 1993 Chadwick et al. [160] have demonstrated the feasibility of a hydrogen sensor based on SPR. The sensor consisted of a Pd layer deposited on a prism (Kretschmann's configuration) [161]. In contrast to common SPR sensors based on the changes in the dielectric permittivity of the medium surrounding the metallic layer, the hydrogen detection is based, in this case, on the changes in the complex permittivity of the metallic layer itself with the absorption of hydrogen. Figure 4.1a shows the reflectance of a Pd layer with a thickness of 12 nm, deposited onto glass substrate, as a function of the angle $\theta$. $\theta$ defines the angle between the normal and the incident light. The reflectance curve shows a broad SPR peak that account for the highly absorbing character of Pd ($\epsilon_1 \approx \epsilon_2$). The resonant angle is found at 53° for a wavelength of 670 nm. Upon hydrogenation, the width of the SPR peak decreases (dash line), which results in increasing the reflected intensity light (in the resonance range). By measuring this changes, Chadwick quantified the hydrogen concentration.

In 2001, Bevenot et al. proposed to use this increase of reflectivity upon hydrogenation in an optical fiber configuration [71]. The sensor consisted of a Pd layer deposited on a section of a step-index multimode fiber core, after removing the optical cladding. The optical fiber is illuminated by a laser diode with a given incidence angle as described in fig. 4.1c. Only the TM polarization (magnetic field perpendicular to incidence plane) was taken into account in their model. The excited group of mode, is reflected one or several times at the Pd interface, depending on the incidence angle and the length of the Pd section. The transmitted intensity, blue line in fig.4.1b decreases due to the losses induced by the Pd section ( the reflection coefficient is inferior to 1). Upon hydrogenation, these losses are reduced as shown by the red line in fig. 4.1b since the Pd hydride reflectivity for the angle of the guide modes is higher. Because of the wide resonance, the guide modes, corresponding to angles above the resonant angle, are altered. Finally, Bevenot et al. quantified the hydrogen concentration by measuring the transmitted intensity of a selective group of modes (for

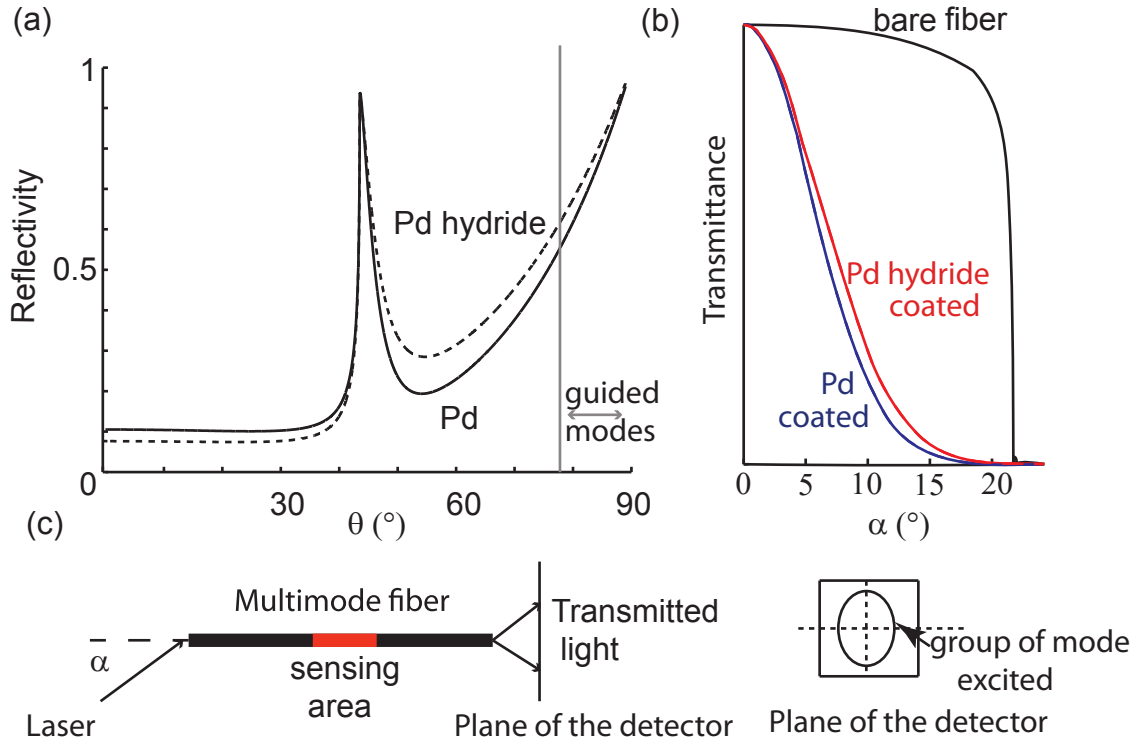


Figure 4.1 – (a) Reflectance of a Pd layer with a thickness of 12 nm onto glass substrate as a function of the angle $\theta$. The line and dashed line represent the metallic state and the hydrogenated state, respectively. The permittivity of Pd hydride is described as $\epsilon_{Pd,c(\%H_2)} = h(c\%) \times \epsilon_{Pd,0\%H_2}$ , where $\epsilon_{Pd,0\%H_2} = -7.64 + j8.45$ is the dielectric permittivity of the pure palladium [71]. At room temperature, h=1 and h=0.8 mean approximately a concentration of 0% and 4% $H_2$, respectively, from [71]. (b) Normalized transmitted intensity as a function of the injection angle.

a given injection angle). However, the power distribution mode of light in a multimode fiber is very sensitive to perturbations. The excited group of modes can be disturbed and converted into another group of modes through the fiber, simply due to fiber impurities.

We present here the response of a Pd-SPR multimode hydrogen sensor, where all modes are equally excited in the optical fiber in order to decrease the effect of modal conversion. Furthermore, we consider both TE- (electric field perpendicular to incidence plane) and TM-polarization. The first section of this chapter shows the experimental response of the sensor. We measure the total intensity transmitted (sum of the TE and TM polarization) as a function of the hydrogen concentration for a spectral range of $[450nm - 850nm]$. The response time and the reproducibility of the sensor response are also presented, as well as the noise effect of $O_2$, to validate the possibility of using this sensor for practical safety applications. The second section compares the experimental and theoretical response for different data of Pd dielectric function found in the literature. Our aim is to demonstrate the role of the changes in the real and in the complex parts of the Pd dielectric permittivity on the SPR peak. We study also the influence of the TE polarization on the sensitivity of the sensor in order to know whether we can consider the case of only the TM polarization

| sample | deposition | length |
|---|---|---|
| 1 | 1min20 at 3 $\mu$bar Ar | 2 cm |
| 2 | 1min20 at 3 $\mu$bar Ar | 1.5 cm |
| 3 | 1min20 at 3 $\mu$bar Ar | 2 cm |
| 4 | 10 s at 40 $\mu$bar Ar, then 1min20 at 3 $\mu$bar Ar | 2 cm |
| 5 | 10 s at 40 $\mu$bar Ar, then 1min20 at 3 $\mu$bar Ar | 3 cm |
| 6 | 10 s at 40 $\mu$bar Ar, then 1min20 at 3 $\mu$bar Ar | 2.5 cm |

Table 4.1 – Description of each realized sensor.

for hydrogen SPR sensors. Finally, we optimize the sensor parameters, such as the fiber Numerical Aperture (NA), the length of the transducer and discuss the performance of the proposed sensor.

## 4.2 Sensor fabrication

We used, in our experiment, a Newport step-index multimode fiber as described in section 3.3. The optical cladding is removed with a flame torch over a length of 2 cm, and cleaned with IPA. The sensor response increases as the optically sensing length L increases. The length L is limited to 2 cm in order to handle the optical fiber without breaking it. We deposited the Pd film as described in 3.3.2 for the configuration 1. The deposition results in a slight gradient of the thickness along the fiber. For a deposition over a width of 2 cm along the fiber, the thickness varies from 9 nm to 14 nm. We realized two sets of samples. For the first one, called sample 1 to 3, the background pressure was $5.10^{-7}$ mbar and the sputter pressure was 3 $\mu$bar Ar. Palladium was sputtered at an average rate of 1.5 Å/s using 100 W DC power supply. For the second, called sample 4 to 6, the sputter pressure is set at 40 $\mu$bar during the first 10 s (due to manipulation errors) and then set again at 3 $\mu$bar Ar. The thickness deposited for a pressure of 40 $\mu$bar is neglected, but may influence the Pd microstructure. Due to fabrication errors, the length of the sensitive section can vary from 1.5 to 3 cm between the different samples. Sample 4 is use as a reference.

## 4.3 Experimental result

We measure the total intensity transmitted (sum of the TE and TM polarization) as a function of the hydrogen concentration for a light spectral range of $[450nm - 850nm]$. For future safety applications, the sensor is evaluated first in an inert gas, and then in an oxygen environment. The relative transmission defines the intensity measured $I_{H2}$, divided by the intensity measured without hydrogen $I$. The sensitivity defines the relative change in intensity, and equal to $|1 - I_{H2}/I|\,\%$

### 4.3.1 Discussion on the measurement setup

As described in section 3.9, the NA of the measurement system is limited to 0.22 (inferior to the fiber NA of 0.37). However, this limitation does not disturb our measurements. After depositing the Pd film, the optical fiber sensor presents a new NA due to the loss induced by the Pd section. In fact, the sensitive layer modulates the fiber NA (depending on the Pd thickness, and on the length of the transducer) as depicted in fig. 4.1b for

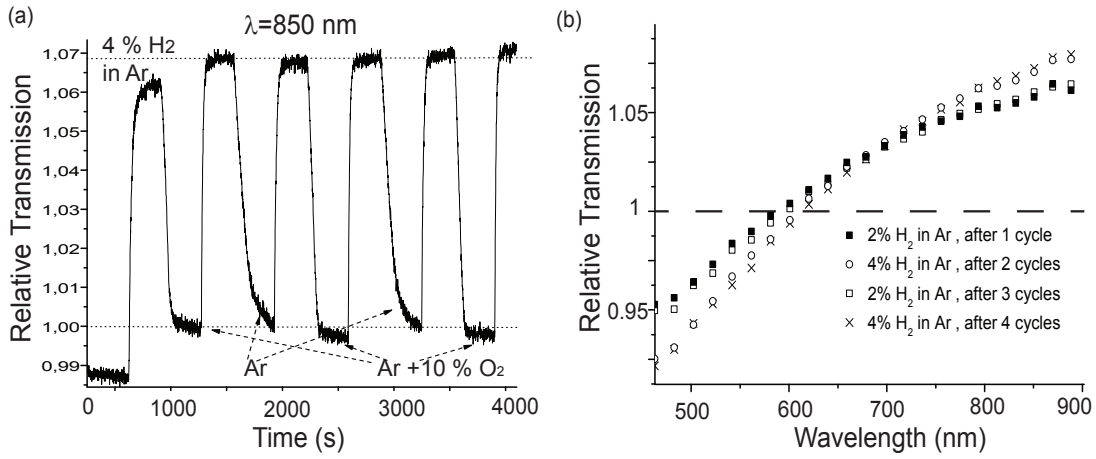


Figure 4.2 – (a) Sensor response (sample 4) reproducibility for a concentration of 4% $H_2$ in Ar at a wavelength of 849.96 nm. Unloading are successively repeated in Ar + 10% $O_2$ and in Ar. (b) Relative Transmission as a function of the wavelength for different hydrogen concentrations. Figure shows the reproducibility of wavelength response of the sensor (sample 1)

instance. For a Pd film, deposited over a length of 2 cm, we experimentally obtained a comparable NA to the one of the spectrometer. Theoretically, the NA is actually larger : 0.3 (for a 10 nm and 2 cm lengths Pd film). However, the transmitted intensity, for the ray propagating between the theoretical and experimental critical angle, is less than 1% of the total intensity. Upon hydrogenation, the NA of the sensing section increases. As a result, we only measure the change for all angles corresponding to the spectrophotometer NA. In order to compare our experimental results with our predictions, we limit the NA to 0.22 in our simulations.

### 4.3.2 Reproducibility of the sensor response

Figure 4.2a shows the relative transmission as a function of time during the ab-desorption hydrogen cycles. While fig. 4.2b shows the relative transmission as a function of the wavelength at different $H_2$ concentration for different cycles. The Pd film needs at least one cycle in order to stabilize the micro-structure, and to remove most « poisonous »elements from the Pd surface, which are gathered by transport of the sample through air, for instance. After the first cycle, we observed that the sensor response is reproducible. As expected, Pd thin films show a very good reproducibility over cycling. As a result, the sensitivity study will be done after one cycle.

A slight drift appeared over cycles. This drift observed is in fact smaller when the recovery is done in the same conditions (Ar use as recovery gas over all cycles). The drift seems mainly to come from the effects of pollutants onto the Pd surface rather than the formation of Pd micro-cracks over time.

### 4.3.3 Spectral response of the sensor

A continuous change in intensity is observed as a function of the hydrogen concentration between 0.5 % and 4 % $H_2$ in Ar, as depicted in fig. 4.3a. During the hydrogenation the

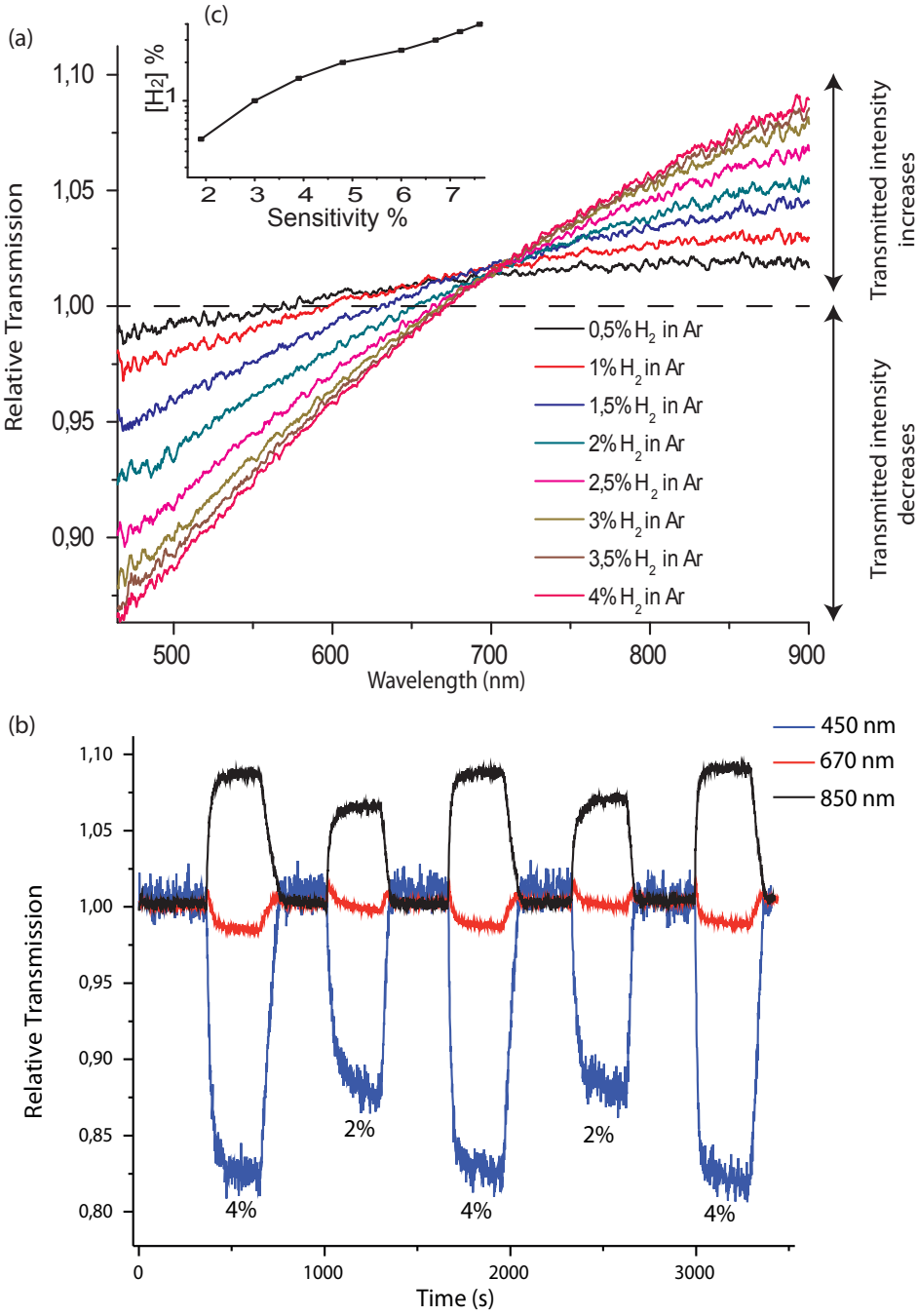


Figure 4.3 – (a) Relative Transmission as a function of the wavelength for different hydrogen concentrations. Inset : Hydrogen concentration as a function of the sensitivity(semi-logarithm scale) (b) Relative Transmission as a function of time over ab-desorption hydrogen cycles(Ar+20%$O_2$/4% $H_2$ in Ar/Ar+20%$O_2$/2% $H_2$ in Ar) at a wavelength of (blue line) 450 nm, (red line) 670 nm and (dark line) 850 nm.

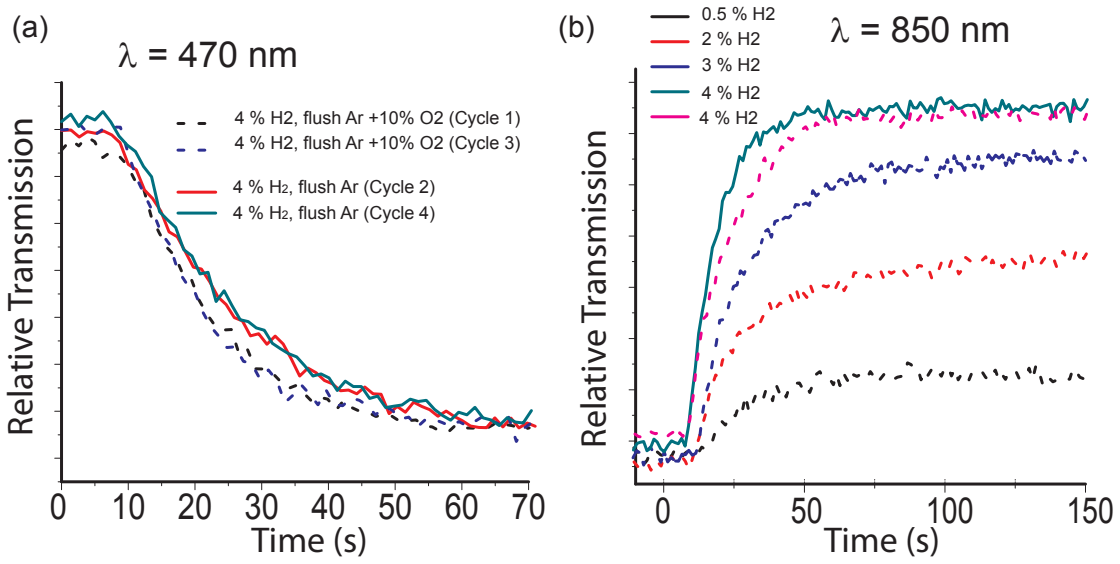


Figure 4.4 – (a) Response times at 4% $H_2$ in Ar for different pre-flush gases, at different cycles. (b) Response time for different $H_2$ concentration. The pre-flush gas is respectively Ar and a mix of Ar and 10% $O_2$ for line and dash lines.

transmitted intensity through the optical fiber decreases and increases for shorter and longer wavelength, respectively. The sensor response shows a wavelength dependence which was not observed in previous works. Figure 4.3b shows the response of the sensor over several ab-desorption cycles at wavelengths of 450 nm (blue line), 670 nm (red line) and 850 nm (dark line) corresponding to the three types of behavior. While the transmitted intensity increases at a wavelength of 850 nm, the transmitted intensity decreases at a wavelength of 450 nm. At a wavelength of 670 nm, where the relative transmission is about 1 for 2% $H_2$, we observe a competitive effect. The response shows, first an increase, and then a decrease in intensity.

The inset in fig. 4.3a plots the sensor sensitivity as a function of the hydrogen concentration on a semi-logarithm scale. We do not observe a flat pressure plateau as we would expect from the Pd pressure composition isotherm (pcT). Above 3 % $H_2$ in Ar, the signal starts to saturate, corresponding to the $\beta$-phase. As emphasized in our review (see section « Hydrogen concentration range » 1.4.1), Evanescent/SPR sensor show an increase in sensitivity in the $\alpha$-phase in comparison with the hydrogen solubility into the Pd film. We believed this sensitivity is mainly due the contribution of H sites at the surface and subsurface of Pd. Finally, the absence of a flat plateau is likely due to (i) the gradient of Pd thickness along the optical fiber : the response is the sum of pcT curves since each Pd thickness has its own pcT, and (ii) the high sensitivity of the sensor in the $\alpha$ phase.

#### 4.3.3.1 Response time & recovery time

Before explaining the spectral response of the sensor, we first report the performance of the sensor.

The response time (hydriding time) and recovery time (dehydriding time) define respectively 90 % of the rise and fall time of the response.

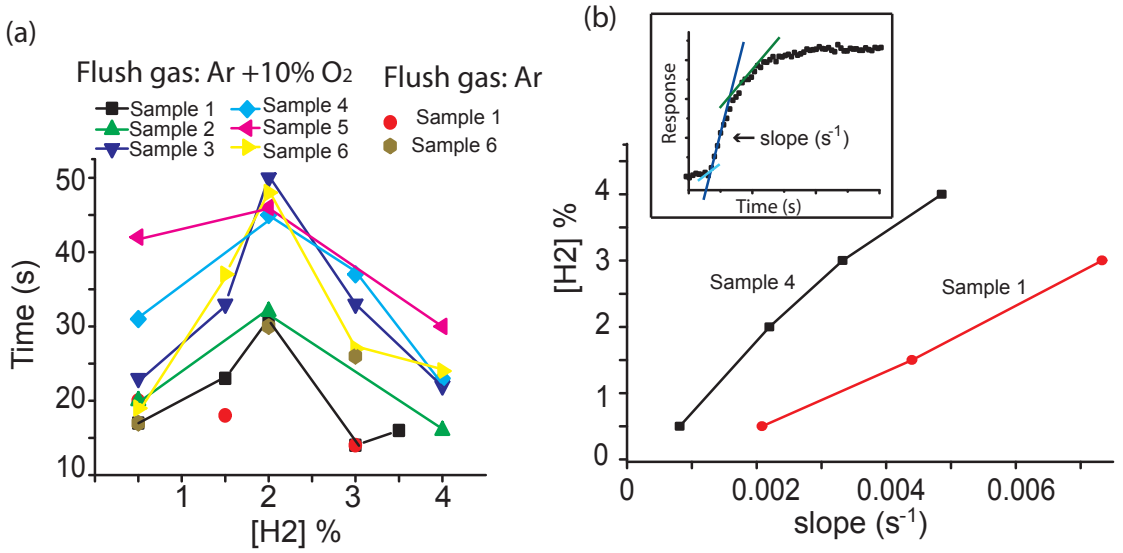


Figure 4.5 – (a) Response time at different $H_2$ concentration for different sensors. (b) $H_2$ concentration as a function of the slope of the second regime. The inset described the three regimes of the hydrogenation kinetic.

The signal starts changing after 7 s, corresponding to the time for the transport of the mixed gas through the pipe to the sensor. The response time is 50 s for a concentration of 4 % of $H_2$ in Ar during the first loading and decreases to 30 s after the first cycle, when the recovery was done with a mix of Ar and $O_2$. We observe that the response time can vary from 20 to 40 s during different cycles.

As discussed in section 1.4.2, the reaction is likely to be catalytically limited. Therefore, the response time depends strongly on the used deposition technique and the environmental conditions (temperature, pollutants, humidity and available sites on the surface). Hence we believe that the differences observed for the response times is due to the pollutants on the Pd surface. In fact, we observe from fig. 4.4a that the presence of $O_2$ during the recovery may increase the response time of about 10 s (dash lines) compare to the response where the recovery is done with Ar (lines). Finally, the obtained response time ( at 4 % $H_2$) is of the order of the value found in the literature for this range of thickness, chapter.1.

The response time does not significantly depend on the hydrogen concentration. The response time vary to 23 s to 44 s, when the gas cell is flushed with a mix of Ar and $O_2$, fig. 4.4b . Nevertheless, we observe that the response time increases for concentration corresponding to the phase transition, in agreement with previous reports (see section 1.4.2). Figure 4.5a shows the response times for various individual sensors. We obtain different times, but of the same order. The discrepancy is explained in part by the different pre-flush gas used and the different cycles. Probably caused also by a deviation in the Pd deposited thickness (due to a change of the fiber position in the fiber holder during the deposition). The latter point is deduced in the section 4.5.2.

Although the response time is slightly different between the $\alpha$ and $\beta$ phase, we can clearly observe different slopes as a function of hydrogen concentration. In order to discuss the hydrogenation kinetics, we decompose the response time into three regimes, depicted in fig.4.4b, as proposed by Delmelle et al. 's work [75]. In our case, the first constant slope,

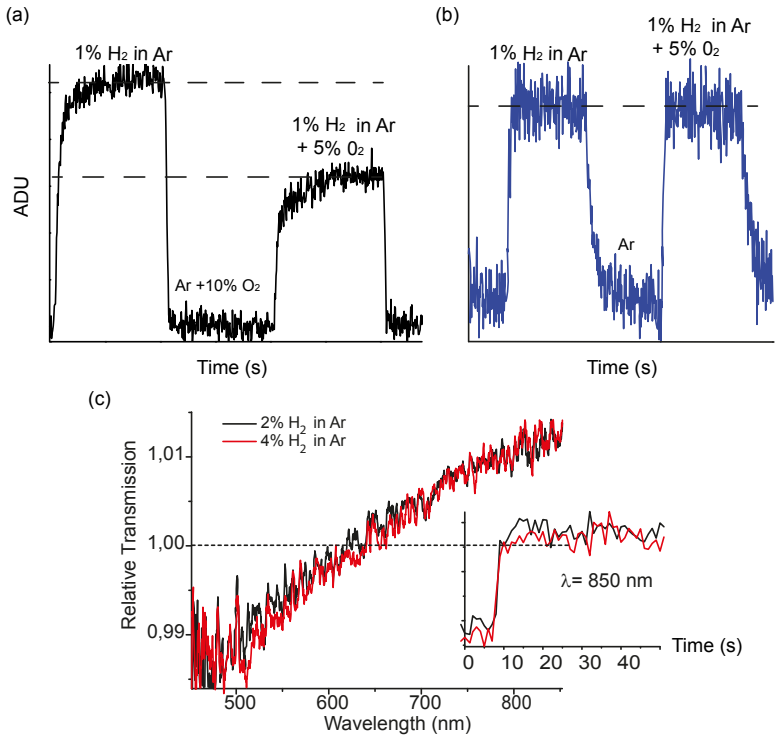


Figure 4.6 – The effect of $O_2$ on the response of (a) the Pd based sensor and (b) Pd alloy based sensor. (c) Relative Transmission as a function of the wavelength for different hydrogen concentrations for the Pd alloy based sensor. The inset shows the corresponding response time for such sensors.

likely to be due to the absorption process, cannot be characterized due to the measurement limitation (the response is recorded every 1 s). The second constant slope, attributed to the rate of dissociative-H-adsorption by Delmelle et al., is well defined and depends on the hydrogen concentration. In fact, fig. 4.5b shows a linear pressure dependence, which corresponds to a surface limited kinetics. Nevertheless, in fig. 4.4b, we observe that the slope for 4 % $H_2$ is unchanged between different pre-flush gases (between purple dash line and green line), but the third regime is altered. The third regime, non linear, can be fitted with an exponential. Delmelle et al. attributed this latter to the equilibrium concentration of H inside the Pd thin film. Here, we observe that the third regime is responsible for the increase in the response time for concentration corresponding to the phase transition. Note that we limit the effect of the third regime since we define the response time at 90 %.

The unloading time is longer than 150 s, and can be decreased to 80 s by using $O_2$ in the Ar flow as shown in fig. 4.2a. Oxygen on the surface of Pd promotes the formation of $OH$ and $H_2O$ molecules [76], which increases the desorption rate significantly.

### 4.3.4 Cross-sensitivity

Figure 4.6a shows the sensor response for 1% $H_2$ in Ar and 1% $H_2$ in Ar mixed with 5% $O_2$. Oxygen molecules during the hydrogenation lead to a reduced sensitivity level. The sensor response can decrease to one half of its value, depending on the selected wavelength. The presence of $O_2$ influences the absorption of $H_2$, and is capable of limiting the amount of $H_2$ absorped due to the formation of $OH$ and $H_2O$ onto the Pd surface. Our observations are in agreement with the literature as described in section 1.4.4.

To overcome, the cross-sensitivity issue, scientists recommend to replace Pd by Pd alloys. As a proof of concept, we deposited a 5 nm thick Pd-Au alloys instead of Pd on the optical fiber core. As result, for the same previous ratio between $H_2$ and $O_2$, no significant change is observed by the presence of oxygen. Furthermore, we observe that the sensitivity decreases compared to Pd, which is in agreement with the decrease of hydrogen solubility in Pd alloys. We note also that the spectral response of the sensor remains. The response time is enhanced, especially for concentrations around the Pd phase transition. The third regime is now neglected since the phase transition « tends »to disappear (depends on the alloy content) for Pd alloys. Further investigations have to be done to find the right Au content or the right material (Au, Ag, Cu, Ta...).

## 4.4 Discussion

#### 4.4.0.1 Assumption

In order to understand the behavior of the proposed sensor, we first simulate its theoretical response as described in section 3.2. For that, we define the sensing multilayer and the dielectric permittivity for each layer. The multilayer consists of an infinite layer of silica, covered by a layer of Pd with a certain thickness and an infinite layer of air.

**Silicon dioxide layer :** The silica refractive index as a function of the wavelength is given by the Sellmeier equation :

$$n(\lambda) = P_1 + P_2\lambda^2 + P_3\lambda^{-2} + P_4\lambda^{-4} + P_5\lambda^{-6} + P_6\lambda^{-8} \tag{4.1}$$

where the coefficient $P_1$, $P_2$, $P_3$, $P_4$, $P_5$, and $P_6$ are the Schott coefficient, industry standard coefficient as determined by Schott for use with their glasses. The value of coefficients are $P_1 = 1.45179$, $P_2 = -0.00365$, $P_3 = -0.00243$, $P_4 = 0.00012$, $P_5 = -4.605 \times 10^{-6}$ and $P_6 = 9.635 \times 10^{-8}$ and $\lambda$ denotes the wavelength measured in $\mu$m. Eq. (1) is valid for the studied wavelength range.

**Pd layer :** As reported by Sullivan [162], the dielectric permittivity data of a dc-sputtered Pd, especially the imaginary part, is very sensitive to the sample preparation and measurement technique. The possible contamination, or oxide over layers on the thin film, can introduce significant errors. We decided to use the dielectric permittivity of Pd obtained by von Rottkay et al. [163] from ellipsometry measurements because the experimental conditions were very close to ours. The von Rottkay's sample was sputtered in a high vacuum deposition facility, as in our case. The thickness of the von Rottkay 's samples corresponds also to the thickness range of our Pd film.

**Pd hydride layer :** For the dielectric permittivity of Pd hydride, two ways were considered.

1. The data of the experimental dielectric permittivity of palladium hydride obtained at $10^5$ Pa hydrogen pressure from von Rottkay is used [163]. We assume in our simulation that the Pd hydride data corresponds to a concentration of 4% $H_2$ since the Pd hydride is in the $\beta$-phase.
2. The effect of the absorption of hydrogen on the dielectric permittivity of palladium is approximated by the following relation [71] :

$$\epsilon_{Pd,c(\%)H_2} = h(c(\%)) \times \epsilon_{Pd,0\%H_2} \tag{4.2}$$

where $\epsilon_{Pd,0\%H_2}$ is the dielectric permittivity of pure palladium and h represents a nonlinear relation with hydrogen concentration c(%). h=1 and h=0.8 represent a concentration of 0 % and 4 % at room condition, respectively.

Finally, we assume that the Pd expansion is neglected compared with the change of the refractive index, which is legitimate for very thin films (3.5 % lattice expansion for the $\beta$-phase [11]).

### 4.4.1 Simulated sensor response

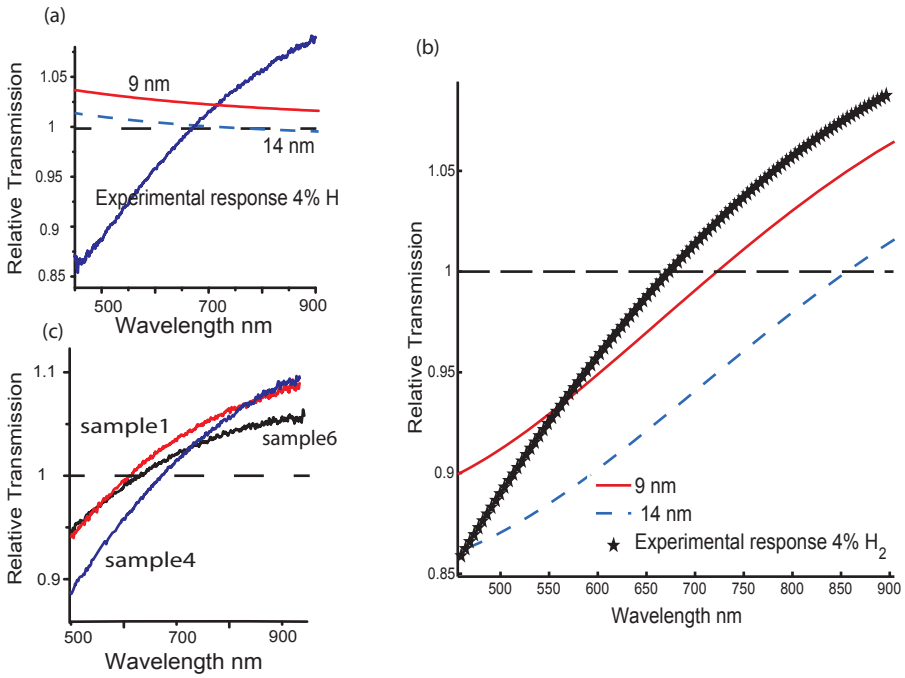


Figure 4.7 – Relative Transmission as a function of the wavelength. (a-b) Red line and blue dash line represent, respectively, the simulated relative transmission for 9 nm and 14 nm Pd deposited over a length of 2cm. The dielectric permittivity of palladium hydride (a) is approximated by the Bevenot's relation and (b) is determined from von Rottkay et al. [163].(Star symbols represent the experimental data for 4% $H_2$ in Ar). (c) Experimental spectral response for different sensors.

Figure 4.7a shows the relative transmission simulated with the dielectric permittivity following the relation (2). There is no significant wavelength dependence, and the simulated

response does not match with our experimental results. The relation (2) is not satisfying for simulating our sensor (because the real and the imaginary part of the dielectric permittivity of the Pd hydride cannot be linked by the same constant h, as it will be discussed in next section).

Figure 4.7b shows the relative transmission simulated with the von Rottkay' s experimental dielectric permittivity. The simulated response, depending on the selected wavelength, shows a similar spectral behavior as our sensor : the intensity decreases or increases. Nevertheless, the sensitivity of the simulated response is slightly different, in comparison with our experimental results. The minimum of the simulated sensitivity is obtained respectively at the wavelengths : 752 nm and 909 nm, for a thickness of 9 nm and 14 nm. In comparison, the experimental minimum is obtained around 600 nm for a concentration of 4 % of $H_2$ in Ar. Finally, the values of the experimental response are close to the simulated response of a 14 nm Pd thick film (blue dash line) at short wavelengths, whereas they are close to the one of 9 nm Pd thick film (red line) at long wavelengths. The difference with the simulated results is most likely come from the thickness gradient of our sensor sample.

The used Pd/ Pd hydride dielectric permittivity may also be different from the actual one in our Pd sample. In fact, Vargas et al. pointed out that the optical constants of the Pd films due to hydrogen absorption depends on the nature of the substrate [164]. Since in our sample the Pd is deposited on glass, the change in optical constants upon hydrogenation may be smaller than those obtained from von Rottkay (deposited on ITO). In addition, we have previously seen in chapter 1 that the substrate affects the Pd morphology which results in different Pd pcT. Nevertheless, Yamada et al. have recently obtained the same optical constants for a Pd deposit onto a glass substrate [165] as von Rottkay.

Sensor 1 and sensor 4 show different spectral responses. We first assumes that the discrepancy come from different Pd microstructure since the deposition condition were different. However, after studying several sensors, we observe that the reproducibility of the spectral response was in fact poor even when we use the same deposition condition. Figure 4.7c shows that the spectral response of sample 6 is really different than reference sample 4. The poor reproducibility of the sensor is due to fabrication errors during the etching (different sensing length) and deposition steps.

In conclusion, although there is a discrepancy between the simulated and experimental result, the data from von Rottkay appears to be relevant to qualitatively study the sensor response.

### 4.4.2 Description of the sensor response : relation between $\epsilon_1$ and $\epsilon_2$

We can now use the experimental dielectric permittivity to understand the observed response. Before explaining the response of the sensor, we describe the change of the dielectric permittivity upon hydrogenation.

The dielectric permittivity of Pd and Pd hydride obtained by von Rottkay et al. [163] is plotted in chapter 1. The real part of the refractive index n increases upon hydrogenation at short wavelength, in the range of 275 to 600 nm and decreases at long wavelength, in the range of 600 to 1750 nm. While the imaginary part of the refractive index k always decreases. Therefore, the complex dielectric permittivity decreases upon hydrogenation and the change of the optical constant is wavelength dependent.

The variation between the real part ($\Delta\epsilon_1 = |\epsilon_1(PdHx) - \epsilon_1(Pd)|$ ) and the imaginary part ($\Delta\epsilon_2 = |\epsilon_2(PdHx) - \epsilon_2(Pd)|$) of the dielectric permittivity upon hydrogenation is different, depending on the wavelength. Both of them are increasing toward the infrared wavelength in the sense that the variation $\Delta\epsilon$ is larger at longer wavelength. The value of $\Delta\epsilon_1$ and $\Delta\epsilon_2$ are respectively 5.546 and 1.385 at 468 nm, and 8.900 and 12.543 at 992 nm.

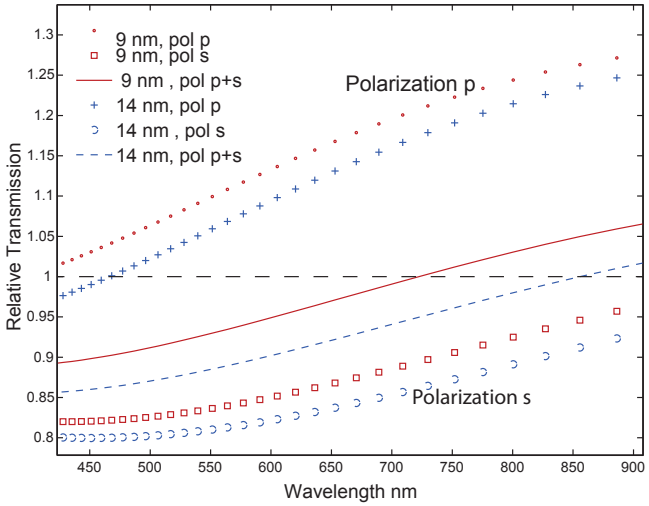


Figure 4.8 – Relative Transmission as a function of the wavelength for different thicknesses. Square/circle , point/plus and Line/ dash line represent the response for s-, p- and the sum of both polarization The relative transmission is simulated by using the dielectric permittivity of Pd hydride (from von Rottkay et al.[163])

The transmitted intensity through the optical fiber is unpolarized. We can decompose (locally at the reflection point) the light into the TE (s polarization) and TM (p polarization) polarizations. Figure 4.9 displays the reflectance curve of the $SiO_2$/Pd/air system for both polarizations. In our study, we consider only the angles within the NA of our optical measurement system are considered (i.e. above 77°).

**p polarization :** According to our simulation, the transmitted intensity increases upon hydrogenation, and the change is larger at longer wavelengths (fig. 4.8 (red dots and blue plus for 9 and 14 nm Pd, respectively). The origin of this behavior is due to the variation of the SPR peak upon hydrogenation depends on the wavelength.

Pd presents a broad SPR peak since it is a highly absorbing metal ($\epsilon_2 \approx \epsilon_1$). As previously noted, the width of the SPR peak decreases upon hydrogenation because the Pd hydride is less absorbing ($\epsilon_2$ decreases). Thus, the propagation length of the SP wave is longer for Pd hydride : the imaginary part of the SP propagation constant (noted $\mathrm{Im}(k_x^{SP}$ in chapter 2) decreases.

The decrease of the SPR peak width results in an increase of the reflectance for the propagating ray upon hydrogenation as shown in the SPR curve, fig. 4.9 (lines and dash lines). Consequently, the transmitted intensity increases in presence of hydrogen. The width of the peak is characterized by the ratio between $\epsilon_2$ and $\epsilon_1$. As a rule of thumb, the smaller $\epsilon_2$ is as compared to $\epsilon_1$, the thinner the SPR peak is. Since the ratio $\Delta\epsilon_2/\Delta\epsilon_1$ is larger at longer wavelengths, the change in the width upon hydrogenation is more significant near the infrared, fig. 4.9a, than the blue wavelength, fig. 4.9b. As a result, the change in the

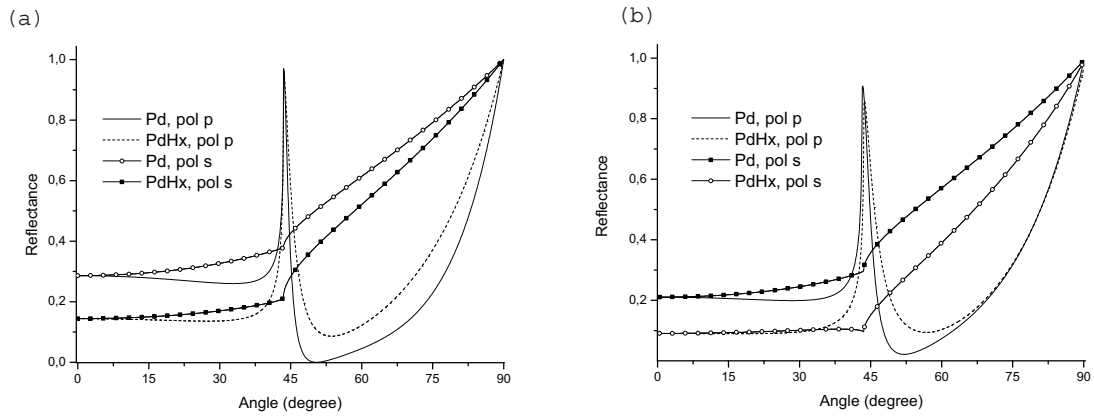


Figure 4.9 – Reflectance of a Pd layer and a PdHx layer of 12 nm onto glass substrate as a function of the angle theta (0 degree corresponds to the normal incidence). The dielectric permittivity of pure and hydride palladium (from von Rottkay et al.[163]) are used. (a) The wavelength is 800.45 nm. (b) The wavelength is 468 nm.

transmitted intensity is smaller at shorter wavelength, and increases toward the infrared wavelength, as depicted in fig. 4.8 (red dots, blue plus).

**s polarization :** The transmitted intensity decreases upon hydrogenation, and the change is larger at shorter wavelengths than at longer wavelengths, fig. 4.8 (red squares, blue circles). The reflectance curves (fig. 4.9) show the reflected intensity decreases upon hydrogenation (line symbols).

It is explained by a more semi-conductive behavior of the Pd film upon hydrogenation. In fact, at a normal incidence, the Pd hydride film becomes more transparent. Moreover, the decrease is larger at shorter wavelengths since the amount of hydrogen seen by the probe light increases.

In our case, the observed intensity at the output of our sensor is the sum of the both p- and s polarization light beam, fig. 4.8 (blue and red lines). Finally, the wavelength dependence of the sensor response comes from (i) the difference in reflectance as a function of hydrogenation between polarization s and p and (ii) the wavelength dependence of the reflected light for each polarization. The latter wavelength dependence is related to the difference between the real ($\epsilon_1$) and the imaginary part ($\epsilon_2$) of the dielectric permittivity with hydrogenation.

In conclusion, for simulating and designing SPR sensor, we have to consider the both polarizations. In particular, the change due to the modification of the SPR is attenuated. Figure 4.8 clearly shows that the sensitivity is higher when only one polarization is considered. However, it is difficult, especially for multimode, to maintain the polarization until the transducer region, and will involve the use of complex polarization-controlling elements.

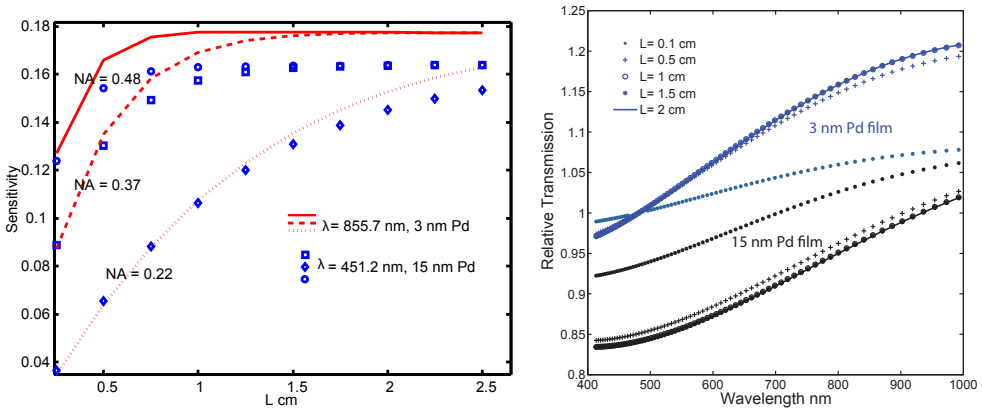


Figure 4.10 – (a) Sensitivity as a function of the length of the Pd film deposited onto the fiber for different wavelengths and NA. (b) Relative transmission as a function of the wavelength for different lengths with a fiber NA of 0.48.

## 4.5 Optimization

We propose to optimize the response in order to improve the sensitivity of the sensor by tuning the optical fiber and transducer parameters. To find the best optimization, we first decide which values are given and then we determine the seek parameters. By a looping process, we determine then all parameters.

### 4.5.1 Choice of the parameter to be simulated

The sensor responses depends on the optical fiber parameters, the transducer layer and the power distribution, chapter 2. Figure 4.10 shows the influences of the transducer length and the fiber NA. The sensor response is characterized by the transducer layer if the transducer numerical aperture (NA) is less than the fiber NA. We take therefore a large value for the fiber NA : 0.48. Furthermore, the length of the transducer and the diameter of the fiber, which determine the number of reflections for each propagating ray, characterize the ratio between the transmitted optical power and the optical power to be dissipated/coupled into the sensitive film for each propagating ray. We set the deposit length L at 2 cm and the fiber radius r at 100 $\mu$m in order to focus only on the influence of the Pd thickness. It is worth noting that the light source, in this case, does not affect the responses of the sensor, since we assume that there is an uniform power distribution through the ray due to mode mixing, inherent to a non ideal fiber.

### 4.5.2 Pd thickness

We calculate the relative transmission in the 3 - 15 nm thickness range for the TM-, TE- and both polarized light, as shown in fig. 4.11. The thickness range is chosen such that fast hydrogen detection and a good reproducibility of the sensor occur, see chapter 1.

The losses for the TM polarized light decrease upon hydrogenation due to the narrowing of the Pd SPR peak, as previously explained. Although the SPR peak is maximal for the 12 nm thick Pd film at a wavelength of 670 nm, shown in fig. 4.12, the maximum sensitivity is obtained for the 3 nm thick Pd film where the resonance is weak. The sensor sensitivity for the TM polarization is related on the change in the width of the SPR peak rather than

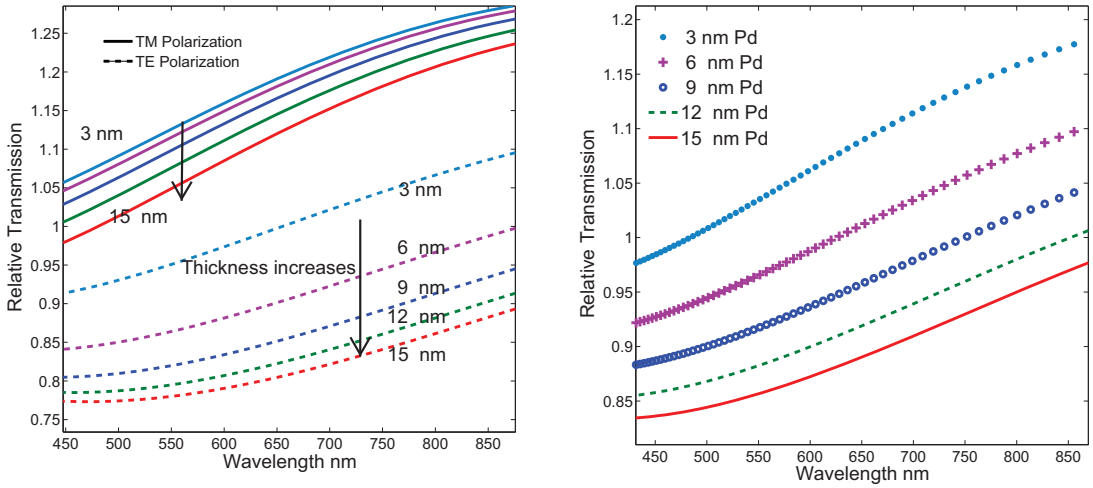


Figure 4.11 – Relative Transmission as a function of the wavelength for different thickness of Pd (a) for p- (lines) and s-polarization (symbols) and (b) for both polarizations.

in the shift of the resonance (i.e. related to the imaginary part of the propagation of the SP than the real part).

The losses for the TE polarized light increase upon hydrogenation for a Pd layer thickness above 4 nm, as previously explained. The sensitivity increases with the thickness (and for shorter wavelength). In analogy to the spectral dependence, the probe light « see »more hydrogen absorbed in the Pd thick film than in the thinner film. We observe a particular case for a 3 nm film thickness at long wavelength, where the losses decreases.

Figure 4.11b shows the relative transmission of the sensor for Pd film in the 3-15 nm thickness range, when both TE and TM polarized light propagate through the optical fiber. The maximum sensitivity is obtained for a 3 nm Pd film and for a 15 nm Pd film below and above 665 nm, respectively. In conclusion, the sensor response depends more on the TM polarization, i.e. on the « SPR effect »for thinner film. Contrary to thick films where the sensor response depends more on the TE polarization.

In order to validate our simulation we realize the sensor with a 7 nm and 3 nm Pd film. We deposit the Pd film as described in 3.3.2 with the configuration 2 in order to obtain an uniform thickness along the optical fiber.

**7 nm :** For a 7 nm thick film, our simulation are in qualitative agreement with our experimental results : the intensity increases upon hydrogenation for wavelength shorter than the previous configuration (9-14 nm). Figure 4.13a shows the spectral response of the sensor.

**3 nm :** For a 3 nm thick film, our model fails. A wavelength dependence is still observed, but the transmitted intensity increases for all considered wavelengths, with a maximum around 600 nm. Figure 4.13c shows the spectral response of the sensor. The discrepancy is explained by the difference in the optical data used in our simulation. For a 3 nm Pd film, the Pd film may not be anymore continuous. Several studies reported that Pd thin films below 5 nm consist of the film are made of Pd disconnected island [166]. The response is most likely due to the Pd expansion of the film. Further investigations have to be done to determine the Pd optical constant for such films. In spite of the fact that the mechanism

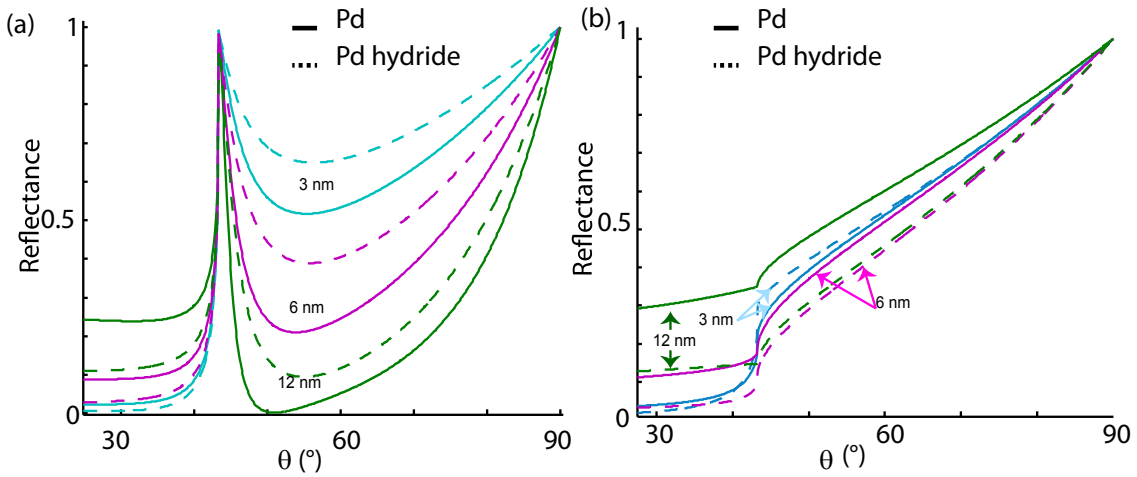


Figure 4.12 – Reflectance of a Pd layer and a $PdH_x$ layer on glass substrate as a function of the angle $\theta$ for different thicknesses (0° corresponds to the normal incidence) for (a) p-polarization and (b) s-polarization. The used wavelength is 670 nm.

is probably based on the Pd expansion, the sensor is reproducible as shown in fig. 4.13d.

#### 4.5.2.1 Dependence of the Pd thickness on the response time

Based on the study of the state of the art, thin Pd films seem to be the solution to realize fast and reproducible hydrogen sensor. In the previous section of this chapter, we have demonstrated the reproducibility. We focus now on the dependence of the Pd thickness on the response time.

By decreasing the thickness, we found that the response time is enhanced. The response time, varies between 10 to 20 s ( fig. 4.13b) and between 3 to 15 s for 7 nm and 3 nm thick Pd film, respectively. In all cases, the maximum is obtained for concentrations corresponding to the phase transition (1.5 %-2 % $H_2$ in Ar), as discussed in section 4.3.3.1. For very thin films, the response time is comparable to the fast optical fiber hydrogen sensor based on Pd alloys [81]. The enhancement of the response is likely due to the microstructure of the Pd film. Assuming that the Pd film is discontinuous, the response time enhancement is explained by the large surface area, which maximizes the hydrogen adsorption.

Furthermore, we observe that the response time film of a 7 nm thick Pd film is comparable to sample 1, while is enhanced in comparison with sample 4. The Pd deposited thickness of sample 1 and 4 was 9-14 nm. By comparing the response times and the spectral responses of the realized samples, we observe that the fast response time are obtained when the minimum of sensitivity is shifted toward shorter wavelengths. We deduce that the Pd deposit is thinner for these samples. Thus, we conclude that the discrepancy of the response (i.e. the reproducibility of the sensor) between the different realized samples is due to an error in the Pd deposited thickness.

In order to confirm the importance of using very thin Pd films for hydrogen sensor based on metal hydride, we report the response of a thick Pd film (approximately between 70-100 nm) coated on the core of a multimode fiber, over a length of 2 cm. Figure 4.14 shows the experimental response of the sensor.

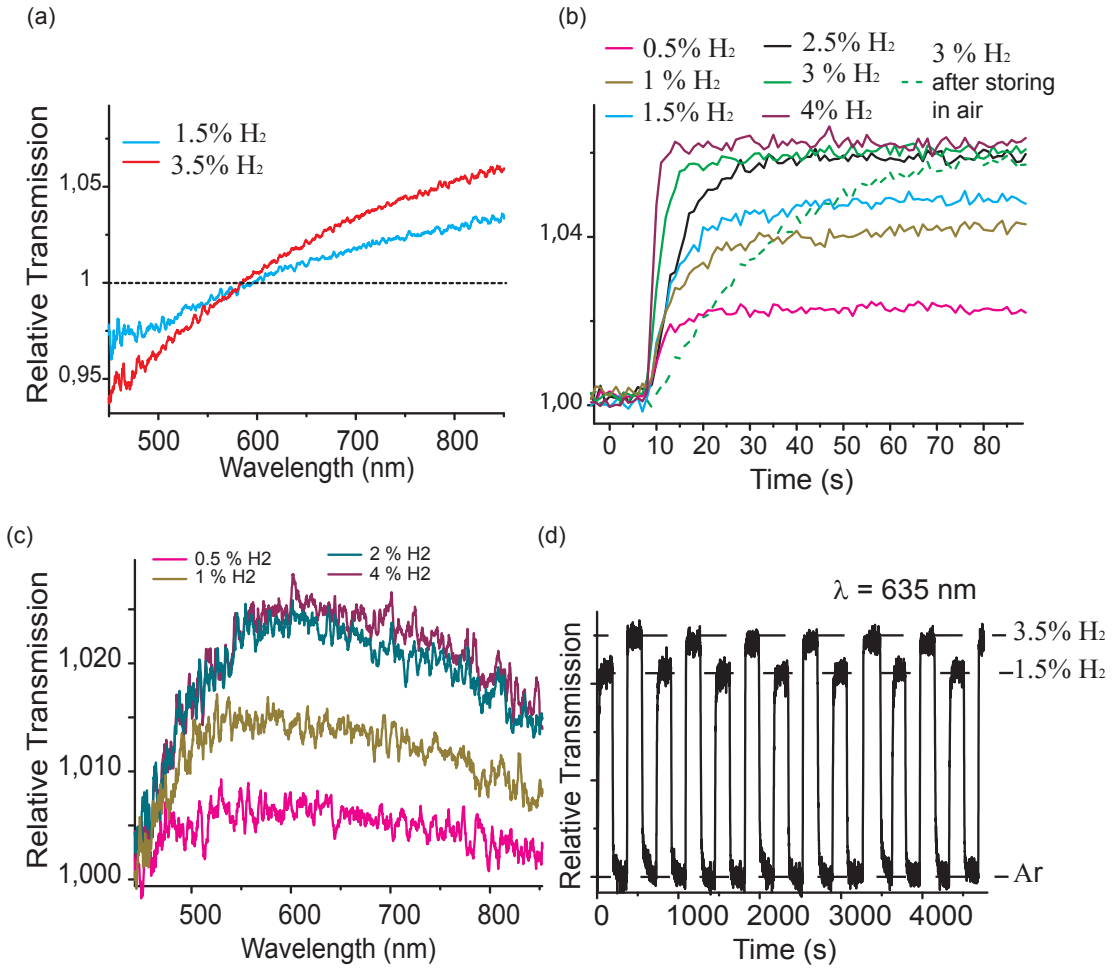


Figure 4.13 – (a-b) Performance of a 7 nm Pd thick film coated on the core of a multimode fiber. (a) Spectral response : relative transmission as a function of the wavelength. (b) Response time for different $H_2$ concentration (Ar used as a pre-flush gas). (c-d) Performance of a 3 nm Pd thick film coated on the core of a multimode fiber. (c) Spectral response : relative transmission as a function of the wavelength. (d)Reproducibility of the response.

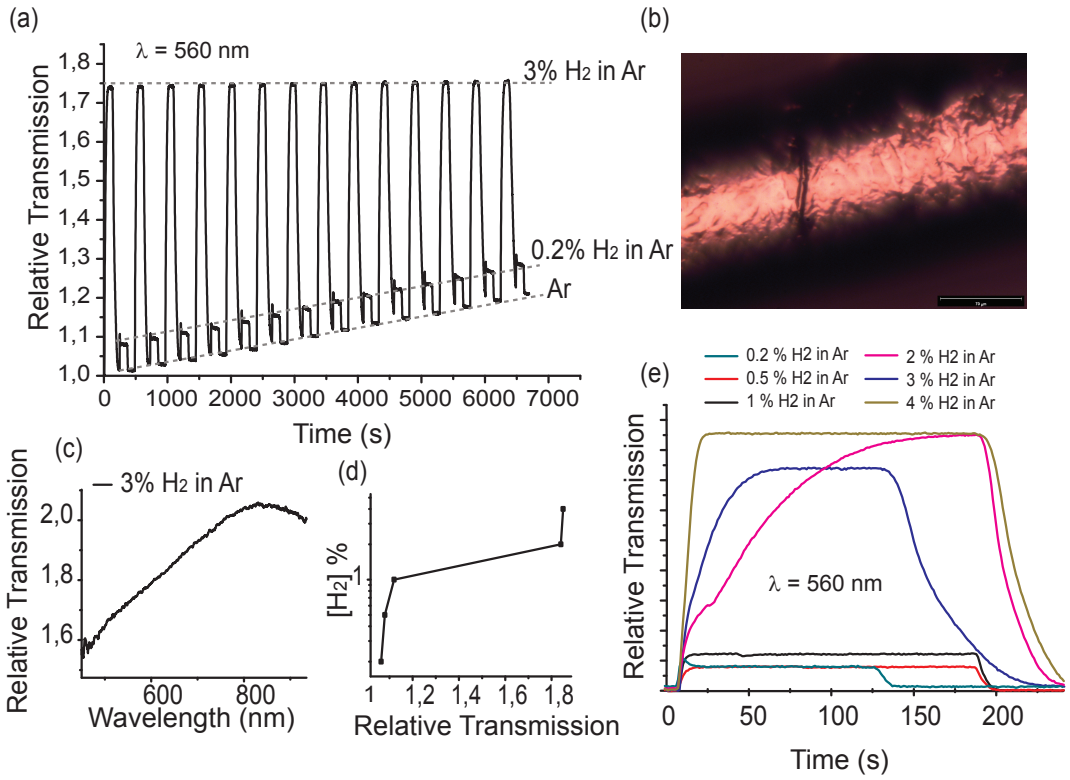


Figure 4.14 – Performance of a Pd thick film (70-100nm) coated on the core of a multimode fiber. (a)Reproducibility of the response. (b) Optical microscope images of the fiber core surface. (c) Spectral response : relative transmission as a function of the wavelength. (d) Hydrogen concentration as a function of the sensitivity(semi-logarithm scale). (e) Response time for different $H_2$ concentration.

- The transmitted intensity increases upon hydrogenation for all wavelengths in the considered range. In contrast to thin film, there is no surface plasmon resonance. The intensity increase is explained by the decrease of the imaginary refractive index (« pure evanescent wave sensors »). The sensing cladding is less absorbing with the formation of the Pd hydride.
- The sensitivity of the sensor is much higher than the one previously reported (and based on thin film). A sensitivity of about 80 % and 8 % is respectively obtained for 3 % and 0.2 % $H_2$ in Ar, while we obtained only a maximum sensitivity of about 10 % for 4 % $H_2$.
- The sensitivity as a function of the hydrogen concentration shows the same allure as the Pd pressure composition isotherm (pcT). The presence of a plateau, in fig. 4.14d, reflects the coexistence of the $\alpha$ and $\beta$ phases. The observed phase transition, between 1 to 2 % $H_2$ in Ar (10-20 mbar), is in agreement with the literature values.
- Reproducibility : The response based on Pd thick film is non reproducible for the hydrogen concentrations corresponding to the $\beta$-phase. Figure 4.14a shows a non reproducible baseline. This phenomenon, described in detail by Gremaud et al. [26] is explained by the presence of reversible cracks and buckles. Figure 4.14b shows the Pd surface under the microscope after several ab-desorption cycles. The Pd surface presents cracks (black line) and buckles which explains that the transmitted intensity does not recover its initial value. It is interesting to observe a reproducible signal for the hydrogenated state. In fact, Pd expansion, during hydrogenation, causes the cracks to closes.
- The response time varies between 10 to 96 s, as depicted in fig. 4.14e. For concentration corresponding to the $\alpha$ and the $\beta$ phase, the response time is of the same order as for thin film (7-10 nm) and sometimes faster for the $\alpha$ phase (4 s and 10 s for 0.5 % and 1 % $H_2$ in Ar, respectively). However, for concentration close to the phase transition, the response time is drastically slower (purple line) (96 s for 2% $H_2$).

In conclusion, the choice of using thin Pd film is a good approach to obtain reproducible hydrogen sensor though the sensitivity decreases. Regarding the response time, the response is barely depending on the thickness for nanometric continuous film, which confirms that the reaction is limited by the surface reaction. However, by decreasing the thickness in order to obtain (supposed) discontinuous films, we enhance significantly the response time.

Finally, we conclude this section by mentioning that a protective layer needs to be deposited on the Pd layer to maintain the response time performance. In fact, we observe that the response time for the first next cycles increases significantly ( green dash line in fig. 4.13b), when the sample is stored in air without any precaution. Repeated cycling with hydrogen enhance the response time, but may remain slower than at the term it was deposited. Although Pd does not oxidize, we assume this behavior accounts for the presence of a PdO cap layer. In conclusion, a protective layer has to be considered for Pd SPR sensors in the future. The protective coating should be chosen in order to avoid the extinction of the SPR, since it directly influences the confinement of the field into the metal. This protective layer could also enhance the SPR, for instance, by moving the SPR peak toward an angle that will be within the NA optical fiber. The protective layer could also improve the robustness of the sensor. Material engineering studies have to be pursued in this direction.

## 4.6 Low-cost multi point sensor ?

Due to the sensor design, it is possible to deposit several sensing layers along the optical fiber. The number of sensing sections is limited by the length of the total section since the Pd section induced losses (e.g. decreases the optical fiber NA). However, the localization and quantification is most likely unreliable for multiple sensors. Each sensitive section is modulated by the number of sensitive sections along the fiber. As each section responds continuously to the hydrogen concentration in a range of 0.5-4 % $H_2$ in Ar and is modulated by all sensitive sections along the fiber, an intensity fluctuation could easily lead to false alarm.

## 4.7 Conclusion

We report a novel and simple hydrogen sensor based on intensity modulation. This « low cost »sensor (if mass produced) is easily embeddable and adaptable to industry applications. Because of this configuration, the hydrogen detection can be made at a remote distance and several sensing points can be used. In the latter case, the detection localization is difficult however. It can be done by combining the sensor with FBG or OTDR at the expense of an increase cost. The main advantage of the proposed Pd sensor is to monitor the hydrogen concentration at several wavelengths. By comparing the different measured intensities, false alarms can be avoided even when the signal is prone to intensity fluctuations such as temperature dependent shifts or mechanical vibration effects, for instance. The response and recovery times are acceptable and comparable to the one found in literature, but are below the recommendation for an ideal hydrogen sensor. By decreasing the Pd thickness, we can enhance the response time. We succeeded in predicting the wavelength dependence for thin films having a thickness ranging from 6 to 15 nm. However, our model fail for very thin film, where we have to take into account the Pd expansion. We experimentally demonstrate that fast hydrogen sensor is achievable with the « SPR configuration ». However, the cross-sensitivity, in particular for oxygen and humidity, is an issue. Future work has to be done to find the best Pd alloys and protective layers.

# Chapter 5

# A fiber optic Surface Plasmon Resonance sensor based on wavelength modulation for hydrogen sensing

## 5.1 Introduction

At present, the fast optical fiber hydrogen sensors are mainly based on light intensity modulation. They show a typical response time of 10 s for 4 % $H_2$ in $N_2$ for a nano tapered fiber coated with a 4 nm thick Pd layer [58], and decreases to 5 s with thin Pd alloy layers in a heterostructure configuration [60]. However, the response time increases significantly (around 30 s, see chapter 1) for optical fiber sensors based on wavelength modulation. Nevertheless, they are more reliable (and preferably used in industry) since they are insensitive to light fluctuations of the source. Our aim is to develop a fast hydrogen sensor based on wavelength modulations.

In the previous chapter, we have seen that Pd Surface Plasmon Resonance (SPR) fiber hydrogen sensors show a fast response with a wavelength dependence, which increases the sensor reliability. Nevertheless, due to the absence of resonance in the transmitted spectrum, the hydrogen detection cannot be based on a wavelength modulation. Because of the limited numerical aperture of the optical fiber, the resonance condition of Surface Plasmon (SP) are not satisfied. In chapter 2, we have seen that the dispersion relation of SP can be tuned by changing the dielectric media surrounding the metal layer. A multilayer stack made of Ag, $SiO_2$ and Pd overcome the mismatch of the propagative constant between the guided modes and the SP propagating at the Pd air interface. To understand the principle of the sensor, and the role of each layer, we first study the SPR reflectivity curves. Then we determine the optimal parameters for hydrogen sensing. Finally, to test the viability of the structure that we propose, we study the hydrogen sensitivity, the dynamical range as well as the reproducibility and the cross-sensitivity. To study the experimental response of the sensor, we replace the silver layer by a gold layer for pratical reasons, as explained latter. Note that the parameters of this new multilayer have been optimized in the same way as the silver multilayer.

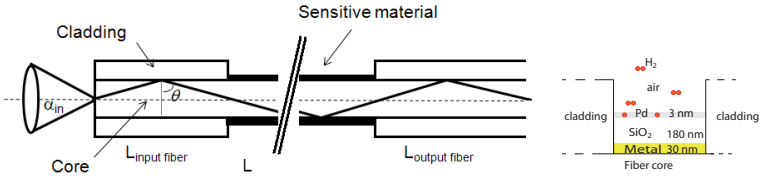


Figure 5.1 – Schematic representation of the way the sensitive material is deposited on the fiber core, after removing the cladding.

## 5.2 Simulation model

The proposed sensor consists of a multilayer stack deposited on a section of the core of a multimode step index fiber, as drawn in fig. 5.1. For the fiber Numerical Aperture (NA), the deposit length L and fiber radius r we take 0.22, 1 cm, 100 $\mu$m, respectively. The multilayer is made of : a Ag, a $SiO_2$ and a Pd layer. Ag is chosen since it is well known as a good candidate for SPR sensors [121], as described in chapter 2. The Ag layer can be replaced by any other plasmonic metals such as Au, Al... or bi-metal [132]. In fact, in the experimental section the Ag layer will be replacedby a Au layer in order to avoid the oxidation during the fabrication. Pd is chosen for its ability to dissociatively split and absorb hydrogen.

We simulate the multimode fiber SPR sensor as explained in chapter 3. We use the same optical constants for $SiO_2$, Pd and Pd hydride than previously. Note that although the optical constant of Pd and Pd hydride from von Rottkay [163] shows some limitations, they allow us to propose qualitatively new design. For the optical constant of Ag and Au, we use the Drude model, with the values given by [167].

## 5.3 Principle

To demonstrate the principle of the new proposed sensor, we simulate the 35 nm Ag/ 180 nm $SiO_2$/ 3 nm Pd multilayer stack. Figure 5.2a shows the transmitted intensity of the optical fiber. The sensor response shows a spectral resonance peak, in contrast to the Pd SPR fiber sensor in which the Pd layer is deposited on the fiber core as shown in fig. 5.2b. Upon hydrogenation, the resonant wavelength shifts to higher wavelengths. The observed peak corresponds to the excitation of the SP.

When the resonance condition of the SP is fulfilled, a sharp dip in the transmitted intensity is observed. In our multilayer structure, the resonance condition occurs when the evanescent wave ($kev$) (generated from the reflection of the guided light) matches with the propagation constant $\beta$ ($k_x^{SP}$ in chapter 2 of the SP. $\beta$ is determined from the dispersion relation of the corresponding multilayer waveguide. Upon hydrogenation, the propagation constant $\beta$ is altered due to the decrease in the both parts of the Pd complex dielectric permittivity. The position (related to the real component of $\beta$) and the shape of the SPR (related to the imaginary component of $\beta$) is therefore changed.

The variation of the partially reflected field at the $SiO_2$/Pd and Pd/air interface upon hydrogenation affects the interference between the incoming and the reflective wave. The hydrogenation of Pd changes the electromagnetic field distribution inside the multilayer. As emphasized by Pockrand and Raether [108], the depth of the SPR minimum is related

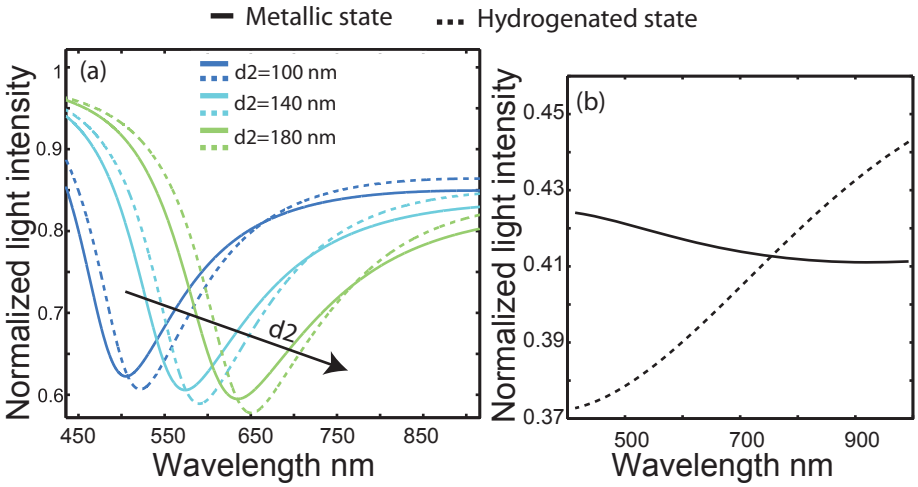


FIGURE 5.2 – (a) The transmitted light intensity as a function of the wavelength for different thickness of $SiO_2$. The transducer is a multilayer stack composed of 35 nm Ag/ d2 nm $SiO_2$/ 3 nm Pd. (NA = 0.22, the core radius = 100 $\mu$m, L = 1 cm). (b) The transmitted light intensity is a function of the wavelength, where the transducer is a 10 nm Pd layer (NA = 0.22, core radius = 100 $\mu$m, L = 2 cm)

to the field distribution and determined by the ratio of the intrinsic and radiation damping (section 2.6.1.1). Therefore, the minimum of the SPR peak changes upon hydrogenation.

Figure 5.3(a) shows the electric field distribution inside the multilayer for wavelengths of 670 nm (red and pink lines for polarization s and p, respectively) and 855 nm (black and gray lines for polarization s and p, respectively). The electric fields are plotted at the resonant angle of $\theta_{SPR,Pd}$ for the both metallic and hydrogenated states, respectively. Figure 5.3(b) shows the SPR reflectance curves. At resonance, the electric field intensity is maximum at the $SiO_2$/Pd interface for the short wavelengths. This wavelength distribution is opposite to the penetration depth distribution. It is explained by the optical metal properties : the metal is more transparent and less absorbing for the blue than the red wavelength, as emphasized by Shalabney et al. [168]. Figure 5.3(a) shows that the electric field increases upon hydrogenation at the $SiO_2$/Pd interface. The hydrogenation of the Pd layer makes the metal more transparent and less absorbing. The electric field is then redistributed into the multilayer and consequently, the SPR curve is altered.

## 5.4 Choice of the layer thicknesses

The thicknesses of the silver (d1), silica (d2) and Pd (d3) layers as well as the ratios of the thickness define the resonance conditions and the performances of the SPR sensor. The performance of a SPR fiber sensor based on spectral modulation is described in terms of the sensitivity S and the signal-to-noise ratio (SNR) (section 2.7 ). The former defines, here, the shift of the resonant wavelength $\delta\lambda_{res}$ due to a concentration of 4 % hydrogen. The latter is inversely proportional to the full width at the half-maximum (FWHM) corresponding to the SPR ($SNR = \delta\lambda_{res}/\delta\lambda_{FWHM}$). FWHM should be as small as possible to get the best resolution.

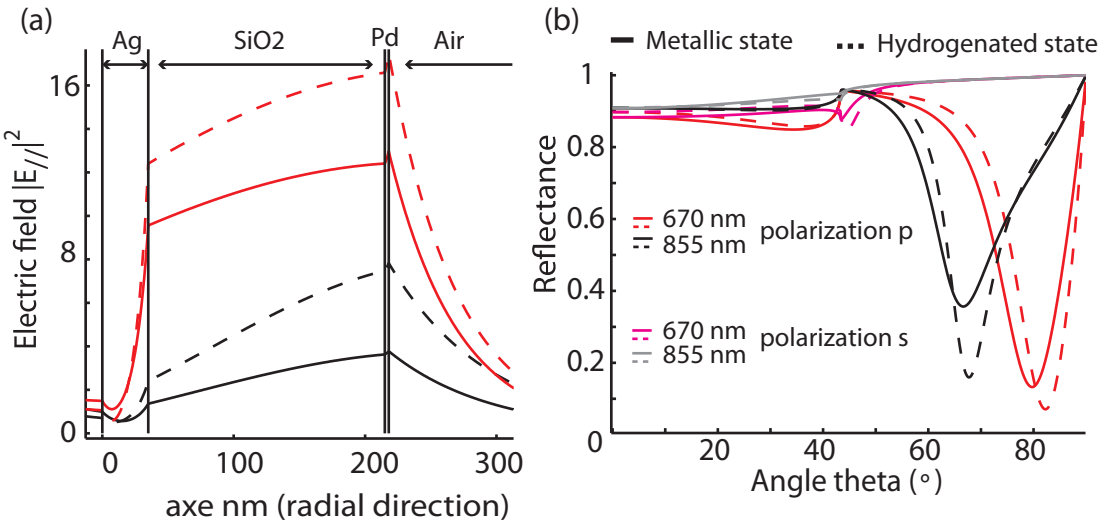


FIGURE 5.3 – (a) The electric field ($E_{//}$) distribution into a multilayer made of 35 nm Ag / 180 nm $SiO_2$ / 3 nm Pd for the metallic (line) and hydrogenated state (dash line) at the resonance ($\theta_{SPR,Pd}$ = 79.73° and 66.68° for $\lambda$ = 670.64 nm (red and pink for polarization p and s, respectively) and 855.65 nm (black and gray lines for polarization s and p, respectively), respectively). (b) Reflectance as a function of the angle theta (0° corresponds to the normal incidence) for p and s-polarization at different wavelengths.

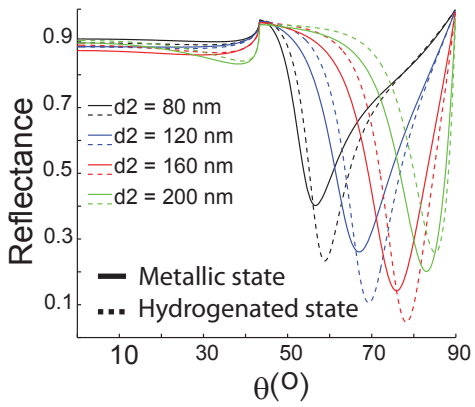


FIGURE 5.4 – Reflectance of a multilayer made of 35 nm Ag / d2 nm $SiO_2$ / 3 nm Pd for a wavelength of 670 nm. The lines and dash lines represent the metallic and hydrogenated state, respectively.

The first metal layer support the SP, in the sense that the main collective oscillations of free charge occurs at its interface. In addition, this layer made the sensor insensitive to the TE polarization, since the SP is only coupled by TM polarized light. The TE polarized light is reflected without being affected by the change in the surrounding index as shown in fig. 5.3(a) in contrast to our previous sensor described in chapter 4. Roughly speaking, the Au layer prevents the TE- polarized wave from reaching the sensing medium (here the Pd layer) due to the ohmic loss in the metal layer as it is commonly observed in the Au SPR fiber index refractive sensor. The transmitted intensity through the optical fiber is therefore only determined by the reflection coefficient of the TM polarized light for the propagating rays.

Figure 5.6(b) shows that the sensitivity increases with the Ag thickness. However, the peak minimum is negatively affected due the radiations damping, and the SNR decreases with an increase of the thickness of the Ag layer, as depicted in fig. 5.5(b). The resonant wavelength is also shifted to the longer wavelengths. A value of 35 nm seems a good trade-off.

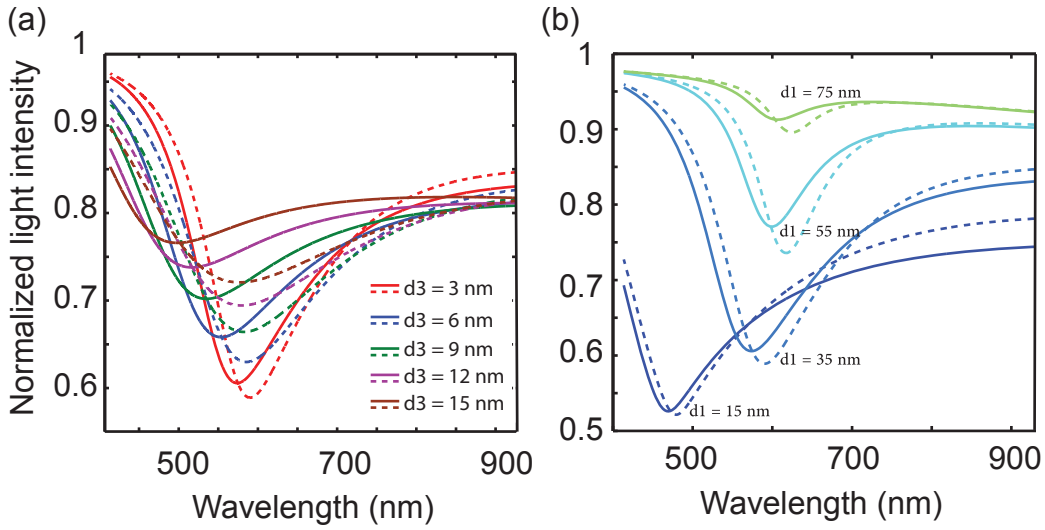


Figure 5.5 – Normalized light intensity as a function of the wavelength for (a) different thicknesses (d3) of Pd and (b) different thicknesses (d1) of Ag. The transducer is a multilayer made of d1 nm Ag / d2 nm $SiO_2$ / d3 nm Pd. (NA = 0.22, core radius = 100 $\mu$m, L = 1 cm). The lines and dash lines represent the metallic and hydrogenated state, respectively.

The second layer positions the resonance into the angular range of the optical fiber. By increasing the thickness of the $SiO_2$ layer, the effective index ($n = \beta/k_0$) of the SP increases, i.e. the resonance position is shifted to greater angles at a given wavelength, as depicted in fig. 5.4. Note that the intermediate $SiO_2$ layer is thin enough to avoid multi modes in the Metal Insulator Metal waveguide (MIM) and thick enough to decouple the SP (supporting by Ag and Pd).

The choice of the $SiO_2$ thickness allow us to define the resonant wavelength in the sensor responses, as shown in fig. 5.1(a). It shifts toward the long wavelengths with the increase of the $SiO_2$ thickness. The minimum of the peak changes as the radiation dam-

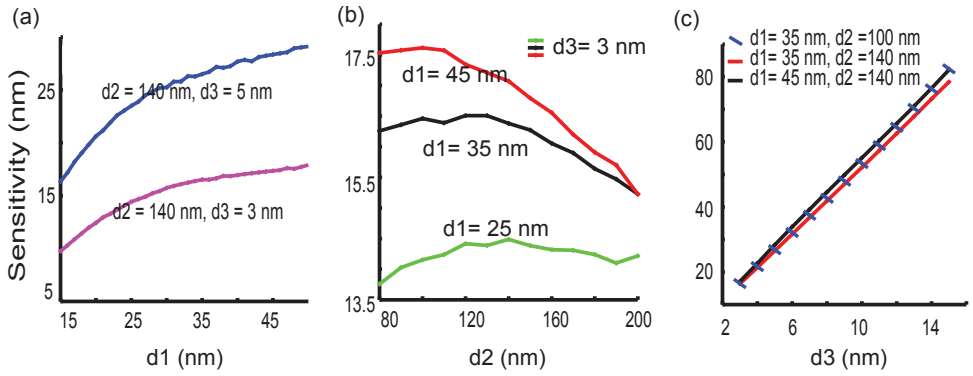


Figure 5.6 – Sensitivity as function of (a) the $SiO_2$ thickness for different Ag thicknesses, (b) of the Ag thickness for different Pd thicknesses and (c) of the Pd thickness for different Ag and $SiO_2$ thicknesses.

ping is affected. The peak widens at longer wavelength due to the increase of the metal absorption. Nevertheless, the sensitivity, as depicted in fig. 5.6, and the SNR are weakly altered by the silica thickness compared to the silver and Pd thicknesses. (The irregularity on the sensitivity curves is due to the wavelength discretization pitch in the simulation).

The Pd layer makes the multilayer sensitive to hydrogen. Increasing the Pd thickness widens the resonance peak and increases the peak minimum value, as shown in fig. 5.5(a). The absorption of Pd causes the broadening of the resonance. The change of the resonance depth is related to the change in the ratio of the two damping processes. It is worth noting that an increasing Pd thickness shifts the SPR peak toward shorter wavelengths due to the decrease of the effective index of the SP.

Figure 5.6(c) shows the sensitivity increases with the increase of the Pd thickness. A trade off has to be found between the sensitivity and the SNR. A 3 nm Pd thickness appears as optimal, appealing to conceive a fast and reproducible hydrogen sensor (in agreement with our previous experimental observation concerning very thin film). Nevertheless, the experiment response could be different due to the limitation of the Pd permittivity dielectric for discontinuous film.

In our design, the NA, the core diameter and the deposit length play a crucial role in the performance of the sensor. As previously reported for the SPR fiber sensor : an increase of the number of reflections decreases the value of the minimum peak, but trends to widen the peak ; a decrease of the NA gives a narrower SPR peak, as depicted in fig. 5.8. Therefore, we choose a value of 0.22 for the NA and 1 cm for L, with a core radius of 100 $\mu$m. According to our simulation, for a multimode step index, we find that the 35 nm Ag/ 100 nm $SiO_2$/ 3 nm Pd multilayer is the optimal design to obtain the best trade-off between the sensitivity and the SNR. Regarding the sensitivity, the resonant wavelength shows a shift of 17.6 nm at a concentration of 4 % $H_2$ in Ar (NA =0.22, L=1cm, core radius=100 $\mu$m, 35 nm Ag/ 100 nm $SiO_2$/ 3 nm Pd).

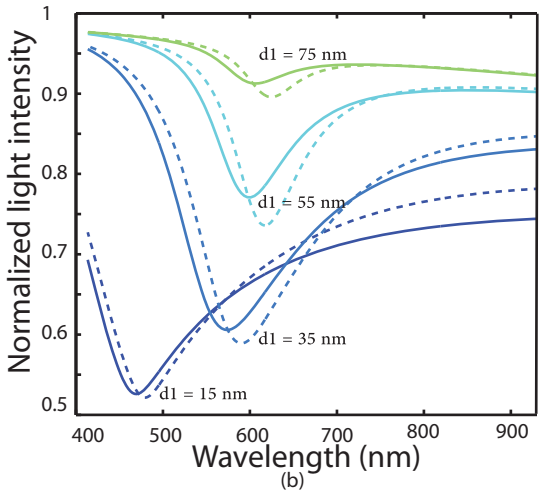


Figure 5.7 – Normalized light intensity as a function of the wavelength for different thickness d1 of Ag. The transducer is a multilayer made of d1 nm Ag / 140 nm $SiO_2$ / 3 nm Pd. (NA = 0.22, core radius = 100 $\mu$m, L = 1 cm). The lines and dash lines represent the metallic and hydrogenated state, respectively.

## 5.5 Experimental results

To study the performance of the proposed sensor, we realized a prototype that consists of a stacked layer of 35 nm Au/ 180 nm $SiO_2$/ 0-6 nm Pd on a multimode fiber core. The Ag layer was replaced by an Au layer for experimental reasons. The thickness of each layer have been optimized as previously discussed. (The thickness of the $SiO_2$ have been chosen to position the resonance in the middle of the spectrum of the light source -around 700 nm- in order to obtain the best Signal Noise Ratio (SNR)). We first study the spectral response to underline the functional mechanism of the proposed sensor. Then, we report the dynamical range, the sensitivity, the reproducibility and the cross-sensitivity to oxygen and air of the sensor in order to evaluate its use in hydrogen sensing application.

### 5.5.1 Experimental method

We used for our experiment a Newport multimode fiber and remove the optical cladding (heat treatment with chemical bath for cleaning) as described in section 3.3. The length L is limited to 0.5 cm($\pm$ 0.2 cm) in agreement with our simulation.

We deposit the stack multilayer with the configuration 2 as described in section 3.3.2 to ensures a uniform thickness around the optical fiber. At a background pressure of $10^{-7}$ mbar and Ar sputter pressure of 3 mbar was applied. Au, $SiO_2$ and Pd were sputtered at an average rate of 1.4 Å/s, 0.234 Å/s and 1.5 Å/s respectively, using 100 W RF, 150 W RF and 100 W DC power supply. To obtain the $SiO_2$ layer, a pure Si target is sputtered using oxygen as a reactive gas. Because of the use of reactive gas during the $Si0_2$ deposition, we choose to deposit a layer of gold instead of Ag to circumvent the oxidation of the metal. As a matter of course, a Ag layer can be used if a $SiO_2$ target is directly used.

To measure the response of the SPR sensor, we used the measurement bench described in section 3.4.2.

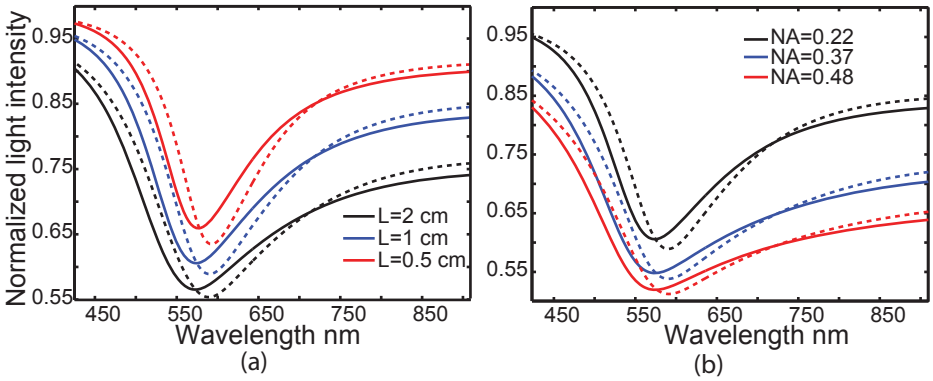


Figure 5.8 – Normalized light intensity as a function of the wavelength for (a) different lengths (the core radius, and the NA is 100 $\mu$m and 0.22, respectively) for (b) different fiber NA ( the core radius, and the deposit length is 100 $\mu$m and 1 cm, respectively). The transducer layer is made of 35 nm Ag / 140 nm $SiO_2$ / 3 nm Pd. The lines and dash lines represent the metallic and hydrogenated state, respectively.

### 5.5.2 Result

**SPR peak :** First we determine the normalized spectral response, which is defined as the measured spectrum divided by the reference spectrum of the bare optical fiber.

For various layer stacks figure 5.9a and 5.9b show the raw and normalized spectral response in the wavelength range from 450 to 850 nm. At wavelengths between 600 and 800 nm, a SPR peak is observed in the transmitted light. The resonant wavelength is mainly determined by the thickness of the $SiO_2$ layer. Theoretically, the resonant wavelength is 640 nm and 704 nm, respectively, for a 140 nm and a 180 nm thick $SiO_2$ layer. Furthermore, the SPR peak tends to disappear with an increasing Pd thickness while shifting to shorter wavelengths.

Our experimental results are in relatively good agreement with our simulations. The discrepancy of 0.5 to 5 % between the measured and simulated value of the resonant wavelength, is most likely caused by a small uncertainty in the deposited thickness of $SiO_2$ (due to the optical fiber orientation during the deposition).

To investigate the sensor response, we studied the relative change in the transmitted response for each individual sensor. In fact, we cannot directly compare the width and the minimum value of the SPR resonance peak experimentally obtained with our simulations, since the losses may also come from the coupling (source/detector-fiber connection) and the sensing interface (cladding-core interface). Nevertheless, the relative change of the SPR peak in the presence of hydrogen is the same between the different samples and insensitive to the intensity fluctuation.

We present in the following the response of the sensor with a $SiO_2$ thickness of 180 nm in order to obtain the better SNR, between the reference and the measured spectrum.

**$H_2$ response :** The measurements were carried at hydrogen concentrations between 0.5% and 4% $H_2$ in Ar, at atmospheric pressure and room temperature. We use the same gas cell as previously and described in section 3.4.2. The gas loading cell is purged several

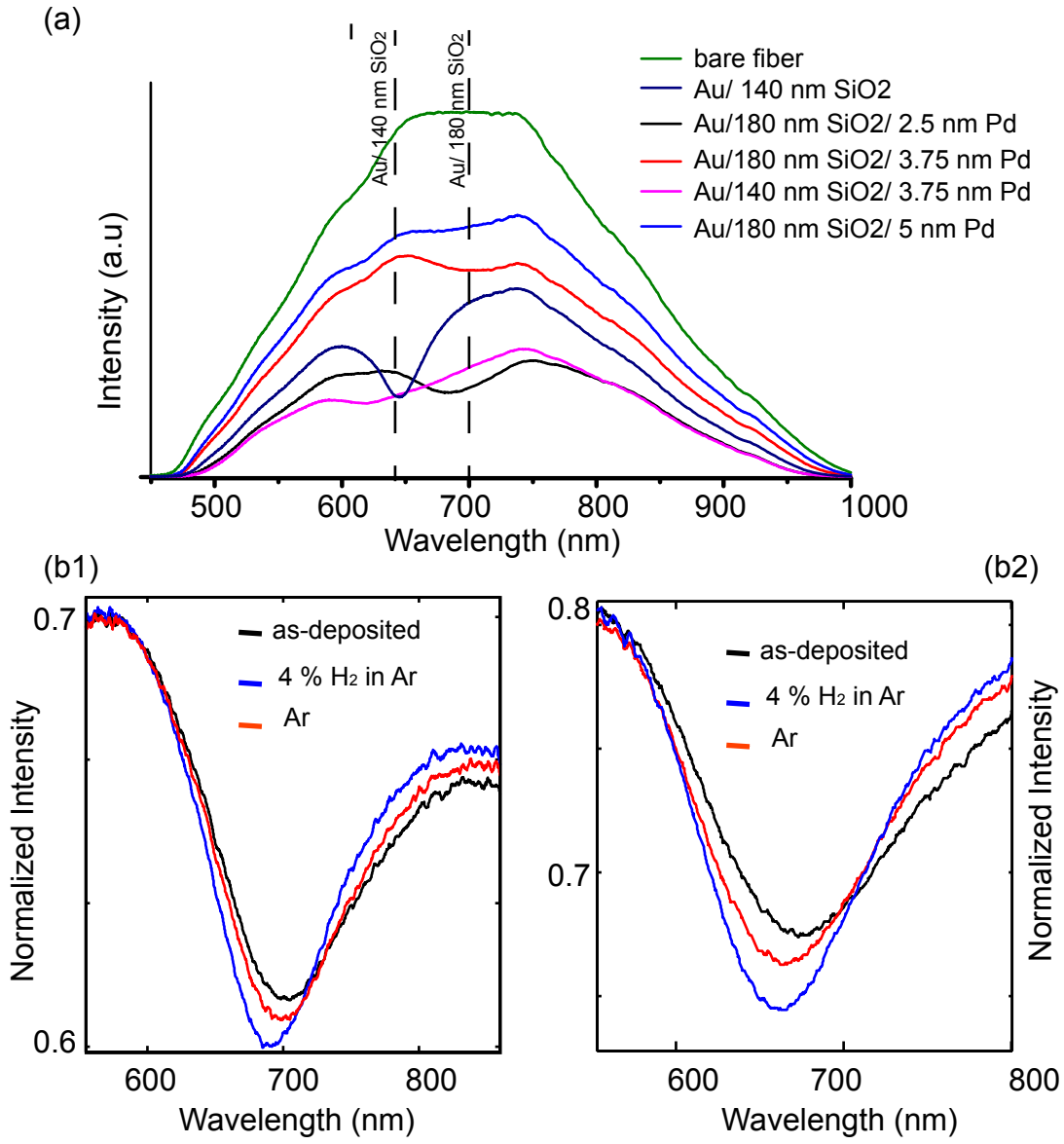


Figure 5.9 – (a) Raw spectra for various layer stacks.(b1-2) Normalized transmitted spectrum for (1) Au/ SiO2 (180 nm)/ Pd (2.5 nm) and for (2) Au/ $SiO_2$ (180 nm)/ Pd (5 nm)

minutes with Ar before all measurements, in order obtain a minimum of impurities in the gas system.

Adding $H_2$ to the Ar, we observe that the SPR peak changes in all layer geometries. Figures 5.9b1 and b2 show the normalized intensity after as-deposited, after 4% $H_2$ in Ar (blue line) and Ar after recovering for two different multilayer stacks. The shift of the SPR peak causes a change in the transmitted intensity and in the minimum resonant wavelength (defined in the following as the resonant wavelength). Figures 5.10a and b show respectively these both changes upon hydrogenation cycles at 2% and 4% $H_2$ in Ar for the Au (35 nm)/ $SiO_2$ (180 nm)/ Pd (2.5 nm) multilayer.

**Intensity modulation :** The transmitted intensity decreases for wavelengths shorter (orange, red lines) than the resonant wavelength and increases for longer wavelength (black and purple lines). Note that the transmitted intensity for wavelengths smaller than the resonance is barely changed ( green line ). While the transmitted intensity is affected for the longer wavelength outside the resonance. At the resonance, the intensity decrease in agreement with our simulation. The imaginary part of the SP wavevector decreases since the Pd hydride phase is less absorbing.

**Wavelength modulation :** At resonance, the signal is strongly limited by the shot noise since the intensity is minimal [169]. A curve fitting procedure is used to determine the change in the resonant wavelength in the presence of noise. Contrary to our simulations, the resonant wavelength shifts to shorter wavelengths with the presence of hydrogen. This discrepancy between simulation and the experimental results is explained by the difference of optical data of our Pd/ Pd hydride film and the one determined by von Rottkay [163] as emphasized in the chapter 4. The deposition of Pd at room temperature causes an island growth mode. As previously discussed in section 4.5.2, Pd films are made of Pd disconnected island below 5 nm [82]. Upon hydrogenation, the island Pd microstructure may have an inverse effect on the effective index of refraction of the stack layer upon hydrogenation. In analogy, we refer to the work of Kalli [50] mentioned in the chapter 1 : for a Pd film deposited on a glass substrate, the reflectivity increases for film inferior to 3 nm in presence of hydrogen instead of decreasing as for bulk film. Assuming a discontinuous film, we believed that the expansion of the Pd film upon hydrogenation lead to a more continuous film causing a increase of the real part of the refractive index.

In conclusion, we assume that the change in the real part of the SP wavevector is predominantly caused by the Pd expansion, while the change in the imaginary part of the SP wavevector is predominantly caused by the Pd dielectric permittivity. Further investigations have to be done to validate the origin of the SPR shift.

**Reproducibility :** After the first hydrogenation cycle, the optical response of the sensor becomes reproducible for both changes in intensity and resonant wavelength, apart from a negligible drift. As previously reported in chapter 4 : the first hydrogenation cycle causes a relaxation of the build-in stress as a result from deposition [52, 26]. Besides, the first hydrogenation cycle may also remove any adsorbed gas species gathered at the surface during transport.

The observed drift may be due to the poor adhesion between the individual layers. To improve the adhesion a thin Ti or Cr adhesion layer can be deposited prior to the Pd (chapter 2). It is interesting to mention that SPR sensor are sensitive to the change in temperature since the refractive index are strongly dependent on the temperature. Here, the measurement were carried out without any temperature control device. The temperature is the room temperature (varying from 20° to 25° during the day). Consequently, a

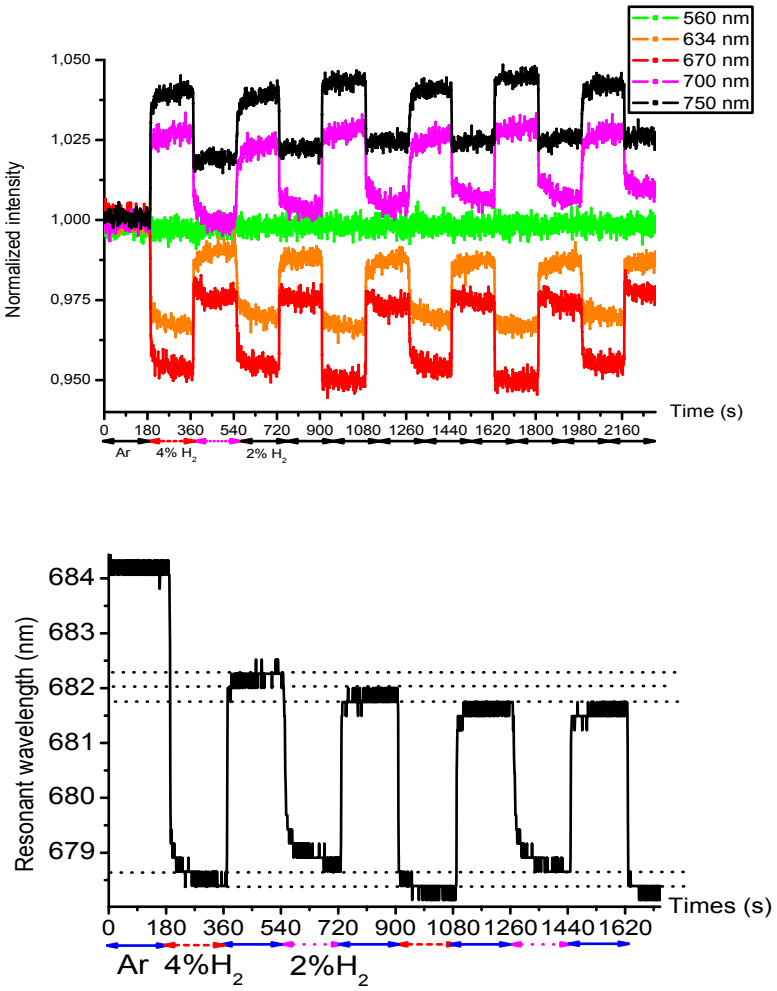


Figure 5.10 – Au (35 nm)/Sio2(180 nm)/Pd (2.5nm) sensor response reproducibility (a) of the transmitted intensity at different wavelengths and (b) of the fitting resonant wavelength. The sensor successively responses to a concentration of 4% and 2 % $H_2$ in Ar. Recovery are successively repeated in Ar.

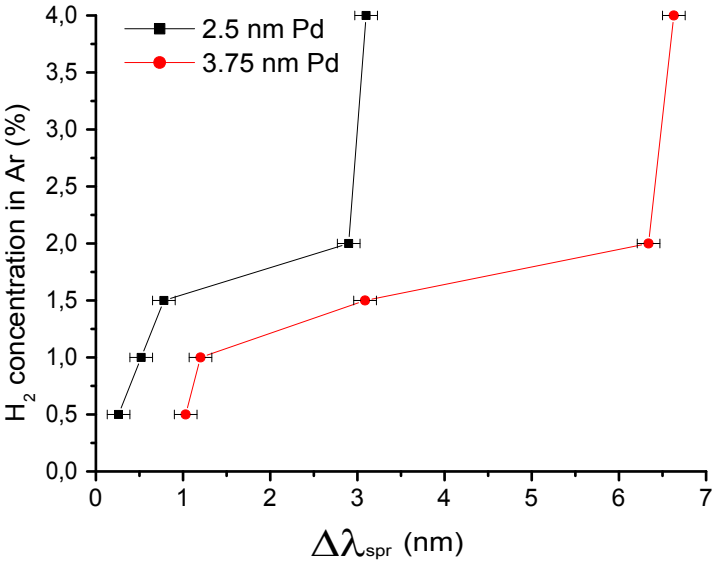


Figure 5.11 – Au (35 nm)/Sio2(180 nm)/Pd sensor dynamical range at room temperature and ambient pressure for different Pd thicknesses.

supplementary drift due to a temperature change may be observed between different experiments. However, we assume that this drift is neglected during one run ( the temperature change is less than 1°). For industrial applications, we have to calibrate the sensors as a function of the temperature.

**Dynamic range & sensitivity :** The resonant wavelength is a function of the hydrogen concentration (fig. 5.11) and represents the Pd pressure-composition-isotherm (pcT) at room temperature, as discussed in the previous chapters 1.

In particular, the change of the optical signal is related to hydrogen solubility in the metal ( i.e. on the amount of hydrogen in the metal lattice determined by the exterior hydrogen pressure). Below the critical temperature, the metal hydride exists in two phases called $\alpha$ and $\beta$. The $\alpha$ phase characterizes a low solubility (the H atoms occupy randomly the interstitial sites of the metal host lattice). The $\beta$ phase characterizes a high solubility with 60-70% of all the sites being occupied). During the phase transition (where both phases coexist at the so-called plateau pressure) the number of H atoms increases significantly, which induces a Pd lattice expansion due to the H-H interactions. This 2-phase character is reflected in the behaviour of the sensor. Below the pressure plateau, small changes are observed corresponding to the $\alpha$ phase, which limit the minimal detection to 0.5 % $H_2$ in Ar. The observed phase transition, around 1.5 to 2 % $H_2$ in Ar (15-20 mbar), is in agreement with the literature values. The observed sloped plateau is characteristic for an ultrathin Pd film. Above 3 % $H_2$ in Ar, the sensor response saturates corresponding to the formation of the $\beta$ phase. As with all Pd based sensors, a large signal is obtained when applying hydrogen concentrations well above the plateau pressure. In our case, the detection based on wavelength modulation is reliable even for small changes in the hydrogen concentration, well below the plateau pressure. In the case of amplitude sensors small changes in intensity

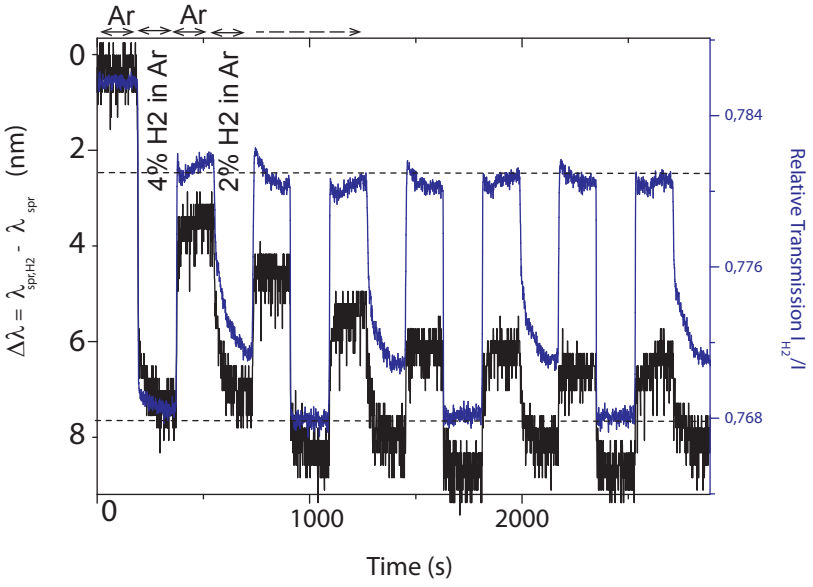


Figure 5.12 – Reproducibility of the Au(35 nm)/ $SiO_2$(160 nm) / Pd(6 nm) sensor response based on wavelength (dark line) and intensity modulation (blue line).

could simply be the result of noise (from the fluctuation of the light source or the presence of bending) instead of hydrogen. Note, that in our geometry a reliable detection based on amplitude modulation can be done by measuring at several wavelengths having an opposite effect.

Let us mention that the minimal detection level could be decreased either by using a reference signal, more sophisticated fitting algorithms [170], electronic filters [169] or replacing the multimode by a single mode fiber (The us eof a multimode fiber induces a broad SPR peak) at the expense of the sensor robustness.

In order to further optimize the sensor response, we varied the thickness of the Pd film between 0 and 6 nm. In fact, the detectable change is dependent on the Pd thickness : our simulations show that a larger change in resonant wavelength is obtained, when the Pd film is thicker. Experimentally, increasing the Pd thickness improves the shift of the resonant wavelength as depicted in fig. 5.11. However, the SPR peak is also attenuated (minimum and peak broader for thicker films, as shown in fig.3c) since Pd is a highly absorbing material. In addition, we experimentally found that the resonant wavelength modulation becomes less reproducible for Pd films which are thicker than 5 nm. Notwithstanding the resonant wavelength shift of about 8 nm is obtained for the first cycl, the change decreases continuously over hydrogen ab-desorption cycles as depicted in black line in fig 5.12. Note that the detection can, suprisingly, still be done based on intensity measurement (blue line) : the change in the width of the SPR peak is reproducible. For a 5 nm Pd thick, we believe that the film becomes more and more continuous over time due the Pd expansion. Finally, we conclude that the Pd layer has an optimal thickness of about 3.75 nm.

**Response time :** The sensor responses almost immediately after the gas reach the cell measurement (i.e. after 7 s, see section 3.4.2). The response time is approximately

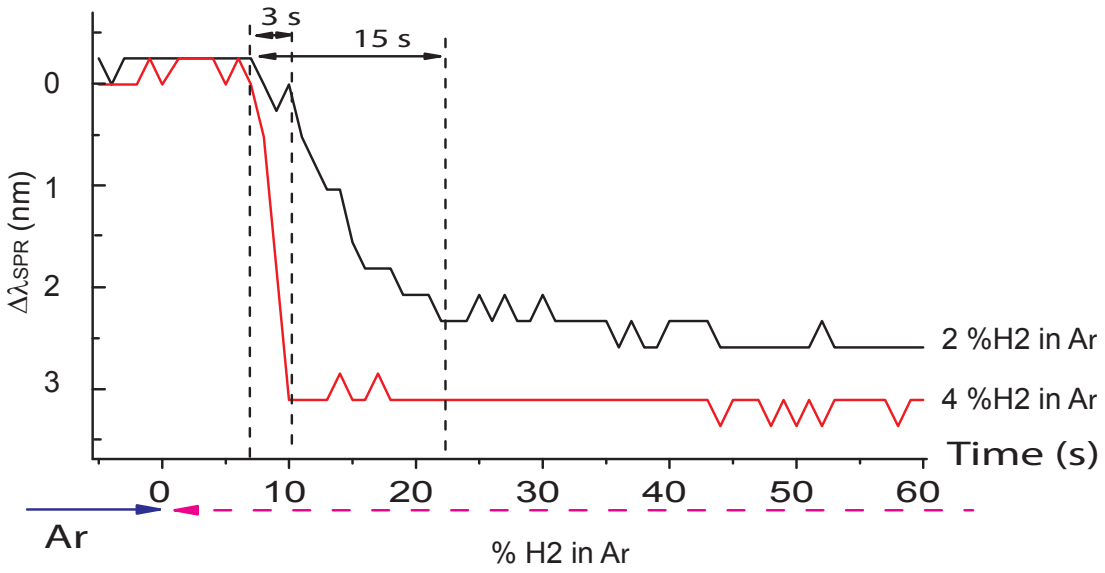


Figure 5.13 – Au (35 nm)/$Sio_2$(180 nm)/Pd (2.5nm) sensor response time for a concentration of 4% and 2 % H2 in Ar. Ar is used as a pre-flushed gas.

3 s for 4 % $H_2$ in Ar, which becomes only slightly slower, between 3 and 7 s, at lower hydrogen concentrations corresponding to the alpha phase. Nevertheless, we observe that the response time significantly increases for concentrations close to the phase transition, about 17 s for 2 % $H_2$ in Ar. The plastic deformation occurring during the phase transition could be responsible for this phenomenon.

For thin Pd films, the response time is limited by surface processes since the hydrogen diffusion through the Pd layer is negligible. We assume that the improvement of the response time (in comparison with wavelength fiber sensors based on a Pd films thicker than 30 nm) is due to the presence of a discontinuous Pd surface. At room temperature the deposition of Pd causes an island growth mode and for Pd films thinner than 5 nm. It is reported that such a film is made up of a discontinuous network of interconnected islands. The increase of the surface area improves the hydrogen adsorption which may explain our fast response, in analogy to discontinuous film for electrical hydrogen sensor. Furthermore, this assumption could explain the anomalous direction of the SPR peak shift, as explained previously. In conclusion, a very Pd thin film provide a fast hydrogen detection.

**Cross-sensitivity :** The selective hydrogen absorption by the Pd layer is a necessary condition for the selectivity of the sensor. In fact, without the Pd layer deposited on the $SiO_2$ layer, the sensor is sensitive to the surrounding environment. For the sensor of a Au (35 nm)/ $SiO_2$ (140 nm) multilayer stack, the transmitted intensity decreases and increases respectively at shorter and longer wavelength when the air in the measurement cell is replaced by Ar and by 2% $H_2$ in Ar. Figure 5.14 shows the relative transmission of the sensor in different surrounding atmospheres. As a result, the resonance peak shifts to shorter wavelengths due to the change of the refractive index of the gas.Our simulations, depicted in the inset of fig. 5.14 are in qualitative agreement, but the observed amplitude change of 2 orders of magnitude is much larger than expected. It cannot be explained only by the refractive index of the surrounding medium. The change may due to (i) interaction of adsorbed gases at the $SiO_2$ surface or (ii) the account for a change of temperature of

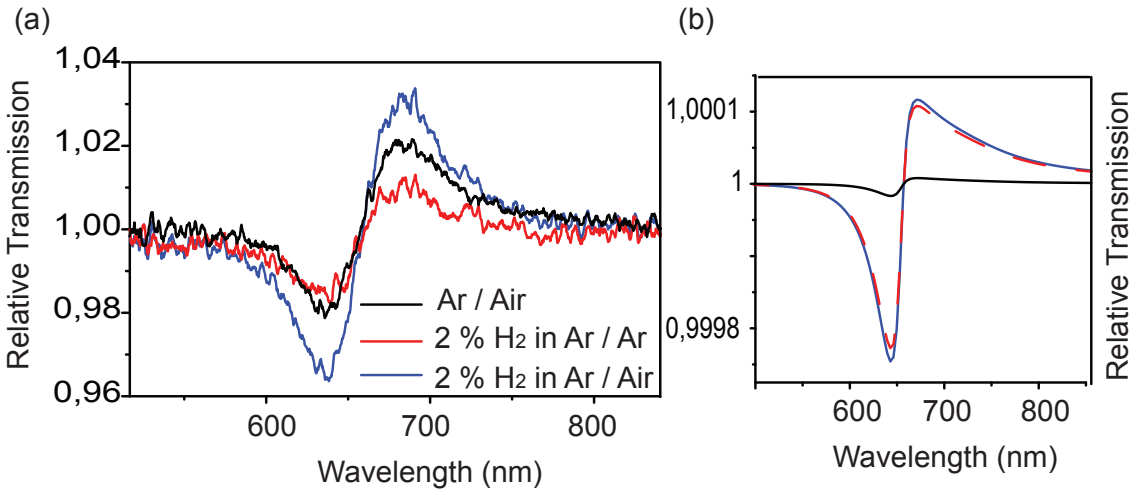


Figure 5.14 – Experimental and (b) simulated response to Ar, air and 2 % H2 in Ar of the Au (35 nm)/ SiO2 (140 nm) sensor.

the gas cell due to the thermal conductivity of the gases. Further investigations have to be done to find the contribution of each effect on the observed signal.

In conclusion, the Pd layer is need for the selectivity of the sensor. By increasing the Pd layer thickness, the sensor becomes more selective to $H_2$ and become less sensitive to the exterior background (Air, Ar) since the SP is attenuated. The change in the refractive of the Pd layer due to hydrogenation will be much larger that due to the adsorption at the surface, which could be due to many different gases. Nevertheless, other chemical reactions than hydrogenation can occurs at the Pd surface. As already reported, oxygen can change the response time and the final value of the signal. This cross-sensitivity is all the more significant for thinner Pd films, since the $O_2$ penetrates and diffuses into sub sites, as mentioned by Maier et al. [66]. In order to operate the sensor in air, Pd has to be replaced by Pd alloys to prevent the Pd surface contaminations (see section 4.3.4) . Since the Pd layer is simply used to change the surrounding index medium, any other sensitive material such as Pd alloys can be used in the proposed design. In addition, a protective layer could be also added in this design to decrease the cross-sensitivity and increase the lifetime of the sensor.

## 5.6 Conclusion

We have proposed an innovative SPR fiber hydrogen sensor based on wavelength modulation. We have demonstrated that fast optical fiber hydrogen sensor based on wavelength modulation is possible with SPR.The response of our sensor shows a good reproducibility required for application purposes. The proposed design is simple, can easily be embedded in industrial systems. The operating wavelength is tuned by adjusting the intermediate layer thickness. Furthermore, the intrinsic fiber sensor developed provides remote sensing and possibility of multi-points sensing. A multi-point sensor could be realized by adding Fiber Bragg grating after each sensing region. Finally, the minimal detection level, limited by the intensity fluctuation, can be improved either by using a reference signal, signal processing or the use of single mode fiber in the future. Adding an intermediate dielectric

layer before the silver layer (Long range Surface Plasmon [124, 171]) or a Bragg multilayer system [172, 173, 174] made of $TiO_2/SiO_2$ could be another possible way to enhance the sensor resolution. One major challenge is to improve the sensitivity of the plasmonic sensor with respect to the exterior background, which is most often disregarded. Therefore it is necessary to develop a protective layer or improve the selectivity toward hydrogen. Our proposed sensor could be extended to Pd alloys. Alternatively to thin film, a sensing film based on embedded metal nanoparticles in a protective polymer film could be developed.

In conclusion, SPR are a promising approach for industrial hydrogen sensing, where reliability and fast response are required.

# Chapter 6

# Intrinsic multimode fiber based on Mg Ti alloys

## 6.1 Introduction

This chapter focuses on the improvement of the sensitivity and the detection dynamic range of SPR based hydrogen sensors. Our goal is to figure out how to decrease the minimum level and to increase the maximum level of detection. In addition, we would like to quantify the hydrogen concentration. From the literature analysis (section 1.4.1) and from our results, it has been shown that the dynamic range of the hydrogen sensor is related to the Pd pressure composition isotherms (pcT). The $\alpha$-phase limits the minimal detection due to low hydrogen solubility in the host lattice, while the $\beta$-phase limits the maximal detection due to saturation of hydrogen sites. The width and the pressure of the equilibrium phase transition, where the change in optical constant is maximum, define the dynamical range of the sensor. Recently, Slaman et al. [12, 13] developed a hydrogen micro-mirror fiber sensor based on Mg alloys. A 50 nm layer of $Mg_{70}Ti_{30}$ was deposited at the end of a cleaved multimode fiber (200$\mu$m/15$\mu$m), covered by a 20 nm Pd layer. The advantages of those switchable materials are : (i) a low equilibrium pressure plateau, (ii) a large optical contrast and (iii) a fast kinetics with (iv) high stability over time and with ab-desorption cycles. Figure 6.1 illustrates the optical change after the hydrogenation of a 200 nm thick $Mg_{70}Ti_{30}$ film covered with 10 nm of Pd before (left) and after (right) exposure. As depicted Mg-Ti shows a large optical change upon hydrogenation. Before hydrogen exposure, the film shows a high reflectance (and low transmittance). With the presence of hydrogen, the film exhibits a black state, in the sense that the film shows a low reflectance and transmittance over the whole solar spectrum : the film is highly absorbing [175]. This optical change is continuous, and depends on the hydrogen pressure and the Mg alloy composition. At a temperature of 25° C, the phase transition and the largest optical change of a $Mg_{70}Ti_{30}$ film is obtained at a pressure of 0.88 Pa (i.e. for a concentration of 0.0088% $H_2$). The phase transition (pressure plateau) is determined by the alloy composition as shown in fig. 6.2 [26]. The pressure plateau shifts toward higher pressures and widens with increasing Ti content in the Mg alloys. Thus, by tuning the composition of the Mg alloys, we can change the dynamical range of the hydrogen sensor.

Our design, previously proposed and described in chapter 5, is not explicitly based on the SPR of the Pd layer in the sense that the free oscillating charges are mainly supported by the Au layer at the Au $SiO_2$ interface. Pd is rather used to change the effective index of


Figure 6.1 – Appearance of a 200 nm thick $Mg_{70}Ti_{30}$ film covered with 10 nm of Pd before (left) and after (right) exposure to $10^5$ Pa of a 4% $H_2$ in Ar mixture at room temperature. The pictures are taken from the substrate side. [176]

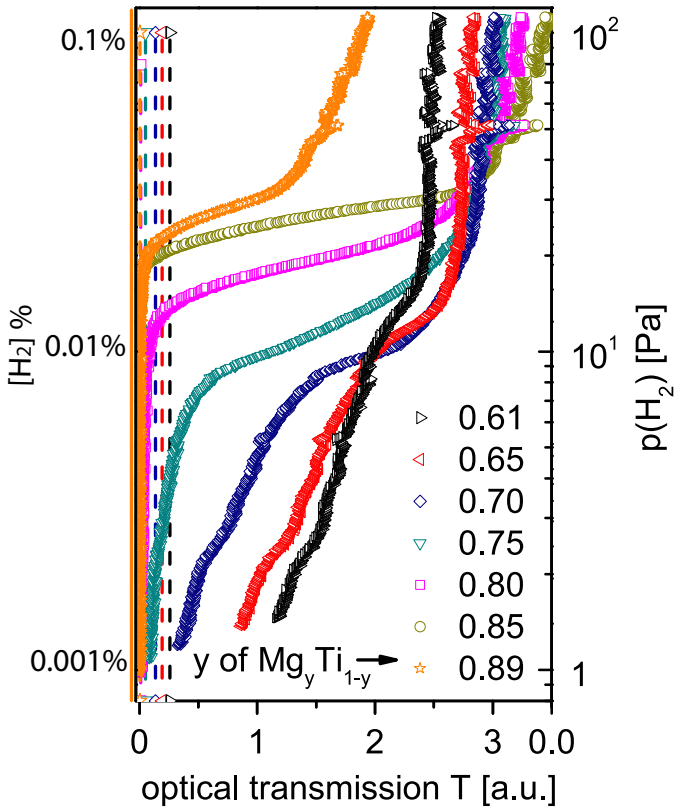


Figure 6.2 – Optical transmission for a selection of composition y, at a temperature of 25°C. [26]

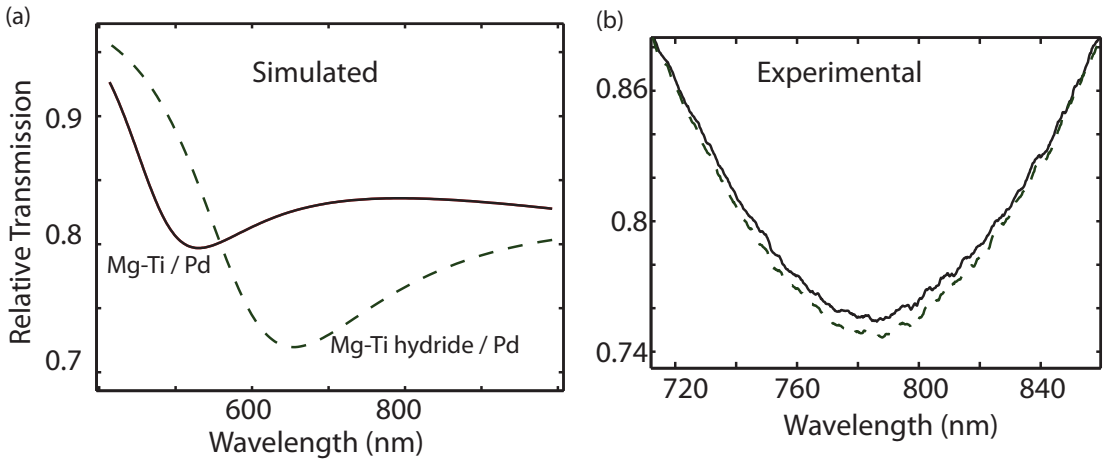


Figure 6.3 – Normalized spectrum for a multilayer consisting of 35 nm Au/ 100 nm $SiO_2$/ 10 nm $Mg_{70}Ti30$ / 5 nm Pd. (a) Simulated and (b) experimental response. The lines and dash lines represent respectively the metalic and hydrogenated state.

the multilayer upon hydrogenation. Therefore, we should be able to replace the Pd by any other hydrogen sensitive layer (metal or not). Replacing Pd by a Mg alloy thin film will result in a larger shift of the SPR peak, which will improve the resolution of the sensor. To stress our point, we present in fig. 6.3 the simulated response of the sensor with the following multilayer : 35 nm Au/ 100 nm $SiO_2$/ 10 nm $Mg_{70}Ti_{30}$ / 5 nm Pd. We clearly observe the shift of the SPR peak in absence (black line) and in presence of hydrogen (dash line). Nevertheless, our experimental result of such structure is far from the predicted one. To understand this negative result, we propose to study first the properties of Mg alloys in a simple optical fiber configuration. To do so, we study the response of the sensor where a Mg alloy film is coated on an intrinsic multimode optical fiber. Contrary to the micro-mirror presented by Slaman et al., our range of considered angles is now different, and is defined by the optical fiber NA. The following questions arise : Does the switchable material still show a large optical contrast ? For which thickness, and length of the deposit, is the response optimal ? Is the performance of such sensors adaptable for hydrogen leak detection ?

The first part of this chapter shows the simulated response of optical fiber sensors based on a Mg alloy. The aim is to understand the role of each layer in the configuration we proposed. In particular, does the SP at the Pd air interface play a role in the response ? In the second part, we study the experimental response of the sensor for various alloy compositions and thickness ranges. Finally, we conclude on the possibility to use Mg alloys in a SPR fiber sensor for industrial uses.

## 6.2 Intrinsic multimode fiber based on Mg-Ti alloys

The sensor consists of a thin-film Mg-alloy layer, covered by a Pd layer deposited on the core of an optical fiber. The Mg-alloy layer plays the role of the indicator material, while the Pd layer prevents the oxidation and promotes the hydrogen dissociation. The Pd layer has to be thin enough to obtain a reproducible and fast response as previously described in section 4.5.2. The Pd thickness has to be larger than 3 nm in order to maintain the

catalytic property of Pd [52].

The principle of the sensor is the same as the sensor described in chapter 4. The change in the dielectric permittivity of the stack layer causes a modification of the reflection coefficient, which results in a local change of the numerical aperture (NA) of the optical fiber. Therefore the transmitted intensity at the output of the optical fiber is modulated by the hydrogen concentration. To study the effective role of each layer, we calculate the reflectivity of various multilayer stacks as a function of the light incident angle for different wavelengths. We deduce then the response of the optical fiber sensor as explained in section 3.2.

### 6.2.1 Simulation

For the simulation, we use the same optical constants as in the previous chapters while the dielectric permittivity of Mg-Ti-H is derived from measurements on thick films by Borsa et al. [175]. In contrast to Pd, Mg alloys show a large change in lattice constant. We take this expansion into account by assuming an expansion volume of 30 % in the direction perpendicular to the optical fiber. In our study, we consider only the angles within the NA of our optical measurement system (i.e. above 81.2°). Finally, to distinguish the hydrogenation effect of the Pd and Mg alloy layer, we calculate the reflectance for the three final (equilibrium) states : (i) both materials are first in the metallic state (lines), (ii) the Mg-alloy layer is then hydrogenated whereas the Pd layer is still in metallic state (dash lines), and (iii) both Mg-alloy and Pd are hydrogenated (symbol lines). Note that the Mg alloys layer is hydrogenated before the Pd layer.

It is clear that for thick Mg-Ti layers (superior to 100 nm), the Pd layer does not affect the reflectance of the multilayer stack since the Mg-Ti layer is either metallic or highly absorbing (in the hydrogenated state). By decreasing the Mg-Ti thickness, the Pd layer can not be neglected anymore due the penetration depth of the field in this layer. The penetration depth depends on the wavelength and the polarization. To stress our point, we considerer two multilayer stacks with different ranges of thickness. The former consists of a 50 nm thick $Mg_{70}Ti_{30}$ layer and a 25 nm thick Pd layer, while the latter consists of a 10 nm thick $Mg_{70}Ti_{30}$ layer and a 12 nm thick Pd layer.

**50 nm $Mg_{70}Ti_{30}$ / 25 nm Pd :** Figure 6.4 plots the reflectance as a function of the incident angle ($\theta$) for polarization s and p, at a short wavelength (blue line) and at a long wavelength (red line). Basically, in almost all cases the reflectance decreases for the range of angles considered upon hydrogenation. The change is predominant for polarization s.

For polarization s, the change is almost wavelength independent. The decrease in reflectance is mainly caused by the hydrogenation of Mg-Ti layer (blue versus green dash lines 6.4a). Due to the highly absorbing character of the Mg-Ti hydride, the light is strongly attenuated in the $Mg_{70}Ti_{30}$ layer as depicted in fig. 6.4c. Roughly speaking, the light does not « see »the Pd layer. The Pd layer is not used as a transducer layer in this case, but only as a catalyst.

For polarization p, the optical change is wavelength dependent and function of the hydrogenation of both layers. At a shorter wavelength, the reflectance decreases (blue line-dash, fig. 6.4b), while it increases at a longer wavelength with the formation of Mg-Ti hydride. The reflectance change tends to decrease with the formation of Pd hydride. In the hydride state, (dash line in fig. 6.4b) the reflectance curve shows a broad SPR peak (around 60°. In fig. 6.4d, we observe the enhancement of the SP field at the Pd air interface upon

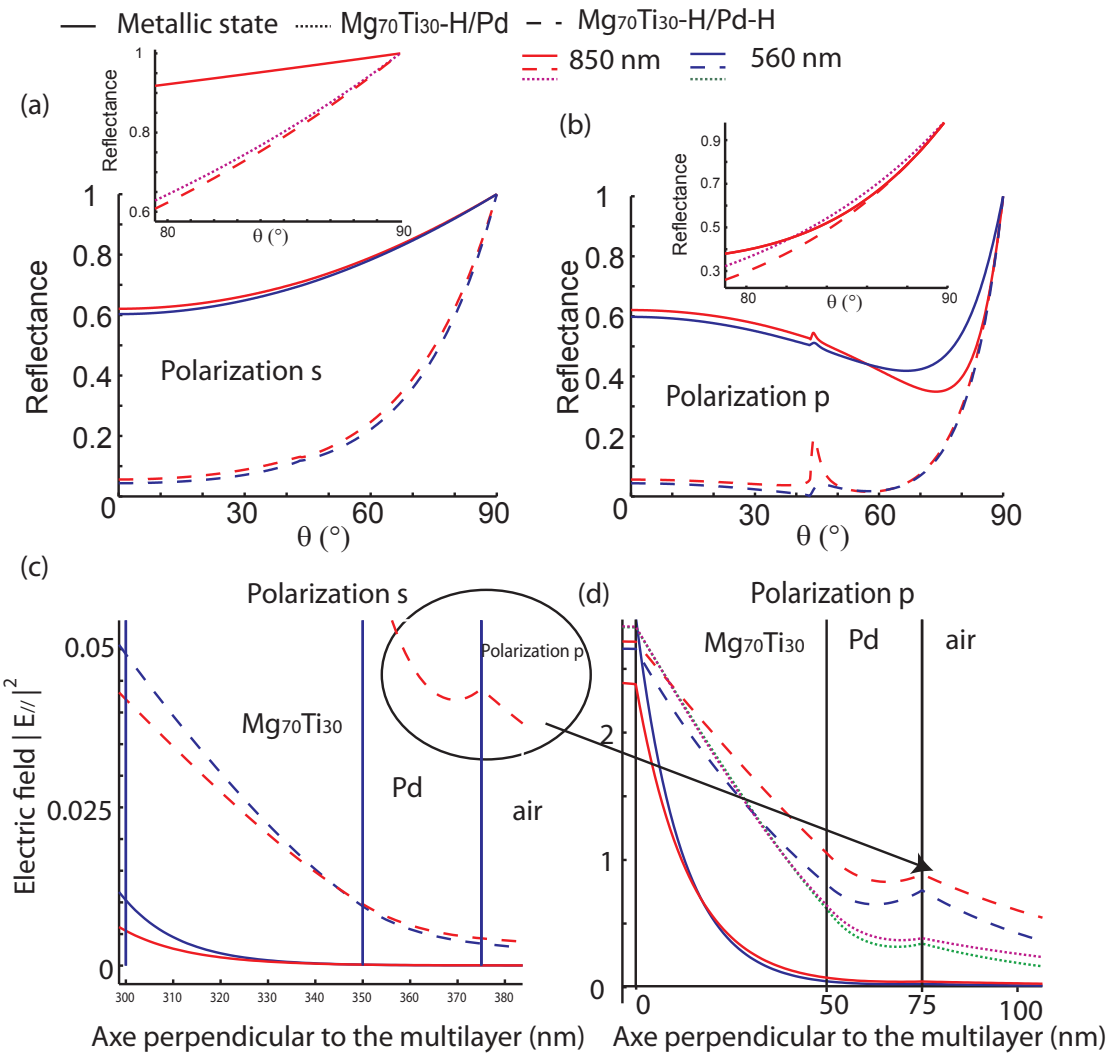


Figure 6.4 – (a-b) Reflectance of a stack multilayer of a 50 nm thick $Mg_{70}Ti_{30}$ layer and a 25 nm thick Pd, deposited onto glass substrate, as a function of the angle $\theta$ (0° corresponds to the normal incidence), for polarization (a) s and (b) p, respectively. (c-d) represent the field distribution ($\theta = 82°$). The electric field is parallel to the multilayer stack. At the left of the Mg-Ti layer, the field corresponds to the interference between the incident and reflected field. The amplitude fields are not normalized. The expansion of the metal is neglected for simplicity

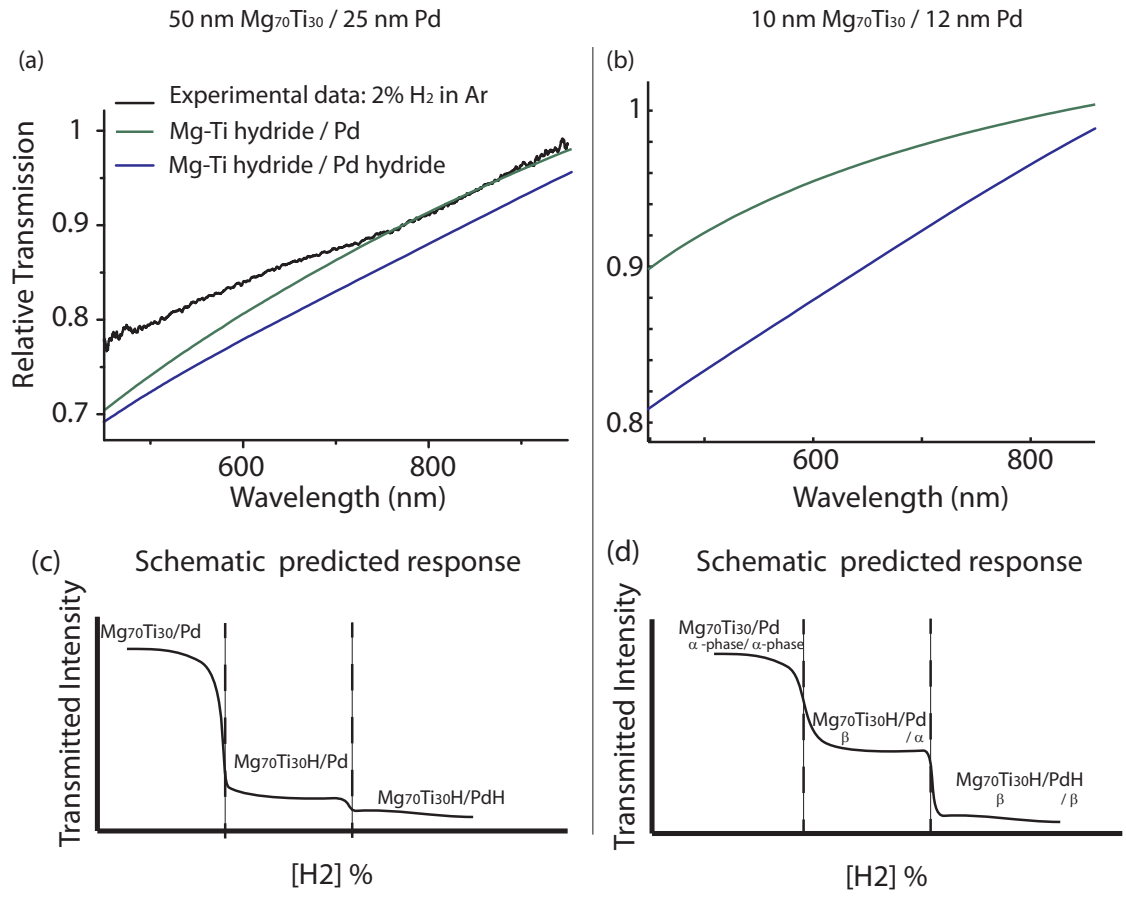


Figure 6.5 – Simulated relative transmission of a multilayer stack of (a) 30 nm $Mg_{70}Ti_{30}$/ 25 nm Pd and (b) 10 nm $Mg_{70}Ti_{30}$/ 12 nm Pd (c-d) Transmitted intensity as a function of hydrogen for a multilayer stack of (c) 30 nm $Mg_{70}Ti_{30}$/ 25 nm Pd and (d) 10 nm $Mg_{70}Ti_{30}$/ 12 nm Pd

hydrogenation.

In conclusion, at short wavelengths the reflectance decreases for both polarizations, while it is reduced at long wavelengths for polarization p. The decrease of the reflectance means in an optical fiber structure that the transmitted intensity decreases. Finally, the transmitted intensity decreases upon hydrogenation, with a larger change at short wavelength, as depicted in fig. 6.5a. We can consider that the change is mainly due to the formation of the Mg-Ti hydride (fig. 6.5c).

**10 nm $Mg_{70}Ti_{30}$ / 12 nm Pd :** For thin films, the change in reflectance due to the formation of Pd hydride, is none neglected compared to the change induced by the formation of Mg-Ti hydride.

For polarization s, the reflectance still decreases as depicted in fig 6.6a. The film is less metallic, which results in increasing the penetration depth as shown in fig 6.6c.

For polarization p, the reflectance curve, in fig 6.6b, shows a SPR peak for all states (hydrogenated or not). Upon hydrogenation, the SP field is enhanced at the Pd air interface. The modification of the peak leads to an increase and a decrease in reflectance at shorter

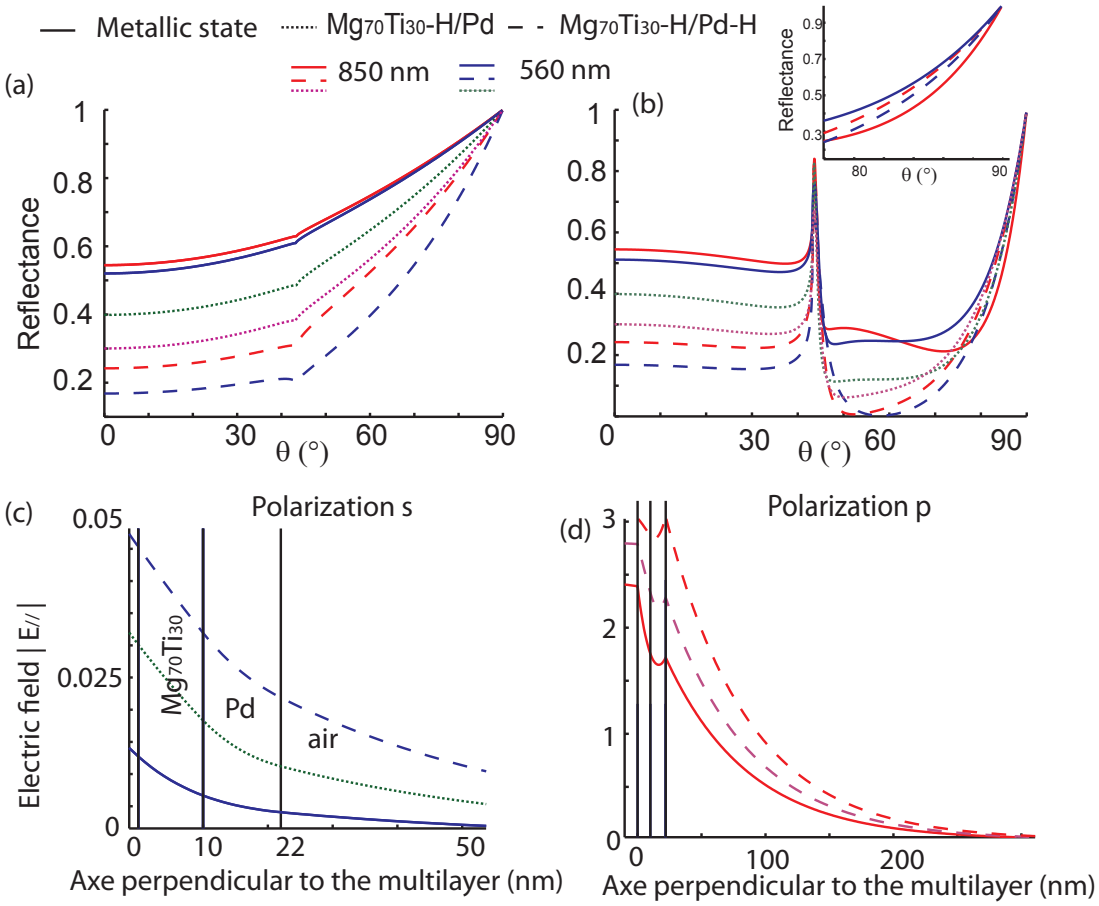


Figure 6.6 – (a-b) Reflectance of a multilayer stack of a 10 nm thick $Mg_{70}Ti_{30}$ layer and a 12 nm thick Pd, deposited onto glass substrate, as a function of the angle $\theta$ (0° corresponds to the normal incidence), for polarization (a) s and (b) p, respectively. (c-d) represent the field distribution ($\theta = 82°$). The Electric field is parallel to the multilayer stack. At the left of the Mg-Ti layer, the field corresponds to the interference between the incident and reflected field. The amplitude fields are not normalized.

and longer wavelengths, respectively. In contrast to chapter 4 where the change is due to a decrease in the imaginary part of the SP (i.e. decrease in the width of the peak), the change is now related to a change in both part of the SP. Future investigations have to be done to understand clearly the mechanism. In fact, we have now a bimetallic layer. The SPR may result from a contribution of each layer : Mg-Ti and Mg-Ti hydride present a SPR peak in the reflectance curve for a three layer system (Prism/Mg-Ti/air).

Finally, the reflectance change is predominant for the polarization s. In the presence of hydrogen, the transmitted intensity of the optical fiber decreases. We expect two dynamical ranges related to the Mg-Ti and Pd pressure composition isotherm, as illustrated in fig. 6.5d.

### 6.2.2 Experimental deposition

We used, for our experiment, a Newport multimode fiber and we removed the optical cladding (heat treatment with chemical bath for cleaning), as described in section 3.3. The sensor response increases as the optically sensitive length L along the fiber increases since the number of reflections increases. As previously, we limited the length of the deposit for practical reasons. The length L is limited here to 0.5 cm ($\pm 0.2$).

We deposit the multilayer stack with the configuration 2, as described in 3.3.2. The deposition results in a uniform thickness and composition. Mg and Ti targets are facing each other and perpendicular to the rotating axis of the optical fiber. By adjusting the power applied to each gun the desired composition is obtained. For instance, for a composition of $Mg_{70}Ti_{30}$, Mg and Ti are respectively sputtered at a rate of 1.06 and 0.345 Å/s using a 67 W RF and 150 W DC power supply. The Pd target is along the same axis of the optical fiber, which results in a slight gradient of thickness. Palladium is sputtered at an average rate of 1.5 Å/s using 100 W DC power supply. The sputter pressure is always set at 3 $\mu$bar Ar.

We study the response of a multilayer stack consisting of a 50 nm thick $Mg_{70}Ti_{30}$ layer and a 25 nm thick Pd layer. A protective layer, made of a sputtered polytetrafluoroethylene (PTFE), is added on the top of the Pd layer. This layer protects the Pd surface of pollutants during the transport and the storage of the sensor in air. The permeability coefficient through PTFE is about 6 times higher for hydrogen than oxygen. We have observed that this layer is necessary to obtain a reproducible and fast kinetic. We think that, in absence of the PTFE layer, oxygen oxidizes the Mg alloys layer in spite of the Pd cap layer (oxygen diffuse into the multilayer through eventual cracks or grain boundary -for thin film). This hypothesis is still under investigation.

### 6.2.3 Result

In this section, we report the performances of the sensor tested between a hydrogen concentration of 0.2 % and 2 % $H_2$ in Ar. In this concentration range, Pd remains in the $\alpha$ phase. Thus, the optical change is mainly caused by the Mg alloy layer.

**Hydrogen response :** In the presence of hydrogen, the transmitted intensity decreases (fig. 6.7) as theoretically predicted. It is interesting to note that the transmitted intensity actually increases first before decreasing. This point will be discussed further in paragraph « Reproducibility ». For all hydrogen concentrations above 0.4%, the signal reaches the same value. This indicates that the metal (Mg-Ti) is always transformed to the $\beta$-phase. At low concentration (below 0.4 % $H_2$ in Ar), the signal of the sensor is not stabilized.

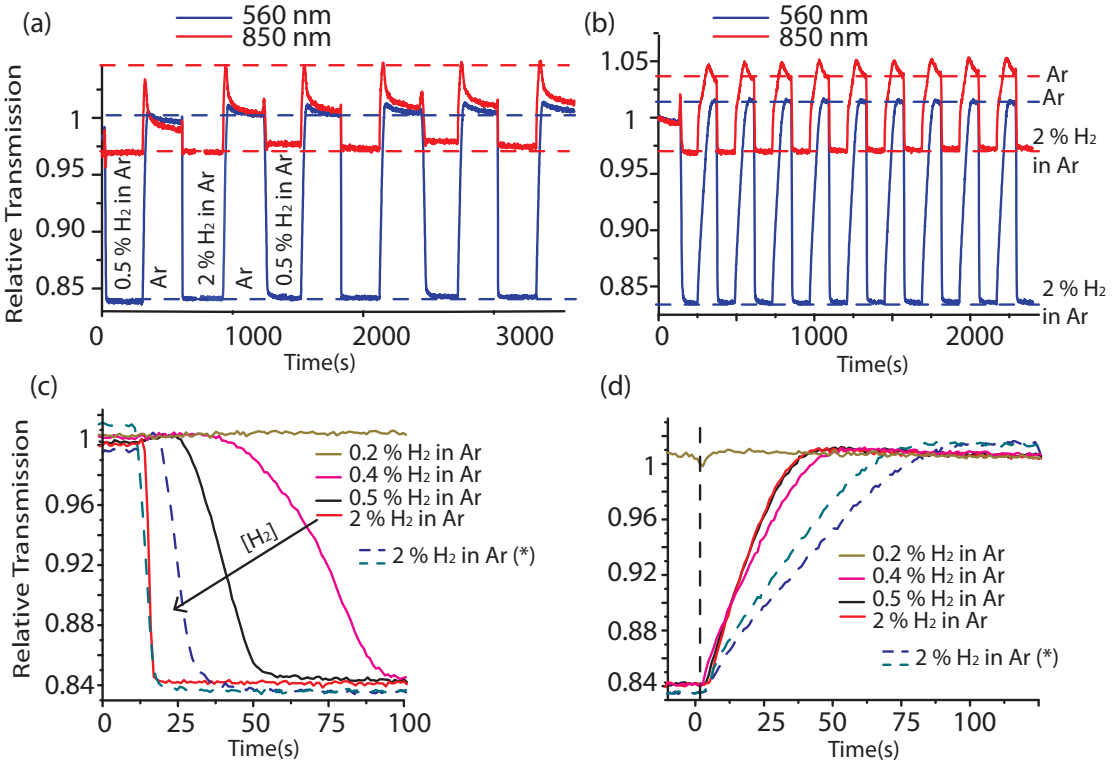


Figure 6.7 – (a-b) Reproducibility of the sensor (based on 50 nm $Mg_{70}Ti_{30}$/ 25 nm Pd) response over cycling and time. (b) The sensor was stored three weeks in air. (c) Response and (d) recovery time for different hydrogen concentration. (*) corresponds to the response of the first cycle (green dash line) and 10 cycles (blue dashline) after three weeks.

The equilibrium is not reached due to kinetic issues [12]. Remarkably, the sensor based on $Mg_{70}Ti30$ does not extend the dynamical range compared to Pd sensor.

The change in transmitted intensity is larger at shorter wavelengths and decreases toward the longer wavelengths (fig. 6.7a-b), in agreement with our simulation, as depicted in fig. 6.5.

**Recovery :** The recovery time is barely hydrogen dependent. It is fast enough (around 30 s) for general purpose applications (fig. 6.7d). However, oxygen is essential for fast dehydrogenation. The recovery time becomes extremely long in a flow of Ar. While Slaman et al. [12] noted that the amount of oxygen for concentrations between 1 to 20 % , is not important, we dehydrogenate our sensor with a gas mixture of 20% $O_2$ in Ar.

**Reproducibility :** To verify the stability and the reversibility of the detection layer, we measure the transmitted intensity for successively ab-desorption cycles. The sequence of cycles is defined by a gas mixture of 0.5% $H_2$ (or 2% $H_2$), followed by desorption in a mixture of 20 % $O_2$ in Ar. The response is reproducible after the first cycle. As previously observed in the case of Pd, the sensing layer needs one cycle to be stabilized and to remove the pollutants on the Pd surface gathered during the device transport and storage. After storing the sample in air for 3 weeks, a small deviation is observed for cycles after the first one.

Furthermore we observe that the recovery time is slower and increases slightly over cycles and time, as previously noted by Borsa et al. [175] . This effect has been related to poisoning of the Pd cap layer and/or intermixing at the interface. In fact, the drift becomes important with the absence of a protective layer. In addition, we observe that the response time is slower after storing. However, repeated cycling clean the surface which result in gradually improving the response time. Figure 6.7 shows the response and the recovery time of the sensor at 2 % in Ar after few cycles (red line), after storing in air (black line) and after storing in air and few cycles (green dash line).

Finally, we observe a small drift over time. After multiple cycles, the change is larger, but can be neglected compared to the relative change. The reproducibility of the response is in agreement with the reported results for Mg-Ti alloys and acceptable for general purpose applications.

Surprisingly, the reproducibility of the signal, especially for the recovery is wavelength dependent. For the first set of cycles (first day), the response shows a bump for the ab- and de-sorption. The bump is predominant for longer wavelengths, as depicted in fig 6.7a for a wavelength of 850 nm (red line). After 3 weeks, the observed bump tends to disappear (fig. 6.7b).

To understand the origin of the bump in the response, we go back on the reflectivity of the multilayer stack. We first notice that the bump cannot be related to changes in the Pd layer since the bump is observed at a concentration of 0.5 %, which is lower than the pressure plateau of Pd. At this concentration, only the MgTi layer is hydrogenated. Hence, the bump comes either from (i) the expansion of the metal hydride or (ii) the surface Plasmon at the Pd air interface (competitive effect of the losses). However, the expansion of the metal hydride does not cause an increase in reflectance in our simulations ( i.e. an increase in the transmitted light in our case). According to our simulation, the reflectance can only increase at long wavelength when only Mg-Ti is formed for the polarization p. This change is related to a modification of the SPR peak. Consequently, we assume that the bump is due to a modification of the SPR peak caused by the presence of H surface

and subsurface sites at the beginning of the Mg-Ti hydride formation.

**Response time :** To investigate the response time of the sensor, we used the same measurement bench as described in chapter 3. The mixed gases arrives in the gas cell (i.e. interact with the sensitive layer) after 7 s. However, the sensor does not immediately respond after this time. The latency time seems to depend slightly on the $H_2$ concentration. Because a mixture of 20 % $O_2$ and Ar is used as a pre-flush gas, oxygen agents decrease significantly the beginning of the response as explained in section 4.3.3.1. Without taking the latency time into account, we observe that the response time is drastically slower with decreasing hydrogen concentration (fig. 6.7c). The response time is in fact too slow to reach the equilibrium at 0.2 % $H_2$. The response times are of the order of the ones observed with the Slaman's sensor, but slightly slower in our case, probably due to the presence of oxygen.

Slaman et al. reported a linear pressure dependence for the hydriding rate. They concluded that the kinetic is limited by the surface reaction. In our case, the hydriding rate seems also linear. However, the surface dissociation can not be the kinetic limited step since the response time, at low concentration, is longer than the one of our Pd sensor with the same range of thickness. In fact, Gremaud et al. [26] emphasized that a linear dependence does not necessarily mean that the hydriding rate is determined by surface properties only , but it may be the association of both processes (bulk and surface). In particular, Pasturel et al. [177] demonstrated that the kinetic for a bi(tri)-layer system for switchable material, simulated with a diffusion model, is strongly correlated to the enthalpy of formation. The proper study of the kinetic is out of the scope of this thesis. We conclude only that the response time depends strongly on the hydrogen concentration, as depicted in fig. 6.7c, and is too slow for safety application (acceptable for stationary system).

**Cross-sensitivity** Due to the use of Pd, the sensors suffer of a cross-sensitivity. Slaman et al. reported that oxygen slows down the response of the detector. In our case the oxygen pollutants can even lead to cancel the drop in intensity, and will give then false alarms. The protective layer does not stop the cross-oxygen sensitivity. To overcome the cross sensitivity, Pd alloys can be used as explained in section 1.4.4.

In conclusion, most of our results are in agreement with formerly reported results on $Mg_{70}Ti_{30}$ films.(i) The film is stable over ab-desorption cycles and time. (ii)The detection layer shows a large optical contrast which decrease drastically losses in the optical fiber. (ii) The response time is strongly depending on the hydrogen concentration.

We conclude that Mg alloys can be employed with an intrinsic fiber sensor configuration. In contrast to reproducible Pd film (i.e. around 10 nm), Mg alloys provide a considerable large optical change. In particular, the length of the sensitive layer can be smaller than for Pd coated sensors (the length is here 0.5 cm compared to 2 cm in chapter 4.5.2). However, the response time does not fulfill the automotive industry requirement (inferior to 1, or 3 s). In addition, due to the kinetic issue, the dynamical range is not improved compared to Pd thin film, which contradicts our working hypothesis, unfortunately.

## 6.3 $Mg_{60}Ti_{40}$ film

Gremaud et al. [26] demonstrated that the speeds of hydrogen absorption and desorption are strongly dependent on the metal ratio in the initial alloy. In particular, increasing the Ti content improves the kinetic. We have decided to study a $Mg_{60}Ti_{40}$ alloys in order

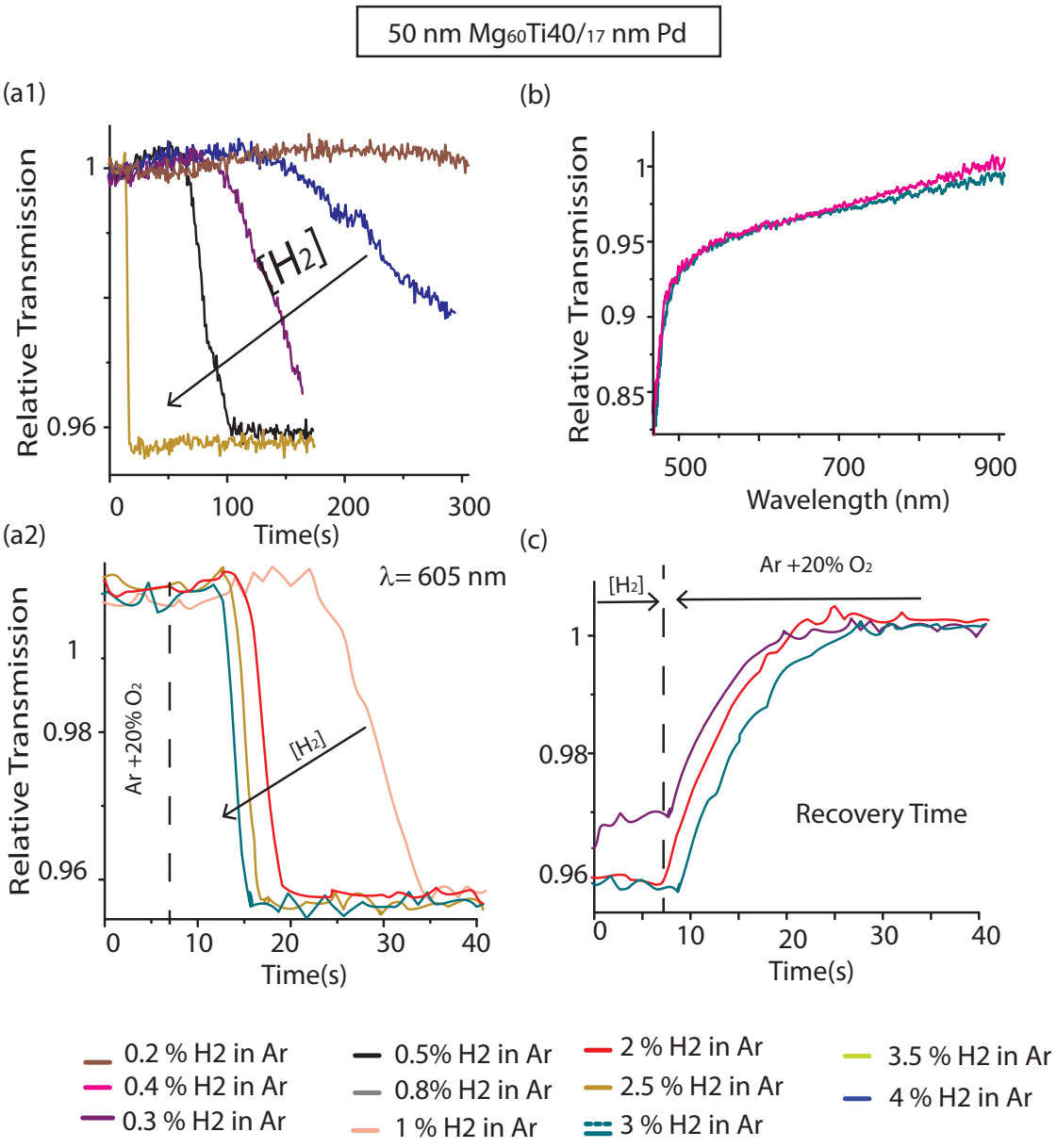


Figure 6.8 – Response of the sensor for a multilayer stack consisting of 50 nm $Mg_{60}Ti_{40}$/ 17 nm Pd (a1-2) Response time of the sensor at a wavelength of 605 nm. (b) Relative transmission as a function of the wavelength for different hydrogen concentrations : Pressure-composition isotherm. (c) Recovery time of the sensor at a wavelength of 605 nm.

to try to obtain a fast hydrogen sensor.

The sensors are realized in the same condition as previously. The length of the deposit is now 1 cm. for a composition of $Mg_{70}Ti_{40}$, Mg and Ti are respectively sputtered at a rate of 1.06 and 0.345 Å/s by using 67 W RF and 150 W DC power supply. The sensor is tested between 0.2 % and 4 % $H_2$ in Ar. In this range of concentration, Mg alloy hydride and Pd hydride is formed.

**Hydrogen response :** In the presence of hydrogen, the transmitted intensity decreases due to the hydride formation. As predicted, the change in intensity is maximal at short wavelength and increases toward longer wavelengths.

Figure 6.8 plots the relative transmission of the sensor as a function of time at a wavelength of 605 nm. For all $H_2$ concentrations above 0.4 %, the transmitted intensity reaches the same final value as previously. This indicates that the metal (Mg-Ti) is always transforms to the $\beta$-phase. Our range of concentration used are indeed above the phase transition of the $Mg_{60}Ti_{40}$ (below 0.1 %) as depicted in fig. 6.2 (black symbols). The absence of differences between 0.4 % and 3 % $H_2$ in Ar indicates that optical change is caused by the Mg-Ti hydride formation since the Pd hydride is formed above 2% $H_2$ in Ar.

At longer wavelength, the Pd hydride formation affects the response. A small deviation is observed between a concentration of 0.4 % and 3 % $H_2$ in Ar as shwon in fig. 6.8b. The transmitted intensity decreases again with the Pd hydride formation.

In comparison with the simulated response, the experimental one shows a smaller change upon hydrogenation. It is explained by a wrong dielectric permittivity. The dielectric permittivity used in our simulation derived from the $Mg_{30}Ti_{70}$ films . $Mg_{60}Ti_{40}$ show actually a smaller optical change, as depicted in fig. 6.2 (black symbols). In addition, a non predicted large change is obtained below 500 nm.

In spite of a wrong dielectric permittivity, the simulated results are in good agreement with our simulations. The transmitted intensity decreases upon hydrogenation and the maximum change is obtained at short wavelength. The Pd hydride formation is predominant at longer wavelengths than shorter wavelengths.

**Reproducibility :** The film is stable over ab-desorption cycles and time. We observe the same behavior than for $Mg_{70}Ti_{30}$ film, described in section 6.2.3.

**Response time :** Our first motivation for increasing the Ti content was to improve the response time. However, we observe that the response time (fig. 6.8a) is in the same order of time than the sensor based on $Mg_{70}Ti30$. The response is even slightly slower than with the previous composition. However, we cannot make any relevant remark concerning the difference in the kinetic. The measurements were, in fact, carried out for different conditions and cycles. The response time is still too slow for our concerns.

## 6.4 Thinner film

We propose to study the response of a thin Mg-Ti film in order to (i) combine later this detection layer to our SPR sensor based on wavelength modulation and at the same time,(ii) we expect to improve the response time.

### 6.4.1 10 nm $Mg_{60}Ti_{40}$/ 12 nm Pd

In this section, we present the response of a 10 nm $Mg_{60}Ti_{40}$/ 12 nm Pd deposited on the core of a multimode fiber. According to our simulation, we expect that the sensor responses equally to the optical change of the Mg-Ti and Pd hydride upon hydrogenation. The sensor is tested between 0.2 % and 4 % $H_2$ in Ar to form the Mg alloy hydride and Pd hydride.

**Hydrogen response :** Adding $H_2$ in Ar decreases the transmitted intensity. A continuous change in transmitted intensity is observed as a function of the hydrogen concentration between 0.2 - 4 % $H_2$ in Ar, as shown in fig. 6.9a. In addition, the sensor response shows a surprisingly wavelength dependence (fig. 6.9b). An optimal change is obtained for wavelengths around 650 nm. We experimentally studied the sensor at a wavelength of 605 nm in order to compare with our results with thicker films of same composition.

Figure 6.11 plots the sensor sensitivity as a function of the hydrogen concentration on a semi-logarithm scale in order to point out the pressure composition of the multilayer. We observe three ranges :

- between 0.2-2% : the transmitted intensity changes slightly as a function of hydrogen,
- between 2-2.5% : a large optical change is observed at an almost constant hydrogen concentration,
- between 2.5-4% $H_2$ : the transmitted intensity changes slightly as a function of hydrogen, and tends to saturate above 3.5%.

To discuss the dynamical range presented by thin Mg-Ti film, we report on the same graph the hydrogen sensitivity previously obtained for thick $Mg_{60}Ti40$ (red line). We extrapolated from the expected response at lower concentration (dash line). In contrast to thicker film, the thin Mg-Ti hydride seems to be not formed for concentration below 2 % $H_2$. The phase transition is observed at 2 %, which correspond to the formation of the Pd hydride. The sensor can quantify the hydrogen concentration due to this higher pressure plateau. Nevertheless, the dynamical range seems similar to the Pd. Contrary to our simulation, we do not observe the two expected large optical changes corresponding to the Mg-Ti hydride and Pd hydride formation, as illustrated in fig. 6.5d.

**Reproducibility :** The film is stable over ab-desorption cycles and time after three cycles, as shown in fig. 6.10. We observe the same behavior as for the previous Mg alloy films. However, the increase in the transmitted intensity over cycling and time seem larger. Further investigation has to be done to study the stability of the multilayer.

**Response time :** The response time is hydrogen dependent. For concentration above 2 % $H_2$ in Ar, the response time is in the order of 30 s. The response decreases first linearly, and then gradually decreases. Note that the second behavior was not observed for thicker film. As previously, a small bump can be observed at the beginning. The response is slower at low hydrogen concentration. Below 0.8 % $H_2$ in Ar, the response time is inferior to 100 s. In spite of the different behavior in the kinetic, the response time is still too slow for hydrogen safety applications.

Remarkably, the experimental response of the sensor does not match with the predicted results : a new dynamical range, a new kinetic and a new wavelength behavior is observed. It can be explained either by (i) a wrong dielectric permittivity, (ii) the protective layer or

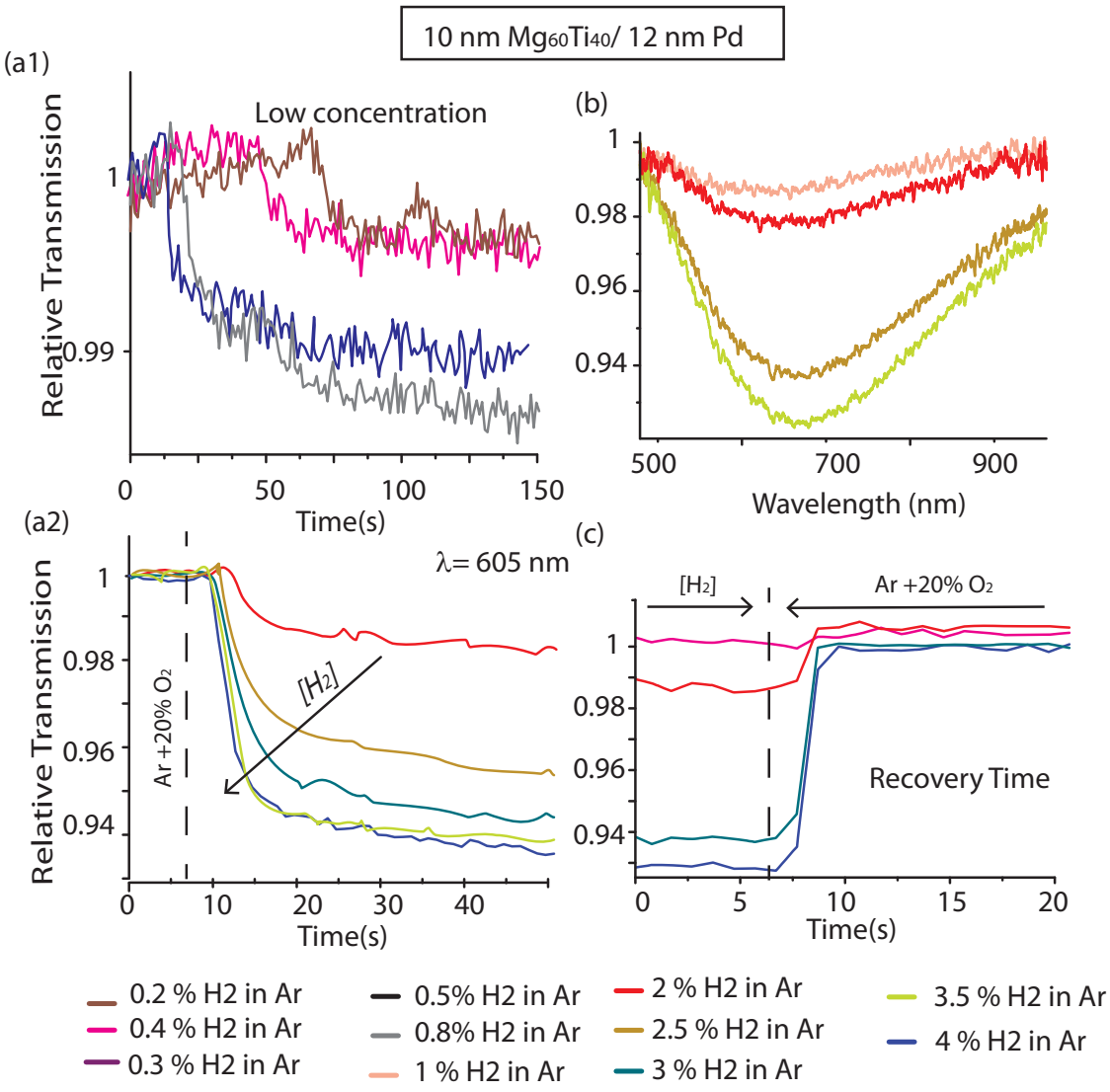


FIGURE 6.9 – Response of the sensor for a multilayer stack consisting of 10 nm $Mg_{60}Ti_{40}$/ 12 nm Pd. (a1-2) Response time of the sensor at a wavelength of 605 nm. (b) Relative transmission as a function of the wavelength for different hydrogen concentrations : Pressure-composition isotherm. (c) Recovery time of the sensor at a wavelength of 605 nm.

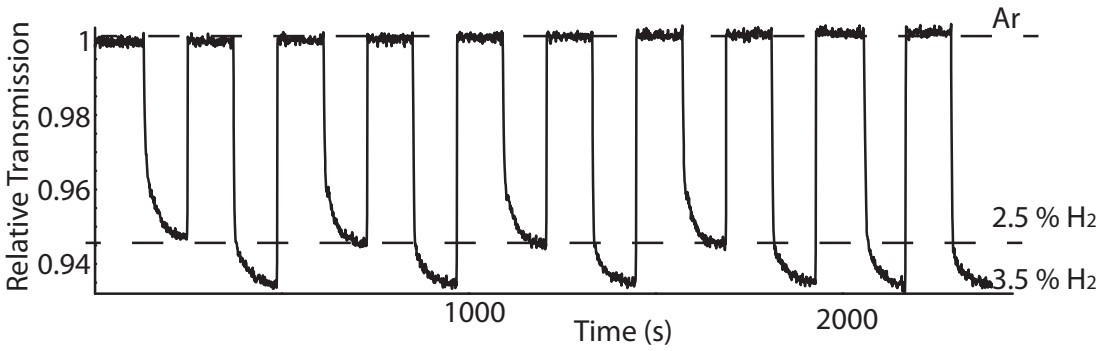


Figure 6.10 – Reproducibility of the sensor (based on 10 nm $Mg_{60}Ti_{40}$/ 12 nm Pd) response over cycling and time. The absorption is done successively with 2.5% and 3.5% $H_2$. desorption in done with a mixture of 20% $O_2$ in Ar

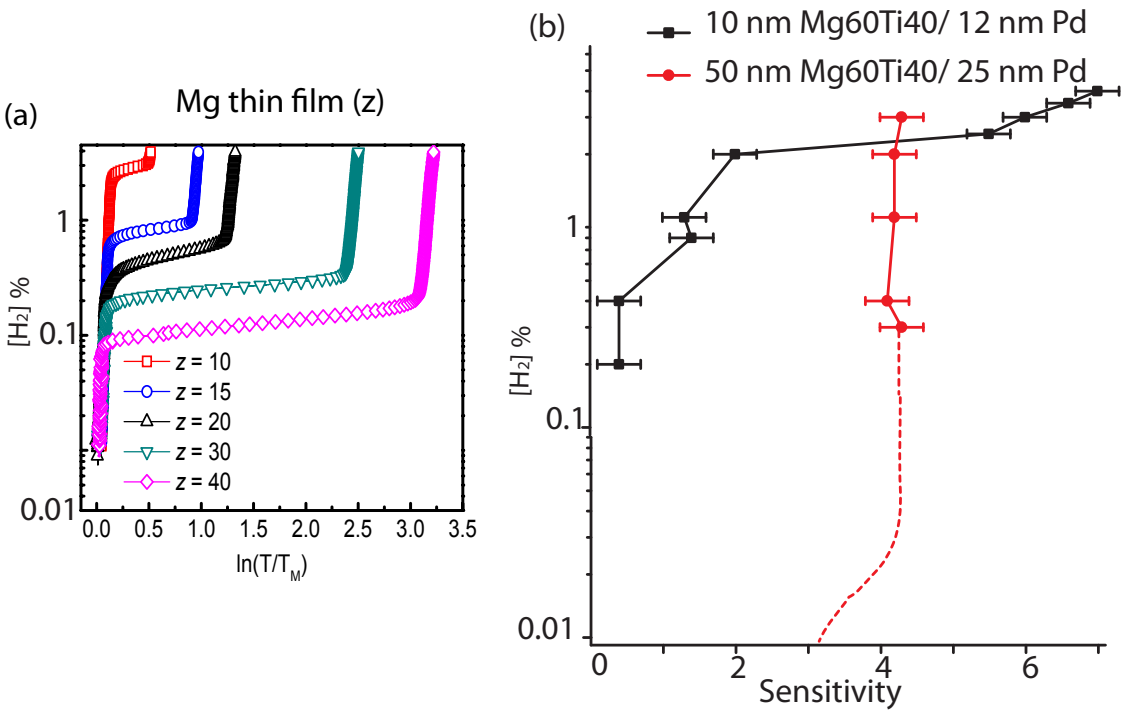


Figure 6.11 – (a) Pressure-optical-Transmissions measured by hydrogenography at 333 k for Ti(10nm)/Mg(z nm)/Pd(40 nm) thin films, with z varying from 10 to 40 nm. [176] (b) The sensitivity of the sensor based on $Mg_{60}Ti_{40}$ for various multilayers as a function of the hydrogen concentration

(iii) a structure effect on the Mg-Ti thin film.

Wrong dielectric permittivity : As previously seen, the simulations are relatively satisfying to predict the experimental response of $Mg_{60}Ti_{40}$/ 12 nm Pd though the dielectric permittivity used is different. The discrepancy in the wavelength dependence can barely come from that.

Protective layer : In our simulation, we did not take into account the presence of a cap layer on the top of the multilayer stack. This layer, which can be neglected in relatively thick Mg-Ti, becomes important for thin films. At this stage, we do not have the dielectric permittivity of this layer to conclude on its real effect on the wavelength behavior of the sensor. Nevertheless, this layer does not explain the observed kinetics and thermodynamics.

Structure effect : It is known that when the metal hydride film is reduced to the nanoscale, the thermodynamics of hydrogen ab- (de-)sorption can be different from the bulk film. For example, we have seen in chapter 1 that the pressure composition isotherms of Pd thin films are altered by the nature of the substrate. In the sense that the level and the width of the pressure plateau are slightly different than bulk film. The surface or interface energies have to be considered for studying metal hydride thin film. The thickness dependence of Mg thin film on the pressure composition isotherms is a perfect example. Assuming a Mg film covered with Mg-alloy-forming film (such as Mg/Pd), Baldi et al. [176] showed that the thermodynamics of the system could be tailored by changing the thickness of the Mg film. He observed that the equilibrium pressure plateau is at higher pressures for thinner film. This effect is explained by means of elastic constraints, in the sense that the pressure composition isotherms depend on the clamping exerted by the Pd layer. The change in clamping is due to the formation of an intermetallic alloy at the Mg Pd interface.

By extending this result of Mg alloys, we assume that the phase transition occurs at higher hydrogen concentration by decreasing the thickness of the Mg-Ti alloy. Finally, the phase transition observed corresponds likely to the Mg-Ti hydride and Pd hydride formation. Valerio et al. [178] confirmed that the pressure composition isotherms of Mg alloys can be tailored by changing the thickness of the Mg alloy films. Current researches are under investigation on the understanding of this effect. Furthermore, the « clamping/alloying »could also result in changing the optical constant of the Mg alloy film.

In conclusion, the dynamical range of the sensor is explained by the clamping effect. While the wavelength behavior is explained either by the effect of the protective layer or/and by the clamping effect, which causes new optical changes.

### 6.4.2 SPR sensor based on wavelength modulation

One purpose of this chapter was to improve the dynamic range of our proposed SPR sensor by replacing the Pd layer by Mg alloys. To avoid the extinction of the SPR in our configuration, the sensitive layer has to be as thin as possible. Therefore, our working hypothesis was to realize a sensor based on Mg-Ti thin film. Our multilayer consisted of 35 nm Au/ 100 nm $SiO_2$/ 10 nm $Mg_{70}Ti30$ / 5 nm Pd. A protective layer was also added on the top of the Pd layer as explained in section 6.2.2.

Unfortunately, we have found that thin Mg alloys film seems to exhibit new optical changes, with new thermodynamics properties. In addition, these changes seem to be opposed to the benefit of Mg alloys film for hydrogen sensing. In fact, the dynamical range

is similar to the sensor based on Pd as sensitive layer and the optical change seems to decrease compared to thicker films. This observation attempts to explain the response of our sensor. With thin Mg-Ti film, the SPR peak shifts only of 1 nm upon hydrogenation, whereas the simulated SPR peak shifts to 100 nm. Further investigation on the optical change shown by thin metal hydride would allow us to optimize the performance of the propose sensor.

Another alternative to thin films for improving the dynamic range of the sensor will be using metal hydride nanoparticles such as Mg/Pd, for instance.

## Conclusion

In conclusion, we have demonstrated that an intrinsic optical fiber sensor based on Mg alloys can be realized. In contrast to the micro-mirror sensor, multi-point sensing can be achieved. The sensor consists of a thin-film Mg-alloy layer, covered by a Pd layer deposited on the core of an optical fiber. The transmitted intensity decreases as function of hydrogen concentration. The optical change and dynamical range of the sensor depend on the thickness of the Mg alloys.

However, we did not succeed in improving the dynamical range of the sensor compared to Pd (in the time range considered). For concentrations below the detectable range by the Pd, the response time is too slow for hydrogen sensing in safety application. Mg-Ti remains interesting in stationary system for monitoring hydrogen concentration.

Improving the catalytic properties of the Pd or increasing the Pd surface area may be a solution to enhance the response time of sensors based on Mg alloys.

# Conclusion

In this thesis, we have studied the hydrogen detection by means of intrinsic optical fiber sensors. New hydrogen sensors have been proposed, realized and characterized. We have successfully demonstrated that it is possible to obtain a fast response and reproducible intrinsic optical fiber sensor based on Surface Plasmon Resonance.

The first sensor, based on intensity modulation, consists of a Pd layer deposited on a section of a multimode fiber core, after removing the optical cladding. By measuring the transmitted intensity after the sensitive section, we detect the hydrogen concentration. The originality of our work is to illuminate and measure all the guided modes of the fiber, in order to make the sensor easily embeddable and adaptable for industry applications. The sensor shows an interesting wavelength dependent response. The simultaneous monitoring of several different wavelengths results in avoiding false hydrogen detection alarms.

The second sensor consists of a multilayer stack of Au, $SiO_2$ and Pd layer deposited on a section of a multimode fiber core, after removing the optical cladding. This new design is suitable for tailored the resonance condition. A plasmonic resonance has been successfully observed in the transmitted intensity. Thus, the sensor can be based on intensity or wavelength modulation. In contrast to current hydrogen sensors based on wavelength modulation, our sensor shows a fast response due to the use of very Pd thin films (likely discontinuous films). Optical fiber sensors based on discontinuous films would provide a fast response comparable to electric sensors.

The sensors that we propose are able to detect and quantify hydrogen concentration in a range of 0.5% to 4%. The minimal detection is mainly limited by the intensity fluctuation, while the maximal detection is limited by the $\beta$-phase of the Pd hydride. In order to improve the dynamical range, Mg alloys as sensitive material could be used in intrinsic optical fiber sensor configuration. However, we found that the response time is too slow for the applications considered in this thesis. Further investigation has to be done to decrease the hydrogenation kinetic of Mg alloy materials. One solution will be to enhance the catalytic propetries of Pd.

The proposed hydrogen sensor could be adapted for industrial applications. However, in this perspective some enhancements have to be done. There are four majors aspects to develop for industrialization. Research has to focus on the development of a protective layer to ensure stability and robustness of the sensor. The protective layer could be also used to decrease the loss induced by the Pd. Due to the fragility of bare fiber, it is also necessary to develop encapsulation techniques to employ the sensor in extreme condition. In addition, research has to be done on the Pd alloy cross-sensitivity to decrease the eventual false alarms due to the presence of pollutants. Lastly, the optical fiber sensors have to be calibrated to the exterior constraints such as temperature fluctuation.

Finally, the results obtained in this thesis show that SPR sensors are suitable for industrial hydrogen sensing. In this perspective, several directions can be taken in order to improve the performance of the sensors. It will be interesting to study new structures such as optical fibers based on Long-range Surface Plasmon or based on single mode fiber. SPR based on nanostructured hydrogen sensitive may be another direction. The post-processing was out of the scope of this thesis, but it could improve the final performance of the realized sensors.

# Annexe A

# Hydrogen sensors

An impressive number of hydrogen sensors have already been proposed in the literature. We describe here the principle of common hydrogen sensors.

## A.1 Principle

### A.1.1 Catalytic sensors

Catalytic sensors measure the heat released from the gas combustion. Two configurations are used : the pellistor and thermoelectric sensor.

A pellistor sensor consists of heating a filament covered by a catalytic material such as Pd or Pt embedded in a ceramic bead. The device is electrically heated at a temperature above 300 °C, typically. The filament acts as a resistance thermometer. During the exothermic reaction of the combustion, the temperature of the filament is altered, which results in changing its resistance. Typically, two filaments are mounted in the Wheastone bridge circuit, whose one is inactive. The differential resistance between the two filaments is then correlated to the hydrogen concentration. The inactive filament is used as a reference to compensate the environmental parameter such as the temperature or the humidity, for instance.

For thermoelectric sensors, the change in the resistance of the filament is induced by the thermoelectric effect. The thermoelectric effect arises when there is a temperature difference between two points of a (semi-)conductor. In the active area, the temperature of the active sensor increases due to the oxidation of hydrogen. The temperature difference between the active and reference filament results in a differential resistance between them. In contrast to pellistor sensor, the device has to be heated.

### A.1.2 Thermal sensors

Thermal sensors are based on the difference of the thermal conductivity of gas. The change in the resistance of the filament is not induced by the catalyzed exothermic oxidation reaction of hydrogen. The two filament are heated at a constant temperature. With the difference of heat loss between the two elements, we can detect the presence of gases in the active area.

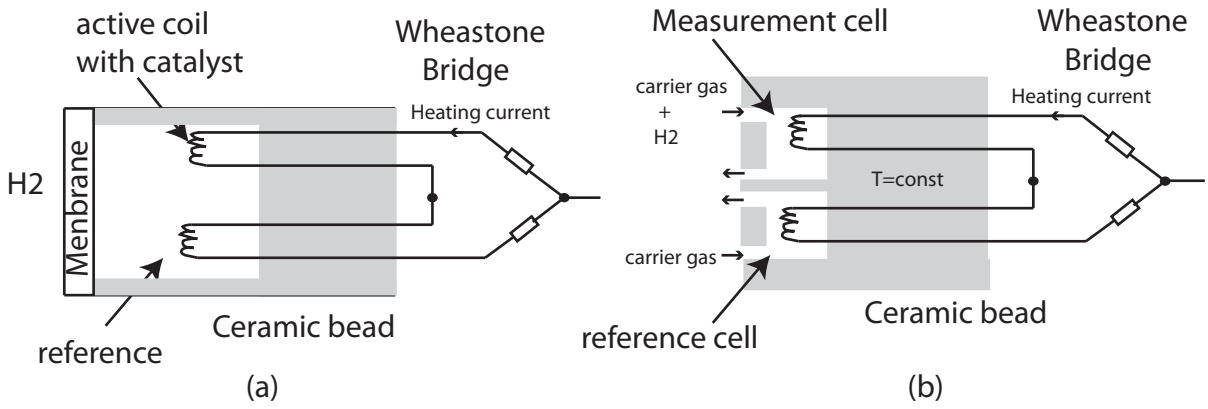


Figure A.1 – Schematic of (a) pellistor sensor and thermal conductivity sensor connected in a Wheaston bridge circuit.

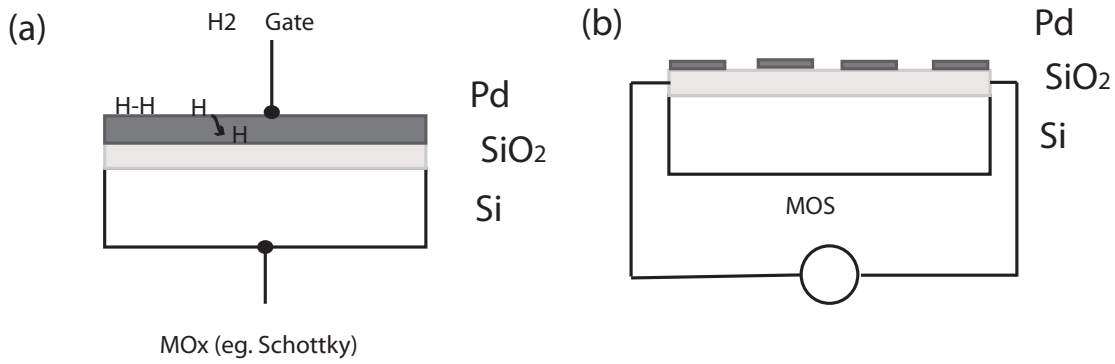


Figure A.2 – Schematic of (a) a Mox and (b) MOS sensor

### A.1.3 Electrochemical sensor

A typical electrochemical sensor consists of a sensing electrode (or working electrode), and a counter electrode separated by a thin layer of electrolyte. This sensing approach is based on the difference in the oxidation rate of hydrogen on the different electrode materials. The amount of electrons due to the hydrogen oxidation is directly proportional to the concentration of hydrogen. The device function is either in amperometric or potentiometric mode.

### A.1.4 Resistance based

We can distinguish : the metallic and Metal oxide resistor.

Metallic resistor : The device consists of measuring the conductivity change of a metal (hydride). During the hydrogenation reaction, the electrical properties of the metal are altered. Pd is preferably used due to its high selectivity.

Mox : The electrical properties of metal oxides change when they are exposed to re-

ducing gas. To promote the reduction, the film is heated to high temperature (Typically between 180 to 450°C, depending on the material used).

### A.1.5 Work function based sensors

Metal Oxide Semiconductor (MOS) sensors consist of a metal, an oxide and semiconductor layer. In the presence of hydrogen, the catalytic metal dissociate the hydrogen molecule. Hydrogen atoms diffuse through the metal and absorb at the metal oxide interface. The presence of Hydrogen sites at the interface give rising to a dipole , which results in changing the work function. Since the hydrogen concentrations at the air metal interface and at the metal oxide interface are in equilibrium, the change of the work allow to measure the hydrogen concentration.

The three major configurations are the Schotkky diode, MOS capacitor and the MOS field effect transistor (MOSFET).

## A.2 Performances

| | Catalytic | Termoelectric | MOS | Metallic resistor | MOx | Optical | Electrochemical | Targets |
|---|---|---|---|---|---|---|---|---|
| Sensitivity | / | X | / | X | X | X | / | 0.1-10% H2 in air |
| Temperature range | / | / | X | X | / | X | / | -30-80 °C |
| Response time | | | | / | X | | | < 1s |
| Accuracy | X | X | / | X | / | X | | 5% |
| Lifetime | X | X | X | | X | | | 5 years |
| cross-sensitivity | X | X | X | X | X | / | / | Humidity range: 10-98% |

Figure A.3 – Comparison of the performances of existing hydrogen sensors with the requirements of the US departmental of energy specification. X means the sensor meets the requirements. / means the sensor meets partially the requirement. Empty box means the sensor fails the requirements.

We compare the performances of each type of sensors with the requirement. Note that one sensor may be different than the typical response observed in this category. We observe that all sensors are more or less close to the requirement for the sensitivity, the range of temperature and the lifetime. However, the response time of the sensors are often too slow compared to the specifications. Only MOS and metallic resistor based on discontinuous film show fast response time.

# Bibliographie


[1] L.C. Cadwallader, J.S. Herring, Idaho National Engineering, and Environmental Laboratory. *Safety issues with hydrogen as a vehicle fuel.* Idaho National Engineering and Environmental Laboratory, 1999.

[2] H. Beeson and S. Woods. Guide for hydrogen hazards analysis on components and systems. Technical report, NASA report TM-2003-212059, Texas, 2003.

[3] U. Bossel. Does a hydrogen economy make sense ? *Proceedings of the IEEE*, 94(10) :1826–1837, 2006.

[4] T. Hubert, L. Boon-Brett, G. Black, and U. Banach. Hydrogen sensors - a review. *Sensors and Actuators B : Chemical*, 157(2) :329–352, 2011.

[5] A.A. Kazemi, D.B. Larson, and M.D. Wuestling. Fiber optic hydrogen detection system. In *Proceedings of SPIE*, volume 3860, page 507, 1999.

[6] L. Boon-Brett, J. Bousek, G. Black, P. Moretto, P. Castello, T. Hubert, and U. Banach. Identifying performance gaps in hydrogen safety sensor technology for automotive and stationary applications. *International Journal of Hydrogen Energy*, 35(1) :373–384, 2010.

[7] J.T. Ringland et al. *Safety issues for hydrogen-powered vehicles.* Sandia National Laboratories, 1994.

[8] C. Yeh. Optical waveguide theory. *Circuits and Systems, IEEE Transactions on*, 26(12) :1011–1019, 1979.

[9] A.W. Snyder and J.D. Love. *Optical waveguide theory*, volume 190. Springer, 1983.

[10] R. Paschotta. Optical fiber technology. *Optik & Photonik*, June No. 2 :52, 2008.

[11] FA Lewis. Hydrogen in palladium and palladium alloys. *International Journal of Hydrogen Energy*, 21(6) :461–464, 1996.

[12] M. Slaman, B. Dam, M. Pasturel, D.M. Borsa, H. Schreuders, J.H. Rector, and R. Griessen. Fiber optic hydrogen detectors containing mg-based metal hydrides. *Sensors and Actuators B : Chemical*, 123(1) :538–545, April 2007.

[13] M. Slaman, B. Dam, H. Schreuders, and R. Griessen. Optimization of mg-based fiber optic hydrogen detectors by alloying the catalyst. *International Journal of Hydrogen Energy*, 33(3) :1084–1089, February 2008.

[14] D.K. Benson, C.E. Tracy, G.A. Hishmeh, P.E. Ciszek, S.H. Lee, and DP Haberman. Low-cost, fiber optic hydrogen gas detector using guided wave, surface plasmon resonance in chemochromic thin films. In *Proc. SPIE International Symposium on Industrial and Environmental Monitors and Biosensors*, pages 185–202, 1998.

[15] S. Sekimoto, H. Nakagawa, S. Okazaki, K. Fukuda, S. Asakura, T. Shigemori, and S. Takahashi. A fiber-optic evanescent-wave hydrogen gas sensor using palladium-supported tungsten oxide. *Sensors and Actuators B : Chemical*, 66(1-3) :142–145, 2000.

[16] S. Okazaki, H. Nakagawa, S. Asakura, Y. Tomiuchi, N. Tsuji, H. Murayama, and M. Washiya. Sensing characteristics of an optical fiber sensor for hydrogen leak. *Sensors and Actuators B : Chemical*, 93(1-3) :142–147, 2003.

[17] P. Liu, S.H. Lee, H.M. Cheong, CE Tracy, and JR Pitts. Stable pdv2o5 optical h2 sensor. *Journal of the Electrochemical Society*, 149(3) :H76–H80, 2002.

[18] E. Wicke, H. Brodowsky, and H. Z
"uchner. Hydrogen in palladium and palladium alloys. *Hydrogen in Metals II*, pages 73–155, 1978.

[19] C. Nutzenadel, A. Zuttel, D. Chartouni, G. Schmid, and L. Schlapbach. Critical size and surface effect of the hydrogen interaction of palladium clusters. *The European Physical Journal D-Atomic, Molecular, Optical and Plasma Physics*, 8(2) :245–250, 2000.

[20] C. Sachs, A. Pundt, R. Kirchheim, M. Winter, M. T. Reetz, and D. Fritsch. Solubility of hydrogen in single-sized palladium clusters. *Physical Review B*, 64(7) :075408, 2001. PRB.

[21] Ming Lee, x, Way, and R. Glosser. Pressure concentration isotherms of thin films of the palladium, hydrogen system as modified by film thickness, hydrogen cycling, and stress. *Journal of Applied Physics*, 57(12) :5236–5239, 1985.

[22] L.J. Gillespie and L.S. Galstaun. The palladium-hydrogen equilibrium and new palladium hydrides1. *Journal of the American Chemical Society*, 58(12) :2565–2573, 1936.

[23] Y. Fukai. *The metal-hydrogen system : basic bulk properties*, volume 21. Springer Verlag, 2005.

[24] A. Züttel. Materials for hydrogen storage. *Materials today*, 6(9) :24–33, 2003.

[25] T.B. Flanagan Clewley and J.D. Hysteresis in metal hydrides. *J. Less-Common Metals*, 83(127.), 1982.

[26] R.F.A. Gremaud. *Hydrogenography : a thin film optical combinatorial study of hydrogen storage materials*. PhD thesis, Vrije universiteit, 2008.

[27] Y. Pivak, H. Schreuders, M. Slaman, R. Griessen, and B. Dam. Thermodynamics, stress release and hysteresis behavior in highly adhesive pdh films. *Internation Journal of Hydrogen Energy*, 36(6) :4056, 2011.

[28] A. Pundt and R. Kirchheim. Hydrogen in metals : microstructural aspects. *Annual Review of Materials Research*, 36 :555–608, 2006.

[29] F. Favier, E.C. Walter, M.P. Zach, T. Benter, and R.M. Penner. Hydrogen sensors and switches from electrodeposited palladium mesowire arrays. *Science*, 293(5538) :2227, 2001.

[30] E. Maciak and Z. Opilski. Transition metal oxides covered pd film for optical h2 gas detection. *Thin Solid Films*, 515(23) :8351–8355, 2007.

[31] M. A. Butler. Optical fiber hydrogen sensor. *Applied Physics Letters*, 45(10) :1007–1009, 1984.

[32] M. A. Butler and D. S. Ginley. Hydrogen sensing with palladium-coated optical fibers. *Journal of Applied Physics*, 64(7) :3706–3712, 1988.

[33] W.M. Mueller, J.P. Blackledge, and G.G. Libowitz. Metal hydrides. Technical report, 1968, 1968.

[34] R. Hughes and J. Jarzynski. Static pressure sensitivity amplification in interferometric fiber-optic hydrophones. *Applied Optics*, 19(1) :98–107, 1980.

[35] F. Farahi, P.A. Leilabady, JDC Jones, and DA Jackson. Interferometric fibre-optic hydrogen sensor. *Journal of Physics E : Scientific Instruments*, 20 :432, 1987.

[36] D. A. Jackson, R. Priest, A. Dandridge, and A. B. Tveten. Elimination of drift in a single-mode optical fiber interferometer using a piezoelectrically stretched coiled fiber. *Applied Optics*, 19(17) :2926–2929, Sep 1980.

[37] J. S. Zeakes, K. A. Murphy, A. Elshabini-Riad, and R. O. Claus. Modified extrinsic fabry-perot interferometric hydrogen gas sensor. In *Lasers and Electro-Optics Society Annual Meeting LEOS'94, Conference Proceedings IEEE*, volume 2, pages 235–236. IEEE, 1994.

[38] D. Iannuzzi, S. Deladi, M. Slaman, J.H. Rector, H. Schreuders, and M.C. Elwenspoek. A fiber-top cantilever for hydrogen detection. *Sensors and Actuators B-Chemical*, 121(2) :706–708, February 2007.

[39] Y.H. Kim, M.J. Kim, M.S. Park, J.H. Jang, B.H. Lee, and K.T. Kim. Hydrogen sensor based on a palladium-coated long period fiber grating pair. *Journal of the Optical Society of Korea*, 12(4) :221–225, 2008.

[40] Raymond E. Dessy and Eric W. Richmond. Birefringent single-arm fiber optic enthalpimeter for catalytic reaction monitoring. *Analytical Chemistry*, 64(13) :1379–1382, 1992.

[41] M. A Butler. Fiber optic sensor for hydrogen concentrations near the explosive limit. *Journal of the Electrochemical Society*, 138(9) :L46–L47, September 1991.

[42] M. A. Butler. Micromirror optical-fiber hydrogen sensor. *Sensors and Actuators B-Chemical*, 22(2) :155–163, November 1994.

[43] M. A. Butler and R. J. Buss. Kinetics of the micromirror chemical sensor. *Sensors and Actuators B : Chemical*, 11(1-3) :161–166, March 1993.

[44] X. Bevenot, A. Trouillet, C. Veillas, H. Gagnaire, and M. Clement. Hydrogen leak detection using an optical fibre sensor for aerospace applications. *Sensors and Actuators B : Chemical*, 67(1-2) :57–67, August 2000.

[45] X. Bevenot. *Etude de la faisabilite et realisation d'un capteur d'hydrogene a fibres optiques pour des applications aerospatiales.* PhD thesis, Universite Jean Monnet de Saint-etienne, 1998.

[46] M. Armgarth and C. Nylander. Blister formation in pd gate mis hydrogen sensors. *Electron Device Letters, IEEE*, 3(12) :384–386, 1982.

[47] A.A. Kazemi, K. Goswami, E.A. Mendoza, L.U. Kempen, and R.A. Lieberman. Fiber optic hydrogen sensor leak detection system for launch vehicle applications. In *Proceedings of SPIE 6379, 63790D*, 2006.

[48] J.A. Garcia and A. Mandelis. Study of the thin-film palladium/hydrogen system by an optical transmittance method. *Review of scientific instruments*, 67(11) :3981–3983, 1996.

[49] G.A. Frazier and R. Glosser. Characterization of thin films of the palladium-hydrogen system. *Journal of the Less Common Metals*, 74(1) :89–96, 1980.

[50] K. Kalli, A. Othonos, and C. Christofides. Characterization of reflectivity inversion, a-and b-phase transitions and nanostructure formation in hydrogen activated thin pd films on silicon based substrates. *Journal of Applied Physics*, 91(6) :3829–3840, 2002.

[51] R. J. Matelon, J. I. Avila, U. G. Volkmann, A. L. Cabrera, Erie H. Morales, and D. Lederman. Substrate effect on the optical response of thin palladium films exposed to hydrogen gas. *Thin Solid Films*, 516(21) :7797–7801, 2008.

[52] A. Borgschulte, R. Gremaud, S. De Man, RJ Westerwaal, JH Rector, B. Dam, and R. Griessen. High-throughput concept for tailoring switchable mirrors. *Applied Surface Science*, 253(3) :1417–1423, 2006.

[53] B. Dam, R. Gremaud, C. Broedersz, and R. Griessen. Combinatorial thin film methods for the search of new lightweight metal hydrides. *Scripta Materialia*, 56(10) :853–858, 2007.

[54] M. Tabib-Azar, B. Sutapun, R. Petrick, and A. Kazemi. Highly sensitive hydrogen sensors using palladium coated fiber optics with exposed cores and evanescent field interactions. *Sensors and Actuators B : Chemical*, 56(1-2) :158–163, June 1999.

[55] J. Villatoro, D. Luna-Moreno, and D. Monzon-Hernandez. Optical fiber hydrogen sensor for concentrations below the lower explosive limit. *Sensors and Actuators B : Chemical*, 110(1) :23–27, September 2005.

[56] J. Villatoro, A. Diez, JL Cruz, and MV Andres. Highly sensitive optical hydrogen sensor using circular pd-coated singlemode tapered fibre. *Electronics Letters*, 37(16) :1011–1012, 2001.

[57] J. Villatoro, A. Diez, J.L. Cruz, and M.V. Andres. In-line highly sensitive hydrogen sensor based on palladium-coated single-mode tapered fibers. *IEEE Sensors Journal*, 3(4) :533–537, August 2003.

[58] J. Villatoro and D. Monzon-Hernandez. Fast detection of hydrogen with nano fiber tapers coated with ultra thin palladium layers. *Optics Express*, 13(13) :5087–5092, June 2005.

[59] D. Zalvidea, A. Diez, JL Cruz, and MV Andres. Wavelength multiplexed hydrogen sensor based on palladium-coated fibre-taper and bragg grating. *Electronics Letters*, 40(5) :301–302, 2004.

[60] Donato Luna-Moreno and David Monzon-Hernandez. Effect of the pd-au thin film thickness uniformity on the performance of an optical fiber hydrogen sensor. *Applied Surface Science*, 253(21) :8615–8619, 2007. Times Cited : 4.

[61] K.T. Kim, H.S. Song, J.P. Mah, K.B. Hong, K. Im, S.J. Baik, and Y.I. Yoon. Hydrogen sensor based on palladium coated side-polished single-mode fiber. *Sensors Journal, IEEE*, 7(12) :1767–1771, 2007.

[62] Y.O. Barmenkov, A. Ortigosa-Blanch, A. Diez, JL Cruz, and MV Andres. Time-domain fiber laser hydrogen sensor. *Optics letters*, 29(21) :2461–2463, 2004.

[63] B. Sutapun, M. Tabib-Azar, and A. Kazemi. Pd-coated elastooptic fiber optic bragg grating sensors for multiplexed hydrogen sensing. *Sensors and Actuators B : Chemical*, 60(1) :27–34, November 1999.

[64] G. Meltz, S. J. Hewlett, and J. D. Love. Fiber grating evanescent-wave sensors. In *Proceedings of SPIE Chemical, Biochemical, and Environmental Fiber Sensors VIII*, volume Vol. 2836, pages pp. 342–350, 1996.

[65] C.L. Tien, H.W. Chen, W.F. Liu, S.S. Jyu, S.W. Lin, and Y.S. Lin. Hydrogen sensor based on side-polished fiber bragg gratings coated with thin palladium film. *Thin Solid Films*, 516(16) :5360–5363, 2008.

[66] R.R.J. Maier, B.J.S. Jones, J.S. Barton, S. McCulloch, T. Allsop, J.D.C. Jones, and I. Bennion. Fibre optics in palladium-based hydrogen sensing. *Journal of Optics A-Pure and Applied Optics*, 9(6) :S45–S59, June 2007.

[67] A. Trouillet, E. Marin, and C. Veillas. Fibre gratings for hydrogen sensing. *Measurement Science & Technology*, 17(5) :1124–1128, May 2006.

[68] X.T. Wei, T. Wei, H. Xiao, and Y.S. Lin. Nano-structured pd-long period fiber gratings integrated optical sensor for hydrogen detection. *Sensors and Actuators B : Chemical*, 134(2) :687–693, September 2008.

[69] M. Buric, T. Chen, M. Maklad, P.R. Swinehart, and K.P. Chen. Multiplexable low-temperature fiber bragg grating hydrogen sensors. *IEEE Photonics Technology Letters*, 21(21) :1594–1596, November 2009.

[70] J. Villatoro, D. Monzon-Hernandez, and E. Mejia. Fabrication and modeling of uniform-waist single-mode tapered optical fiber sensors. *Applied Optics*, 42(13) :2278–2283, May 2003.

[71] X. Bevenot, A. Trouillet, C. Veillas, H. Gagnaire, and M Clement. Surface plasmon resonance hydrogen sensor using an optical fibre. *Measurement Science & Technology*, 13(1) :118–124, January 2002.

[72] M. Buric, K.P. Chen, M. Bhattarai, P.R. Swinehart, and M. Maklad. Active fiber bragg grating hydrogen sensors for all-temperature operation. *IEEE Photonics Technology Letters*, 19(5-8) :255–257, March 2007.

[73] B.D. Kay, C.H.F. Peden, and D.W. Goodman. Kinetics of hydrogen absorption by pd (110). *Physical Review B*, 34(2) :817, 1986.

[74] Z. Zhao, Y. Sevryugina, MA Carpenter, D. Welch, and H. Xia. All-optical hydrogen-sensing materials based on tailored palladium alloy thin films. *Analytical chemistry*, 76(21) :6321–6326, 2004.

[75] R. Delmelle and J. Proost. An in situ study of the hydriding kinetics of pd thin films. *Physical Chemistry Chememical Phys.*, 13 :11412–11421, 2011.

[76] L.G. Petersson, H.M. Dannetun, and I. Lundstrom. Hydrogen detection during catalytic surface-reactions - evidence for activated lateral hydrogen mobility in the water-forming reaction on pd. *Physical Review Letters*, 52(20) :1806–1809, 1984.

[77] Z. Zhao, MA Carpenter, H. Xia, and D. Welch. All-optical hydrogen sensor based on a high alloy content palladium thin film. *Sensors and Actuators B : Chemical*, 113(1) :532–538, 2006.

[78] K. Baba, U. Miyagawa, K. Watanabe, Y. Sakamoto, and TB Flanagan. Electrical resistivity changes due to interstitial hydrogen in palladium-rich substitutional alloys. *Journal of Materials Science*, 25(9) :3910–3916, 1990.

[79] T.B. Flanagan and Y. Sakamoto. Hydrogen in disordered and ordered palladium alloys. *Platinum Metals Review*, 37(1) :26–37, 1993.

[80] E. Lee, J.M. Lee, E. Lee, J.S. Noh, J.H. Joe, B. Jung, and W. Lee. Hydrogen gas sensing performance of pd-ni alloy thin films. *Thin Solid Films*, 519(2) :880–884, 2010.

[81] D. Luna-Moreno, S. Monzon-Hernandez, D.and Calixto-Carrera, and R. Espinosa-Luna. Tailored pd-au layer produced by conventional evaporation process for hydrogen sensing. *Optics and Lasers in Engineering*, 49(6) :693–697, 2011. Times Cited : 0 Si.

[82] JN Huiberts, R. Griessen, JH Rector, RJ Wijngaarden, JP Dekker, DG De Groot, and NJ Koeman. Yttrium and lanthanum hydride films with switchable optical properties. *Nature*, 380(6571) :231–234, 1996.

[83] I. Giebels. Shining light on magnesium based switchable mirrors. *Doktorarbeit, Department of Physics and Astronomy, Vrije Universiteit Amsterdam*, 2004.

[84] P. Van der Sluis, M. Ouwerkerk, and PA Duine. Optical switches based on magnesium lanthanide alloy hydrides. *Applied physics letters*, 70(25) :3356–3358, 1997.

[85] JLM Van Mechelen, B. Noheda, W. Lohstroh, RJ Westerwaal, JH Rector, B. Dam, and R. Griessen. Mg–ni–h films as selective coatings : Tunable reflectance by layered hydrogenation. *Applied physics letters*, 84 :3651, 2004.

[86] L. Mooij, A. Baldi, C. Boelsma, K. Shen, M. Wagemaker, Y. Pivak, H. Schreuders, R. Griessen, and B. Dam. Interface energy controlled thermodynamics of nanoscale metal hydrides. *Advanced Energy Materials*, 2011.

[87] J.E. Benson, H.W. Kohn, and M. Boudart. On the reduction of tungsten trioxide accelerated by platinum and water. *Journal of Catalysis*, 5(2) :307–313, 1966.

[88] B. Orel, N. Groelj, U.O. Kraovec, M. Gabrek, P. Bukovec, and R. Reisfeld. Gasochromic effect of palladium doped peroxopolytungstic acid films prepared by the sol-gel route. *Sensors and Actuators B : Chemical*, 50(3) :234–245, 1998.

[89] S. Sumida, S. Okazaki, S. Asakura, H. Nakagawa, H. Murayama, and T. Hasegawa. Distributed hydrogen determination with fiber-optic sensor. *Sensors and Actuators B : Chemical*, 108(1-2) :508–514, 2005.

[90] N. Matsuyama, S. Okazaki, H. Nakagawa, H. Sone, and K. Fukuda. Response kinetics of a fiber-optic gas sensor using pt/wo3 thin film to hydrogen. *Thin Solid Films*, 517(16) :4650–4653, 2009.

[91] C. Caucheteur, M. Debliquy, D. Lahem, and P. Megret. Hybrid fiber gratings coated with a catalytic sensitive layer for hydrogen sensing in air. *Optics Express*, 16(21) :16854–16859, October 2008.

[92] J.R. Pitts, P. Liu, S.H. Lee, C.E. Tracy, RD Smith, and C. Salter. Interfacial stability of thin film hydrogen sensors. *Proceedings of the 2002 DOE Hydrogen Program Review, US Department of Energy, Baltimore, Maryland*, 2002.

[93] H. Cheong, H.C. Jo, K.M. Kim, and S.H. Lee. Hydrogen sensors based on gasochromic oxide thin films. *Journal of the Korean Physical Society*, 46 :S121–S124, 2005.

[94] E. Maciak, Z. Opilski, and M. Urbanczyk. Pd/vo fiber optic hydrogen gas sensor. In *Journal de Physique IV (Proceedings)*, volume 129, pages 137–141, 2005.

[95] J. Liu, X. Wang, Q. Peng, and Y. Li. Vanadium pentoxide nanobelts : highly selective and stable ethanol sensor materials. *Advanced Materials*, 17(6) :764–767, 2005.

[96] J. Dakin and B. Culshaw. *Optical fiber sensors*. Artech House on Demand, 1988.

[97] R.H. Ritchie. Plasma losses by fast electrons in thin films. *Physical Review*, 106(5) :874, 1957.

[98] C.J. Powell and J.B. Swan. Origin of the characteristic electron energy losses in aluminum. *Physical Review*, 115(4) :869, 1959.

[99] R.W. Wood. Xlii. on a remarkable case of uneven distribution of light in a diffraction grating spectrum. *Philosophical Magazine Series 6*, 4(21) :396–402, 1902.

[100] J.E. Inglesfield and E. Wikborg. The van der waals interaction between metals. *Journal of Physics F : Metal Physics*, 5 :1475, 1975.

[101] R.H. Ritchie. Surface plasmons and the image force in metals. *Physics Letters A*, 38(3) :189–190, 1972.

[102] P.M. Echenique, RH Ritchie, N. Barberan, and J. Inkson. Semiclassical image potential at a solid surface. *Physical Review B*, 23(12) :6486, 1981.

[103] B.E. Sernelius. Effects of spatial dispersion on electromagnetic surface modes and on modes associated with a gap between two half spaces. *Physical Review B*, 71(23) :235114, 2005.

[104] D.C. Langreth and J.P. Perdew. Exchange-correlation energy of a metallic surface : Wave-vector analysis. *Physical Review B*, 15(6) :2884, 1977.

[105] W.L. Barnes, A. Dereux, and T.W. Ebbesen. Surface plasmon subwavelength optics. *Nature*, 424(6950) :824–830, 2003.

[106] M.I. Stockman. Nanoplasmonics : past, present, and glimpse into future. *Optics Express*, 19(22) :22029–22106, 2011.

[107] T.W. Ebbesen, HJ Lezec, HF Ghaemi, T. Thio, and PA Wolff. Extraordinary optical transmission through sub-wavelength hole arrays. *Nature*, 391(6668) :667–669, 1998.

[108] H. Raether. *Surface plasmons on smooth and rough surfaces and on gratings*. Springer, 1988.

[109] S.A. Maier. *Plasmonics : fundamentals and applications*. Springer Verlag, 2007.

[110] B. Liedberg, C. Nylander, and I. Lunstrom. Surface plasmon resonance for gas detection and biosensing. *Sensors and Actuators*, 4 :299–304, 1983.

[111] R.L. Rich and D.G. Myszka. Survey of the year 2006 commercial optical biosensor literature. *Journal of Molecular Recognition*, 20(5) :300–366, 2007.

[112] B.P. Nelson, T.E. Grimsrud, M.R. Liles, R.M. Goodman, and M. Robert. Surface plasmon resonance imaging measurements of dna and rna hybridization adsorption onto dna microarrays. *Analytical chemistry*, 73(1) :1–7, 2001.

[113] E. Stenberg, B. Persson, H. Roos, and C. Urbaniczky. Quantitative determination of surface concentration of protein with surface plasmon resonance using radiolabeled proteins. *Journal of colloid and interface science*, 143(2) :513–526, 1991.

[114] U. Jönsson, L. Fägerstam, B. Ivarsson, B. Johnsson, R. Karlsson, K. Lundh, S. Löfås, B. Persson, H. Roos, and I. Rönnberg. Real-time biospecific interaction analysis using surface plasmon resonance and a sensor chip technology. *Biotechniques*, 11(5) :620, 1991.

[115] K. Matsubara, S. Kawata, and S. Minami. Optical chemical sensor based on surface plasmon measurement. *Applied optics*, 27(6) :1160–1163, 1988.

[116] H.E. de Bruijn, B.S.F. Altenburg, R.P.H. Kooyman, and J. Greve. Determination of thickness and dielectric constant of thin transparent dielectric layers using surface plasmon resonance. *Optics communications*, 82(5-6) :425–432, 1991.

[117] J. Homola. Present and future of surface plasmon resonance biosensors. *Analytical and bioanalytical chemistry*, 377(3) :528–539, 2003.

[118] X.D. Hoa, A.G. Kirk, and M. Tabrizian. Towards integrated and sensitive surface plasmon resonance biosensors : a review of recent progress. *Biosensors and Bioelectronics*, 23(2) :151–160, 2007.

[119] E. Wijaya, C. Lenaerts, S. Maricot, J. Hastanin, S. Habraken, J.P. Vilcot, R. Boukherroub, and S. Szunerits. Surface plasmon resonance-based biosensors : From the development of different spr structures to novel surface functionalization strategies. *Current Opinion in Solid State and Materials Science*, 2011.

[120] S.A. Zynio, A.V. Samoylov, E.R. Surovtseva, V.M. Mirsky, and Y.M. Shirshov. Bimetallic layers increase sensitivity of affinity sensors based on surface plasmon resonance. *Sensors*, 2(2) :62–70, 2002.

[121] M. Mitsushio, K. Miyashita, and M. Higo. Sensor properties and surface characterization of the metal-deposited spr optical fiber sensors with au, ag, cu, and al. *Sensors and Actuators A : Physical*, 125(2) :296–303, 2006.

[122] I. Garces, C. Aldea, and J. Mateo. Four-layer chemical fibre optic plasmon-based sensor. *Sensors and Actuators B : Chemical*, 7(1-3) :771–774, 1992.

[123] C.R. Lavers and J.S. Wilkinson. A waveguide-coupled surface-plasmon sensor for an aqueous environment. *Sensors and Actuators B : Chemical*, 22(1) :75–81, 1994.

[124] D. Sarid. Long-range surface-plasma waves on very thin metal films. *Physical Review Letters*, 47(26) :1927–1930, 1981.

[125] V.N. Konopsky and E.V. Alieva. Long-range propagation of plasmon polaritons in a thin metal film on a one-dimensional photonic crystal surface. *Physical review letters*, 97(25) :253904, 2006.

[126] A. Lahav, A. Shalabney, and I. Abdulhalim. Surface plasmon resonance sensor with enhanced sensitivity using nano-top dielectric layer. *Journal of Nanophotonics*, 3 :031501, 2009.

[127] J. Homola, S.S. Yee, and G. Gauglitz. Surface plasmon resonance sensors : review. *Sensors and Actuators B : Chemical*, 54(1-2) :3–15, 1999.

[128] C.E.H. Berger, T.A.M. Beumer, R.P.H. Kooyman, and J. Greve. Surface plasmon resonance multisensing. *Analytical Chemistry*, 70(4) :703–706, 1998.

[129] J. Homola, H.B. Lu, G.G. Nenninger, J. Dostálek, and S.S. Yee. A novel multichannel surface plasmon resonance biosensor. *Sensors and Actuators B : Chemical*, 76(1-3) :403–410, 2001.

[130] C. Boozer, Q. Yu, S. Chen, C.Y. Lee, J. Homola, S.S. Yee, and S. Jiang. Surface functionalization for self-referencing surface plasmon resonance (spr) biosensors by multi-step self-assembly. *Sensors and Actuators B : Chemical*, 90(1-3) :22–30, 2003.

[131] R.C. Jorgenson and S.S. Yee. A fiber-optic chemical sensor based on surface plasmon resonance. *Sensors and Actuators B : Chemical*, 12(3) :213–220, 1993.

[132] A.K. Sharma, R. Jha, and BD Gupta. Fiber-optic sensors based on surface plasmon resonance : a comprehensive review. *Sensors Journal, IEEE*, 7(8) :1118–1129, 2007.

[133] S. Roh, T. Chung, and B. Lee. Overview of the characteristics of micro-and nano-structured surface plasmon resonance sensors. *Sensors*, 11(2) :1565–1588, 2011.

[134] D. Monzon-Hernandez and J. Villatoro. High-resolution refractive index sensing by means of a multiple-peak surface plasmon resonance optical fiber sensor. *Sensors and Actuators B : Chemical*, 115(1) :227–231, 2006.

[135] R.K. Verma, A.K. Sharma, and BD Gupta. Surface plasmon resonance based tapered fiber optic sensor with different taper profiles. *Optics Communications*, 281(6) :1486–1491, 2008.

[136] D. Monzón-Hernández, J. Villatoro, D. Talavera, and D. Luna-Moreno. Optical-fiber surface-plasmon resonance sensor with multiple resonance peaks. *Applied optics*, 43(6) :1216–1220, 2004.

[137] J. Homola and R. Slavik. Fibre-optic sensor based on surface plasmon resonance. *Electronics Letters*, 32(5) :480–482, 1996. Times Cited : 42.

[138] R. Slavik, J. Homola, et al. Miniaturization of fiber optic surface plasmon resonance sensor. *Sensors and Actuators B : Chemical*, 51(1-3) :311–315, 1998.

[139] G. Nemova and R. Kashyap. Fiber-bragg-grating-assisted surface plasmon-polariton sensor. *Optics letters*, 31(14) :2118–2120, 2006.

[140] E.J. Smythe, E. Cubukcu, and F. Capasso. Optical properties of surface plasmon resonances of coupled metallic nanorods. *Optics Express*, 15(12) :7439–7447, 2007.

[141] A.W. Snyder and J.D. Love. *Optical waveguide theory*, volume 190. Springer, 1983.

[142] F. Abelès. Investigations on the propagation of sinusoidal electromagnetic waves in stratified media. application to thin films. *Ann. Phys.(Paris)*, 5 :596–640, 1950.

[143] AF Garito, J. Wang, and R. Gao. Effects of random perturbations in plastic optical fibers. *Science*, 281(5379) :962, 1998.

[144] Proper handling and storage. Technical report, Laser components GmbH, Werner-vos-Siemens-Str 15, 82140.

[145] A.D. Yablon. *Optical fiber fusion splicing*, volume 103. Springer Verlag, 2005.

[146] M.J. Matthewson, C.R. Kurkjian, and J.R. Hamblin. Acid stripping of fused silica optical fibers without strength degradation. *Journal of Lightwave Technology*, 15(3) :490–497, 1997.

[147] A. Abdelghani, JM Chovelon, N. Jaffrezic-Renault, C. Ronot-Trioli, C. Veillas, and H. Gagnaire. Surface plasmon resonance fibre-optic sensor for gas detection. *Sensors and Actuators B : Chemical*, 39(1-3) :407–410, 1997.

[148] H. Nagata, N. Miyamoto, T. Saito, and R. Kaizu. Reliable jacket stripping of optical fibers. *Journal of Lightwave Technology*, 12(5) :727–729, 1994.

[149] V.V. Rondinella and M.J. Matthewson. Effect of chemical stripping on the strength and surface morphology of fused silica optical fiber. In *Proceedings of SPIE*, volume 2074, page 52, 1994.

[150] *O.F stripper : denudage chimique des fibres optiques, LUMER, societe industrielle des produits chimiques Lumer.*

[151] B. Diers and F. Maze-Coradin. Le remplacement du mélange sulfochromique. *Actualite chimique*, pages 33–34, 2004.

[152] P.G. Urben. *Bretherick's handbook of reactive chemical hazards.* Elsevier, 2007.

[153] *Material Safety Data Sheet SULFURIC ACID.*

[154] A.J. Johnson and G.H. Auth. *Fuels and combustion handbook.* McGraw-Hill, 1951.

[155] JS Weber et al. Fiber-optic fluorimetry in biosensors : comparison between evanescent wave generation and distal-face generation of fluorescent light. *Biosensors and Bioelectronics*, 7(3) :193–197, 1992.

[156] H. Park, S. Lee, U.C. Paek, and Y. Chung. Noncontact optical fiber coating removal technique with hot air stream. *Journal of lightwave technology*, 23(2) :551, 2005.

[157] F. Barnier, P.E. Dyer, P. Monk, HV Snelling, and H. Rourke. Fibre optic jacket removal by pulsed laser ablation. *Journal of Physics D : Applied Physics*, 33 :757, 2000.

[158] B. Johnston, A. Lee, M. Withford, and J. Piper. Laser assisted jacket removal and writing of fiber bragg gratings using a single laser source. *Optics Express*, 10(16) :818–823, 2002.

[159] J.E. Mahan. *Physical vapor deposition of thin films*, volume 1. John Wiley & Sons, 2000.

[160] B. Chadwick and M. Gal. Enhanced optical detection of hydrogen using the excitation of surface plasmons in palladium. *Applied surface science*, 68(1) :135–138, 1993.

[161] E. Kretschmann and H. Raether. Radiative decay of non radiative surface plasmons excited by light(surface plasma waves excitation by light and decay into photons applied to nonradiative modes). *Zeitschrift Fuer Naturforschung, Teil A*, 23 :2135, 1968.

[162] B.T. Sullivan. Optical properties of palladium in the visible and near uv spectral regions. *Applied optics*, 29(13) :1964–1970, 1990.

[163] K. Von Rottkay, M. Rubin, and PA Duine. Refractive index changes of pd-coated magnesium lanthanide switchable mirrors upon hydrogen insertion. *Journal of applied physics*, 85 :408, 1999.

[164] WE Vargas, I. Rojas, DE Azofeifa, and N. Clark. Optical and electrical properties of hydrided palladium thin films studied by an inversion approach from transmittance measurements. *Thin solid films*, 496(2) :189–196, 2006.

[165] Y. Yamada, K. Tajima, S. Bao, M. Okada, A. Roos, and K. Yoshimura. Real time characterization of hydrogenation mechanism of palladium thin films by in situ spectroscopic ellipsometry. *Journal of applied physics*, 106 :013523, 2009.

[166] JN Huiberts, JH Rector, RJ Wijngaarden, S. Jetten, D. De Groot, B. Dam, NJ Koeman, R. Griessen, B. Hjorvarsson, S. Olafsson, et al. Synthesis of yttriumtrihydride films for ex-situ measurements. *Journal of alloys and compounds*, 239(2) :158–171, 1996.

[167] MA Ordal, LL Long, RJ Bell, SE Bell, RR Bell, RW Alexander Jr, CA Ward, et al. Optical properties of the metals al, co, cu, au, fe, pb, ni, pd, pt, ag, ti, and w in the infrared and far infrared. *Applied Optics*, 22(7) :1099–1119, 1983.

[168] A. Shalabney and I. Abdulhalim. Electromagnetic fields distribution in multilayer thin film structures and the origin of sensitivity enhancement in surface plasmon resonance sensors. *Sensors and Actuators A : Physical*, 159(1) :24–32, 2010.

[169] X. Wang, M. Jefferson, P.C.D. Hobbs, W.P. Risk, B.E. Feller, R.D. Miller, and A. Knoesen. Shot-noise limited detection for surface plasmon sensing. *Optics Express*, 19(1) :107–117, 2011.

[170] K. Johansen, R. Stålberg, I. Lundström, and B. Liedberg. Surface plasmon resonance : instrumental resolution using photo diode arrays. *Measurement Science and Technology*, 11 :1630, 2000.

[171] F.Y. Kou and T. Tamir. Range extension of surface-plasmons by dielectric layers. *Optics Letters*, 12(5) :367–369, May 1987.

[172] C.W. Lin, K.P. Chen, C.N. Hsiao, S. Lin, and C.K. Lee. Design and fabrication of an alternating dielectric multi-layer device for surface plasmon resonance sensor. *Sensors and Actuators B : Chemical*, 113(1) :169–176, 2006.

[173] A.K. Sharma and G.J. Mohr. Theoretical understanding of an alternating dielectric multilayer-based fiber optic spr sensor and its application to gas sensing. *New Journal of Physics*, 10 :–, February 2008.

[174] V.N. Konopsky, D.V. Basmanov, E.V. Alieva, D.I. Dolgy, E.D. Olshansky, S.K. Sekatskii, and G. Dietler. Registration of long-range surface plasmon resonance by angle-scanning feedback and its implementation for optical hydrogen sensing. *New Journal of Physics*, 11 :063049, 2009.

[175] D.M. Borsa, A. Baldi, M. Pasturel, H. Schreuders, B. Dam, R. Griessen, P. Vermeulen, and P.H.L. Notten. Mg–ti–h thin films for smart solar collectors. *Applied physics letters*, 88 :241910, 2006.

[176] A. Baldi, M. Gonzalez-Silveira, V. Palmisano, B. Dam, and R. Griessen. Destabilization of the mg-h system through elastic constraints. *Physical review letters*, 102(22) :226102, 2009.

[177] M. Pasturel, RJ Wijngaarden, W. Lohstroh, H. Schreuders, M. Slaman, B. Dam, and R. Griessen. Influence of the chemical potential on the hydrogen sorption kinetics of mg2ni/tm/pd (tm= transition metal) trilayers. *Chemistry of materials*, 19(3) :624–633, 2007.

[178] V. Palmisano. *Thermodynamic of Pd-capped Mg-Ti layers, effect of the cap layer.* Tu delft, Chemical Engineering, MECS group, 2011.

# Annexe B

# Résumé Long - Français

À l'heure où l'énergie est au coeur des préoccupations internationales, l'hydrogène [1], source d'énergie propre et inépuisable, pourrait s'imposer comme l'énergie de demain. Ses applications s'étendent de la production d'électricité, via une pile à combustible, jusqu'au stockage de l'énergie renouvelable intermittente. En dix ans, de nombreux progrès ont été fait pour produire, stocker et convertir l'hydrogène en énergie à moindre coût. L'utilisation de l'hydrogène dans le domaine public soulève cependant des questions de sécurité. L'hydrogène est un gaz inflammable, volatile et hautement explosif : sa limite d'explosivité est de 4 à 76 % dans l'air. Son minimum d'énergie d'ignition est seulement de 0.02 mJ. Il est ainsi nécessaire de maîtriser la détection de toutes les fuites pour éviter les explosions.

Nous proposons dans cette thèse de développer un capteur à fibres optiques pour la détection d'hydrogène. Nous présentons en introduction le contexte actuel des capteurs à hydrogène et identifions les paramètres clés pour réaliser un capteur idéal. En outre, ce chapitre explicite nos objectifs et notre démarche. Dans le premier chapitre, nous présentons un état de l'art des capteurs à fibres optiques pour la détection d'hydrogène, mettant en avant leurs avantages et inconvénients. Suite à ces travaux, nous avons décidé de développer un capteur à fibres optiques multimode exploitant la résonance de plasmon de surface (SPR) pour répondre aux mieux aux exigences industrielles. L'objectif scientifique de cette thèse est d'étudier le potentiel des capteurs plasmoniques à fibres optiques. Ainsi, nous étudions deux designs dont l'un est basé sur la modulation d'amplitude et l'autre sur la modulation de longueur d'onde. Dans le deuxième chapitre, nous présentons théoriquement les capteurs SPR et explicitons leurs principes et fonctionnements. Le troisième chapitre présente les modèles et les méthodes utilisés pour simuler et réaliser ces différents capteurs. Nous présentons, respectivement, dans le cinquième et sixième chapitre le principe, la caractérisation et la réponse des deux capteurs proposés. Enfin, nous proposons d'optimiser la plage de détection des précédents capteurs en modifiant les matériaux sensibles à l'hydrogène dans le dernier chapitre.

Notre conclusion porte sur les avantages des capteurs plasmoniques pour la détection de fuites d'hydrogène.

1. L'hydrogène (Hydrogen dans ce mémoire) correspond à la molécule dihydrogène. Sa forme atomique est précisée si besoin (Hydrogen atom dans ce mémoire)

## Introduction

Ce chapitre décrit le contexte actuel des capteurs à hydrogène. Nous mettons notamment en avant l'avantage des capteurs à fibres optiques pour la détection de fuites d'hydrogène.

De nombreux capteurs à hydrogène ont été proposés et développés depuis plus d'un demi-siècle. À l'heure actuelle aucun capteur ne permet de satisfaire toutes les recommandations. Les spectromètres de masse sont les capteurs les plus fiables pour détecter et quantifier la concentration d'hydrogène. Par leur encombrement, leur poids et leur coût élevés, ces moyens de détection sont néanmoins difficiles à mettre en place dans des systèmes embarqués tel que les lanceurs de satellites, ou dans un futur proche les véhicules automobiles. Pour répondre à ce besoin industriel de nombreux micro-capteurs ont été développés comme les capteurs chimiques à état solide (CMOS, MIS, MOS ...), électrochimiques, catalytiques, ... et thermoélectriques.

Depuis une dizaine d'années, une recherche active se développe autour des capteurs à fibres optiques (C.F.O). En effet, les capteurs à fibres optiques peuvent être utilisés dans des environnements explosifs sans risque d'ignition : isolation électrique, sécurité intrinsèque (faible énergie lumineuse et confinée) et détection à distance. De plus, leur insensibilité électromagnétique, leur très faible dimension (diamètre de 1 à 400 $\mu$m), leur flexibilité et légèreté, ainsi que leur capacité à multiplexer les signaux et à réaliser des capteurs distribués les rendent particulièrement attrayants pour les systèmes embarqués.

Des capteurs à fibres optiques pour la détection d'hydrogène basés sur la modulation de phase, d'amplitude et de longueur d'onde ont déjà été étudiés ces dernières années. Cependant leurs temps de réponses, leurs sensitivités, leurs fiabilités (précision, cross-sensitivité) et leurs reproductibilités restent toujours en dessous des performances obtenues par les capteurs électriques. L'objectif de cette thèse est de développer un capteur à fibres optiques pour la détection d'hydrogène répondant aux exigences de l'industrie. Nous avons notamment axé nos recherches vers l'amélioration de leurs temps de détections.

## Chapitre 1

Nous présentons dans ce chapitre un état de l'art des capteurs à fibres optiques utilisant le Pd comme matériaux sensible pour la détection des fuites d'hydrogène. Nous détaillons le fonctionnement des capteurs existants et soulignons leurs avantages et inconvénients. Dans une seconde partie, nous discutons de la possibilité d'utiliser d'autre matériaux que le Pd, sensibles à l'hydrogène, dans les capteurs à fibres optiques pour détecter l'hydrogène. Enfin, à partir de ces résultats, nous explicitons la technologie choisie.

Le Pd est fréquemment utilisé dans les capteurs à hydrogène comme catalyseur et transducteur. Le Pd forme avec l'hydrogène un hydrure métallique. Le Pd dissocie l'hydrogène et absorbe les atomes d'hydrogènes pour former un hydrure métallique. La composition du Pd hydride $PdH_x$ (x définissant la solubilité de l'hydrogène dans le Pd, c'est-à-dire la concentration d'hydrogène dans le métal) est fonction de la pression partielle de l'hydrogène et de la température extérieure. En particulier, la formation de l'hydrure est caractérisée par des courbes appelées « isothermes de pression-composition »(pcT). Pour chaque isotherme, correspondant à une température inférieure à la température critique, on observe deux phases où la solubilité croit avec la pression, appelées respectivement $\alpha$ et $\beta$. Une

zone d'iso-pression, où les deux phases coexistent sans miscibilité entre elles, sépare ces deux phases. Pour la phase $\alpha$ (pressions inférieurs à l'iso-pression) la solubilité est faible. Les atomes d'hydrogène diffusent dans les sites interstitiels. L'hydridation du Pd s'accompagne d'une augmentation du paramètre de maille. Dans la phase $\beta$ (pressions inférieures à l'iso-pression), tous les sites disponibles pour l'atome d'hydrogène sont occupés dans le métal.

Pendant la formation de l'hydrure métallique, les propriétés physiques du Pd (paramètre de maille, conductivité et indice de réfraction) sont modifiées, et dépend du nombre d'atomes d'hydrogène absorbés par le Pd. La fibre optique sert à mesurer ces changements. Pour mesurer les changements physiques du Pd, la couche de Pd peut être déposée (i) à l'extrémité de la fibre optique sur sa face clivée, ou (ii) autour de son coeur ou de sa gaine optique. Dans le premier cas, la fibre optique est dite passive : elle sert seulement à transporter la lumière (capteur extrinsèque). Dans le second cas, la fibre optique est dite active. La réaction de l'hydrogène avec le Pd entraine une contrainte sur une zone locale de la fibre optique qui modifie les propriétés opto-géométriques de la fibre optique. La mesure de l'intensité, de la phase, de la polarisation ou de la longueur d'onde en sortie de la fibre optique permet d'accéder à la contrainte exercée sur la section sensible de la fibre optique et ainsi de détecter et quantifier la présence d'hydrogène autour de la zone sensible.

De nombreux capteurs à modulation de phase, d'amplitude et de longueur d'onde ont été développés dans la littérature depuis une trentaine d'années. Dans la section 1.3, nous détaillons leur principe, leur design et les avantages et inconvénients de chaque capteur (capteurs interférométriques, capteurs à onde évanescent, micro-miroir, ..., et capteurs à réseaux de Bragg). Cette étude permet de mettre en évidence le lien entre la réponse du capteur et les propriétés physiques du Pd.

La plage de sensibilité est fortement déterminée par les courbes pcT : les concentrations minimum et maximum détectables sont respectivement liés à la phase $\alpha$ et $\beta$. Par exemple, à température ambiante, la concentration minimum détectée est généralement de 0.5 % $H_2$)[2], et peut être diminuée jusqu'à 0.01% pour les capteurs les plus sensibles (types interférométrique). Les capteurs fonctionnent généralement jusqu'à une concentration de 100 % $H_2$, mais à partir de 4 % $H_2$ la réponse du capteur sature.

La reproductibilité et le temps de réponse dépendent fortement des propriétés du Pd (morphologie du film, épaisseur...). Nous observons que la réponse est plus rapide et reproductible pour les couches de Pd les plus minces. Cependant, la sensibilité des capteurs utilisant des couches minces est diminué (la « contrainte »transférée à la fibre optique lors de la formation de l'hydrure métallique est moindre). En fonction de la configuration choisie, il est plus ou moins « facile »d'utiliser des couches extrêmement fines sans détériorer de manière significative la sensibilité du capteur. Les capteurs basés sur le changement de l'indice de réfraction du Pd tels que les capteurs à modulation d'amplitude, type évanescent, permettent d'utiliser des couches de Pd d'une dizaine de nanomètres. À l'opposé, les capteurs basés sur l'expansion, type capteurs à réseaux de Bragg, utilisent des couches plus épaisses de l'ordre d'une centaine de nanomètres.

La caractérisation des capteurs est principalement faite dans une atmosphère inerte. Or il est essentiel de pouvoir faire fonctionner le capteur en présence d'oxygène ou d'autres composés chimiques tels que les hydrocarbures. Il est pourtant démontré que la présence

2. Les concentrations d'hydrogène correspondent à des pourcentages volumétriques à pression atmosphérique.)

d'autres composés chimiques, tels que l'oxygène, affectent la réponse du capteur. Dû aux propriétés catalytiques du Pd, d'autres réactions chimiques peuvent avoir lieu à sa surface. Par exemple, l'oxygène peut être adsorbé à la surface du Pd bloquant des sites pour la dissociation et l'absorption de l'hydrogène. Pour limiter cet inconvénient, le Pd est remplacé par des alliages métalliques tels que Pd-Au, Pd-Ag, ou bien encore Pd-Ta, etc.

Dans la section 1.5, nous discutons dans la section de la possibilité d'utiliser d'autres matériaux, tels que le tungstène oxyde, comme transducteur. Cependant, dans la plupart des cas, une fine couche de Pd est nécessaire pour dissocier la molécule d'hydrogène.

Dans cette thèse, nous avons décidé d'utiliser le Pd comme modèle pour proposer un nouveau design. Il est important de noter que nos résultats pourront être adaptés ensuite aux cas d'autres hydrures métalliques.

En conclusion, les performances des capteurs à fibres optiques sont en-dessous des recommandations. En particulier, le temps de réponse et la cross-sensitivité ne sont pas satisfaisants. Dans le contexte de cette thèse, nous avons décidé d'axer nos recherches pour améliorer le temps de réponse des capteurs à fibres optiques intrinsèques. Afin d'obtenir une réponse rapide et reproductible, nous avons décidé de développer un capteur à fibres optiques utilisant des couches minces de Pd. Bien qu'une couche épaisse permet de transférer une contrainte plus importante (et donc une très bonne sensibilité), le temps de réponse est ralentie. Pour limiter la baisse de sensibilité du capteur, nous proposons de développer un capteur à fibres optiques basé sur le principe de Résonance de Plasmon de Surface (SPR). Comme décrit dans les chapitres 4 et 5, cette architecture permet d'utiliser des couches de Pd extrêmement fines. De plus, les capteurs SPR sont reconnus comme extrêmement sensibles à l'interface métal diélectrique. Ainsi, cette technologie, peu étudiée pour la détection d'hydrogène, apparaît prometteuse pour la réalisation d'un capteur à hydrogène ayant à la fois une bonne sensibilité et un temps de réponse acceptable. Pour étudier le potentiel des capteurs à fibres optiques à résonance de plasmon de surface (SPR) nous proposons, réalisons et caractérisons deux nouveaux dispositifs.

## Chapitre 2

Ce chapitre définit et explicite tout d'abord les propriétés des Plasmons de Surfaces (PS). Dans une deuxième partie, nous discutons des conditions de couplage PS - onde lumineuse. Ces rappels théoriques nous permettent de décrire le principe et l'évolution des capteurs SPR. Enfin, nous abordons le cas des fibres optiques.

Un Plasmon de Surface (PS) ou plutôt un Plasmon Polariton de Surface (PPS) est une onde Transversale Magnétique (TM) se propageant à l'interface d'un métal et d'un milieu diélectrique, accompagnées par une oscillation collective de charges libres.

Pour décrire les propriétés fondamentales des PS, nous considérons une interface plane entre deux milieux semi-infinis. La résolution des équations de maxwell permet de déterminer la relation de dispersion des PS (i.e. la réponse du vecteur d'onde du PS en fonction de la fréquence). Les PS existent seulement pour la polarisation TM à l'interface de deux milieux de permittivité diélectrique opposés, c'est-à-dire à l'interface d'un métal et d'un diélectrique.

Le vecteur d'onde des PS est composé d'une composante perpendiculaire et parallèle à l'interface (eq. 2.1). La composante du vecteur d'onde perpendiculaire à l'interface est purement complexe, c'est à dire le champ électromagnétique est évanescent dans la direction

normale à la surface. En particulier, son amplitude décroit exponentiellement dans les deux milieux en s'éloignant perpendiculairement à l'interface (fig. 2.1c). La composante du vecteur d'onde parallèle à l'interface est quant à elle complexe. Sa partie réelle traduit la propagation de l'onde le long de l'interface, tandis que sa partie imaginaire traduit l'amortissement de l'onde le long de l'interface.

En conclusion, un PS est confiné à l'interface métal diélectrique et se propage sur une longueur finie L (L définit à la section 2.5).

D'après la relation de dispersion des PS, nous observons que la lumière radiative ne peut pas être couplée avec les PS (la conservation du vecteur d'onde n'étant pas satisfaite, fig.2.5b). La lumière incidente (polarisée TM) est couplée aux PS par l'intermédiaire d'une structure de couplage (configuration Otto-Kretschman, corrugation de surface...).

Les structures de couplages sont explicitement décrites dans la section 2.6. Elles permettent d'ajouter une valeur $\Delta k$ à la composante du vecteur d'onde de la lumière incidente $k_0$ et ainsi d'égaliser la composant parallèle du vecteur d'onde des PS ($k_{0x}+\Delta k_x = k_x^{sp}$, fig. 2.5b).

Un capteur SPR est constitué d'une structure de couplage, d'une couche métallique et d'un milieu diélectrique. Le PS joue le rôle de sonde dans le milieu. Le confinement du champ électromagnétique du PS permet de réaliser des dispositifs très sensibles à l'interface. Un capteur à Plasmon de Surface mesure la modification du vecteur d'onde du PS lorsque les conditions limites sont modifiées. Le milieu diélectrique est généralement le transducteur. Par exemple, le greffage de molécules à la surface d'un métal engendre la modification du PS. La structure du couplage permet d'exciter le PS et de collecter l'information. Dans le cas de la configuration de Kretschman, la lumière réfléchie (l'intensité, la phase, l'angle de résonance) permet de mesurer ces modifications.

La performance des capteurs plasmoniques (sensibilité, limite de détection et gamme de fonctionnement) dépend fortement du design et du milieu transducteur. Pour illustrer cette influence, nous explicitons brièvement le choix du métal, puis étudions des systèmes à multicouches. L'objectif de ce paragraphe (2.7.2) est de montrer comment réaliser un capteur SPR et améliorer ses performances.

Enfin, nous abordons le cas des fibres optiques comme structure de couplage (section 2.7.3). Les fibres optiques multimodes ont été récemment proposées comme structure de couplage pour miniaturiser les capteurs SPR. De plus, les capteurs SPR à fibres optiques bénéficient des avantages de la fibre optique tels que la mesure à distance, la flexibilité, la possibilité de multiplexage et de mesures distribuées le long de la fibre. Ces capteurs consistent à utiliser le coeur de la fibre optique comme structure de couplage. Pour cela, une partie de la gaine optique est enlevée et une fine couche métallique est déposée autour du coeur de la fibre optique multimode (fig. 2.9). Le principe est analogue à la configuration de Kretschman. En effet, la lumière est guidée par réflexion interne totale dans une fibre optique multimode. Les ondes évanescentes associées aux rayons guidées peuvent être ainsi couplées aux PS lorsque la condition de résonance est satisfaite.

## Chapitre 3

Nous détaillons tout d'abord dans ce chapitre les modèles utilisés pour simuler les capteurs à Résonance de Plasmon de Surface (SPR) utilisant des fibres multimodes. Dans une

deuxième partie, nous expliquons nos choix technologiques et décrivons les étapes nécessaires à la réalisation de capteurs SPR à fibres optiques.

Dans cette thèse, nous avons développé un programme sous matlab pour simuler la réponse des capteurs plasmoniques à fibres optiques multimode. Nous considérons la fibre optique comme un guide plan. La propagation de la lumière est modélisée par l'approximation de l'optique géométrique. Nous considérons seulement les rayons méridiens et nous négligeons le couplage de modes (la fibre optique est dite idéale).

Les rayons guidées se propage le long de la fibre optique par réflexion à l'interface coeur gaine optique. Au point de réflexion, la lumière est décomposée (approche locale) selon la polarisation Transversale Electrique (TE ou dite s) et Transversale Magnétique (TM ou dite p). L'intensité transmise en sortie de fibre est déterminée par les coefficients de réflexions, en supposant que le coeur est un milieu sans pertes (eq. 3.11).

Les coefficients de réflexion pour une onde polarisée TE et TM sont calculés par une méthode matricielle développée par Abeles (section 3.2.1).

Nous explicitons ensuite nos choix technologiques. Une fibre optique multimode à saut d'indice, ayant un large diamètre de coeur (200 $\mu$m/230$\mu$m) est utilisée. Le coeur est en silice, la gaine optique est en polymère et la gaine mécanique est en Tefzel. Ce choix permet de simuler simplement la réponse de la fibre optique (approximation opto-géométrique), facilite la fabrication et confère aux capteurs réalisés une bonne solidité.

La fibre optique est dénudée de ses gaines mécanique et optique sur une longueur L (fig.3.1), section sensible à l'hydrogène. La gaine mécanique est enlevée mécaniquement avec une lame de scalpel. Tandis qu'un simple traitement thermique est suffisant pour enlever la gaine optique en polymère. La fibre optique est ensuite nettoyée dans des bains chimiques (dichlorométhane et acétone) à ultrason pour enlever les dernières traces de polymère sur le coeur. Nous observons la surface de la fibre optique à l'aide d'un microscope optique et d'un microscope électronique à balayage. La surface présente une bonne qualité (fig. 3.5 et fig.3.6).

En fonction du design du capteur, les couches métalliques sont ensuite déposées par pulvérisation cathodique autour du coeur de la fibre. Un bâti a été réalisé (fig.3.8b) à cet effet pour obtenir une couche d'épaisseur uniforme le long de la fibre optique. Les vitesses de dépositions ont été déduites en mesurant l'épaisseur des dépôts sur des substrats quartz plans.

Enfin, un banc optique a été réalisé pour mesurer la réponse des capteurs à l'hydrogène. Le montage expérimental comprend une source de lumière, une cellule gazeuse et un spectromètre connecté à un ordinateur pour l'acquisition et le traitement des données. La fibre optique traversant la cellule gazeuse est connectée à la source et au détecteur via un connecteur 905 SMA. Le mélange gazeux composé d'Ar, H2 et O2 est réalisé en amont avant d'être injecté dans la cellule. Toutes les mesures sont faites à température ambiante et pression atmosphérique.

## Chapitre 4

Ce chapitre décrit la réponse d'un capteur à fibres optiques à modulation d'amplitude pour la détection d'hydrogène. Nous présentons dans une première section les travaux précédents et décrivons le principe du capteur proposé. Dans une deuxième section, nous

présentons la réponse expérimentale du capteur. Enfin, nous étudions l'influence des paramètres de la fibre optique et de la zone sensible sur la réponse du capteur.

Le premier capteur proposé consiste à déposer par pulvérisation cathodique une couche de Pd sur le coeur d'une fibre optique à saut d'indice multimode. L'intensité de la lumière guidée à travers la fibre optique est modulée par la section sensible lorsque l'hydrogène interagit avec le Pd.

Le principe de ce capteur est basé sur la variation de l'indice optique de la gaine dans la partie sensible. Lors de l'hydrogénation du Pd, l'indice de réfraction du Pd est modifié, changeant la proportion de lumière réfléchie à l'interface Pd air. Dans le cas de la polarisation Transversale Magnétique (TM), la modification du coefficient de réflexion est liée aux propriétés du PS se propageant à l'interface du Pd Bévenot et al. ont utilisé cette propriété pour réaliser un capteur à hydrogène. Le dispositif consiste à mesurer la variation de l'intensité transmise en sortie de la fibre optique lorsqu'un groupe de mode est excité (i.e. la fibre optique est illuminée sous un angle d'incidence par une diode laser). La modification du pic de résonance du PS, due à l'hydridation du Pd, cause une augmentation de l'intensité transmise en sortie de la fibre optique (fig. 4.1). Par sa géométrie, ce dispositif est peu compatible pour des applications industrielles.

L'originalité de nos travaux repose sur l'excitation de tous les modes de la fibre. La détection est faite en mesurant l'intensité totale transmise en sortie de fibre. De plus, nous prenons en compte la polarisation TM mais aussi la polarisation Transversale Electrique (TE), contrairement aux travaux précédents.

Nous décrivons tout d'abord la réponse expérimentale du capteur. L'étude de la réponse est faite sur une plage de longueur d'onde allant de 450 à 900 nm.

Nous obtenons une réponse reproductible sur plusieurs cycles d'hydrogénation déshydrogénation et dépendante de la longueur d'onde (fig.4.2). Remarquablement, l'intensité en sortie de fibre peut soit augmenter ou diminuer en fonction de la longueur d'onde sélectionnée. En sélectionnant plusieurs longueurs d'ondes, il est alors possible de limiter les fausses alarmes et ainsi d'augmenter la fiabilité des capteurs.

La réponse est fonction de la concentration d'hydrogène (fig. 4.3c). Le capteur détecte une concentration d'hydrogène entre 0.5 % et 4 % $H_2$ dans une atmosphère inerte (Ar). Le temps de réponse, inférieure à 30 s, dépend de l'environnement (oxygène ou non) et des capteurs réalisés (fig. 4.5). Ce dernier point est discuté par la suite en comparant le temps de réponse et la réponse spectrale des différents capteurs réalisés.

Enfin, nous observons que l'oxygène peut interférer avec l'hydrogène et diminuer la réponse du capteur. Nous vérifions expérimentalement que la couche de Pd pourra être remplacée par un alliage de Pd pour éviter la cross-sensitivité (fig.4.6).

Dans une deuxième partie, une analyse théorique nous permet d'expliquer la réponse spectrale du capteur proposé. Pour cela, nous calculons la réflectivité de la couche mince de Pd en fonction de l'hydrogène pour la polarisation s (TE) et p (TM) (fig.4.7), à l'aide d'une approche matricielle, basée sur les équations de Fresnel et explicitée au chapitre 3. Pour les angles correspondants aux rayons guidés, la réflectivité à l'interface silice/Pd/air augmente en présence d'hydrogène pour la polarisation p tandis qu'elle diminue pour la polarisation s. Pour la polarisation p, la réflectivité augmente due à la modification de pic de résonance lors de la formation de l'hydrure Pour la polarisation s, la réflectivité diminue parce que l'hydrure métallique présente un caractère moins "métallique".

Finalement, la réponse spectrale du capteur est le résultat de deux contributions opposées : l'intensité diminue et augmente respectivement pour la polarisation s (TE) et p (TM) (fig.4.8). D'autre part, la variation du rapport entre la partie réelle et imaginaire de l'indice de réfraction du Pd au cours de l'hydrogénation accentue cette dépendance spectrale de la réponse du capteur comme expliqué dans la section 4.4.2.

Nous étudions ensuite la réponse du capteur pour différentes longueurs et épaisseurs de Pd. En optimisant la longueur et l'épaisseur, nous modifions l'amplitude de la modulation et la réponse spectrale. Les résultats obtenus sont consistants avec les résultats expérimentaux Cependant, en dessous d'une certaine épaisseur (3 nm), nos simulations ne correspondent plus avec les résultats expérimentaux (fig.4.13). Nous pensons que la morphologie des films pour des couches extrêmement fines est responsable de cette différence.

En conclusion, nous avons réalisé un capteur à fibres optiques à modulation d'amplitude pour la détection d'hydrogène. La réponse est relativement rapide et reproductible. De plus, le capteur proposé présente une dépendance spectrale, en accord avec nos résultats théorique. Cette réponse spectrale permet d'augmenter la fiabilité du capteur, en mesurant l'intensité en sortie de la fibre optique pour plusieurs longueurs d'ondes.

## Chapitre 5

Dans ce chapitre, nous proposons, simulons et réalisons un nouveau design pour permettre de détecter l'hydrogène par modulation de longueurs d'ondes. En effet, bien que notre précédent capteur à modulation d'amplitude permette de diminuer le nombre de fausses alarmes, la quantification d'hydrogène devient problématique si le capteur est sujet à des fluctuations d'intensité et de polarisation. Dans la première partie, nous décrivons le principe du capteur et déterminons ses paramètres. Dans une seconde partie, nous étudions sa réponse expérimentale. Enfin, nous concluons sur les avantages du design proposé.

Nous proposons de remplacer la couche de Pd dans notre précédent capteur (chapitre 5) par une cavité résonante constitué par une couche d'Ag, de $SiO_2$ et de Pd. Cette architecture permet de coupler les groupes de modes guidés de la fibre optique aux PS. La couche intermédiaire permet d'ajuster le vecteur d'onde du PS : elle permet de déplacer l'angle de résonance dans l'ouverture numérique de la fibre optique (fig.5.3). Lorsqu'un groupe de mode guidé est couplé aux PS, l'intensité transmise diminue. En conséquence, l'intensité totale transmise est minimale lorsque la condition de résonance décrite aux chapitres 3 est satisfaite. La position et l'amplitude du pic de résonance sont définies par le vecteur de propagation du PS. Celui-ci est caractérisé par les épaisseurs et les permittivités diélectriques des différentes couches (système à multicouches). Lorsque le Pd interagit avec l'hydrogène, la variation de l'indice de réfraction du Pd modifie le vecteur de propagation du PS. Le déplacement du pic de résonance permet alors d'accéder à la concentration d'hydrogène. Ainsi, nous pouvons détecter l'hydrogène soit en mesurant l'intensité en sortie de fibre pour plusieurs longueurs d'onde ou soit en mesurant la longueur d'onde de résonance.

Nous présentons une étude théorique pour choisir les paramètres du transducteur et de la fibre optique comme décrit dans la section 5.4. En particulier, l'épaisseur de la couche intermédiaire définit la longueur d'onde de résonance. La sensibilité du capteur (déplacement de la longueur d'onde de résonance en présence d'hydrogène) est fortement déterminée par

l'épaisseur de la couche du Pd. Augmenté l'épaisseur de la couche de Pd permet d'obtenir un déplacement du pic de résonance plus important mais diminue la résonance due aux caractères absorbant du Pd (la valeur de la partie réelle de la partie imaginaire est comparable à sa partie imaginaire). Notons que la couche de Pd est limitée à 15 nm dans notre étude pour obtenir une réponse rapide comme expliqué dans le chapitre 1. Finalement, la réponse pour une multicouche Ag (35 nm), $SiO_2$ (180 nm), (Pd 3 nm) déposé sur une longueur de 0.5 cm permet d'obtenir un bon compromis entre la résolution et la sensibilité du capteur. Ce nouveau design permet notamment de réduire la zone sensible et ainsi de miniaturiser dans le future ce type de capteur.

Dans une deuxième partie, nous caractérisons la réponse du capteur. Pour des raisons expérimentales, nous remplaçons l'Ag par l'Au.

Les résultats expérimentaux confirment le déplacement du pic de résonance pour des concentrations comprise entre 0.5 et 4 % d'$H_2$ dans l'Ar (fig. 5.9). Cependant, le déplacement observé est opposé à celui prédit. Nous supposons que la microstructure du Pd (film discontinue composé d'ilot de Pd) est responsable de cette différence.

La réponse est reproductible sur plusieurs cycles d'hydrogénation-déshydrogénation. Nous obtenons une réponse rapide, de 3 s pour 4 % $H_2$ dans de l'Ar, grâce à l'utilisation de couches minces (et probablement discontinues) de Pd. A l'heure actuelle, ce temps de réponse est le plus rapide pour les capteurs à fibres optiques par modulation de longueur d'ondes pour la détection d'hydrogène.

En conclusion, nous avons démontré théoriquement et expérimentalement pour la première fois un capteur à fibres optiques SPR à modulation de longueur d'onde pour la détection d'hydrogène. En particulier, ce design permet de proposer un capteur d'hydrogène fiable et rapide.

## Chapitre 6

Dans le but d'étendre la plage de détection, nous avons étudié la possibilité d'utiliser un alliage de Mg-Ti comme couche sensible pour réaliser un capteur à fibres optiques intrinsèque pour la détection d'hydrogène. Dans ce chapitre, nous présentons successivement le principe et les réponses expérimentales de plusieurs configurations pour mettre en avant les caractéristiques du Mg-Ti. Dans une première partie, nous déposons une multicouche MgTi/ Pd directement sur le coeur d'une fibre optique multimode. L'étude est faite pour différentes compositions et différentes épaisseurs. Dans une deuxième partie, nous déposons la couche multicouche MgTi/ Pd sur la couche plasmonique (Au/Sio2) proposée au chapitre 6.

Dans les deux précédents chapitres, nous avons mis en avant le lien entre la réponse du capteur (plage de détection) et les courbes « isothermes de pression-composition »(pcT) du système Pd-H. Contrairement au Pd, la formation de la phase $\beta$ de l'hydrure métallique Mg-Ti a lieu pour des pressions d'hydrogène beaucoup plus faibles que le Pd. De plus, l'hydrogénation du Mg-Ti présente un large contraste optique. Le matériau métallique devient transparent (fig. 6.1) et peut être considéré comme un diélectrique sous la forme d'hydrure de Mg-Ti. Une couche de Pd est déposée sur l'alliage Mg pour dissocier l'hydrogène et protéger l'oxydation de la couche sensible.

Tout d'abord, nous déposons une multicouche MgTi/ Pd directement sur le coeur d'une fibre optique multimode. Dans un premier temps nous simulons la réponse du capteur (section 6.2.1). Ce design est semblable au capteur décrit au chapitre 4. La détection est basée sur la modulation de l'intensité en fonction de la concentration d'hydrogène. La formation de l'hydrure modifie l'ouverture numérique de la section sensible. Cette modulation dépend fortement de l'épaisseur de l'alliage Mg-Ti. En effet, en fonction de l'épaisseur du Mg-Ti, la couche Pd peut modifier la réponse du capteur. En particulier, lorsque l'épaisseur de la couche de Mg-Ti diminue (de l'ordre d'une dizaine de nanomètre), la couche de Pd (négligeable lorsque la couche Mg-TI est supérieure à 50 nm) doit être considéré. Dans un deuxième temps, nous étudions expérimentalement la réponse des capteurs pour différentes compositions et épaisseurs de l'alliage.

Pour une multicouche $Mg70Ti_{30}$ (50 nm) / Pd (25 nm), l'intensité diminue en présence d'hydrogène (fig.6.5a). Le capteur réalisé est sensible à une concentration de 0.5 % $H_2$ dans l'Ar. La réponse est reproductible sur plusieurs cycles d'hydrogénation-déshydrogénation et dépendante de la longueur d'onde. L'intensité diminue pour toutes les longueurs d'ondes comprises dans notre plage d'étude (450-900 nm). Nos résultats expérimentaux et théoriques (section 6.2.2) sont cohérents. Il est intéressant de noter que la valeur finale est la même pour des concentrations entre 0.2 % et 0.5 % $H_2$ dans l'Ar. En effet, la phase $\beta$ de l'hydrure est formée au dessus de 0.1 % $H_2$, comme expliqué à la section 6.2.3. D'autre part, nous observons que la réponse dépend fortement de la concentration d'hydrogène. En dessous de 0.4 % $H_2$ dans l'Ar, la réponse est trop lente pour être utilisé pour des applications de sécurité.

Pour une multicouche $Mg_{60}Ti_{40}$ (50 nm)/ Pd (17 nm), l'intensité diminue en présence d'hydrogène et est fonction de la longueur d'onde, comme prédit. Cependant, une légère déviation est obtenue entre nos résultats théoriques et expérimentaux. En effet, la permittivité diélectrique du $Mg70Ti_{30}$ a été utilisée dans nos simulations. Enfin, nous observons que le temps de réponse et la plage de détection ne sont pas modifiés, de manière significative, en changeant la composition de l'alliage.

Lorsque l'épaisseur de la couche de Mg-Ti diminue (de l'ordre d'une dizaine de nanomètre), le capteur présente une réponse surprenante : (i) la réponse spectrale du capteur ne correspond pas à nos résultats théoriques, (ii) le temps de réponse et (iii) la plage de détection du capteurs est différentes de nos précédents résultats (couches d'épaisseurs 50 nm), comme illustré dans la section 6.4. Nous supposons que l'épaisseur de l'alliage et la présence de couches voisines modifient les propriétés thermodynamiques du système Mg-Ti. Nous devons dans le futur étudié les propriétés physiques et optiques des couches minces de Mg-Ti au cours de la formation de l'hydrure métallique.

Dans une deuxième partie, nous déposons la couche multicouche Mg-Ti/ Pd sur la couche plasmonique (Au/Sio2) proposée au chapitre 6. Bien que les résultats théoriques montrent un large déplacement du pic de résonance, les résultats expérimentaux ne sont pas concluant (fig.6.3). En effet, dans le but d'éviter l'extinction du pic de résonance, la couche de Mg-Ti doit être extrêmement fine. Or d'après notre précédent résultat, l'alliage Mg-Ti est susceptible de présenter de nouvelles caractéristiques lors de la formation de l'hydrure pour des couches extrêmement fine.

En conclusion, il est possible d'utiliser un alliage de Mg-Ti comme couche sensible pour réaliser un capteur à fibres optiques intrinsèque. Cependant, la plage de détection n'est pas nécessairement améliorer par rapport à une couche de Pd, limité par le temps de réponse.

## Conclusion

Nous avons développé plusieurs capteurs à fibres optiques SPR pour la détection d'hydrogène. Au vu de nos résultats, il apparait clairement que les capteurs plasmoniques à fibres optiques sont une technologie prometteuse pour réaliser un capteur sensible, rapide et fiable. Les prochaines investigations devront permettent d'améliorer la fabrication des capteurs et leurs intégrations dans des systèmes industrielles (« packaging »). Il serait par la suite intéressant d'étendre le design proposé aux fibres optiques monomodes et à l'optique intégré pour améliorer les performances des capteurs proposés.